

Universidad de
Oviedo

Tesis Doctoral

**QUANTUM-MECHANICS SIMULATIONS OF BI
AND TRIDIMENSIONAL PERIODIC SYSTEMS**

Thermal Models, Friction and Self-Assembly

David Abbasi Pérez

Febrero 2015

Programa de Doctorado: Química Teórica y Modelización Computacional
Departamento de Química Física y Analítica



primer lugar la molécula de pTmDC en fase gas: la geometría de equilibrio y barrera de isomerización de los monómeros. Encuentran un amplio número de dímeros, trímeros o conectores (linkers), y cadenas o cintas asumiendo que todos ellos se encuentran en un mismo plano. Esta ligadura es una primera manera de inferir la influencia de la superficie. Empleando análisis de la densidad electrónica, se describen en detalle los enlaces de hidrógeno responsables de las estructuras poliméricas encontradas. El segundo capítulo de este bloque incluye de manera explícita la superficie. Ahora las dos formas conformacionales del monómero que existían en fase gas, se transforman en tres (cis, D-trans y L-trans), y los posibles sitios de adsorción son en la práctica innumerables. De manera sistemática, se analizan las principales posibilidades de localización de un monómero sobre la superficie, y se describe de forma exhaustiva la variedad de mecanismos asociados con la deposición y crecimiento de estructuras supramoleculares de pTmDC sobre la superficie de plata. La incorporación de la técnica cinética Monte Carlo supone en este estudio un elemento esencial para contribuir a la modelización y al entendimiento del fenómeno del autoensamblado de moléculas orgánicas en superficies metálicas.

RESUMEN (en Inglés)

This thesis has the title "Quantum-Mechanics Simulations of Bi and Tridimensional Periodic Systems. Thermal Models, Friction and Self-Assembly". It addresses the detailed understanding of a number of interesting Materials Science phenomena from a theoretical chemistry and computational modeling perspective. It was motivated by the lack of algebraic and methodological developments (and, therefore, no computational codes) and the absence of efficient computational models able to correctly undertake rigorous studies of the problems that are investigated in this thesis. Thermal effects on crystalline systems, weak chemical interactions or dynamics at a microscopic level of molecular systems on metallic surfaces are representative examples of the subject matter of this thesis.

We can briefly summarize in three blocks the main contents of this research:

- a) Thermal models. A new module to account for thermal effects in solids is implemented in our home-made and popular (more than 500 cites) GIBBS code. A Debye-Einstein like approach is included to calculate thermodynamic properties of crystals. It is also applied to a technological interesting material, scintillator-detector BaWO_4 , which tetragonal-monoclinic pressure-induced transition barrier was determined.
- b) Graphite under general hexagonal-like stresses. Equations for non hydrostatic conditions are proposed and used to explore how graphite behaves under these general hexagonal-like stresses. In combination with micro Raman experiments in anvil cells, a thorough description of friction phenomena at a molecular level is provided.
- c) Self-assembly of p-Terphenyl-m-Dicarbonitrile (pTmDC) on silver (111) surface. Extensive gas phase and on the surface computational studies of equilibrium configurations of different monomers, dimers, linkers, and ribbons of this system were carried out to investigate how pTmDC supramolecular structures evolve on this silver surface. Besides first principles total energy calculations, other computational state-of-the-art computational methodologies are introduced to address this phenomenon. These included the nudged elastic band method and kinetic Monte Carlo technique. Results are confronted with scanning tunnel microscopic images. Analogies and discrepancies are critically analyzed.



All in all, the complexity of the problems under study in this thesis was successfully addressed by means of computational tools and models that can provide unequivocal descriptions and detailed explanations at a molecular level. Step forwards have been given with contributions in a new code to account thermal effects in crystals, the understanding of the origin of static friction in graphite, and the description of how pTmDC molecules combine and form supramolecular structures in silver (111) surface.

**SR. DIRECTOR DE DEPARTAMENTO DE _Química Física y Analítica
SR. PRESIDENTE DE LA COMISIÓN ACADÉMICA DEL PROGRAMA DE DOCTORADO EN _Química Teórica y
Modelización Computacional**

A mi familia.

AGRADECIMIENTOS

Este trabajo ha sido posible gracias a la financiación por parte del extinto Ministerio de Ciencia e Innovación (MICINN) mediante una beca FPI de la que he sido beneficiario, y gracias también al proyecto CONSOLIDER CSD2007-00045, con el que ha sido posible crear el clúster de supercomputación MALTA, donde se han realizado la gran parte de los cálculos de la presente tesis.

Quiero agradecer a todas las personas que han pasado por el grupo de Química Cuántica de la Universidad de Oviedo, por crear un ambiente tan agradable y familiar donde se podía ir a trabajar con una sonrisa y salir con una carcajada. Sin duda alguna, así se trabaja $\frac{1}{0}$ mejor. Aun a riesgo de dejarme nombres en el tintero, intentaré mencionarlos a todos: Miriam, Mamel, Alberto, Julia, Rober, Fonsu, Marcos, Lucía, Marco, Michi, Ángel, Evelio, Aurora, Miguel, Víctor, Marga, José, Marian, Hussien, Dani, Fer. . .

A Jeff y a Elkin, por compartir conmigo las venturas y desventuras del Máster y los largos años de tesis que le siguieron, durante los cuales incontables veces salíamos de la facultad a horas intempestivas de la noche, para cenar y regresar de nuevo una vez rellenado el estómago. Qué noches la de aquellos días. . .

Agradezco también a Mónica Calatayud de la Université Pierre et Marie Curie de París, el haberme acogido para hacer una maravillosa estancia en su grupo. Allí se fraguó la precuela de este trabajo. También agradecer al profesor Lev Kantorovich, por permitirme trabajar con él, primero durante la estancia tan fructífera que hice en el King's College London bajo su dirección, y después por estar a caballo entre Londres y Oviedo con una energía y un humor encomiables.

Mención especial, merecen mis directores de tesis, Miriam Marqués Arias y José Manuel Recio Muñoz, ya que ellos han estado al pie del cañón empujándome hacia adelante cuando estaba perdido entre un mar de dudas transformándolo en un océano de conocimiento, del cuál espero haber podido recoger al menos unas gotas. Y a Mamel también le toca mención especial, que si no ha sido el director, sí ha sido el administrador. Gracias a él esta tesis puede aportar resultados numéricos, calculados en el clúster de supercomputación MALTA, que tan bien ha sabido manejar.

RESUMEN

Esta tesis, titulada "Simulaciones Mecánico-Cuánticas de Sistemas Periódicos Bi y Tridimensionales. Modelos térmicos, fricción y auto ensamblado", aborda desde la perspectiva de la química teórica y computacional la explicación detallada y el entendimiento de diferentes fenómenos de alto interés científico en el campo de la ciencia de materiales. Los efectos térmicos en sistemas cristalinos, las interacciones químicas débiles o la dinámica en la escala microscópica de sistemas moleculares sobre superficies son ejemplos representativos fundamentales en nuestra investigación.

El trabajo está dividido tres bloques:

- a) Modelos térmicos. Se desarrolla un modelo de tipo Debye-Einstein y se implementa dentro del código computacional GIBBS. Se facilita así el uso generalizado de este nuevo modelo a la vez que se enriquece un código que goza de popularidad en la comunidad científica del campo de las altas presiones (más de 500 citas). Esta metodología se aplica al estudio de un sólido complejo, el BaWO_4 , material con interés tecnológico en el desarrollo de detectores centelleadores. Se ilustra la capacidad de los modelos térmicos propuestos en la descripción del diagrama de fases presión-temperatura de este compuesto incluyendo el estudio pormenorizado del efecto de la temperatura en una transición de fase tetragonal-monoclínica inducida por presión.
- b) Comportamiento bajo condiciones hidrostáticas y no hidrostáticas e interpretación microscópica de la fricción estática y dinámica del grafito. Esta investigación está recogida en dos capítulos. A pesar de su simple composición química, las simulaciones computacionales en el grafito no son triviales debido a la naturaleza diversa de las interacciones entre sus átomos. Se ha desarrollado una estrategia computacional capaz de ser aplicada en principio no sólo al grafito sino a materiales con simetría hexagonal.

Se han obtenido las ecuaciones de estado uniaxial, biaxial y triaxial del grafito preservando su simetría hexagonal. Además, con estas ecuaciones ha sido posible acceder a una descripción de la fricción estática que sufre una lámina de grafito al deslizarse entre otras dos fijas. Este trabajo, junto con una novedosa técnica experimental de análisis Raman que permite estudiar la presión en grandes regiones de la muestra, aportan un nuevo enfoque al campo de la investigación de la fricción.

- c) Autoensamblado de para-Terfenil-meta-Dicarbonitrilo (pTmDC) sobre $\text{Ag}(111)$. Esta investigación también está dividida en dos capítulos. El primero de ellos analiza en primer lugar la molécula de pTmDC en fase gas: la geometría de equilibrio y barrera de isomerización de los monómeros. Encuentran un amplio número de dímeros, trímeros o conectores (linkers), y cadenas o cintas asumiendo que todos ellos se encuentran en un mismo plano. Esta ligadura es una primera manera de inferir la influencia de la superficie. Empleando análisis de la

densidad electrónica, se describen en detalle los enlaces de hidrógeno responsables de las estructuras poliméricas encontradas. El segundo capítulo de este bloque incluye de manera explícita la superficie. Ahora las dos formas conformacionales del monómero que existían en fase gas, se transforman en tres (cis, D-trans y L-trans), y los posibles sitios de adsorción son en la práctica innumerables. De manera sistemática, se analizan las principales posibilidades de localización de un monómero sobre la superficie, y se describe de forma exhaustiva la variedad de mecanismos asociados con la deposición y crecimiento de estructuras supramoleculares de pTmDC sobre la superficie de plata. La incorporación de la técnica cinética Monte Carlo supone en este estudio un elemento esencial para contribuir a la modelización y al entendimiento del fenómeno del autoensamblado de moléculas orgánicas en superficies metálicas.

ABSTRACT

This thesis has the title “Quantum-Mechanics Simulations of Bi and Tridimensional Periodic Systems. Thermal Models, Friction and Self-Assembly”. It addresses the detailed understanding of a number of interesting Materials Science phenomena from a theoretical chemistry and computational modeling perspective. It was motivated by the lack of algebraic and methodological developments (and, therefore, no computational codes) and the absence of efficient computational models able to correctly undertake rigorous studies of the problems that are investigated in this thesis. Thermal effects on crystalline systems, weak chemical interactions or dynamics at a microscopic level of molecular systems on metallic surfaces are representative examples of the subject matter of this thesis.

We can briefly summarize in three blocks the main contents of this research:

- a) Thermal models. A new module to account for thermal effects in solids is implemented in our home-made and popular (more than 500 cites) GIBBS code. A Debye-Einstein like approach is included to calculate thermodynamic properties of crystals. It is also applied to a technological interesting material, scintillator-detector BaWO₄, which tetragonal-monoclinic pressure-induced transition barrier was determined.
- b) Graphite under general hexagonal-like stresses. Equations for non hydrostatic conditions are proposed and used to explore how graphite behaves under these general hexagonal-like stresses. In combination with micro Raman experiments in anvil cells, a thorough description of friction phenomena at a molecular level is provided.
- c) Self-assembly of p-Terphenyl-m-Dicarbonitrile (pTmDC) on silver (111) surface. Extensive gas phase and on the surface computational studies of equilibrium

configurations of different monomers, dimers, linkers, and ribbons of this system were carried out to investigate how pTmDC supramolecular structures evolve on this silver surface. Besides first principles total energy calculations, other computational state-of-the-art computational methodologies are introduced to address this phenomenon. These included the nudged elastic band method and kinetic Monte Carlo technique. Results are confronted with scanning tunnel microscopic images. Analogies and discrepancies are critically analyzed.

All in all, the complexity of the problems under study in this thesis was successfully addressed by means of computational tools and models that can provide unequivocal descriptions and detailed explanations at a molecular level. Step forwards have been given with contributions in a new code to account thermal effects in crystals, the understanding of the origin of static friction in graphite, and the description of how pTmDC molecules combine and form supramolecular structures in silver (111) surface.

ÍNDICE GENERAL

1. Introduction and Objectives	1
1.1. Thermal Models	3
1.2. Graphite	3
1.2.1. Theoretical	3
1.2.2. Experimental	5
1.3. Self-assembly	6
1.3.1. Gas Phase	6
1.3.2. On Surface	7
2. Thermal Models	11
2.1. Practical Computational Models for Thermal Effects in Solids	11
2.1.1. Implementation of the Debye model in the GIBBS code	11
2.1.2. Fleche's approach	12
2.1.3. GIBBS - Fleche new module of calculation	13
2.2. Thermodynamics of Barium Tungstate Polymorphs	13
2.2.1. Required calculations: electronic energies and frequencies	13
2.2.2. Static description, frequencies, and thermal EOS	15
2.2.3. Temperature dependence of thermodynamic properties	17
2.2.4. Scheelite \leftrightarrow BaWO ₄ -II phase transition	20
3. Graphite Under Non Hydrostatic Stress	23
3.1. Thermodynamic Potentials	23
3.2. 3D and 2D Periodic Models of Graphite	25
3.3. Results and Discussion	26
3.3.1. Bulk graphite under hydrostatic and non-hydrostatic conditions	26
3.3.2. Graphite slabs under uniaxial conditions	33
4. Frictional Forces on Graphite	41
4.1. Experimental and Computational Details	41
4.1.1. Experiments	41
4.1.2. Computer Simulations	42
4.2. Results and Discussion	43
4.2.1. Stress Analysis	43
4.2.2. Friction Analysis	46
5. Building Motifs of pTmDC	53
5.1. Methods	53

5.2.	Results	54
5.2.1.	Monomers	54
5.2.2.	Dimers	56
5.2.3.	Ribbons	60
5.2.4.	Linkers	62
6.	Self Assembly of pTmDC on Ag(111)	67
6.1.	Methods	67
6.2.	Results	68
6.2.1.	Monomers on the silver surface	68
6.2.2.	Dimers on the silver surface	75
6.2.3.	Linkers and ribbons on the silver surface	81
6.2.4.	Islands on the silver surface	82
6.3.	Kinetic Monte Carlo simulation	84
7.	Conclusions	93
7.1.	Thermal Models. Thermodynamics of Barium Tungstate	93
7.2.	Graphite	93
7.2.1.	Non-Hydrostatic Stress	93
7.2.2.	Static Friction	94
7.3.	Self-Assembly	94
7.3.1.	Gas Phase	94
7.3.2.	On Surface	95
7.4.	Modelos Térmicos. Termodinámica del Wolframato de Bario	97
7.5.	Grafito	97
7.5.1.	Estrés No Hidrostático	97
7.5.2.	Fricción Estática	98
7.6.	Autoensamblado	99
7.6.1.	pTmDC en Fase Gas	99
7.6.2.	pTmDC en Superficie Ag(111)	99
A.	Artículos	103
B.	Informe del Índice de Impacto de las Publicaciones	193
	Índice de figuras	197
	Bibliografía	207

1

INTRODUCTION AND OBJECTIVES

"Sólo sé que no sé nada"

Sócrates

THE properties of materials are ultimately determined by the interactions of electrons and nuclei, being those interactions governed by the laws of quantum mechanics. In 1929, shortly after the Schrödinger equation was formulated,¹¹⁶ Dirac stated:³⁷ "The general theory of quantum mechanics is now almost complete. [...] The underlying physical laws necessary for the mathematical theory of a large part of physics and the whole of chemistry are thus completely known, and the difficulty is only that the exact application of these laws leads to equations much too complicated to be soluble." In 1964, Hohenbergh and Kohn,⁵⁷ and Kohn and Sham⁶⁹ reformulated the Schrödinger equation, which involves all the $3N$ spatial coordinates of N interacting electrons into the density functional theory (DFT). It casts the intractable complexity of the electron-electron interaction into an effective one-electron potential, which is a functional of the electron density (function of only three spatial coordinates) via the exchange-correlation functional. Although the "amazing functional" that would make the reformulation of the many-body Schrödinger equation exact is unknown, approximate functionals have proven to be highly successful in describing many material properties.

Efficient algorithms devised for solving the Kohn-Sham equations have been implemented in a large number of increasingly sophisticated codes. And, nowadays, due to the advances in computing power, these DFT codes are routinely applied in research on materials across physics, chemistry, materials science, and nanotechnology.

High-pressure research is an important and very active field within materials science (see Ref. 133 and references therein). In crystals, the most dramatic effect of pressure is when it causes phase transitions that result in either new polymorphs or different chemical compounds. The new crystal structures, sometimes with unusual stoichiometries, may present unexpected chemical and physical properties. For example, most of the elements become superconductors under sufficient pressure, and simple metals, such as Li and Na, transform into insulators.^{81,82} A novel state of matter is then un-

veiled. Pressure also facilitates chemical reactions by lowering the kinetic barriers. For instance, hydride phases of most transition metals can be obtained.

Experimentally, diamond-anvil-cell devices combined with X-ray and neutron diffraction as well as other experimental probes, such as Raman spectroscopy, have been able to determine crystal structures up to the megabar region (pressure in the Earth's inner core reaches 3.6 Mbar). Most recently, advances in dynamic compression techniques have allowed to reach pressure beyond 10 Mbar.⁸⁷ However, these methods can be expensive and difficult (use of toxic chemicals, reaction between light elements and diamond, etc.). In addition to it, X-ray power diffraction data can be of poor quality or incomplete (the positions of hydrogen atoms cannot easily be determined) and pressures within giant planets, such as Jupiter, are not accessible. Therefore, *ab initio* calculations are necessary to interpret and complement experiments, as well as to predict novel materials as targets for synthesis. For instance, the coupling of global searching methods with DFT codes allows to predict the stable crystal structure of a material and its phase transformations with pressure. However, it remains the challenge of the inclusion of the thermal effects and the prediction under non-hydrostatic conditions.

This thesis is the result of a thorough theoretical and computational study of a variety of chemical and physical properties of materials. Methodological developments, molecular modeling and first principles simulations have been the subject of the investigations that will be reported in this document. The collaboration with experimental groups has been present constantly. Three broad areas have been addressed in detail. First, thermodynamics of crystalline solids. Our contribution is the incorporation of practical thermal models to a home-made computational program that allows a more accurate determination of thermodynamic properties of crystals solids under variable pressure and temperature conditions. Second, the response to non-hydrostatic stresses of a layered material as graphite. New computational strategies and their application to unveil the microscopic origin of the static friction coefficient have been the focus of this second part. And finally, modelling and simulations of self-assembly processes on metal surfaces. A combination of computational techniques and visualization tools illustrate the advantages of our approach in a complex phenomenon of multidisciplinary character. Motivation and specific goals within these three areas are presented below.

The final aim was to add new knowledge to the theoretical and computational chemistry of materials. We pretend to introduce in our research group new computational strategies, broad the thermodynamic conditions under which crystalline materials can be microscopically studied by first principles methodologies, and extend the simulations from previous detailed calculations in the bulk to two dimensional systems. Many interesting results have emerged and compared with others obtained in the laboratory. X-ray data and Raman frequencies from diamond anvil cell experiments in highly oriented pyrolytic graphite or images from scanning tunneling microscopy studies are two examples of observations where the application of our simulation and

model techniques have produced results to compare with. Let us now introduce in separate subsections the three major parts of this thesis.

1.1 THERMAL MODELS

PART of the work presented in this block has to do with the development of a new code aimed at the determination of equations of state and thermodynamic properties of solids using thermal models of different complexity, specially directed to deal with crystalline structures with a large number of atoms in their unit cell.¹⁰² It is an extension of the GIBBS code¹⁴ in the light of the ideas and equations proposed by Fleche⁴³ to account for thermal effects beyond the Debye approximation. Although, already published, a brief description of the original code, Fleche's equations, and the new model will be given to make this part more comprehensive. We will illustrate the performance of the code and the differences between the original and the new thermal models by the evaluation of reliable thermodynamic data for the low pressure tetragonal (scheelite) and the high-pressure monoclinic (BaWO₄-II) phases of BaWO₄.

Experimental results on the high pressure and high temperature behavior of this system provide new insights on the equation of state parameters and phase transformations exhibited by crystalline compounds with A^{II}B^{VI}O₄ stoichiometry. From the ambient conditions scheelite-type structure, a new monoclinic phase, BaWO₄-II, emerges at elevated pressures if temperature is high enough to overcome the kinetic barrier associated with this transformation. Thermal effects appear to be crucial to assess the thermodynamic conditions of phase stability and metastability.

For **tetragonal and monoclinic BaWO₄ phases**, first principles calculations have been carried out to evaluate: **(i) the crystal energy as a function of the unit cell volume, and (ii) the vibrational frequencies at the Γ point of the zero static pressure equilibrium geometries.** Results on thermal effects show that differences between Debye and Debye-Einstein models are not large for properties such as the specific heat at constant volume, but may be important for the zero pressure bulk modulus and, specially, for thermal expansion.

1.2 GRAPHITE

1.2.1 Theoretical

HYDROSTATIC and non-hydrostatic stress conditions open avenues for new synthetic routes and unknown phase transformations, and for novel applications of materials with otherwise undisclosed properties.^{58,131} All these new phenomena induced

by general stress conditions demand fundamental research at both, experimental and theoretical fronts to address many interesting challenges. In anvil cell experiments, it is well-known that the maximum pressure that can be reached under hydrostatic conditions depends on the specific transmitting medium.⁶⁸ Propolenko *et al.* observed the crucial effect of non-hydrostaticity in the phase diagram of silica after carrying out a number of diamond anvil cell experiments without transmitting fluid.¹⁰⁷ More recently, measurements on highly oriented pyrolytic graphite (HOPG) show that a direct examination of the material response to non-hydrostatic stresses is possible, in principle, combining micro-Raman spectroscopy with a careful experimental set up of the cell in which the sample is directly placed between the anvils, without gasket and pressure transmitting media.^{31,32}

First-principles calculations constitute efficient tools to assist these experiments, should we provide a thorough insight on the chemistry and physics of the phenomena. As an illustrative example, Liang *et al.* were able to clarify the experimental controversy on high dense phases of silica "by invoking the important role of non-hydrostatic stresses" through molecular dynamics simulations.⁷⁵ Under general stress conditions, specific thermodynamic potentials have to be introduced for a global searching of the equilibrium stable structures.^{127,121} Two different computational strategies are worth to be remarked. Since one of the main interests from the calculations is the determination of the relationship between stress (σ) and strain (ϵ) tensors, one possibility is the calculation of the equilibrium ϵ components under a given σ tensor. Inversely, and more frequently in standard methodologies, the components of σ are evaluated for different values of the strain tensor, that are given in this second strategy as input data to the computational package. Both schemes have to yield the same ϵ - σ information within the uncertainty of the numerical procedure.

Graphite demands extensive studies concerning its response to hydrostatic and non-hydrostatic stresses, and, at the same time, constitutes a paradigmatic system to check how computational simulations perform under these general stress conditions. In contrast with the hydrostatic regime where graphite have been thoroughly investigated (see for example recent computational works by Savini *et al.*¹¹⁵ and Colonna *et al.*²⁴), there are not explicit calculations of graphite under non-hydrostatic conditions. Simulations that preserve the hexagonal space group of graphite are in principle enough to cover structural and spectroscopic (IR and Raman) observations carried out on HOPG.^{31,32,53,49} In addition, simulations of graphite under specific biaxial stresses can be used to evaluate its resistance to reduce the surface area of a two dimensional (2D) graphite layer. Interestingly, the formal analogy with the well-known bulk scenario allows us the definition of equivalent equation of state parameters for 2D and 1D-like stresses. Furthermore, regarding uniaxial stresses, knowledge of the reduction of graphite interlayer separations under compression provides one of the two legs (the normal force) to evaluate the friction coefficient between two graphite layers. The second leg (the friction force) can be determined from the energetic profile of one graphite layer sliding between other graphite layers.

In this thesis, we aim to contribute to the understanding of the mechanical response of HOPG under general hexagonal-like stress conditions. Structural, vibrational and electronic structure calculations mimicking uniaxial, biaxial, and triaxial stresses have been carried out in graphene to determine: (i) 1D, 2D, and 3D equation of state (EOS) parameters of graphite, and (ii) pressure coefficients for in-plane vibrational modes at the center of the Brillouin zone. These results will provide information to propose equivalences between hydrostatic and non-hydrostatic conditions depending on the specific property of graphite under study. In addition, slab periodic models have been considered to explore the sliding landscape potential energy of a graphite layer at different directions and displacements in bulk graphite. Our goal here is to describe friction phenomena in graphite (not graphene) and, therefore, one graphite layer is confined between other two at interlayer distances following the computed uniaxial equation of state of graphite. These simulations allows us not only to evaluate friction forces and the static friction coefficient of graphite, but also to get insight at an atomic level into the sliding paths that minimize the friction between graphite layers. As far as we know, our study provides for the first time computational results of the behavior of graphite under non-hydrostatic conditions.

1.2.2 Experimental

GRAPHITE is among the best solid lubricants, but it is also known that graphite behaves as a poor lubricant in vacuum.¹¹⁴ Such a diverse behaviour makes graphite a target model in many frictional/tribological studies at both macroscopic¹² and atomic^{13,35,91} levels. Graphite also was the first system studied in the seminal work by Mate et al.⁸⁴ when the friction force microscope (FFM) was developed. Nowadays graphene has emerged into the scene of frictional studies^{74,42,67} and many works have been focused on understanding the underlying mechanisms of friction in graphite^{78,119} and graphene.¹¹⁸ For instance, novel terms like superlubricity^{56,36} have been coined to refer to the near-zero friction force observed between a graphite substrate and a graphite flake in an incommensurate configuration.

Typical FFM results consist of a periodic variation of the lateral force with the sliding distance, reflecting a characteristic stick-slip motion pattern.¹⁹ In stick-slip phenomena, static friction determines the force to be overcome during the stick phase, before the slip takes place at the interface. Key parameters are the static and kinetic friction coefficients, μ_s and μ_k , respectively, which are related to the force required to initiate motion between two contacting surfaces and the force to maintain the surfaces in the subsequent relative motion.¹² Such dynamic experiments have been successfully interpreted in terms of analytical models,^{97,39} like the Prandtl-Tomlinson, Frenkel-Kontorova or a combination of both,¹²⁹ and, with the advancement of computational capabilities, first principles calculations now play a major role to understand atomic-scale interactions.³⁵

FFM studies also present some drawbacks and limitations, since conventional experiments involve one small surface (usually a tip) and application of relatively low loads. As a consequence, there is still little information about static friction between large contact surfaces and at large loads, aspects for which clear understanding at the atomic level is yet to be achieved.

Our investigation **aims to complete the fundamental knowledge of friction phenomena** by examining the static regime emerging when both large loads and large contact surfaces meet simultaneously, conditions which are difficult to achieve in FFM experiments. Again, graphite is particularly suited for our purposes, since a perfect specimen presents an ideal ABA commensurate configuration due to its highly symmetrical layered structure. Graphite can therefore be regarded as a model for studying interlocking single asperity problems⁹⁰ at the atomic scale, in the classical Bowden and Tabor's view.¹⁷ We face this challenge by combining our computational simulations with an experimental approach which is radically different to those existing in the literature. By squeezing highly oriented pyrolytic graphite (HOPG) specimens between two opposed anvils, it is possible to estimate the ensuing static friction forces opposed to the displacement of the graphene layers in graphite. These rather unconventional experiments in anvil devices are monitored by micro-Raman spectroscopy, which is among the most powerful techniques to probe carbon materials.^{128,79} It provides direct access to the stress distribution of both anvils (see Ref. 33) and samples,⁷⁹ and is especially suited for anvil devices.⁴¹

An important effort in our investigation concerns the interpretative capability provided by our computer simulations on graphite under different non-hydrostatic stresses (see above).³ These calculations were performed using density-functional theory (DFT) including corrections to account for dispersion effects (DFT-D2⁵⁰), which are known to yield reliable results for graphite.²¹ We obtained the 2D energy landscape (*i.e.* the corrugation potential) and studied the misfit angle dependence of static friction.³ The load dependence of these quantities was evaluated by varying the interlayer distances of a tri-layer graphene model, exceeding the stress range covered in the experiments. Here, **these simulations are exploited to carry out a deep interpretative analysis of the experimental data**. The whole analysis allows us to assess our measurements and to check the validity under large loads of Hertzian-like contact models including adhesive contacts.⁸⁶

1.3 SELF-ASSEMBLY

1.3.1 Gas Phase

SELF-ASSEMBLY of organic molecules on crystal surfaces is an essential tool in fabricating nanodevices.^{10,7,95} Because of its directionality and significant binding strength, hydrogen bonding between molecules has been widely exploited in building

surface molecular assemblies. Detailed knowledge of the interaction between molecules is crucial in identifying the basic building units, thus providing a simple route in understanding of the self-assembled motifs.^{101,66} Obviously, how these motifs are organized is also influenced by the nature (chemical *versus* physical) of the molecule-surface interaction.

In a recent experimental study,⁸³ deposition of [1,1';4',1'']-terphenyl-3,3''-dicyanide (also known as para-Terphenyl-meta-Dicyanide or pTmDC in short) molecules on the Ag(111) surface was investigated by scanning tunneling microscopy (STM).

By employing *ab initio* density functional theory (DFT) calculations, we investigate in this thesis theoretically possible structures that the pTmDC molecules may form with each other. Our main goals are: (i) to provide a rational explanation at an atomic level of the experimentally observed structures of pTmDC molecules on the Ag(111) surface, and (ii) to demonstrate the dominant role that the hydrogen bond plays in holding these molecules together. It was stated that there is a broad range of H bonds which depend on the particular species participating and the specific atomic environment, all united by a "pronounced local aspect".⁵ Following this criterion, we believe that the binding between the molecules studied here corresponds to an attractive interaction between a nitrile group of one monomer and one or two H atoms from a benzonitrile ring of the other, and can be characterised as an H bond bearing in mind that contribution of the dispersion interaction (as will be shown later on) is essential. If we are to believe that H-bonding is the main binding mechanism of inter-molecular interactions, then dimers would serve as the elementary building blocks in forming various structures on the surface. Both points will be demonstrated in this contribution.

In all of the calculations reported in chapter 5, we do not explicitly simulate the surface when studying various molecular structures; all computations have been done in the molecular gas phase with the role of the surface being implicit: only structures which have two-dimensional character were examined. This is a rational computational strategy, which enabled us to consider at a moderate cost relatively large molecular assemblies needed for direct comparison with those seen in experimental images, and hence evaluate the role played exclusively by the H-bonding between molecules in forming these assemblies. The complete modeling of the phenomena including the role of the surface is reported separately in chapter 6.

1.3.2 On Surface

ONE route of building sophisticated nanodevices, as we have indicated previously, is to explore natural ability of many organic molecules to self-assemble on crystal surfaces into structures of various complexity varying from small clusters to ribbons and islands.^{10,7,95} The structures the molecules form on surfaces are a result of a complex interplay between molecule-molecule and molecule-surface interactions, and knowing these may help in understanding many assemblies observed.⁹ However, in

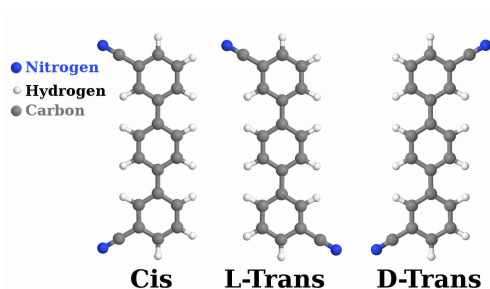


Figure 1: Cis and trans isomers of pTmDC .

order to be able to manipulate the growth of molecules into desired geometries on surfaces, i.e. steer the assembly along a predefined direction to form structures most suitable for the given application, one needs to understand the mechanism of growth of the structures in detail. The latter knowledge cannot be gained just by understanding why the molecules bind to themselves and to the surface, i.e. their ability to form dimers, trimers, and bigger clusters; it requires comprehensive simulations of *kinetics of growth* which in turn necessitates understanding of diffusion mechanism, rates of transformations between different states of molecules on the surface (e.g. between various isomers) and the corresponding rates of formation of clusters of molecules and their decomposition. By means of scanning tunneling microscopy (STM) it is possible to get access to detailed information on how the molecules are organized on the surface and identify the essential building blocks predominant in the self-assembly process. However, time evolution of growth is less accessible to STM based techniques (unless the growth happens much slower than the available scan speeds), and hence theoretical investigation of the factors determining the growth becomes extremely important.

In the gas phase the molecules may exist either in cis (C) or trans (T) forms (isomers) shown in Fig. 1. When evaporated on the silver surface the two isomers can be clearly imaged with STM at room temperature (RT) both appearing in a similar rectangular form. Though the cis isomer is achiral, trans isomer is however prochiral, i.e. depending on which side the molecule gets adsorbed on the surface, two possibilities exist denoted L- and D-trans, Fig. 1.

Using STM, it was found⁸³ that at low coverages upon thermal quenching the molecules form one-dimensional (1D) ribbons which cross with and connect to each other via a number of linkers which molecular arrangement has been resolved. At higher coverages two-dimensional (2D) islands are formed instead. When evaporated on the surface, both cis and trans isomers are expected to be present; however, intriguingly, it was claimed that mostly trans isomers were found in abundance on the surface (e.g. in ribbons) after the self-assembly takes place at either small or large coverage with cis isomers appearing only in small amounts, mostly in linkers and at the ends of the ribbons. Note that it was assumed⁸³ that in all these structures the molecules bind

to each other via double hydrogen bonds. The STM images revealed that both trans species form equivalent structures which are mirror reflections of each other.

Here we go further and consider the silver surface explicitly; moreover, we present a detailed density functional theory (DFT) based theoretical study of the *kinetic processes* responsible for the growth of the observed structures on the Ag(111) surface. Our **main aim is to provide the driving mechanism(s) of self-assembly of pTmDC molecules on this surface at small and up to intermediate coverages.** This includes detailed determination of the transition paths involved in the cis-to-trans isomerization, molecular diffusion, binding and decomposition of molecular structures, followed by extensive kinetics modeling of molecular assemblies themselves based on Kinetic Monte Carlo (KMC) technique. The corresponding energy barriers for the transitions incorporated in the KMC simulations were all calculated using Nudged Elastic Band (NEB)^{61,88} method and DFT.

2 | THERMAL MODELS

WE illustrate here how reliable thermal models can be incorporated to standard first-principles static calculations with the aim to provide thermodynamic properties of crystalline systems. Due to the complexity of the compound and the existence of interesting experimental data, our approach will be applied to the low and high pressure phases of BaWO₄. In a first step, total (electronic) energy calculations were performed under the density functional theory framework including the evaluation of thermal contributions by means of either a simple Debye model or an extended Debye-Einstein approach that requires the calculation of vibrational frequencies at the corresponding Γ points. Secondly, we have undertaken the determination of the Clapeyron slope and the activation energy involved in the low pressure scheelite \leftrightarrow high pressure BaWO₄-II transformation. The pressure-temperature phase boundary is evaluated using the $\Delta G=0$ equilibrium condition at different temperatures, whereas the thermal barrier has been estimated from the experimental temperature at which the metastable scheelite phase converts to the BaWO₄-II structure.

2.1 PRACTICAL COMPUTATIONAL MODELS FOR THERMAL EFFECTS IN SOLIDS

2.1.1 Implementation of the Debye model in the GIBBS code

The GIBBS code has been described extensively elsewhere, see for example Ref. 14 for a thorough explanation of it. Briefly, the only input required by the original version of the model is a set of calculated (E_i, V_i) points, being E_i and V_i the ground state electronic energy and the volume of the solid, both per formula unit. Then, for a given number of pressure (p) values, GIBBS evaluates the enthalpy at each of the input volumes, $H_i = E_i(V_i) + pV_i$, and obtain the equilibrium volume at each pressure using an accurate fitting procedure that ensures numerically stable values for these (p_i, V_i) values. A subsequent calculation of the equation of state (EOS) parameters (the bulk modulus, B_0 , and its pressure derivative, B'_0 , both evaluated at zero pressure), is performed by means of numerical or analytical EOS fittings. This is the procedure that drives to the so-called static description of the solid.

The key for taking into account thermal effects in a simple way within the Debye model at different temperatures (T) is the use of the isotropic approximation in the calculation of the Debye temperature (Θ_D):

$$\Theta_D = \frac{\hbar}{k_B} f(\sigma) \left(6\pi^2 n V_i^{\frac{1}{2}} \right)^{\frac{1}{3}} \left(\frac{B_S}{M_r} \right)^{\frac{1}{2}} \quad (2.1)$$

where M_r is the formula unit molecular mass, B_S is the adiabatic bulk modulus, and $f(\sigma)$ is a function of the Poisson coefficient (σ) that is usually considered constant. Besides, B_S is approximated by the static bulk modulus evaluated from the (E_i, V_i) data points, as seen above (see Ref. ¹⁴ for more details).

Once Θ_D is obtained, the thermodynamics of the solid is at hand using the known expressions of the Debye model.⁶ The computational strategy of GIBBS code consists of evaluating the Gibbs energy of the solid at different formula unit volumes for each of the p and T values given in the input file. From the fitting of this non-equilibrium Gibbs energy, availability or $G^* = E + pV - TS$ (S is the entropy per formula unit), equilibrium G and V values are obtained allowing for the $V(T, p)$ relationship and the evaluation of thermodynamic functions at the specified p and T values.

2.1.2 Fleche's approach

In the light of Fleche's proposal,⁴³ in our investigation we have gone one step beyond the Debye model trying to keep as simple as possible the evaluation of crystalline thermal effects. The procedure consists of computing zone centrum vibrational frequencies ($\nu_j(\Gamma)$) for all the optical modes of the crystal at the zero pressure equilibrium unit cell geometry and the subsequent evaluation of the optical contribution to the Helmholtz function:

$$A_{op} = Nk_B T \sum_{j=4}^{3n} \left[\frac{x_j}{2} + \ln(1 - e^{-x_j}) \right], \quad x_j = \frac{\hbar \nu_j}{k_B T}, \quad (2.2)$$

where N and n are the number of primitive cells and atoms in the cell, respectively, and k_B is the Boltzmann constant.

Thus, $A = A_{st} + A_{ac} + A_{op}$, and other thermodynamic properties are partitioned into static (st), acoustic (ac), and optical (op) contributions. The static one comes from the electronic energy of the solid, E , and the acoustic contribution is evaluated following the Debye model but considering only the 3 acoustic branches when normalizing Θ_D . This explains why the sum in Eq. 2.2 starts in 4.

Obviously, the three contributions change with volume. To evaluate the variation of the optical contribution with V (or p), Fleche approximates the required optical Γ -frequencies at different volumes by scaling the frequencies at the equilibrium zero

static pressure structure by means of computed properties that only depend on the static description of the crystal

$$\nu_i(V) = \nu_i(V_0) \left(\frac{V}{V_0} \right)^{1/6} \left(\frac{B_{st}}{B_0} \right)^{1/2} \left(1 - \frac{2p}{3B_{st}} \right)^{1/2} \quad (2.3)$$

where the 0 subscript refers to the static equilibrium volume at zero pressure, and B_{st} is the bulk modulus corresponding to a different volume (see Eq. 36 in Ref. 43).

2.1.3 GIBBS-Fleche new module of calculation

We will briefly present in this subsection the most important features of the new computational tool. One of the drawbacks of Fleche's scheme is the self-consistent procedure required to determine the equilibrium volume at given (p, T) conditions. This is easily overcome within the GIBBS strategy by evaluating G^* at the formula unit volumes where E was calculated:

$$G^*(V; p, T) = E(V) + pV + A_{vib}(V; T) \quad (2.4)$$

Then, a fitting procedure, as that indicated in subsection 2.1, is carried out to determine the equilibrium volume at the p and T values specified in the input file. $A_{vib}(V; T)$ is evaluated with the Debye-Einstein model, where the three acoustics and the $3n - 3$ optical branches are evaluated in the way described in the previous subsection under Fleche's approach.

The new module was written in FORTRAN77 with the idea to avoid as much as possible modifications of the original GIBBS code. Basically, these modifications consist of programming lines to deal with the new options and the frequencies in the input file, and a new routine to evaluate acoustic and optical contributions to G^* . A FORTRAN90 reimplementation of the original GIBBS program (Blanco *et al.*¹⁴) has been published¹⁰² where this and other new models to introduce temperature effects have been incorporated, from the simple Debye model contained in the original article to a full quasi-harmonic model that requires the phonon density of states at each calculated volume.

2.2 THERMODYNAMICS OF BARIUM TUNGSTATE POLYMORPHS

2.2.1 Required calculations: electronic energies and frequencies

As mentioned in subsection 2.1.1, the only input needed by the code is a set of (E_i, V_i) points for the target system and its zero static pressure vibrational frequencies at Γ . In this work, the electronic structure and the (E_i, V_i) points of the low pressure scheelite and the high pressure monoclinic ($BaWO_4$ -II) phases of $BaWO_4$ were

calculated within a standard first-principles scheme based on the density-functional theory and the pseudopotential method, as implemented in QUANTUM ESPRESSO.⁴⁷ The Perdew-Burke-Ernzerhof (PBE) generalized gradient approximation¹⁰⁶ was adopted for the exchange and correlation potentials in both cases. A kinetic energy cutoff of 80 Ry was employed for the basis set of plane waves. We used a Monkhorst-Pack⁹² grid for the integrations of the Brillouin-zone of $4 \times 4 \times 4$ for the scheelite and $2 \times 2 \times 2$ for the BaWO_4 -II phase. The space groups of scheelite and BaWO_4 -II are tetragonal $I4_1/a$ and monoclinic $P2_1/n$, respectively. The number of geometrical degrees of freedom are 5 (tetragonal) and 40 (monoclinic). This makes a very time consuming task a full quasi-harmonic phonon dispersion calculations and justifies the selection of a more affordable procedure as the Debye-Einstein model we introduce here.

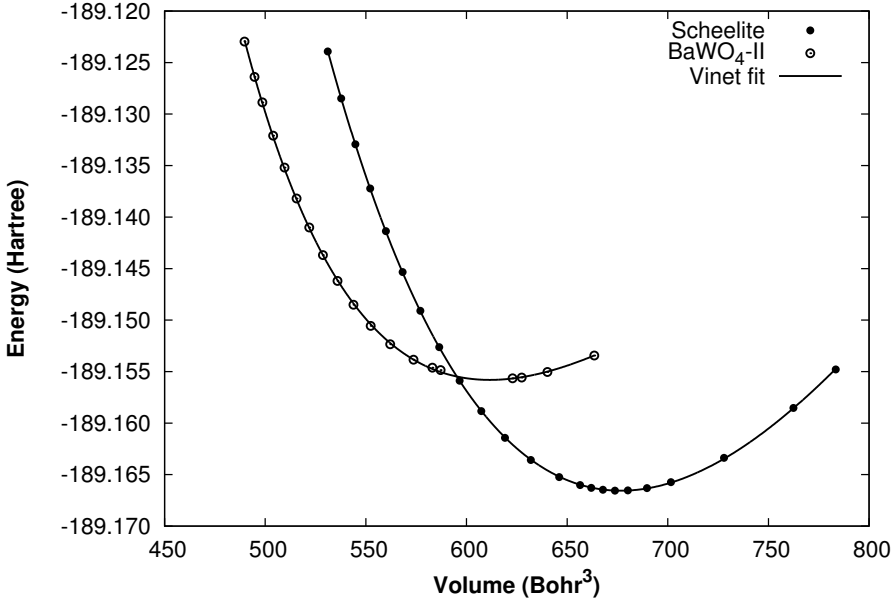


Figure 2: Static $E - V$ fitting Vinet EOS curves. Energy units are given in Hartree and volumes are given in bohr^3 per formula unit.

The calculated static energy-volume points, along with the corresponding Vinet EOS fittings, are shown in Fig. 2. Whereas the tetragonal structure shows a soft energy-volume curve, we have found difficulties in the minimization of the electronic energy of the monoclinic phase specially at volumes around and greater than the zero pressure equilibrium geometry. These difficulties are related to the low curvature and the high number of degrees of freedom. As we will see later, this fact prevents the evaluation of properties for this monoclinic phase when temperature increases if pressure is low.

Vibrational frequencies were computed following two different schemes. For scheelite, we employed the density functional perturbation theory (DFPT) method as implemented in the Quantum ESPRESSO code, while for the high pressure phase the

supercell and small displacements method, combining the Vienna *ab initio* simulation package VASP⁷⁰ with the PHONON code,¹⁰⁴ were used to obtain Γ -frequencies.

2.2.2 Static description, frequencies, and thermal EOS

Following the procedure described in Section 2.1, we obtained the equation of state parameters (V_0 , B_0 and B'_0), and a collection of thermodynamic properties such as entropy (S), Gibbs energy (G), specific heat at constant pressure (C_p), thermal expansion coefficient (α), etc., for the two crystalline polymorphs.

Concerning the static description, we show in Table 1 EOS parameters obtained with the Vinet equation.¹²⁵ In concordance with the stability of the BaWO₄-II phase at high pressure, we obtain a lower zero pressure volume for this polymorph with respect to the scheelite phase. Surprisingly enough, we found, however, a greater B_0 value for scheelite. Although this result is reversed at higher pressure (see Table 1), it can be connected with the set of frequencies evaluated for the two polymorphs at the Γ point and the Clapeyron slope of the scheelite \rightarrow BaWO₄-II transformation (see below). In comparison with ambient conditions experimental values for V_0 , B_0 , and B'_0 (680 bohr³, 52 GPa, and 5.1, respectively, see Ref. 40), static calculations provide a successful description of the scheelite EOS. For the monoclinic phase a volume of 558 bohr³ at 6 GPa and 700 K has been reported by Lacomba-Perales *et al.*⁷¹, that compares well with our static value.

Table 1: Static and different temperature values for V_0 , B_0 and B'_0 at $p = 0$ and $p = 6$ GPa obtained with the new Debye-Einstein model (and Debye in brackets). Volumes are given per unit formula. EOS parameters from the Vinet EOS.

0 GPa						
	Static	Scheelite		Static	BaWO ₄ -II	
		0 K	300 K		0 K	100 K
$V_0(\text{bohr}^3)$	676.7	687.7 (682.2)	697.6 (693.8)	611.5	649.6 (626.5)	659.6 (635.5)
$B_0(\text{GPa})$	53.4	51.1 (51.9)	47.3 (46.9)	40.6	25.2 (34.74)	19.9 (26.9)
B'_0	4.61	4.20 (4.19)	4.35 (4.44)	8.23	11.34 (8.46)	13.17 (11.24)
6 GPa						
	Static	0 K	600 K	Static	0 K	600 K
$V(\text{bohr}^3)$	616.7	624.7 (620.4)	639.7 (636.4)	554.0	572.5 (561.5)	620.9 (613.4)
$B(\text{GPa})$	76.8	74.7 (75.5)	67.0 (66.4)	84.7	74.5 (79.3)	30.1 (29.3)
B'	3.70	3.72 (3.73)	3.95 (4.10)	6.79	6.87 (6.83)	11.58 (12.31)

Previously to the discussion of thermal effects, it is worthy to present the calculated and experimental frequencies of scheelite and BaWO₄-II phases (see Fig. 3). Again,

there is an overall good agreement between the calculated and experimental values. This figure also shows the existence of a significant density of vibrational states at low frequency in both structures, having, in general, slightly higher frequencies the scheelite phase. This result is consistent with the higher B_0 value found for the scheelite phase. The fact that the low frequencies dominate the vibrational spectra of both polymorphs is detected by the lower value of the corresponding average frequency with respect to the half value of the maximum frequency in each structure. In this situation, we notice that taking into account specifically the vibrational modes with low frequencies, as in our Debye-Einstein model, will lead to a more accurate description of thermodynamic properties than in the Debye model as temperature increases.

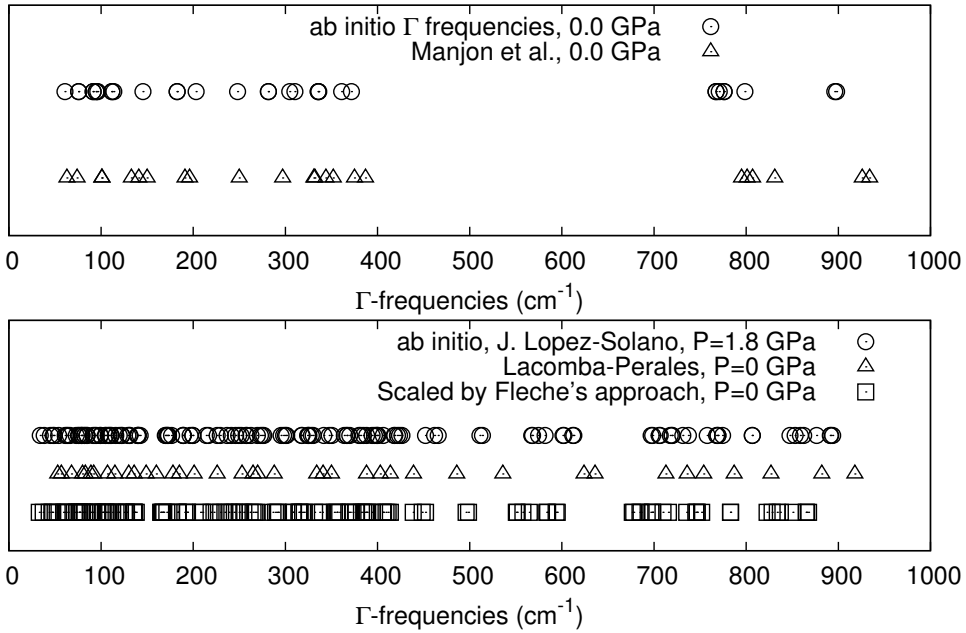


Figure 3: Experimental and calculated Γ -frequencies for the scheelite (top) and $\text{BaWO}_4\text{-II}$ (bottom) phase. The frequencies in the latter were computed at $p = 1.8$ GPa by J. López-Solano (private communication), and scaled down to $p = 0$ GPa using the Fleche's approach. Scheelite and $\text{BaWO}_4\text{-II}$ experimental frequencies taken from Manjón *et al.*⁸⁰ and Lacomba-Perales *et al.*⁷¹

By using Eq. 2.4, the vibrational effects on the static EOS parameters have been studied with the Debye and the Debye-Einstein model. In passing from the static regime to high temperature two steps have been considered: from static to 0 K (zero point vibrational effects) and from 0 K to high temperature (pure temperature effects). The volume change associated with the second step is directly described with the thermal expansion coefficient, and can be accounted for in our quasi-harmonic models since frequencies (and bulk modulus) are volume dependent.

Results in Table 1 show that zero point effects on the EOS parameters are of the same order of magnitude as those due to increasing temperature to 100 K or 300 K. Overall, the lower the bulk modulus, the greater the effect of thermal contributions to the equilibrium volume. Thus, using the Debye-Einstein model, the high pressure BaWO₄-II phase ($B_0 = 40.6$ GPa in the static approximation) increases its volume by around 40 bohr³ when zero point contributions are included, whereas the scheelite phase ($B_0 = 53.4$ GPa) increases only 11 bohr³ at the same conditions.

In Fig. 4, different $p - V$ EOS for the scheelite phase are shown. The static curve (solid line) is the lower limit to the volume and is, although very close, always below the experimental results. The best curve is the one obtained with the inclusion of zero point effect with the Debye model. The volume obtained with the rest of the models are overestimated, but this is mainly due to the functional employed rather than to the thermal model.

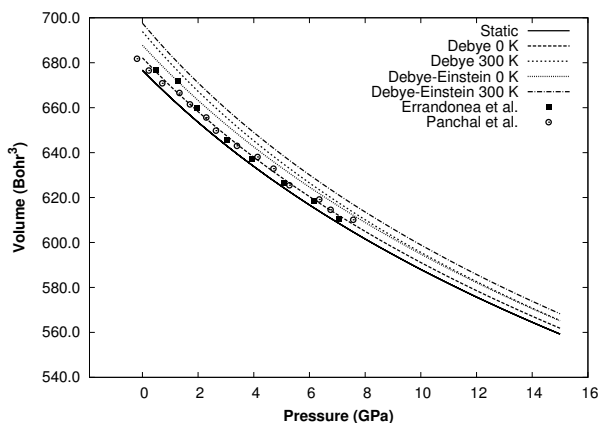


Figure 4: V vs p curves obtained for the scheelite phase with the static, Debye and Debye-Einstein models at 0 K and 300 K. Experimental results are obtained from the results of Errandonea *et al.*⁴⁰ and Panchal *et al.*¹⁰³.

2.2.3 Temperature dependence of thermodynamic properties

It is interesting to illustrate the effect of temperature in the thermodynamic properties of these structures. A selection of the main results obtained for the two systems is given. In Fig. 5, we show the change with T of the specific heat at constant pressure C_p , and the thermal expansion α . The variation of entropy, S , and Gibbs free energy, G , versus temperature is displayed in Fig. 6. Values for the equilibrium volume and the bulk modulus B_0 are given in Table 1 and were discussed above.

We focus on the results of the Debye-Einstein model to comment on the general trends of temperature effects. We observe that, as temperature increases, the bulk modulus lowers and the polymorphs become more compressible. C_p , α , and S increase

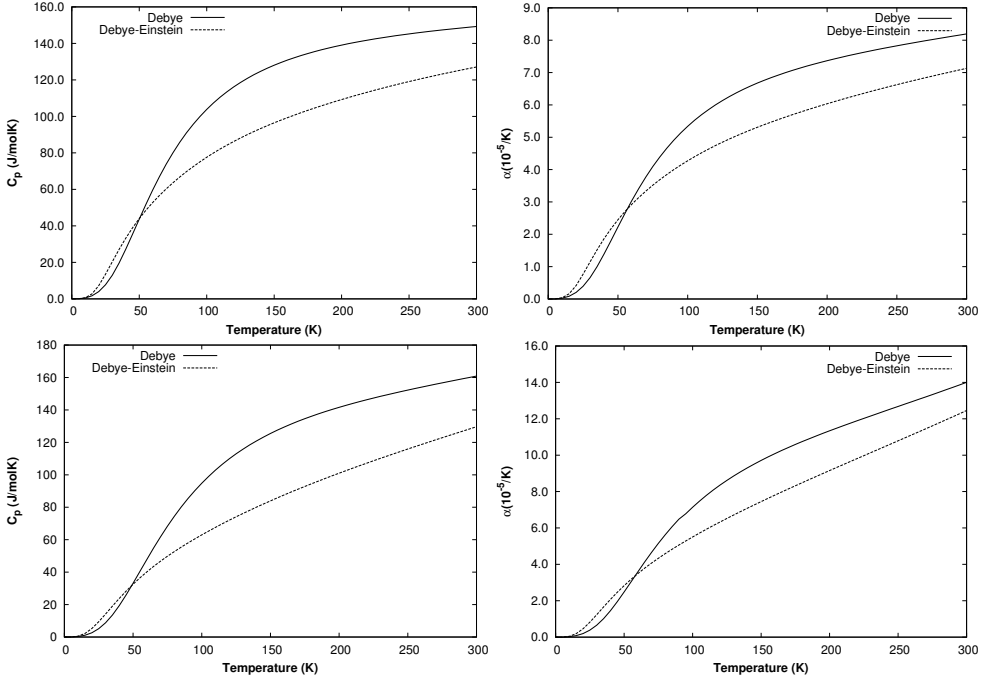


Figure 5: Temperature effects on C_p and α for scheelite at $p = 0$ GPa (top) and BaWO₄-II at $p = 6$ GPa (bottom). Curves stand for Debye (solid line) and Debye-Einstein (dashed line) models.

with T , whereas G ($\frac{\partial G}{\partial T} = -S$) shows a decreasing trend as T increases, this is the expected behavior for these properties. As regards distinctive features among the phases explored, we recall again to their respective vibrational frequency spectra. It is clear, for example, that the high- T classic limit of C_v will be reached at low T in both phases due to the great density of vibrational frequencies at low frequencies (low average vibrational frequency). For example, at 300 K, the Debye model estimates a C_v value greater than $140 \text{ J mol}^{-1} \text{ K}^{-1}$ for the scheelite phase, being the classic limit $149.65 \text{ J mol}^{-1} \text{ K}^{-1}$. Experimental values of C_p for the scheelite at ambient pressure are $123.2 \text{ J mol}^{-1} \text{ K}^{-1}$ at 336 K and $138.6 \text{ J mol}^{-1} \text{ K}^{-1}$ at 573 K.¹⁰⁸ These values are very close to the obtained with the Debye-Einstein model while the Debye model overestimates this property (see Fig. 5). Thermal expansion coefficient α for the scheelite measured at ambient conditions by Ran *et al.*¹⁰⁸ is $5.9 \times 10^{-5} \text{ K}^{-1}$, and at 6 GPa by Lacomba-Perales *et al.*⁷¹ is $2.5 \times 10^{-5} \text{ K}^{-1}$. At 6 GPa the Debye and the Debye-Einstein model predict α values of $4.8 \times 10^{-5} \text{ K}^{-1}$ and $4.41 \times 10^{-5} \text{ K}^{-1}$, respectively. Again, the Debye-Einstein model provides a better description of this property.

Although not displayed, the entropy of the scheelite phase shows greater values at the same pressure than that of the BaWO₄-II phase, in agreement with the higher bulk modulus of the low pressure phase. If we analyse the entropy, we see that the increase

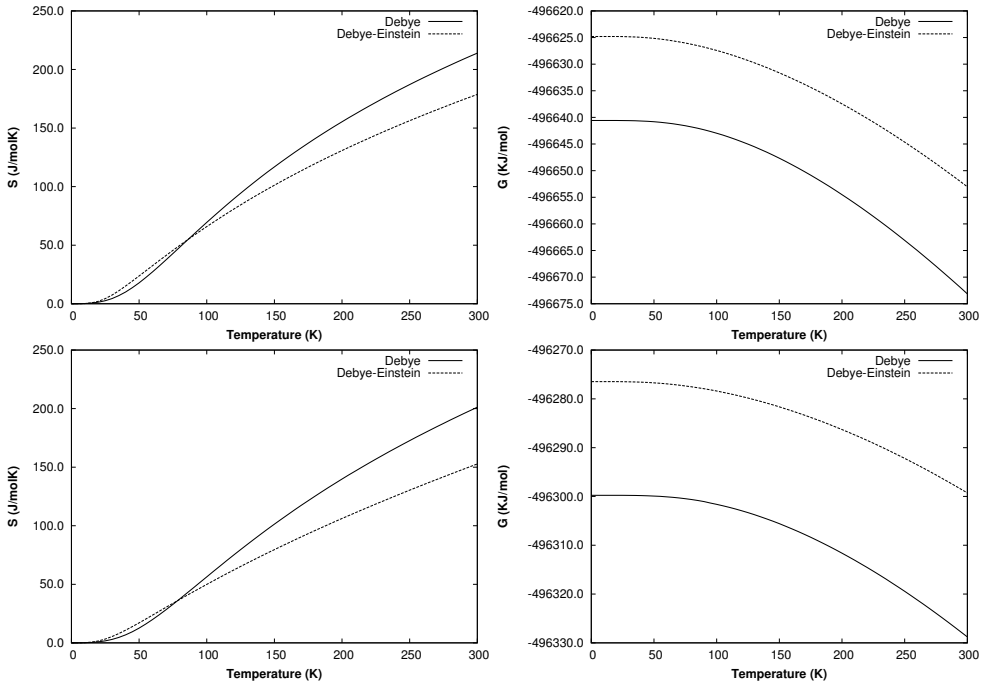


Figure 6: Temperature effects on S and G for scheelite at $p = 0$ GPa (top) and $\text{BaWO}_4\text{-II}$ at $p = 6$ GPa (bottom). Curves stand for Debye (solid line) and Debye-Einstein (dashed line) models.

of this property with the temperature is slightly higher for the scheelite polymorph. Hence, the increase of the temperature have a bigger effect lowering the Gibbs free energy on the scheelite phase. In other words, for a fixed pressure, the increase of temperature favours the stability of the scheelite with respect to the $\text{BaWO}_4\text{-II}$ phase. This result suggest a qualitative agreement with the experiments, where at 6 GPa the scheelite phase is recovered at 1600 K (see Fig. 10 in Ref. 71), after the scheelite \rightleftharpoons $\text{BaWO}_4\text{-II}$ transition observed around 600 K.

As regards the comparison between the Debye and the Debye-Einstein models, we can conclude that differences between the scheelite and $\text{BaWO}_4\text{-II}$ phases are negligible. For all the properties except G , both models show very similar values in the low temperature regime (up to 50 K) with differences that tend to become constant as temperature increases. In the case of the Gibbs energy, the curves are shifted with respect to each other but show the same trend regardless the model. As discussed above, we conclude that the values obtained with the Debye-Einstein model provide a more accurate description of these polymorphs than those from the Debye approximation.

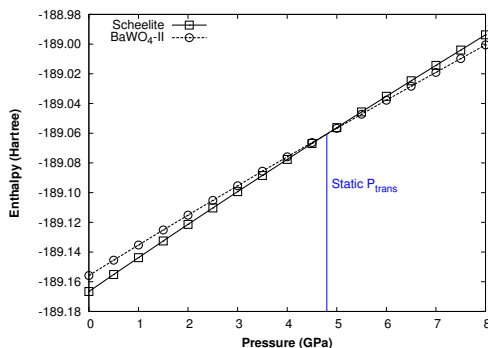
2.2.4 Scheelite \leftrightarrow BaWO₄-II phase transition

Figure 7: Enthalpy of scheelite (solid line) and BaWO₄-II (dashed line) phases. Static transition pressure is obtained at 4.78 GPa.

From the E-V static curves of scheelite and BaWO₄-II structures, we obtain the static transition pressure computing the crossing point where the enthalpies of both phases are the same. This is shown in Fig. 7. The calculated value for the static transition pressure is 4.78 GPa, similar to the value obtained by Errandonea *et al.*⁴⁰.

With our thermal approach we are able to compute the equilibrium curve between both polymorphs in a p-T diagram. GIBBS2¹⁰² automatically calculates the Gibbs free energies for all the phases included in the input at different p and T conditions. Hence we present the calculated p – T phase diagram using the Debye-Einstein model, shown in Fig. 8 (left). The solid line represents the Clapeyron slope where the Gibbs free energy of both phases is the same ($\Delta G = 0$). Above the Clapeyron boundary, $\Delta G = G_{\text{monoclinic}} - G_{\text{tetragonal}} < 0$, and the monoclinic phase is thermodynamically stable, whereas below the boundary, $\Delta G > 0$ and the scheelite phase is the stable one.

The calculated positive Clapeyron slope informs that the temperature range of stability of scheelite phase increases as pressure increases (see Fig. 8 (left)). Thus, the inclusion of zero point contributions shifts the thermodynamic tetragonal to monoclinic (t \rightarrow m) transition pressure (p_t) from 4.8 GPa to 5.6 GPa. At 350 K, p_t is slightly above 6.0 GPa (see Fig. 8). As indicated above, and although the slope is very low, this behavior correlates with the lower compressibility and average higher vibrational frequencies of the low pressure scheelite phase. The effect of temperature on V_0 , B_0 and other properties is higher in the monoclinic phase than in the tetragonal one since the vibrational levels are more available in the high pressure phase due to the overall lower values. The whole thermodynamic picture shows a nice consistence.

Furthermore, we can also provide information on the kinetics of the transformation. Numerical data will be collected in Table 2. Appearance of a fergusonite structure phase has been observed around 7 GPa prior to the transition to BaWO₄-II phase.⁷¹ This is supposed to be due to the existence of a high kinetic barrier that hinders the

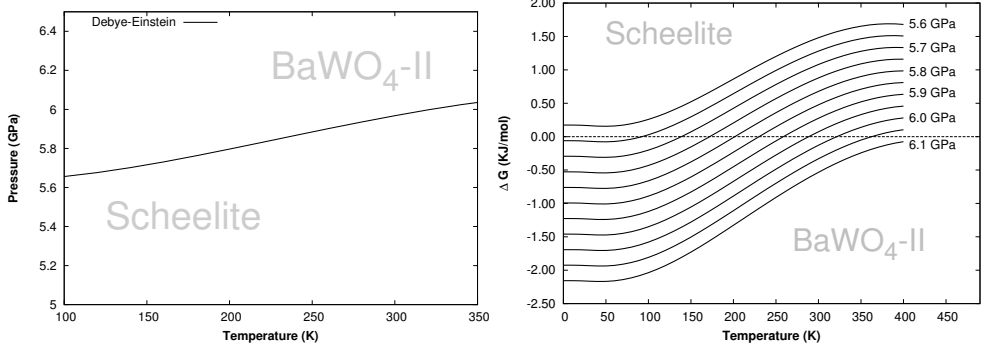


Figure 8: Left: Phase diagram of the barium tungstate obtained with the Debye-Einstein model. Right: Variation of ΔG with the temperature. ΔG is defined as $G_{\text{monoclinic}} - G_{\text{tetragonal}}$, which means that in positive ΔG regions scheelite is the most favourable phase.

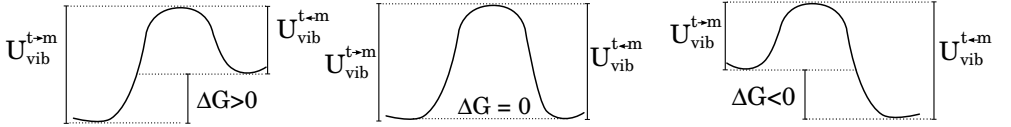


Figure 9: Schematic energy profiles at increasing pressures (from left to right) for the tetragonal to the monoclinic transformation.

phase transition to the monoclinic structure. We can compute the values of this barrier at different pressures and temperatures. In the experimental phase diagram of the barium tungstate there is a $p - T$ region where the scheelite phase is metastable (see Fig. 10 in Ref. 71). The available vibrational energy at the limit of that metastable region is directly related with the energy barrier associated to the phase transition, $U_{\text{vib}}^{t \rightarrow m}$. Schematically, this situations corresponds with the energy profile depicted at in the right panel of Fig. 9, since the initial phase of the transformation (scheelite), is the metastable one and has higher Gibbs energy.

$p(\text{GPa})$	$T(\text{K})$	$U_{\text{vib}}^{t \rightarrow m}(\text{kJ/mol})$
7.0000	525.0	87.96
6.0000	560.0	92.30
5.0000	625.0	100.83
4.0000	685.0	108.83

Table 2: Transition barrier energies ($U_{\text{vib}}^{t \rightarrow m}$) and Gibbs energy differences (ΔG) from scheelite to BaWO₄-II ($t \rightarrow m$) calculated with the Debye-Einstein model at the boundary between metastable scheelite and stable monoclinic structures.

Using the temperatures at which the transition to the monoclinic phase was observed in the laboratory at a given pressure, the values for this vibrational energy barrier have been calculated using our Debye-Einstein model (see Table 2). We obtain energy barriers ($U_{\text{vib}}^{\text{t} \rightarrow \text{m}}$) around 100 kJ/mol, very similar to the calculated values in the zircon \rightarrow scheelite transition in ZrSiO_4 by Flórez *et al.*⁴⁴. $U_{\text{vib}}^{\text{t} \rightarrow \text{m}}$ increases as p decreases and T increases. This is the expected result since scheelite shows lower Gibbs energy (with respect to the monoclinic phase) also as p decreases and T increases.

3

STRESS

GRAPHITE UNDER NON HYDROSTATIC

EXTENSIVE two and three dimensional periodic first principles simulations have been carried out to investigate the mechanical response of graphite to hydrostatic and non-hydrostatic stress conditions. Our results show a clear analogy between uniaxial (σ_z) stress and hydrostatic pressure as far as structural changes in the unit cell are concerned. For intra-layer C-C distances and in-plane graphite vibrational frequencies, the similarity with hydrostatic conditions is however found under biaxial ($\sigma_x=\sigma_y$) stresses. The calculated uniaxial equation of state is further used to investigate sliding mechanisms of a graphite layer in graphite at different inter-layer separations, thus providing insight at an atomic level on the origin of the low static friction coefficient of graphite.

3.1 THERMODYNAMIC POTENTIALS UNDER HEXAGONAL LIKE STRESS CONDITIONS

According to the mechanical work involved in a closed system of a single pure substance under general stress conditions (see for example Ref. 127), the relevant thermodynamic potential can be written as follows:¹²¹

$$\phi = E - V_0 \sigma \epsilon - TS, \quad (3.1)$$

where E gathers the internal energy of the system (in our case only the energy of the electronic ground state), V_0 is the equilibrium volume at free stress conditions, and σ and ϵ are the stress and strain tensors, respectively. The entropic term (TS) will not be discussed here as we will consider the athermal ($T=0$) limit with negligible vibrational zero point contributions. All the quantities are per formula unit which means that are per one single carbon atom.

In our work on graphite, only stress conditions that keep the hexagonal space group of the lattice will be taken into account. In the notation with $i = 4, 5, 6$ standing for non-diagonal elements of the stress tensor, the previous requisite means that only σ_1 , σ_2 and σ_3 can be non zero. Besides, it is required that $\sigma_1=\sigma_2$. In the same way, only the diagonal elements of the strain tensor will participate in the expressions below.

In this study, the role played by the thermodynamic potential is, in principle, restricted to that of a function able to yield the equilibrium strain components of the crystal at arbitrary sets of σ_i values, provided the hexagonal symmetry is maintained. An

operative definition of this thermodynamic potential at zero temperature introduces the explicit dependence on the unit cell lattice parameters through the configurational vector \vec{x} :

$$\phi(\vec{x}; \boldsymbol{\sigma}) = E(\vec{x}) - V_0 \sum_{i=1}^3 \sigma_i \epsilon_i, \quad (3.2)$$

being $V_0 = \frac{\sqrt{3}}{8} a_0^2 c_0$ the zero stress volume per formula unit (one carbon atom), and a_0 and c_0 the corresponding length parameters of the unit cell. For a given set of σ_i values, the equilibrium lattice parameters (\vec{x}_e) are those that minimize the thermodynamic potential ϕ . It should be understood that stresses acting on the unit cell generates compression and have negative values, whereas tensile stresses are positive. In this way, we shall call $\sigma_x = -\sigma_1$, $\sigma_y = -\sigma_2$, and $\sigma_z = -\sigma_3$, and all positive (negative) values for these cartesian components of $\boldsymbol{\sigma}$ represent compression (tensile) forces acting on the corresponding unit cell surface of the crystal.

We will discuss results coming from three different stress conditions. The first one is a triaxial stress (σ_t) consisting of the particular biaxial stress (σ_b) in the α - b plane where $\sigma_b = \sigma_x = \sigma_y$, and a non zero value for σ_z , along the c axis of graphite. If we have the same value for the three stress components then the hydrostatic pressure (p) case is recovered. The thermodynamic potential is easily derived from Eq. 3.2:

$$\phi_t(\vec{x}; \boldsymbol{\sigma}) = E(\vec{x}) + \frac{\sqrt{3}}{4} \sigma_b a a_0 c_0 + \frac{\sqrt{3}}{8} \sigma_z c a_0^2 - (2V_0 \sigma_b + V_0 \sigma_z). \quad (3.3)$$

The second one concerns the biaxial stress $\sigma_b = \sigma_x = \sigma_y$, with $\sigma_z = 0$. The thermodynamic potential reduces to:

$$\phi_b(\vec{x}; \boldsymbol{\sigma}) = E(\vec{x}) + \frac{\sqrt{3}}{4} \sigma_b a a_0 c_0 - 2V_0 \sigma_b. \quad (3.4)$$

The last condition is the uniaxial stress (σ_u) along the z axis. The corresponding expression is:

$$\phi_u(\vec{x}; \boldsymbol{\sigma}) = E(\vec{x}) + \frac{\sqrt{3}}{8} \sigma_z c a_0^2 - V_0 \sigma_z, \quad (3.5)$$

where we keep the symbol σ_z for σ_u to emphasize that the uniaxial stress is applied along the direction perpendicular to the graphite layers. The terms involving V_0 are constant for given σ_i values, and do not affect the minimization process, *i.e.* the same equilibrium \vec{x}_e parameters are obtained if we discard these terms from the potential function. We can define a generalized enthalpy (H_n , subscript n refers to non-hydrostatic) to account, respectively, for triaxial (t), biaxial (b), and uniaxial (u) stress conditions just deleting the constant contributions in these equations:

$$H_t(\vec{x}; \boldsymbol{\sigma}) = E(\vec{x}) + \frac{\sqrt{3}}{4} \sigma_b a a_0 c_0 + \frac{\sqrt{3}}{8} \sigma_z c a_0^2, \quad (3.6)$$

$$H_b(\vec{x}; \boldsymbol{\sigma}) = E(\vec{x}) + \frac{\sqrt{3}}{4} \sigma_b a a_0 c_0, \quad (3.7)$$

$$H_u(\vec{x}; \boldsymbol{\sigma}) = E(\vec{x}) + \frac{\sqrt{3}}{8} \sigma_z c a_0^2. \quad (3.8)$$

These expressions allow us to discuss the relative stability of different structures under the same non-hydrostatic conditions¹¹³ (not considered here), and also for comparing the magnitude of the effects introduced by different types of stress.

To end this section, it is interesting to bring the attention to the two different equivalent computational strategies that can be carried out to determine the ϵ - σ relationship. The first one evaluates the energy of the system at selected strains, usually in a regular grid of a and c . At each of these strained lattices the corresponding set of σ_i values is computed. The second one searches for the minimum of the thermodynamic potential (or better the enthalpy) at selected σ_i values using the equations presented here. Both schemes have been followed in this work and have shown to yield same results within the error bars of the calculations.

3.2 COMPUTATIONAL DETAILS FOR 3D AND 2D PERIODIC MODELS OF GRAPHITE

First-principles total energy calculations for bulk graphite and tri-layer graphite (3LG) were performed within the density functional theory (DFT) formalism with a plane-wave pseudopotential approach. Simulations in bulk graphite were performed using both QUANTUM ESPRESSO⁴⁷ and the Vienna *ab initio* simulation package (VASP)⁷⁰ with the Perdew-Burke-Ernzerhof (PBE) generalized gradient exchange-correlation functional.¹⁰⁶ As shown below, same results were obtained (see section 3.3) within the accuracy of the computational packages. In QUANTUM ESPRESSO we use a RRKJ ultra-soft pseudopotential.¹⁰⁹ A cutoff energy of 816 eV and a $24 \times 24 \times 12$ k-grid were considered in these calculations. In VASP, we follow the standard projector augmented wave all-electron description of the electron-ion-core interaction. Brillouin-zone integrals were also approximated using the Monkhorst-Pack method,⁹³ and the energies converged to 1 meV with respect to k-point density ($16 \times 16 \times 8$ k-meshes) and the plane-wave cutoff (600 eV). In both cases, the Grimme's correction⁵⁰ was included in order to account for the dispersion interactions. Γ -point phonon frequencies were calculated within the DFT perturbation theory implemented in the QUANTUM ESPRESSO code.⁴⁷ The total energies required in the calculation of the phonons were obtained with the same computational parameters specified above.

For the 3LG calculations, we consider a periodic slab model consisted of three graphite layers with an initial ABA stacking representing the Bernal-type configuration of stable bulk graphite. With this model, we carry out a number of computer simulations directed to study friction in graphite. For this reason, in each of these calculations the coordinates of all the atoms in layers A are required to be fixed. One of the two non-equivalent carbon atoms of layer B, originally at $(0,0,0)$, is displaced to a different pair of x and y coordinates, thus defining the sliding (s) and the direction (Θ) of displacement. Along with the z coordinate of this atom, the coordinates of the second non-equivalent carbon atom of the layer B are unconstrained and therefore the C-C distance in this layer is treated as a free parameter. Nevertheless, we found negligible departures from both the initial $z = 0$ value and the bulk C-C intra-layer equilibrium distance (1.42 \AA). By changing the position of the first (singular) carbon atom of layer B, and the subsequent optimization of the position of the second carbon atom, we simulate how layer B slides between the two fixed A layers. We used `tetr`⁶⁴ to displace the central layer (B) a distance up to 4.2672 \AA in steps of 0.0889 \AA at different sliding directions from 0 to 110 degrees. By repeating these calculations using the same sliding parameters and different fixed interlayer distances, we obtain a number of potential energy surfaces, each of them corresponding to a σ_z stress value derived from the linear EOS calculated in our bulk graphite simulations (see below). Therefore, it has to be understood that fixing the positions of atoms in A layers is not an approximation but a requirement of our model to mimic friction in graphite. Fig. 54 shows a finite representation of the 3LG slab model for three different angles and two sliding displacements.

3.3 RESULTS AND DISCUSSION

3.3.1 Bulk graphite under hydrostatic and non-hydrostatic conditions

In order to calculate 1D, 2D, and 3D EOS parameters for graphite, we chose a bi-dimensional strain grid by sampling 11 points in both, the a (from 2.40 to 2.50 \AA) and c (5.72 to 6.77 \AA) unit cell lengths. At each grid node, we calculated the stress obtaining an energy mapping with respect to a (non-uniform) stress grid, with limits -20.4 to 35.6 GPa in σ_b and -1.5 to 12.7 GPa in σ_z . These results are partially plotted in two isoline maps in Fig. 11, where we have restricted the map window to positive stress values not higher than 15 GPa . Following the $\sigma_b=0$, $\sigma_z=0$, and $\sigma_z=\sigma_b$ lines, the response of graphite unit cell parameters under, respectively, uniaxial, biaxial, and hydrostatic conditions can be derived. Given the simplicity of the isoline patterns in both plots, it can be straightforwardly concluded that graphite shows a great anisotropic behavior, with hydrostatic conditions similar to biaxial and uniaxial stress as regards, respectively, $a=b$ and c distortions. Since the effect of the biaxial stress on $a=b$ is shown to be almost negligible in the considered range, we can reasonably state

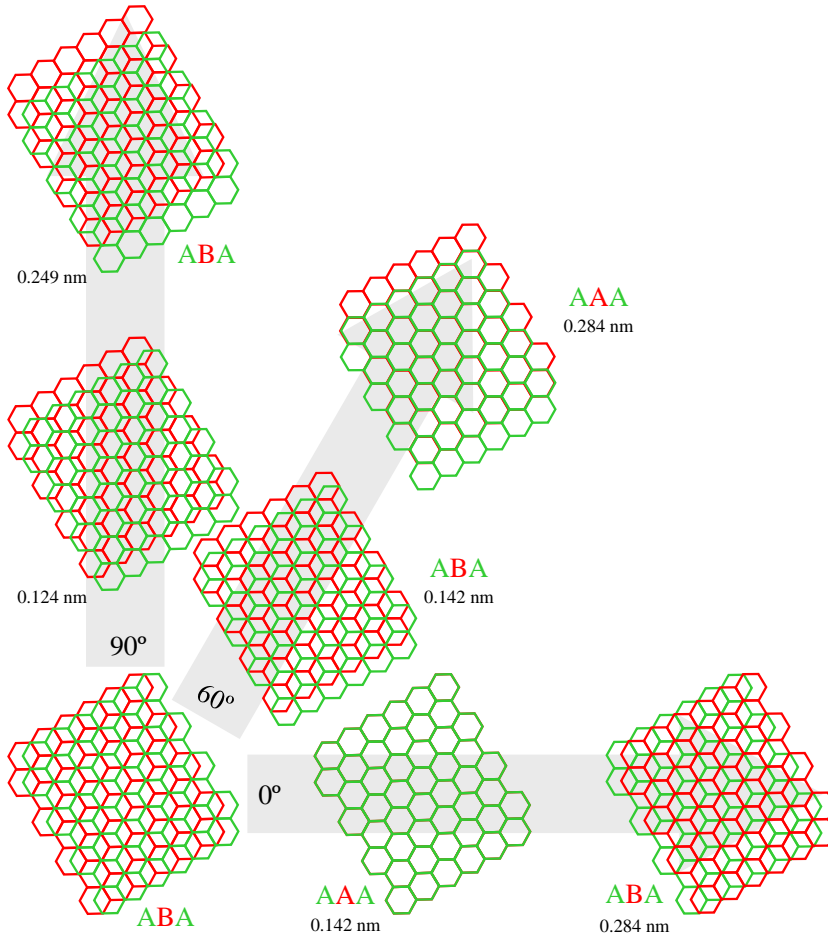


Figure 10: Tri-layer system with the central layer B (in red) sliding two different displacements s (indicated for each direction) at 0, 60 and 90 degrees.

that hydrostatic and uniaxial (σ_z) conditions on graphite behave very much the same as far as structural strains are concerned.

The comparison of our results with a number of experimental and computational investigations is available for hydrostatic conditions. We refer to the recent papers of Savini *et al.*¹¹⁵ and Colonna *et al.*²⁴ since they contain detailed and specific data of the lattice parameters of graphite under hydrostatic pressure including a critical comparison of several measured and calculated data. Our calculated reductions of c , a , and V under hydrostatic pressure are in very good agreement with this general analysis. To give some numbers from our calculations, and in common with the experimental and theoretical data reported in Refs. 115 and 24, the reduction of a and c is close to 1% and 12%, respectively, when hydrostatic pressure reaches 10 GPa. In the same pressure range, volume is reduced less than 14%. Overall, all these results illustrate that c is the easy axis under compression, as expected for this layered compound.

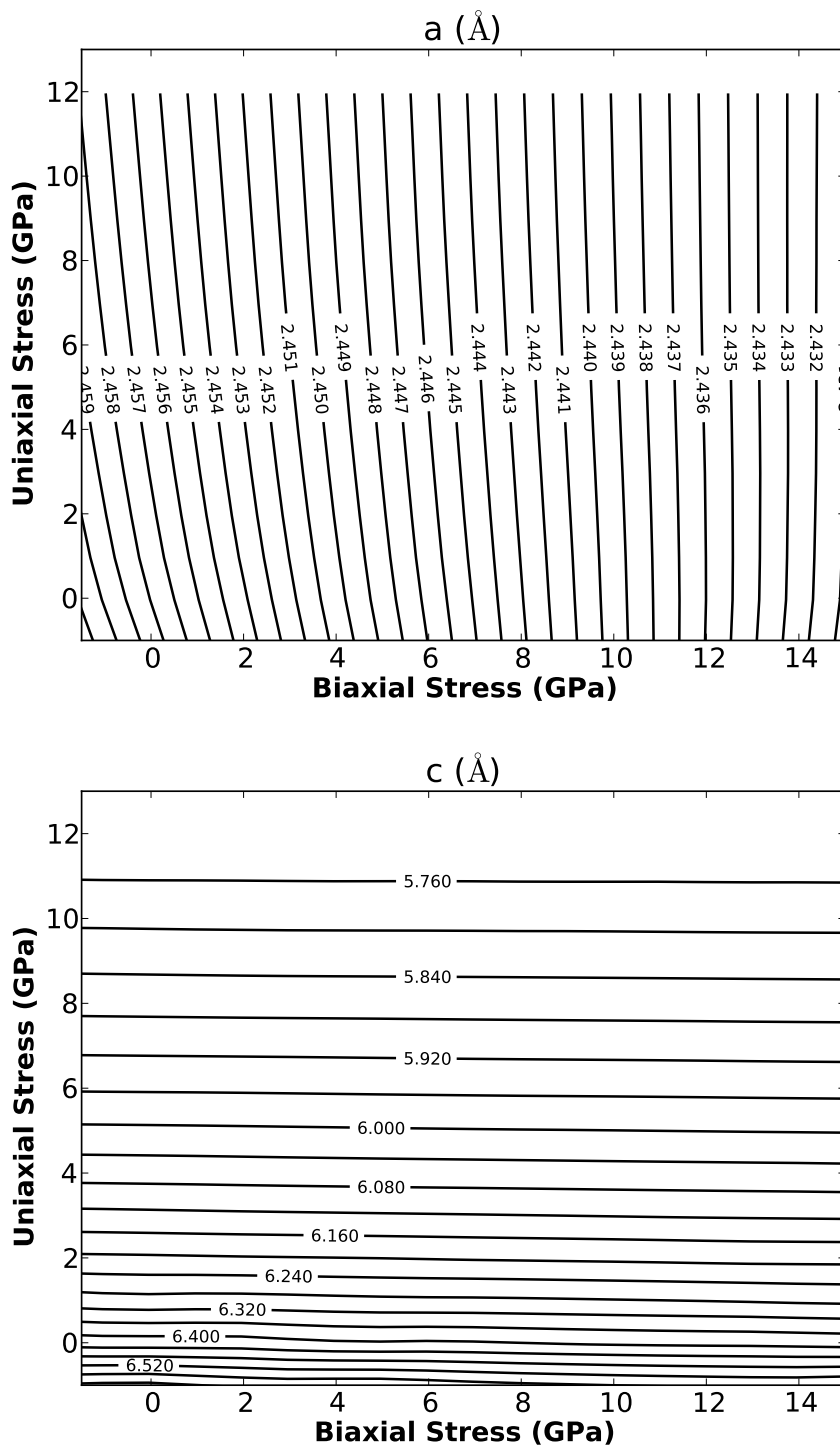


Figure 11: Isoline of the $a=b$ (left) and c (right) lattice parameters of graphite under uniaxial (σ_z) and biaxial ($\sigma_x=\sigma_y$) conditions. Results for triaxialities (including hydrostatic) can also be inferred from this plot (see text).

Quantitative account for the results under hydrostatic and non-hydrostatic conditions are given below (see Table 3) in terms of equation of state parameters. The same formal expressions resembling the isotropic bulk modulus are used:

$$M_0^z = - \left[c \frac{\partial \sigma_z}{\partial c} \right]_{0,T}, M_0^b = - \left[S \frac{\partial \sigma_b}{\partial S} \right]_{0,T}, B_0 = - \left[V \frac{\partial p}{\partial V} \right]_{0,T}, \quad (3.9)$$

where '0' means that the evaluation of the corresponding property is at the equilibrium free stress configuration, and the 1D, 2D and 3D structural parameters are, respectively, the unit cell parameter, c , the C-hexagon area in the α - b plane, S , and the graphite unit cell volume, V . Note that as a result of the definitions in Eq. 3.9, these three parameters have the same units (GPa in our case), and S and V are referred to one C atom.

Results in Table 3 confirm the conclusions derived from the bidimensional plots of Fig. 11. Uniaxial and hydrostatic parameters show similar values (around 64 and 58 GPa, respectively) because the easiest direction to compress the crystal (the c axis) is almost the only contribution to the bulk volumetric compressibility. Colonna *et al.*²⁴ calculate an athermal B_0 value of 36.3 GPa with $B'_0=9.85$, and report experimental values¹³² of B_0 and B'_0 of 37 GPa and 14, respectively. Correlation between the two EOS parameters (B_0 and B'_0) can explain in part the discrepancy with our calculated value of B_0 since in standard EOS fittings it is known that as B'_0 increases B_0 decreases. Notice that our value for B'_0 (3.2) is almost one third of the reported value by Colonna *et al.* The same applies to M_0^z when comparing with the experimental data of Hanfland *et al.*⁵³ To be completely rigorous, we should indicate that other contribution to our greater values for B_0 and M_0^z can also be due to an overestimation of the weak dispersion forces between graphite layers described by the Grimme correction.

More noticeable is the high calculated EOS parameter for the surface bulk moduli, $M_0^b = 636.3$ GPa. It informs on the great resistance to compression of intralayer C-C bonds in graphite. From our discussion above, and also from comparisons between elastic constants in monolayer and bilayer graphene with bulk graphite,²⁷ this value might be similar to other reported values for graphene. The comparison with graphene and few-layers graphene is not straightforward because our calculations aim to simulate the response of bulk graphite to biaxial stresses. Different experimental and theoretical values have been reported (from 500 to 1000 GPa for the Young's modulus, 700 GPa for M_0^b with a zero pressure first derivative of 1) depending on the thickness of the graphene sample and other factors (see for example Refs. 73,46,111). However, the evaluation of the linear bulk modulus ($B_0^\alpha = -(\alpha \frac{dP}{d\alpha})_{0,T}$) describing the variation of the lattice parameter α in graphite as a function of the hydrostatic pressure provides an unequivocal way to compare our data with other calculated and experimental values. Either under hydrostatic or biaxial conditions, our calculations yield B_0^α close to 1300 GPa to be compared with a measured value of 1250 ± 70 GPa⁵³ or with computed values of 1240 GPa and 1171 GPa (see Refs. 115 and 27, respectively) evaluated from the relationship between elastic constants and B_0^α . In all cases, the agreement is quite satisfactory.

Table 3: Equation of state parameters of graphite under uniaxial, biaxial, and hydrostatic conditions according to our calculations. X refers to the corresponding 1D, 2D, and 3D unit cell property under uniaxial, biaxial, and hydrostatic stress, respectively. The 0 superscript refers to the free stress state. Units of Å and GPa are used.

	X_0	$M_0 = -\left[X \frac{d\sigma_i}{dX}\right]_0$	M'_0
Uniaxial	$c_0=6.430$	64.3	4.1
Biaxial	$S_0=5.248$	636.3	5.2
Hydrostatic	$V_0=33.743$	57.9	3.2

We have checked the alternative scheme indicated in section 3.1 to compute the ϵ - σ relationship, that of minimizing the enthalpy of graphite at different stress conditions according to the expressions in Eqs. 3.6-3.8. In Fig. 12 (left), we illustrate how the enthalpy changes with c for different σ_z values. The minima of these curves give us the equilibrium c_e - σ_z relationship. These values reproduce the 1D EOS parameters collected in Table 3 and will be used below in the computation of frictional coefficients. It can be seen that lower c_e values are obtained as σ_z increases, in quantitative agreement with the results obtained using the first strategy illustrated in the isoline map of Fig. 11 (left). But, perhaps more important, it is to see how the enthalpy at the respective equilibrium configuration increases with σ_z (see Fig. 12 (left)). This particular σ_z -enthalpy set of values is reproduced in the enthalpy surface plotted in Fig. 12 (right). In this plot, we can quickly recognize that the weak interactions along the easy axis to compress (c) lead to a lower increase in enthalpy than when the strong C-C bonds in the graphene layer are stretched as σ_b is applied. For the same stress (say 10 GPa), the increase in enthalpy is more than twice under σ_b than under σ_z .

Moreover, from this plot (Fig. 12 (right)), and using the relationship between σ_b and a , we can follow Zakharchenko *et al.*¹³⁰ to evaluate a 2D bulk modulus b defined by

$$\Delta E = 2b(\Delta a)^2, \quad (3.10)$$

where ΔE refers to the increase in the internal energy (elastic energy) due to the biaxial stress that produces an isotropic deformation ($\Delta a = \Delta b$) in the a - b plane. We have obtained a very good parabolic fitting of ΔE with respect to Δa (σ_b up to 15 GPa), and a 2D b value of $12.5 \text{ eV}/\text{\AA}^2$ in good agreement with calculated values of Zakharchenko *et al.*¹³⁰ Notice here that $\frac{\text{energy}}{\text{area}}$ units instead of pressure are used for this b parameter.

Once uniaxial, biaxial and triaxial (including hydrostatic) EOS parameters have been determined, we have proceeded to the evaluation of zone center graphite vibrational modes in all the nodes of our a - c grid. Γ point vibrational modes can be divided in three groups: (i) $E_{2g}(1)$ and $E_{2g}(2)$ Raman active modes, (ii) E_{1u} and A_{2u} IR active modes, and (iii) $B_{2g}(1)$ and $B_{2g}(2)$ optically inactive modes. E-like modes represent

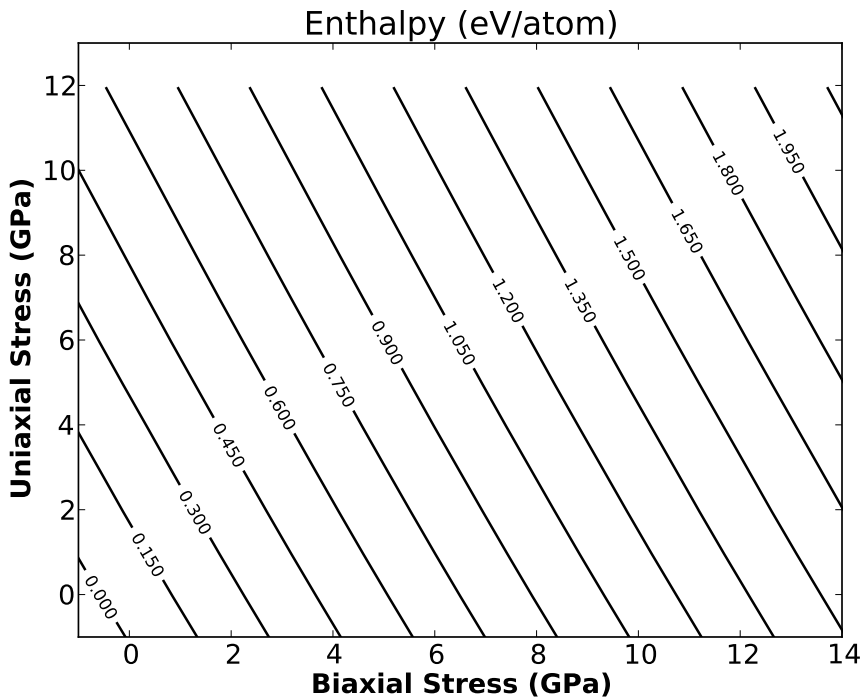
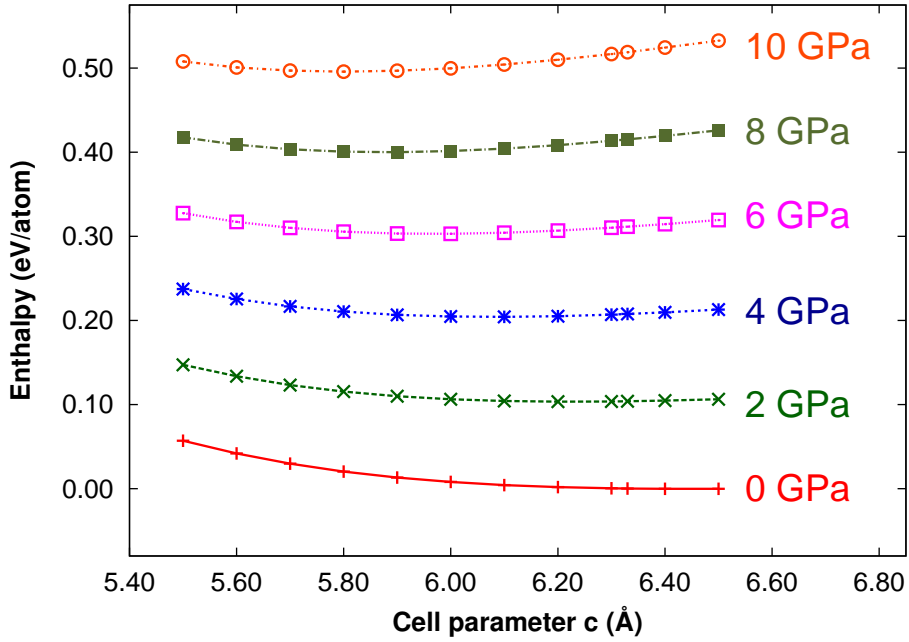


Figure 12: Enthalpy *versus* c for different uniaxial (σ_z) stresses (left). Isolines of the enthalpy potential of graphite (right) corresponding to uniaxial (σ_z) and biaxial ($\sigma_x=\sigma_y$) conditions. Results for triaxialities (including hydrostatic) can also be inferred from this plot (see text).

different in-plane atomic displacements, whereas non-degenerate modes display out-of-the plane atomic movements (see Figs. 13 and 17 in Supplemental Material). All of them have been evaluated in all the nodes of our α -c grid.

In particular, we are interested in stress effects on the in-plane C-C symmetric stretching ($E_{2g}(2)$) mode and on the one related to the relative displacement (rigid shear movement) of consecutive graphite layers ($E_{2g}(1)$). Calculated frequencies for the rest of vibrational modes can be found in Fig. 17 of the Supplemental Material. Experimental frequencies of $E_{2g}(1)$ and $E_{2g}(2)$ modes under hydrostatic conditions have been reported by Hanfland *et al.*⁵³ Similarly to the results for the lattice parameters and the enthalpy, isoline maps illustrate here how the frequencies of these modes changes with σ_z and σ_b (see Fig. 13). Nicely, our calculated values for $E_{2g}(2)$ are in good agreement with the experimental data both in absolute and relative (Grüneisen parameters) terms. At $p=10$ GPa, we compute an increase of $\omega(E_{2g}(2))$ around 43 cm^{-1} from its zero pressure value, 1561 cm^{-1} (1579 cm^{-1} is the experimental value of Hanfland *et al.*⁵³). This is in concordance with the initial pressure coefficient ($4.8(5) \text{ cm}^{-1}/\text{GPa}$) and the sublinear increase with pressure of this mode reported by Hanfland *et al.*⁵³ From the plot of Fig. 13 (left), it is interesting to remark that the effect of σ_z is almost completely negligible. For example, differences in this frequency at 10 GPa between hydrostatic and biaxial conditions are lower than 4 cm^{-1} . This is the expected result for a genuine in-plane vibrational mode involving the stretching of C-C chemical bonds, and work is in progress to exploit this result in the analysis of non-hydrostatic experiments.³⁴ Besides, we have found a very similar behavior for the antisymmetric stretching E_{1u} mode associated with intra-layer C-C bonds. The calculated zero pressure value is 1580 cm^{-1} (1588 cm^{-1} is the experimental value reported by Nemanich *et al.*⁹⁸), and the blue shift induced by 10 GPa is almost 50 cm^{-1} , slightly greater than in the case of the $E_{2g}(2)$ mode. The same negligible dependence on σ_z has been obtained for this mode, thus revealing the equivalent role that biaxial and hydrostatic conditions play in this high frequency in-plane vibrational modes (isoline maps for this E_{1u} and the rest of the modes are collected in Fig. 17 of the Supplemental Material).

Concerning $E_{2g}(1)$, our calculated zero pressure value (58 cm^{-1}) is 14 cm^{-1} above the experimental value of Hanfland *et al.*⁵³ probably reflecting again some overestimation in our description of the interlayer interaction. This low frequency mode can be linked to frictional forces between graphite layers. Notice that all C atoms in each graphite layer move in the same direction, and no changes of intra-layer C-C bonds are explicitly involved in this mode (see Fig. 13 (right)). Here, we check the ability of a harmonic model to account for an estimation of the force constant (k) involved in the relative (opposed directions) displacements of alternate layers associated with this mode. The estimated force constant using the zero pressure calculated frequency is around 1.2 N/m (0.7 N/m using the experimental value), whereas at 10 GPa ($\omega(E_{2g}(1)) \simeq 86 \text{ cm}^{-1}$) k increases up to 2.6 N/m . These values will be compared with direct simulations of graphite layer displacements in the next subsection, and constitu-

te upper limits to force constants due to the strong anharmonicity associated with this mode.^{53,38} To end up with our discussion, it is to be emphasized that the isoline map displayed in Fig. 13 (right) shows a negligible effect of the biaxial stress on this mode, but a clear dependence on σ_z which illustrates the link of this mode with frictional forces between graphite layers.

3.3.2 Graphite slabs under uniaxial conditions

Using our 3LG model, we have computed potential energy surfaces (PES, Z axis) as functions of the sliding displacement of the B graphite layer s (Y axis), and the angle Θ (X axis), for interlayer separations corresponding to σ_z values, as dictated by the 1D EOS (Fig. 14 displays PES for $\sigma_z = 0$ and 16 GPa). The absolute maxima in these plots correspond to the AAA arrangement of the tri-layer, which can be found for all the analyzed angles (except 30° and 90°) provided we do not limit the amount of displacement of the singular atom in layer B.

Intra- and inter-layer interactions in graphite have been studied many times (see for example Refs. 124 and 89, and references therein). They allow us to explain the preference of graphite for the Bernal-type ABA stacking and the existence of maxima at AAA configurations. Other different stacking have been also investigated due to the increased interest in graphene and in the so-called few-layer-graphites or few-layer-graphenes (FLG) (see Refs. 115, 27, 72,52,110, and references therein). In all these works it is revealed that the strong in-plane C-C covalent bonds contrast with the weak inter-layer dispersion forces leading to an "essentially two dimensional character of graphite".^{22,23} The dispersion forces do not come from the σ -type intra-layer chemical bonds, but from the π electron density above and below the plane. As de Andres *et al.*²⁸ have shown in 2LG, the AA stacking facilitates the formation of C-C inter-layer bonds breaking the planar geometry and weakening the intra-layer C-C bonding network. In our 3LG system resembling a graphite slab, although the planar geometry is kept as we move from the ABA to the AAA stacking, the dispersion (attractive) forces between layers are enhanced at the expense of weakening intra-layer C-C bonds leading to the energy maxima at AAA configurations. In this way, we found an increase in energy at these maxima of 13.5 meV/atom with respect to the ABA stacking when the inter-layer distance is kept at the calculated equilibrium value of graphite (3.27 Å). A value of 8.9 meV/atom was obtained by Reguzzoni *et al.*¹¹⁰ for two-layer graphene with optimized inter-layer separations of 3.37 Å (AB stacking) and 3.59 Å (AA stacking). In spite of this and other similarities (see for example a thorough computational study by Guo *et al.*⁵²), we would like to emphasize that our 3LG model is introduced here to analyze friction forces and the friction coefficient only for graphite and, therefore, it does not intend to simulate friction phenomena in graphene. That is why inter-layer separations are kept fixed following the uniaxial (σ_z -c) EOS in each calculation of the PES.

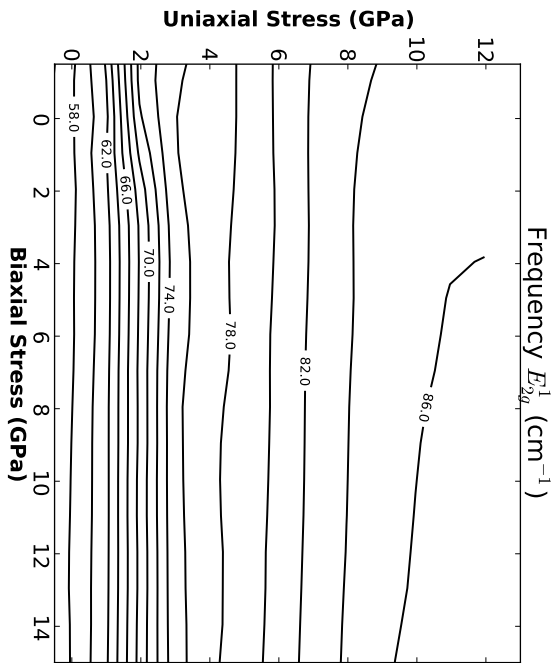
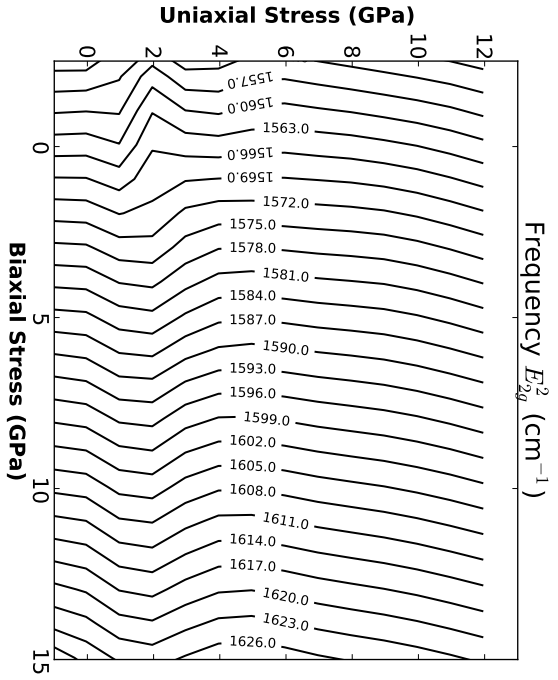


Figure 13: Frequency isoline maps (top) and atomic displacements (bottom) of the vibrational modes $E_{2g}^{(2)}$ (left) and $E_{2g}^{(1)}$ of graphite under uniaxial (σ_x) and biaxial ($\sigma_x = \sigma_y$) conditions. Results for triaxialities (including hydrostatic) can also be inferred from this plot (see text).

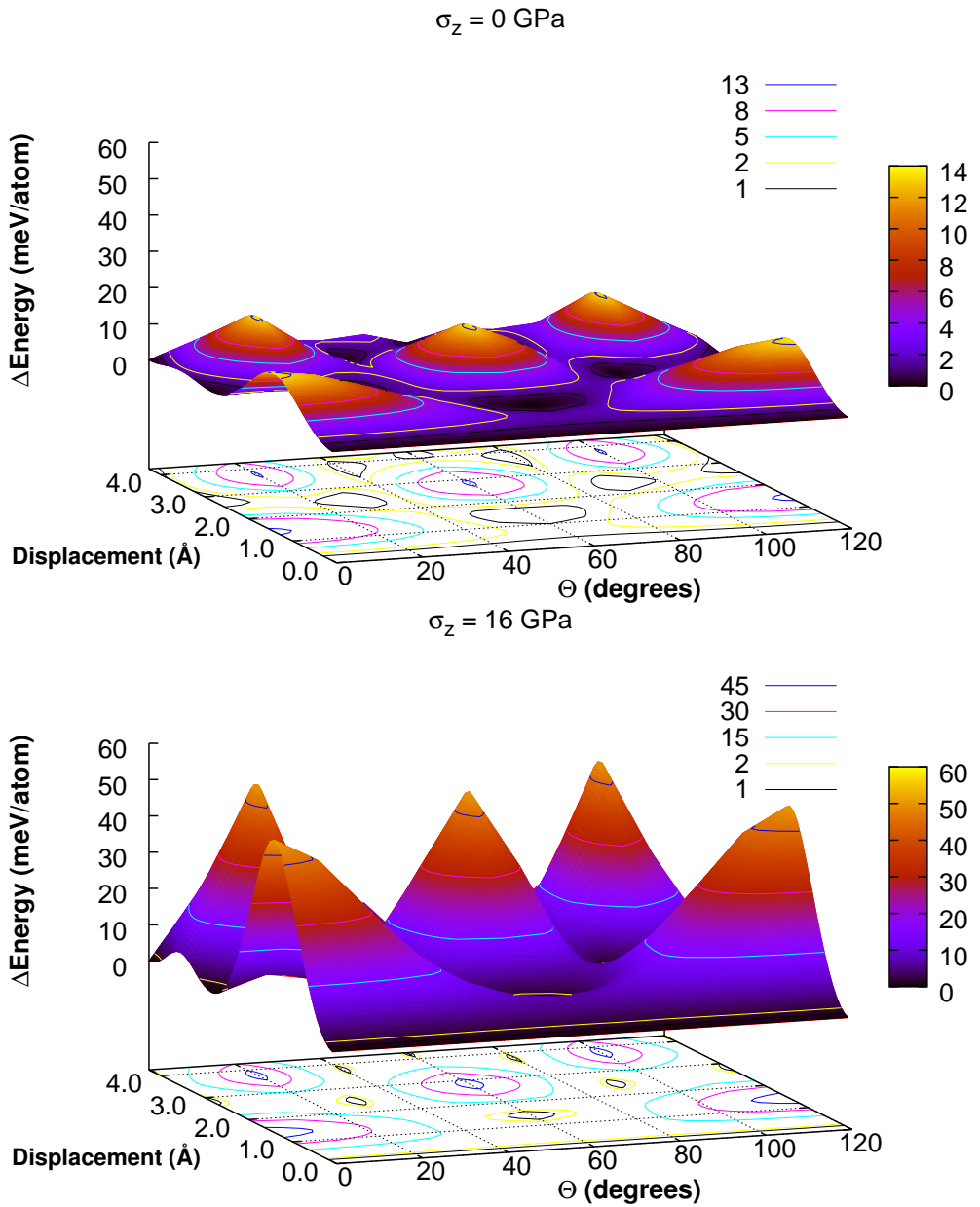


Figure 14: Potential energy surface of the 3-slab model of graphite under zero stress (left) and $\sigma_z = 16$ GPa (right) conditions. Displacements (s) and directions (Θ) ranged by the middle layer start in the ABA configuration.

By comparing the energy surfaces at different interlayer distances, we clearly observe that, while the topology of the energy surfaces remains unaltered, the energy required to displace layer B along a given direction increases when the adjacent layers become closer (equivalent to an increase of σ_z). These theoretical results could be analysed for the case in which the graphite layers could displace without restriction on the angular direction, which is the situation that resembles previous FFM experiments found in the literature where graphite is revealed as superlubricant.⁸⁶ For this purpose we must take into account that the graphite layers can move with a given direction for a certain distance and change, if possible, their sliding direction when they find an energetic barrier; giving rise to potential energetic curves as those shown in Fig. 15. Once again, the effect of stress is to increase these energetic barriers but keeping the whole topology unaltered.

From these potential energy surfaces we are able to calculate the force felt by the B layer when it moves along a given direction as:

$$F = -\frac{\partial E}{\partial s}. \quad (3.11)$$

We evaluate forces along displacement paths of $s=1.5 \text{ \AA}$ and $s=4.2 \text{ \AA}$ long at different sliding directions and interlayer distances from equilibrium to 2.8 \AA . As before, we can convert these interlayer distances into σ_z using the uniaxial equation of state obtained in our calculations in bulk graphite. The corresponding range of σ_z goes from 0 up to 16 GPa. The maximum forces obtained for the 1.5 \AA displacement paths correspond with the forces required to initiate the motion (static friction force), whereas those for the longer displacements are for maintaining the surfaces in the subsequent relative motion. These results lead to the curves shown in Fig. 16.

It is to be noted that the maximum force, F_{\max} , obtained at the 0 degree sliding direction for a displacement value (s_{\max}) is just at the middle of the path between the starting position and the position corresponding to the first maximum in the energy profile. The ratio $\frac{F_{\max}}{s_{\max}}$ is a rough estimation of the force constant associated with $\omega(E_{2g}(1))$. Although the calculated values using this ratio at 0 GPa (0.4 N/m) and 10 GPa (0.9 N/m) are lower than the values assuming harmonic frequencies (see above), it is remarkable to see that they are of the same order of magnitude and show a very similar increase with pressure. Inversely, from the force constant calculated with this ratio, it is also possible to estimate the associated harmonic frequency resulting in 32 cm^{-1} at 0 GPa and 51 cm^{-1} at 10 GPa. These values are also lower than the experimental ones (around 45 cm^{-1} and 70 cm^{-1} , respectively),⁵³ but again of the same order and with very similar pressure coefficient. The whole analysis reveals that this low frequency Raman mode is a good indicator of the frictional forces between graphene layers in graphite. In this respect, it is interesting to notice that this low frequency mode has been recently measured in graphene,¹²⁰ though the effect of stress on it has not been determined yet.

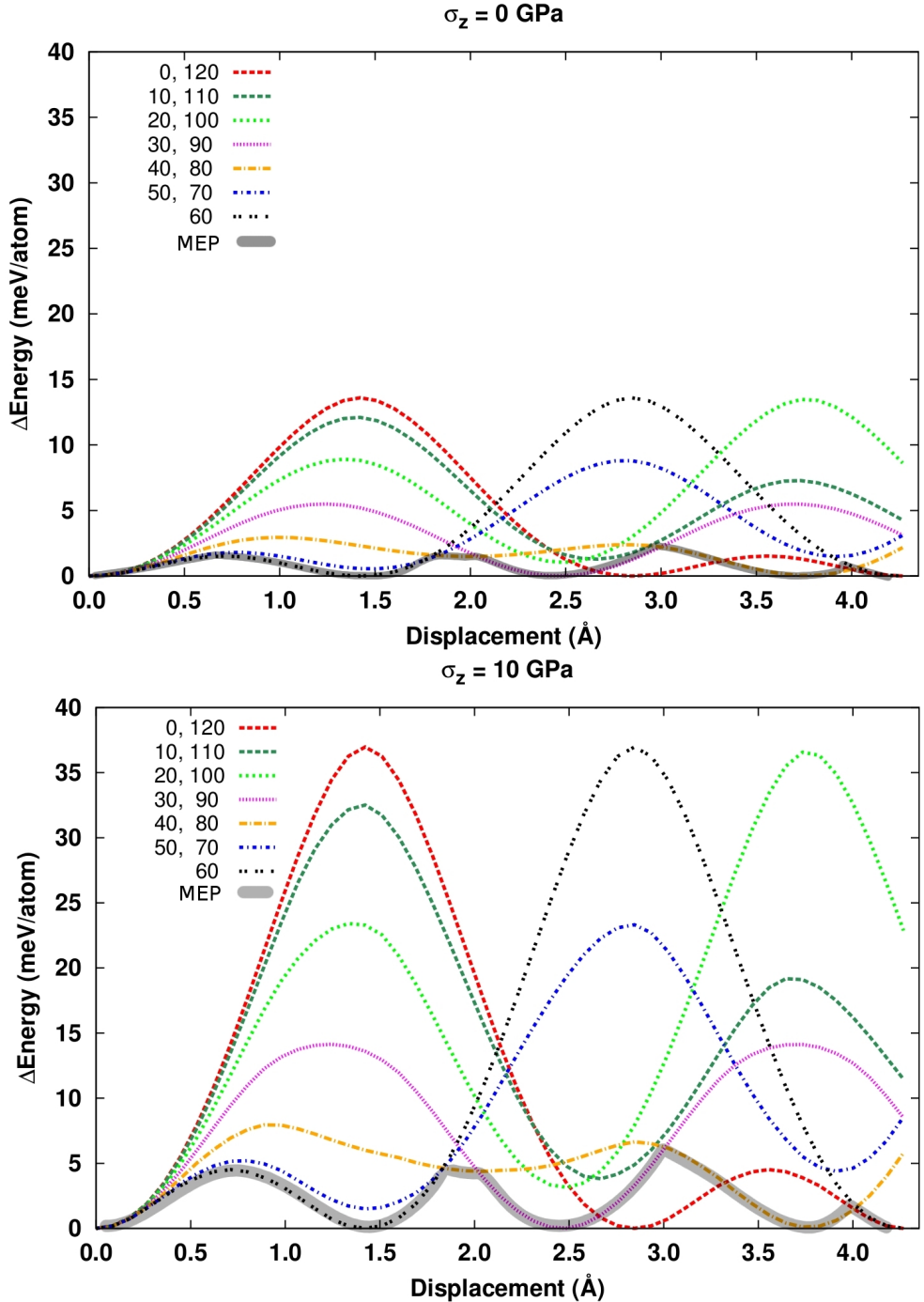


Figure 15: Energy differences relative to the equilibrium energy of 3LG as a function of the sliding displacement of the B central layer, s , at an interlayer distance of 3.25 \AA ($\sigma_z = 0 \text{ GPa}$, left) and at an interlayer distance of 2.91 \AA ($\sigma_z = 10 \text{ GPa}$, right). Different lines mean selected directions at the labeled angles. The solid (colored) wide line represents the minimum energy sliding path for the B layer following different angles.

Now, we transform the calculated frictional forces into stress (σ_{friction} , in GPa) using

$$\frac{1\text{pN}}{S_{\text{atom}}} = 0,0383 \text{ GPa}, \quad (3.12)$$

which is obtained by considering the surface of a C atom, $S_{\text{atom}} = 2.61 \text{ \AA}^2$, calculated as the half of the area of an hexagon of 1.42 \AA side (C-C bonding equilibrium distance in graphite).

From σ_z and σ_{friction} values, the static friction coefficient (μ_S , adimensional) can be straightforwardly calculated along with its load dependence. As expected, μ_S strongly depends on the sliding directions, with values ranging between 0.1 and 0.4, in excellent agreement with the accepted experimental values.³⁶ It is also noticeable that μ_S remains nearly constant around 0.18 along 30 and 90 degrees directions, in close agreement with the low friction regime observed in FFM studies.³⁶ Another interesting issue concerns the strong decrease in μ_S observed with increasing σ_z , which means that the barrier between the regimes of static and dynamic friction in graphite gradually fades under compression.

In terms of microscopic interactions, the existence of frictional forces between graphite layers comes from the loss of π -type interactions within the C-C intra-layer honeycomb pattern. This energetic loss is not compensated by the new dispersion forces connecting graphite layers in the AAA stacking. Those sliding directions where this AAA stacking is not achieved prevent the weakening of the strong C-C intra-layer bonds and facilitates layer displacements leading to lower frictional forces. As normal forces (σ_z) increase, the result of the interplay between intra- and inter-layer interactions induced by the sliding of the graphite layer show an enhanced effect of the weakening of intra-layer C-C bonds. This trend tends to saturate probably because inter-layer interactions start to be competitive.

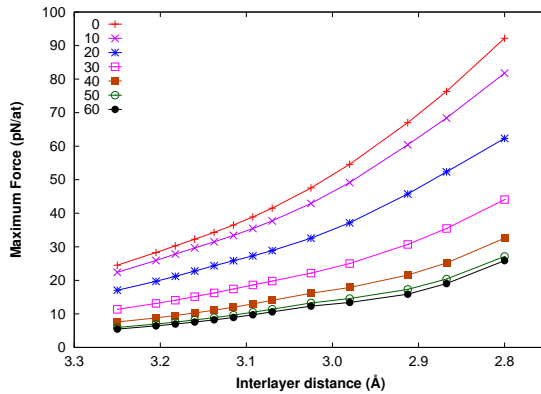


Figure 16: Friction forces between graphite layers *versus* σ_z for displacement directions from 0 to 60 degrees.

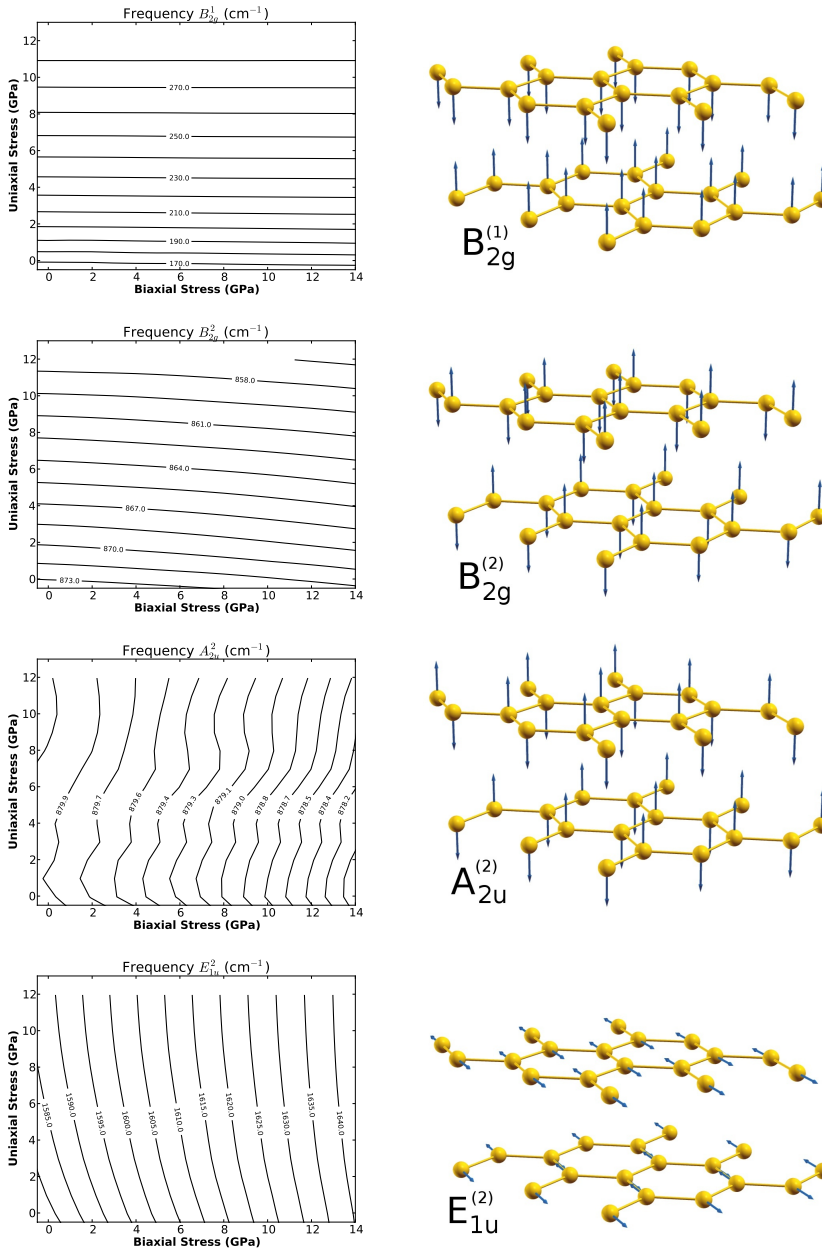


Figure 17: From top to bottom, frequency isoline maps and atomic displacements for the modes $B_{2g}^{(1)}$, $B_{2g}^{(2)}$, A_{2u} , and E_{1u} of graphite under uniaxial (σ_z) and biaxial ($\sigma_x = \sigma_y$) conditions. Results for triaxialities (including hydrostatic) can also be inferred from this plot (see main text).

4

FRICIONAL FORCES ON GRAPHITE

THE technological importance of graphite as a solid lubricant, along with the significant scientific interest of graphene, has stimulated numerous investigations on friction in carbon based materials. However, at the atomic level, there is still some room for improving our knowledge about the nature of the interactions involved in these phenomena. Here, a deep interpretative analysis of results from a novel experimental strategy is carried out to obtain the force that a graphene sheet must overcome for achieving relative motion in graphite at varying stress loads. The experiments are performed by compressing oriented graphite specimens between two opposed anvils. A detailed stress analysis is fully monitored by Raman spectroscopy. The corrugation energy landscape and the static friction parameters calculated in our previous computer simulations on a tri-layer graphene model are used to assist in interpreting the anvil cell Raman experiments. We find a consistent picture between theory and experiment that reveals how the static friction between loaded graphene sheets follows a Hertzian law with attractive forces.

4.1 EXPERIMENTAL AND COMPUTATIONAL DETAILS

4.1.1 Experiments

The general characteristics of the anvil device used have been described elsewhere.^{29,32,8} Silicon carbide (6H-SiC) anvils were obtained as loose gem-quality moissanite stones with standard brilliant cut. The opposed anvil device mounts two gems with culets cut perpendicular to the *c*-axis and polished to optical quality; culet dimensions are optimized for achieving the maximum stress projected in each experiment (about 400 μm in diameter for stresses less than 10 GPa). Since no gasket is used in our experiments, the opposed culets need to be properly aligned by interferometry before compressing the sample in order to prevent breakage of the anvils and non-uniform stresses during the experiments. It is to be noted that special care has been taken to avoid alignments problems that could bias the resulting measurements. When a sample is compressed in such fashion, the load exerted by the anvil along the *c*-axis of graphite (σ_{load}) generates a biaxial stress profile across the sample.³⁰ For this reason, Raman spectra were collected at different locations of the sample.

Raman measurements are performed using a Jobin-Yvon HR460 monochromator equipped with 600 and 2400 grooves/mm holographic gratings and a liquid-nitrogen

cooled charge-coupled detector (CCD). Raman spectra were excited using the 532.0 nm line of a Spectra Physics solid-state laser. Excitation power is optimized for maximizing signal to noise ratios, while avoiding undesired heating effects on the sample. These specifications, along with a continuous calibration of the system using a standard neon discharge lamp, provide spectral resolutions between 1 and 4 cm^{-1} , depending on the grating configuration. We use a 10x Mitutoyo infinity-corrected microscope objective coupled to a Navitar 10x zoom to collect the backscattered radiation from the sample. Confocal conditions are achieved by combining spatial filtering and appropriate CCD binning. This gives access to sampling regions between 2 and 20 μm , which largely exceeds the sampling sizes available in FFM setups. Combination of a Newport XYZ precision stage with digital Mitutoyo actuators provides spatial resolutions close to 1 μm .

4.1.2 Computer Simulations

Two types of simulations were performed in our recent theoretical study on graphite:³ Firstly, we optimized the structural parameters and evaluated the vibrational frequencies at the center of the Brillouin zone of bulk graphite under different uniaxial, biaxial and triaxial stresses preserving its hexagonal symmetry. Secondly, a periodic and infinite three layer graphene (3LG) model was built following the Bernal-type ABA stacking. First-principles total energy calculations for both type of simulations were performed within the density-functional theory (DFT) formalism with a plane-wave pseudopotential approach. Simulations in bulk graphite were performed using both QUANTUM ESPRESSO⁴⁷ and the Vienna *ab initio* simulation package (VASP)⁷⁰ with the Perdew-Burke-Ernzerhof (PBE) generalized gradient exchange-correlation functional.¹⁰⁶ Same results within the accuracy of the two computational packages were obtained. In Quantum ESPRESSO, we use a RRKJ ultra-soft pseudopotential.¹⁰⁹ In VASP, we follow the standard projector augmented wave all-electron description of the electron-ion-core interaction. In both cases, the Grimme's correction⁵⁰ was included in order to account for the dispersion interactions.

In our 3LG model, we displaced the central layer (B) up to 0.42672 nm in 0.00889 nm steps along selected sliding directions from 0 to 120 degrees at intervals of 10 degrees, and the difference in energy was evaluated at each step; these calculations were repeated at 13 decreasing interlayer distances from 0.325 nm to 0.280 nm. In all cases, a DFT-D2⁵⁰ approach was included to account for the weak dispersion forces between graphene layers. The basic characteristics of both experiments and calculations are schematized in Fig. 18.

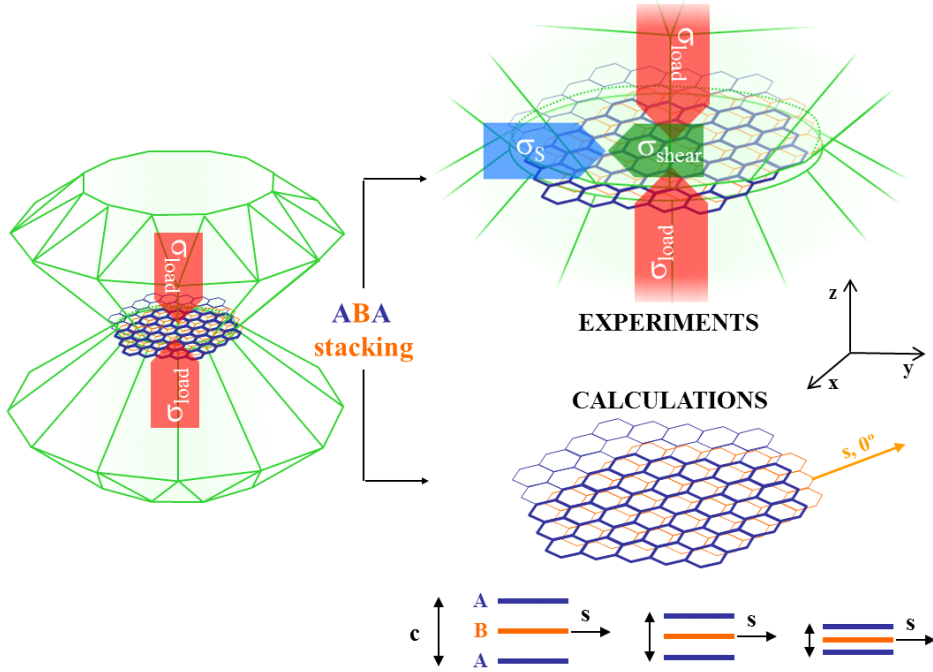


Figure 18: Scheme of our experimental and theoretical strategies. Graphite specimens are directly compressed between the culets of two moissanite anvils. The different stress components acting on the sample are indicated by arrows with size approximately proportional to their relative values. On a tri-layer slab model with an initial ABA structure we displaced the central layer (B) at different sliding directions and for selected interlayer distances.

4.2 RESULTS AND DISCUSSION

4.2.1 Stress Analysis

The value of σ_{load} can be accurately determined at the anvil/sample interface by measuring the Raman spectrum at the anvil culet, as confirmed by the exhaustive study of the stress behaviour of moissanite.³³ For these purposes, one LO phonon overtone of moissanite (2LO) exhibits some desirable features: a) it is a sharp feature, so its frequency can be accurately determined in a second derivative analysis (Fig. 19b) being an overtone, its stress slope ($7.8 \text{ cm}^{-1} \cdot \text{GPa}^{-1}$) almost doubles those of the fundamentals, thus improving the accuracy in the calculation of σ_{load} from the relationship $\sigma_{load} \text{ (GPa)} = \Delta\omega_{2LO} \text{ (cm}^{-1})/7.8$, where $\Delta\omega_{2LO}$ is the frequency shift of the 2LO band with respect to its frequency at room conditions (1712 cm^{-1}), and c) this feature is close to the G band of graphite (1580 cm^{-1}), so both bands can be simultaneously measured

in the same spectral window (Fig. 19a). This allowed us to obtain the specific value of σ_{load} supported by each sampling region and to include the effect of the spatial loading distribution in our analysis.

In order to make our study comparable to existing FFM experiments, stress ought to be converted into force ($1 \text{ GPa} = 1 \text{ nN}\cdot\text{nm}^{-2}$). Previous FFM studies in the low-load regime reached equivalent pressures of about 1.4 (Ref. 84) and 0.5 GPa (Ref. 117), so our experiments (*ca.* 4 GPa) should be regarded as moderate-to-large in terms of applied load. We shall consider here only the results recorded in those sampling regions with no defects or small concentration of defects, which essentially corresponds to measurements at the center of the anvils, where maximum load stress is attained in each run. This was confirmed by the negligible intensity of the so-called D-band^{99,31} in each Raman spectrum of graphite used in our analysis.

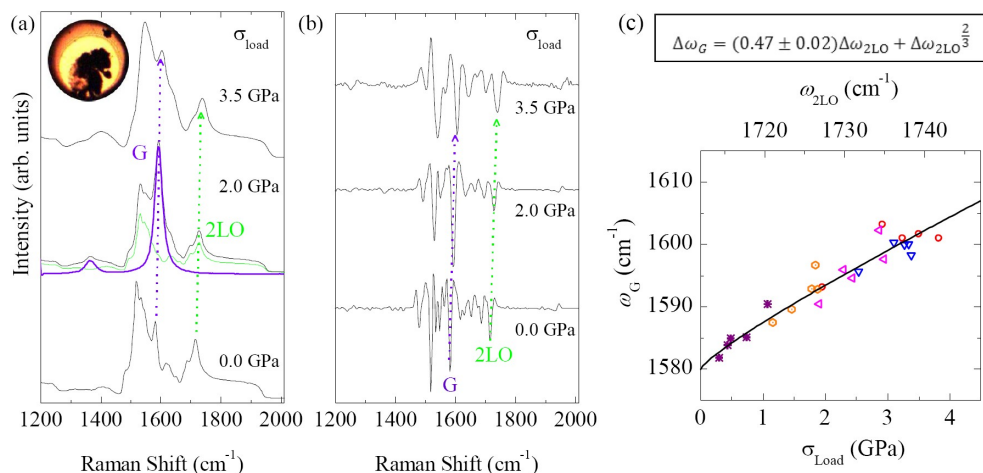


Figure 19: (a) Raman spectra containing superimposed contributions from the front anvil and the sample at selected loading stresses. Both contributions are plotted separately for moissanite (green) and graphite (blue-violet). The inset shows a photograph of the graphite sample (in black) between the moissanite anvils in the pressure cell. (b) Second derivative analysis of the collected spectra providing unambiguous separation of ω_G of graphite and ω_{2LO} of moissanite. (c) Dependence of ω_G with σ_{load} , as measured by the ω_{2LO} of moissanite (upper axis). Different symbols stand for different experimental runs. The black solid line represents the fitting function shown on top to account for the sub-linear dependence of ω_G with σ_{load} .

The Raman spectrum of graphite has been extensively studied and analysed under different stress conditions, both hydrostatic⁵³ and non-hydrostatic,^{29,32,49,105} using conventional gasketed anvil cells. A general observation is that the frequency of the G band, which originates from an in-plane vibration of E_{2g} symmetry, increases when compressive in-plane stresses are present. Thus, it was somewhat unexpected that in our experiments ω_G increases (Figs. 19a and c) when the stress was applied perpendicular to the basal plane of graphite with no gasket between the anvils. As a matter

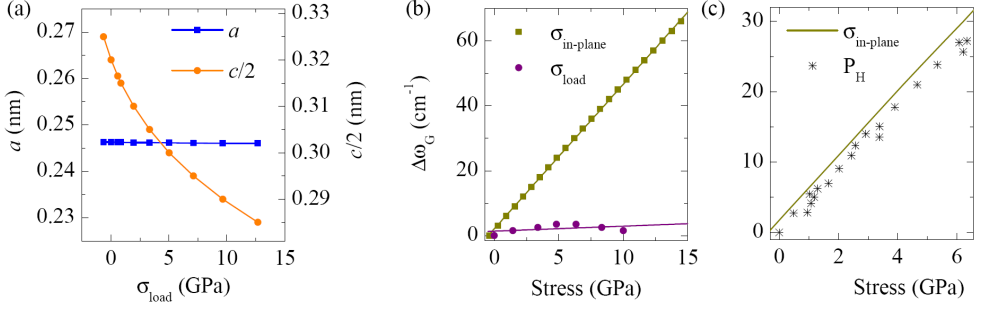


Figure 20: (a) Calculated lattice parameters, a and c , of graphite as function of the stress applied along the normal direction to graphene layers (σ_{load}), ($c/2$) corresponds to the interlayer distance between two graphene sheets. (b) Calculated Raman shift of the G band of graphite (referred to ω_G at zero pressure) as function of different stress components. (c) Comparison of calculated $\Delta\omega_G$ values under biaxial stress (solid line) and hydrostatic pressure (P_H) experiments (symbols) from Ref. 53

of fact, our theoretical calculations predicted negligible changes on ω_G with uniaxial stress (Fig. 20b). Thus, our experiments reveal that, when graphite is squeezed between two opposed anvils, in addition to σ_{load} , other in-plane stress components appear on the sample. As we shall conclude later, the main in-plane stress component acting on the graphene layers derives from friction forces against sliding (σ_S in Fig. 18), resulting from locking confinement of the sample between the anvils (despite the absence of gasket between them).

Our calculations indicate that, when graphite is loaded along the c -axis, the interlayer distance strongly decreases while the lattice parameter a remains essentially constant (as shown in Fig. 20a, within the experimental stress range (σ_{load} : 0-4 GPa), a decreases in 0.13%). Despite the intrinsic interest of this result within the framework of auxetics,¹¹ it agrees with the fact that the c_{13} elastic constant of graphite is essentially null at room pressure,¹⁶ becoming slightly negative under high stress. This also means that if the stress tensor includes only c -axis contributions, the shift observed in ω_G should be negligible or, at most, slightly negative (Fig. 20b), in clear contrast to the experimental results of Fig. 19c. Our calculations also demonstrate that a blue-shift in ω_G is only expected when the stress is applied within the graphene planes, in our case, biaxial stress. Interestingly, our calculated stress coefficient for ω_G (4.6 cm⁻¹/GPa) is in close agreement with that found in hydrostatic experiments,⁵³ as confirmed in Fig. 20c, thus explaining why both hydrostatic and biaxial experiments on graphite and graphene yield similar mode Grüneisen parameters for this band.³²

Overall, the analysis of the experimental data in the light of our previous theoretical results confirms the hypothesis that when graphite is squeezed along the c -axis, compressive in-plane biaxial stress components are present. One may speculate that the largest in-plane contribution is due to frictional stress, but in order to determine its relative value, we must quantify other possible stress contributions during the experi-

ments. Let us begin analysing the possible contributions concerning the graphite-anvil interface. Unlike graphite, moissanite exhibits positive c_{13} values (52 ± 9 GPa)⁶³, so shear stresses (σ_{shear}) may be transferred from the anvil to the sample, since the anvil is also non-uniformly stressed along the axial direction. Thus, an additional contribution to be considered concerns shear components from the center towards the border of the anvil culet (σ_{shear} in Fig. 18). Neglecting such contributions would result in an erroneous determination of the pure friction stress, σ_S , making it necessary to perform a detailed analysis of the anvils response to stress in our particular experimental configuration. A recent procedure³³ to analyse the stress distribution of the anvils has been used to estimate the correlation between load and shear stress in moissanite: $\sigma_{shear} \approx 0.6\sigma_{load}$. This result is in excellent agreement with similar analyses in diamond along the [111] direction,⁴ and agrees with the fact that both diamond and moissanite exhibit comparable ν_{13} Poisson ratios. In any case, the relevant conclusion is that the total stress acting on the sample in the in-plane direction, $\sigma_{in-plane}$, contains contributions from both friction and shear. Since $\sigma_{in-plane}$ can be estimated from existing correlations between ω_G and the applied stress,⁵³ the friction contribution can be calculated simply as $\sigma_S = \sigma_{in-plane} - \sigma_{shear}$. This contribution represents the average stress supported by about 90 graphene layers (considering the penetrability of the 532 nm radiation in graphite samples); being unlikely to discern between the behaviour of the first graphene layer, in direct contact with the anvil, and that of the rest of layers.

4.2.2 Friction Analysis

In order to check whether σ_S can be related to the microscopic sliding friction force between graphene layers, a deep analysis of our computer simulations in 3LG model, presented in the Chapter 3, is carried out. We recover in Fig. 21a the energetic profiles of a graphene layer inside graphite sliding along different directions at zero stress. In Fig. 21b such profiles along the 0° direction at decreasing interlayer distances up to 0.280 nm (about 12.5 GPa) are displayed. The effect of the in-plane stress components has been evaluated and almost negligible variations were observed in the sliding distance, s , at which the energetic barriers appear. Along all the sliding directions considered, the 3LG model reaches the AAA configuration at sufficiently large distances, with the exception of the 30° and 90° ones. When applying load stress (i.e. decreasing the interlayer distances), the energetic barriers just raise their height, but their location remain unaltered, as observed in Fig. 21b.

Our calculations predict that, if incommensurate displacements are allowed between graphene layers, the relative orientations of the layers must change according to the path of minimum energy, which, interestingly, does not change with the applied load (see Ref. 3). A similar behaviour was found in studies of a tip movement over the FCC(111) surface using a 2D Prandtl-Tomlinson model.³⁹ Although we are interested here on the early stages of movement between the graphene sheets, the previous discussion demonstrates that this kind of computer simulations can be successfully

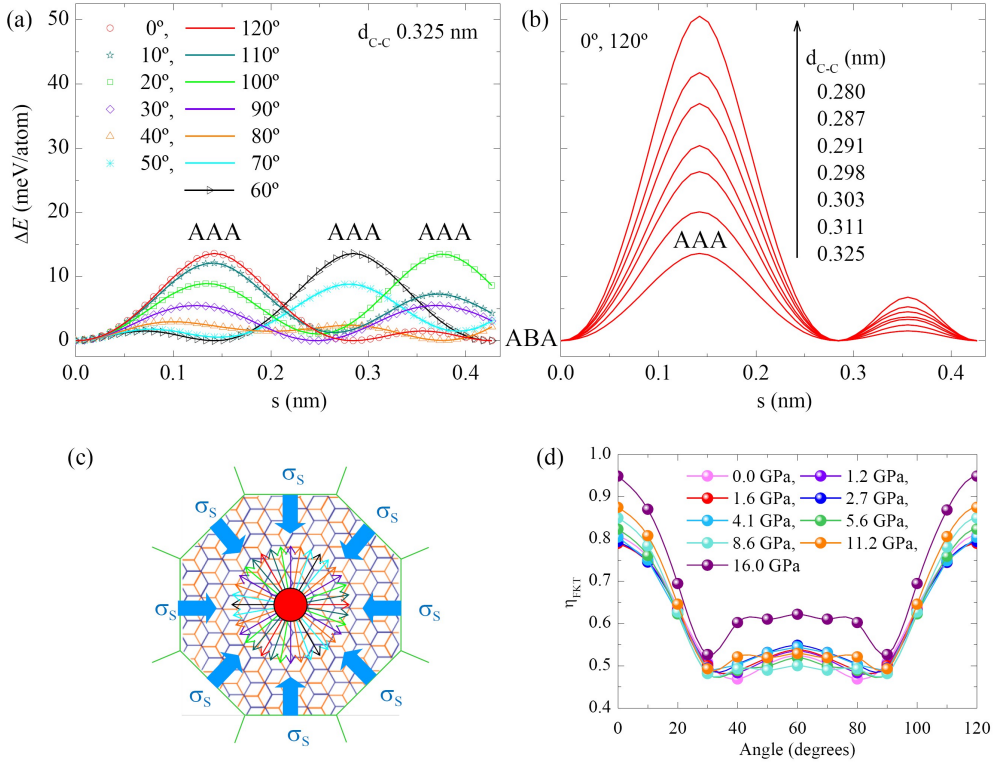


Figure 21: Calculated energy differences relative to the equilibrium energy of tri-layer graphene as a function of the sliding distance of the B central layer, s , (a) for selected sliding angles at an interlayer distance of 0.325 nm and (b) for the 0° direction at selected interlayer distances. (c) Rendering of the load (red) and friction (blue) forces acting on the graphene samples squeezed between the opposed anvils. As the sample is loaded, graphene layers tend to displace in all directions (colored arrows), but the confinement of the sample induces friction stresses opposed to the relative motion of the graphene layers. (d) Friction parameter in the 2D-FKT model (calculated with Eq. (1) at different load stresses) as a function of the sliding angle.

used to analyse dynamic friction problems. The corrugation energy profiles in Fig. 21 resembles the potential of a 2D Frenkel-Kontorova-Tomlinson (FKT) model,³⁹ where different one-dimensional FKT-like potentials appear depending of the sliding angle, with an angle periodicity of 120 degrees. From these profiles it is also possible to analyse the dimensionless parameter, η_{FKT} , which gives the boundary values for stick-slip processes included in the FKT model:¹¹⁹

$$\eta_{FKT} = 2\pi^2 \frac{\Delta E_{1/2}}{ks^2}, \quad (4.1)$$

where $\Delta E_{1/2}$ and s are half the height and the sliding distance of the first energy barrier found along a given sliding direction, respectively, and k is the harmonic elastic constant that is obtained as the second derivative of the energy profile at the equilibrium position (ABA configuration).

In Fig. 21d we plot η_{FKT} as a function of the sliding directions at different interlayer distances (*i.e.* different values of σ_{load}). We find that the preferred sliding directions are $(30+60n)$ degrees, where n represents an integer, whereas those directions at $(120n)$ degrees are the less favourable ones. Once again, the characteristics of the sliding directions are the same regardless the interlayer distance considered, since load does not change the ABA configuration. It is interesting to note that the value of η_{FKT} does not show significant changes with load below 10 GPa. At higher stress (between 10-15 GPa) η_{FKT} increases, regardless the sliding direction considered, so it can be understood that, beyond that point, graphene sheets literally stuck each other with little chances to displace in any direction. Interestingly, within the same stress range (*ca.* 15-20 GPa) a cold-compression phase transition from graphite to a super-hard phase is now under debate,¹⁸ so one would speculate that nucleation of the new phase might start when interlocking takes place between adjacent graphene sheets. This result opens new avenues for understanding the relationship between large friction forces and other phenomena under extreme stress conditions.

In any case, the important improvement against classical FKT analytical models³⁹ is that our DFT calculations provide direct access to numerical values of the corrugation energy and, through the first derivative of the energy with respect to the sliding distance, to the friction force. As described in detailed in Chapter 3, from the results of Fig. 21a, and others similar at interlayer distances between 0.325 nm and 0.280 nm, σ_S can be calculated using the maximum force required to initiate motion between adjacent layers, so the analysis can be restricted to sliding distances below the first maximum in each energy curve. In addition, we can convert interlayer distances into σ_{load} using the equation of state we obtained in bulk graphite.³ The results are plotted in Fig. 22a. These results allow us to compare both experimental and calculated friction forces and to give a global discussion of our study on the basis of existing contact mechanical models.⁶⁰ The main results are summarized in Figs. 22b and 23. The sub-linear variation observed in Fig. 22a, regardless the sliding angle considered,

suggests using a Hertzian-like law⁶⁰ to fit the results, in the line of previous studies of different carbon materials under relatively low loads:¹¹⁷

$$\sigma_S = \sigma_0(\sigma_{\text{load}} - \sigma_R)^H \quad (4.2)$$

In Eq. 4.2, σ_0 , σ_R and H are characteristic parameters of a Hertzian model including attractive forces, and it is analogous to the “*Hertz plus-offset model*” proposed by Schwarz *et al.*¹¹⁷. We are dealing with a microscopic interpretation in terms of interactions involving the electronic density of the graphite layers, and it is not our aim to claim that the simulated behaviour obey Eq. 4.2. However, we think that it is worth to use the *Hertz plus-offset model* in our analysis since our data are well described with the above equation. In our case, we considered H as an adjustable parameter in order to evaluate whether graphite follows a purely Hertzian behaviour (σ_S scales as $\sigma_{\text{load}}^{2/3}$) or not at the atomic level. The parameters σ_0 , σ_R and H obtained from the fit are plotted in Fig. 23, where an evident angular dependence of each parameter is observed, thus reflecting the importance of the shape shown by the corrugation energy. Figure 23 also shows how these parameters change when the friction regime develops from static (black symbols) into dynamic (red symbols). The evolution of H in Fig. 23 reveals that, according to our calculations, loaded graphite tends to follow a Hertzian-like law only in the dynamic regime, in agreement with the low-loading experiments.¹¹⁷

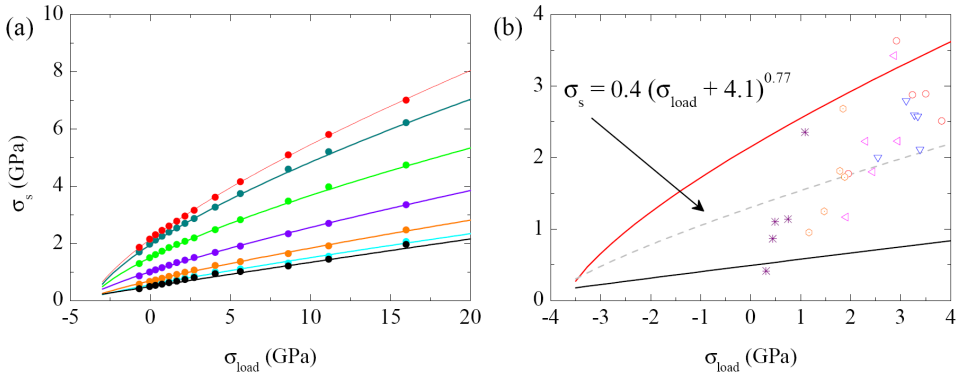


Figure 22: (a) Calculated static friction stress along selected sliding directions as a function of σ_{load} ; symbols stand for different sliding directions using the same color definitions of Fig. 21a; lines are fits to Eq. 4.2. These results correspond to the maximum stresses found along the selected sliding directions before reaching the first energy maximum in Fig. 21a. (b) Comparison of the calculated static friction stress from (a) with the experimental values derived from Fig. 19c. The dashed line represents Eq. 4.2. using averaged values of the characteristics parameters shown in Fig 23; continuous lines represent the limiting values (sliding directions of 0° and 60° plotted in (a)).

What is perhaps even more interesting from a fundamental point of view is the analysis of the parameter σ_R , which indirectly measures the effect of attractive forces included in more sophisticated models.⁸⁵ Thus, according to its definition in Eq. 4.2, σ_R also represents the negative (rupture) stress needed to separate two graphene sheets and gives an indirect measure of the exfoliation energy of graphene. In the field of equations of state (EOS), the same concept stands for the so-called spinodal stress,⁴⁵ which is intimately related to Born's stability conditions.¹⁵ To analyse this, we shall consider the linear, one-dimensional Murnaghan's equation,⁹⁶ which takes the following form for the c -axis length in graphite:⁵³

$$\left(\frac{c}{c_0}\right) = \left(\frac{\beta'}{\beta_0}\sigma_{\text{load}} + 1\right)^{\frac{1}{\beta'}} \quad (4.3)$$

where c_0 is the length of the c -axis at zero stress, β_0 is the linear stiffness coefficient at zero stress and β' its first stress derivative. Thus, σ_R can be simply calculated as $\sigma_R = -(\beta_0/\beta')$ from known values of β_0 and β' . Using the results $\beta_0 = 35.7$ GPa and $\beta' = 10.8$ reported by Hanfland *et al.*⁵³ from EOS measurements using X-ray diffraction experiments in bulk graphite, the estimated value of σ_R is -3.3 GPa. This value is in good agreement with the average value of $\sigma_R = (-4.1 \pm 0.5)$ GPa, obtained from the analysis included in Fig. 23, and with the value of $\sigma_R = (-4.3 \pm 0.3)$ GPa, obtained with the parameters $\beta_0 = (50 \pm 1)$ GPa and $\beta' = 11.5 \pm 0.5$ from the fitting of (c/c_0) results of Fig. 20a to Eq. 4.3.

Figure 23 also provides the appropriate framework to compare them with the experimental results given in Fig. 22b. Performing such a comparison demands transforming calculated friction forces (pN/atom) into stress (GPa) by dividing the calculated friction force by the effective surface occupied by a carbon atom (0.0261 nm^2). This effective surface has been obtained by considering an initial equilibrium carbon-carbon bond-length of 0.142 nm in the hexagonal lattice of graphene. Although experimental results show a large dispersion, they are nicely bounded by the limiting values (0° and 60° sliding directions) of the calculated static friction stress shown in Fig. 22a. This confirms that the Raman measurements average the static friction contributions across large interaction areas along all sliding directions. The dispersion in the experimental data observed in Fig. 22b is very likely related to the generation of defects in the initially perfect commensurate ABA structure of bulk graphite. Notice that in each run the experimental results tends to increase as the average stress increases, which indicates that shear components generate some concentration of defects (not very large though, according to the small intensity of the D band⁷⁹ observed around 1350 cm^{-1} in the Raman spectrum of graphite, see Fig. 19a). Our experimental results thus suggest that, as the concentration of defects increases, the static friction also increases, in agreement with recent dynamic friction experiments in graphene.⁷⁷ However, it is striking that the average friction stress measured in each run nicely fits the average curve shown in Fig. 22b, which has been obtained by averaging the characteristic parameters shown in Fig. 23 a to c.

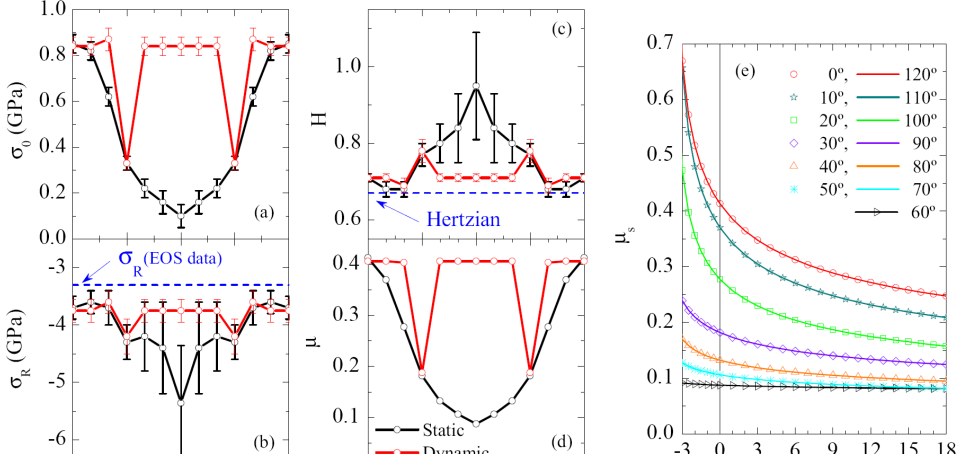


Figure 23: (a to c) Parameters in the Hertzian model with attractive forces, Eq. 4.2, in the static (black) and dynamic (red) regimes. The static results derive directly from the results plotted in Figure 22a, while dynamic results are obtained from the maximum stress found at large, formally infinite, sliding distances. (d) Friction coefficient at zero load as a function of the angle of the selected sliding directions for the static and dynamic regimes. (e) Static friction coefficient calculated along selected sliding directions as a function of σ_{load} , obtained from the derivative of σ_S , with respect to σ_{load} (Fig. 22a), using the parameters of Eq. 4.2.

Finally, the results of Fig. 22 can also be used to estimate boundary values for the static friction coefficient μ_S and its load dependence, Figs. 23d and 23e. Notice that the static friction coefficient is defined as the derivative of the load stress with respect to the load, and, therefore, it is a finite value at zero load stress, where a non-negligible static friction stress (the *offset* in the Hertzian model) is present. As expected, μ_S also strongly depends on the sliding direction, with values ranging between 0.1 and 0.4, in excellent agreement with the accepted experimental values.⁸⁶ It is also noticeable that μ_S remains nearly constant around 0.18 along the 30 and 90 degrees directions, in close agreement with the low friction regime observed in FFM studies.³⁶ Another interesting issue concerns the strong decrease in μ_S observed with increasing σ_{load} , which means that the barrier between the regimes of static and dynamic friction in graphite gradually fades under compression.

5 | BUILDING MOTIFS OF THE SELF-ASSEMBLY OF PARA TERPHENYL META DICARBONITRILE

VARIOUS structural motifs such as one-dimensional ribbons and their interconnections were recently seen in scanning tunneling microscopy experiments when para-Terphenyl-meta-Dicarbonitrile (pTmDC) molecules were deposited on the Ag(111) surface (M. Marschall *et. al.*, ChemPhys-Chem 11:1446, 2010). By using *ab initio* density functional theory calculations, we systematically study the main building blocks that the two isomers of the pTmDC molecules can form in the gas phase, going from dimers to more complex structures involving trimers, chains and various linkers. We show that the hydrogen bonding plays a decisive role in the formation of the different experimentally observed structures. We have also found that the energy barriers for the isomerization transition for a single molecule in the gas phase are always lower than 9.6 kJ/mol proving that there must be equal amounts of both isomers on the surface initially at deposition.

5.1 METHODS

Calculations have been carried out in the framework of the density functional theory (DFT)^{57,69} using the open source computer code CP2K/QUICKSTEP.¹²³ It implements the hybrid gaussian and plane wave method (GPW)⁷⁶ whereby atom-centred Gaussian-type functions are used to describe the Kohn-Sham wave functions; however, an on-the-fly conversion is made to a plane wave basis set to calculate efficiently the electrostatic energy. Atomic cores are represented using Goedecker-Teter-Hutter (GTH)⁴⁸ pseudopotentials. We used the Perdew-Burke-Ernzerhof (PBE) generalized gradient exchange-correlation functional,¹⁰⁶ whereas the Grimme's DFT-D3 method⁵¹ was employed for taking into account the dispersion forces. We have chosen the optimized basis set m-DZVP¹²² for all atoms and a plane wave cutoff energy of 280 Ry. Geometries were relaxed until forces on atoms became less than 0.02 eV/Å. All the calculations have been done using periodic boundary conditions, and in the cases of the calculations on individual clusters of molecules we ensured to consider units cells big enough so as to make the interaction between neighboring clusters negligible. It was suggested in a detailed study based on systematic quantum-chemistry calculations that DFT based methods perform reasonably well for H-bonded systems.⁶²

Binding energy of a complex ABC... obtained by combining species A, B, C, etc. together is defined as

$$E_{\text{bind}} = E_{\text{ABC}\dots} - E_{\text{A}}^0 - E_{\text{B}}^0 - E_{\text{C}}^0 - \dots,$$

where $E_{\text{ABC}\dots}$ is the DFT total energy of the complex, and E_{A}^0 , E_{B}^0 , etc. are the energies of the individually relaxed species A, B, etc., respectively. However, as we employed a localized basis set, for computing the actual binding energy of the complex we need to consider the basis set superposition error (BSSE). It was calculated by means of the (positive) counterpoise (CP) correction²⁰ being added to the above expression for the binding energy. The latter requires calculating species A, B, etc. individually in an extended basis set comprised of orbitals of each respective species and the “ghost” orbitals of other species.

For accessing the energy barriers involved in the cis-trans isomerization process of a monomer, we computed the Minimum Energy Path (MEP) between all stable configurations by means of the Nudged Elastic Band (NEB)^{61,88} method. Both Improved Tangent NEB and the Climbing Image NEB calculations^{54,55} were employed as discussed below.

To illustrate the strength of H bonds, two methods were used. In the first one, we analyzed charge density differences in various structures. These were calculated by subtracting from the electron density $\rho(\mathbf{r})$ of the combined system the densities of the corresponding parts calculated at the geometry of the combined system. In the second method, we analysed the topology of the electron density using the so-called (dimensionless) reduced density gradient^{59,25,26}

$$s(\mathbf{r}) = \frac{1}{2(3\pi^2)^{1/3}} \frac{|\nabla\rho(\mathbf{r})|}{\rho(\mathbf{r})^{4/3}}$$

which is specially designed to identify regions where non-covalent interactions (NCI) play a dominant role. In visualising $s(\mathbf{r})$, the isosurfaces are coloured on a blue-green-red scale according to the values of $\text{sign}(\lambda_2)\rho(\mathbf{r})$, which values range between $-0,02$ and $0,02$. Here λ_2 is the middle eigenvalue of the Hessian matrix of the density. With this color scheme, red indicates strong non-bonding (steric) repulsion, green indicates weak interaction, while blue detects strong attractive interaction, e.g. the H bonding.

5.2 RESULTS

5.2.1 Monomers

We start by discussing structures and energetics of the pTmDC monomers. After an exhaustive search of possible atomic equilibrium configurations, we obtained six stable conformations that can be grouped in three sets, each including the cis (C) and trans (T) isomers, plotted in Fig. 24. The set with higher energies (denoted with a

subindex pl) contains planar geometries in which all atoms are within a plane. The other two sets contain non-planar conformations. We call parallel (labelled with p) those conformations which have the atoms of only the two end benzonitrile rings being in the same plane, whereas the non-parallel configurations (labelled with np) refer to monomer conformations where all three rings are in three different planes. In these two non-planar sets, the dihedral angles between rings lay in the range of 32-40°. Differences between the energies of all p and np structures, including both C and T isomers, are almost negligible, while the planar geometries lie about 14.6 kJ/mol higher in energy, i.e. are much less favorable. Detailed energetic information about all found stable gas phase structures is collected in Fig. 24. Our results clearly illustrate that isolated monomers in the gas phase are preferably non-planar, and that they could be with equal likelihood either in T or C geometries, since both isomers are almost indistinguishable in energy.

We have also calculated dipole moments of the molecules. These for the parallel and non-parallel geometries were found to be 7.9 D and 6.5 D for C, and 0.3 D and 4.4 D for T, respectively.

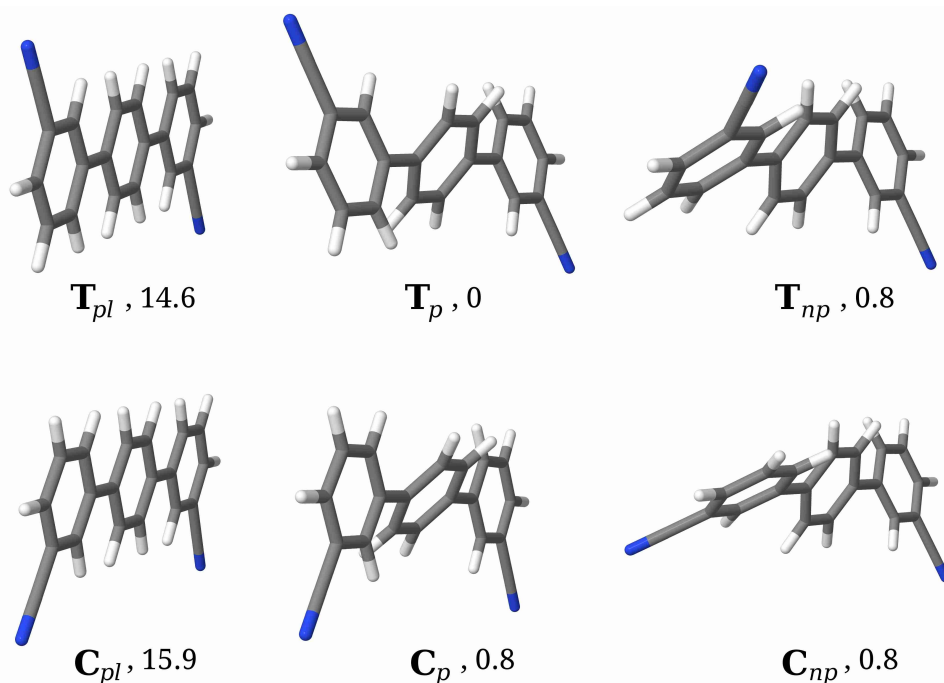


Figure 24: DFT relaxed geometries found for different conformers of the pTmDC molecule. Legends: C- cis, T- trans; subscript pl - planar, p - parallel and np - non-parallel (see definitions in the text). Numbers next to the labels are relative energies in kJ/mol. Blue ends represent the N atoms, white ends H atoms and grey color corresponds to C atoms.

Since it was claimed that the number of cis molecules on the surface is significantly reduced after evaporation and assembly,⁸³ it is essential to understand whether indeed cis to trans isomerization does not happen in the gas phase prior for the molecules to adsorb on the surface. Therefore, in order to obtain a deeper understanding of the isomerization mechanism, and to estimate the energetic cost involved in this process, we carried out NEB calculations. Starting from the C_p conformation, we calculated the MEP for one end ring of the molecule being rotated by 360° along its backbone, passing through three other possible conformers C_{np} , T_p and T_{np} , until the same initial conformation C_p is reached again. We divided the isomerization path in four steps, each step corresponding to the path between two nearest stable geometries. Within each step we created eight replicas (including the two fully relaxed structures at the ends) and computed eleven Improved Tangent NEB steps before moving to the Climbing Image NEB calculation.^{54,55} The energetic profile along this rotation, including schematic views of the relevant intermediate conformations, is shown in Fig. 25. In this way, we obtain all possible isomerization paths for transforming one conformer into any other stable conformer following either a clockwise or anti-clockwise rotation of the ring. As we can see, planar conformations never happen along the isomerization path. If the $C_p \rightarrow C_{np}$ and $T_p \rightarrow T_{np}$ transitions can be attributed to steric hindrance, the other two transitions are most likely to do with peculiar restructuring of the occupied molecular orbitals resulting from the transition between the two isomers.

The highest barrier, ΔE , obtained for the transformation between C and T isomers is about 9.6 kJ/mol. This corresponds, at room temperature, to the rate of around 10^{11} isomerizations per second. This very high rate means that the isomerization process occurs very easily at room temperature. Using this result, we can conclude that the four non-planar isomers are almost equally favorable in the gas phase, and their expected population will be approximately the same. In other words, one should assume that there will be equal amounts of the C and T gas phase isomers prior to their adsorption on the silver surface. Hence, upon deposition, there must be 50 % of cis and by 25 % of each of the trans isomers.

5.2.2 Dimers

As will be shown later on, a rational explanation of the pTmDC structures experimentally observed on the Ag(111) surface can be provided assuming that the hydrogen bonding (H bonding) plays the dominant role in holding the molecules together. As the H bonding is highly directional, it seems very reasonable to think about dimers as the most elementary building blocks of the many pTmDC motifs experimentally found on top of this surface. Thus, the next logical step is to fully characterize all possible dimers two molecules may form.

Therefore, we performed full geometry optimization of a large sample of different dimer configurations. In Fig. 26 we show the relaxed geometries, along with the corresponding binding energies, for 20 dimers found (more were tried, but found unstable;

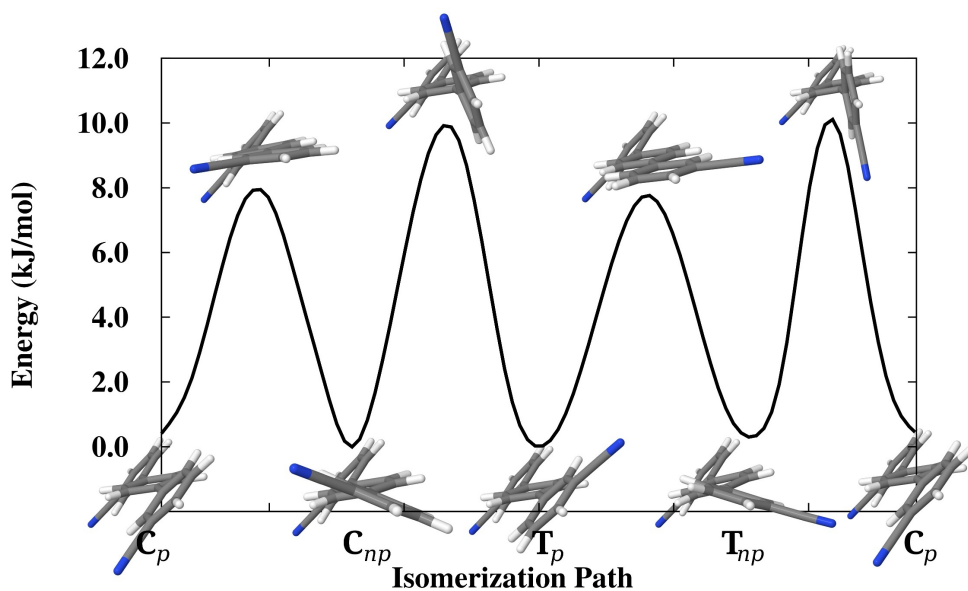


Figure 25: The DFT calculated MEP of the isomerization process considered by rotating one end ring of the molecule by 360° around its backbone using the NEB method. Colors as in Fig. 24. Reading the graph from left to right, the obtained geometries correspond to a clockwise rotation of the front ring. Correspondingly, each conformer has two possible paths for isomerization into another one following one of the two possible directions.

not shown). We have tried to be exhaustive in our search by mimicking, as much as possible, all patterns found in the experimental STM images (see Figs. 3-5 in Ref. 83), as well as many other possibilities, and no more stable dimer conformations were found.

By looking at the results presented in Fig. 26, we can classify all dimers in three main groups according to their binding energies. The first one contains dimers CT-Tri_{2n}, CC-Tri_{2n}, TT-T₂, TT-Lin₂ (numbers 1 to 4), the second group includes TT-P_{2a}, CC-P_{2a}, CT-P_{2a}, TT-P_{2b}, TT-Lin₁, CC-Lin₁, CT-P_{2b}, CC-P_{2b}, TT-Tri₂, CC-Tri₂, CT-Tri₂ (5 to 15), and the rest of the dimers form the last group. The first group consists of stable non-planar monomers bonded by two hydrogen bonds, only one of them presenting a linear C-N-H arrangement. The binding energies in the first group are all around -29.0 kJ/mol with a minimum distance between monomers being around 2.4 Å (measured by the shortest distance between atoms of the two molecules). The dimers of the second group have binding energies between -2.1 and -11.7 kJ/mol. Here, minimum distances between monomers are within the 2.37-2.41 Å range, similar to the dimers in set one. This group is mainly formed (dimers 5 to 8 and 11 to 15) by planar monomers bonded by two hydrogen bonds. Dimers 9 and 10 are bound by a single H bond but are non-planar, which gives them an extra stability. The two H-bonds of the

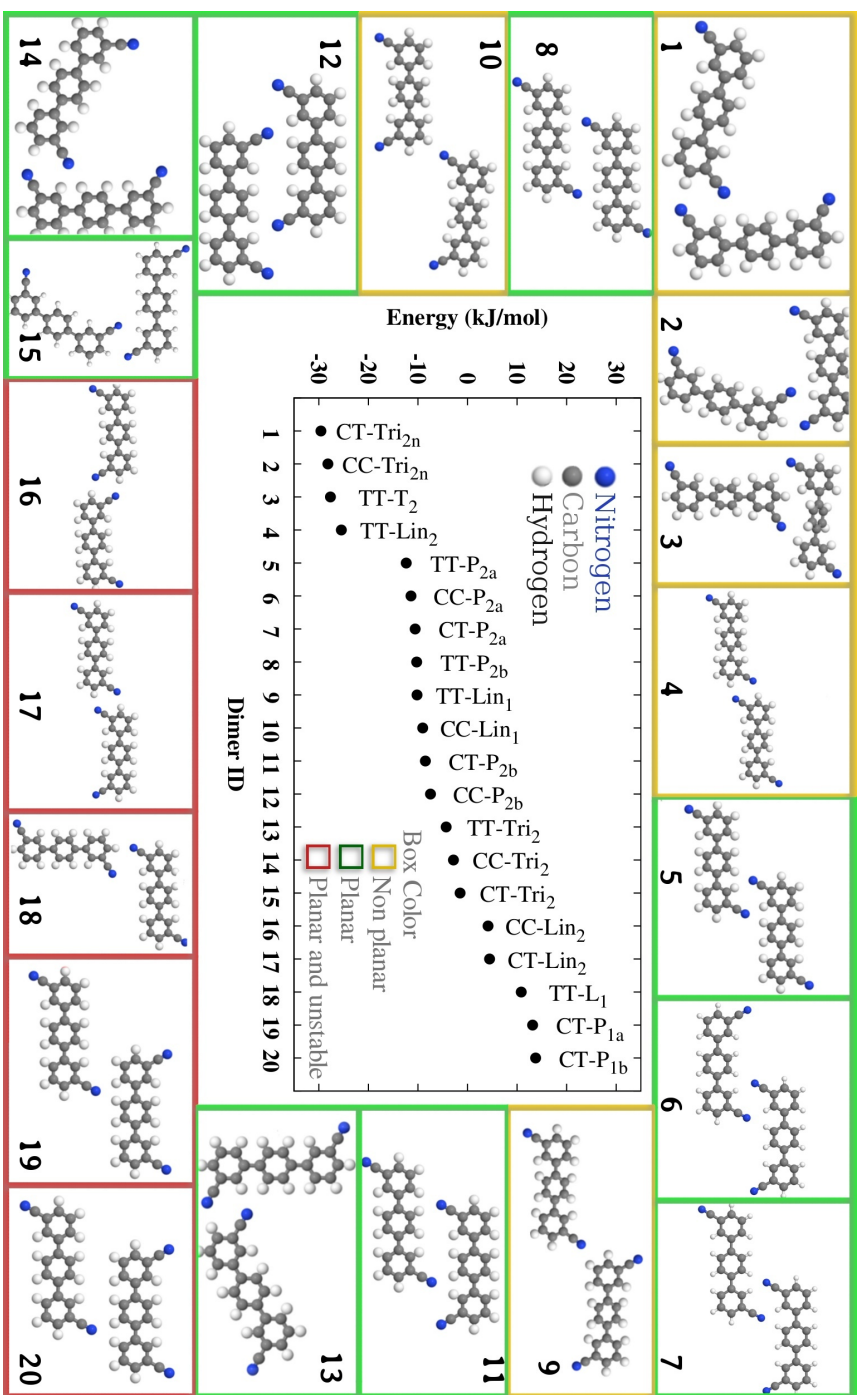


Figure 26: DFT calculated binding energies (in kJ/mol, the central panel) and relaxed geometries of dimers considered here. The legend used to denote the dimers means: the first two characters are composed of either C or T corresponding to the cis or trans conformations of the constituent monomers; the next letter is either L, T, P, Tri or Lin and refers to L-like, T-like, Parallel, Triangular or Linear forms, respectively; the index 1 or 2 that follows corresponds to the number of hydrogen bonds in the dimer; finally, a n subscript is used for non-planar triangular dimers, and a subscript a or b is used to differentiate between similar parallel structures involved in the H-bond, respectively, when they have one or two benzenitrile rings in each monomer. All dimers are numbered from 1 to 20, and their binding energies are shown in the plot in the centre of the Figure. Around the energy plot all 20 relaxed structures are shown. Yellow and green frames are used to indicate stable non-planar and planar geometries, respectively, while the red frame is used for unstable planar structures found.

most stable planar conformations in this group (dimers 5 to 8, 11 and 12) are both linear (in the sense that the three atoms involved align along a line), while the other three planar conformations (dimers 13, 14 and 15) display one linear and one non-linear H-bonds. Dimers 5-8 and 11 and 12 present similar arrangements of the two molecules, with dimers 5, 6 and 7 being found to be slightly more stable. This presumably may be due to lack of steric repulsion of the hydrogens that are between the hydrogen bonds; we shall return to this point later. Differences in energies between the dimers 8, 11 and 12 are due to the specific isomers forming the dimers: T-T is slightly more stable than T-C and the latter is more stable than C-C, but differences are almost negligible. With respect to the third group, these dimers have positive binding energies and distances between monomers are bigger than 2.41 Å. In dimers 16 and 17 monomers are bonded by two non-linear H-bonds. Dimer 18 has lower energy than 19 and 20 even though it presents non-linear H-bond because it does not have this steric repulsion effect.

We note that, in spite of being unstable, dimers of the last group are worth discussing since these conformations may be involved in the self-assembly process of the pTmDC molecules on the silver surface. Moreover, simple rearrangements may lead these dimers to other stable configurations. For example, if we compare dimer 19, which is unstable, with dimer 5, which is the most favorable conformation within the planar dimer set, we see that a cis-trans isomerization of one of the monomers can convert one structure (19) into the other (5). The same happens between dimers 20 and 8. Another interesting example is the formation of the ribbon from the unstable dimer 16 which yields a stable chain (see Ribbons subsection below).

Finishing with the energetics and geometry analysis of the dimers, several general conclusions can be made, most of them are chemically intuitive. Firstly, non-planar structures are clearly more stable than the planar ones. Secondly, the greater the number of H-bonds the more stable the structure is. Thirdly, linear H-bonds when the three atoms involved in it (C, N, H) are arranged along a line are generally stronger than when they are not, i.e. when the H-bond is non-linear. Finally, a rather small destabilization comes from steric repulsion between H atoms not involved in the H-bonds but which are close to them. In addition, there is also a small preference for the T isomers to form a dimer as compared to C isomers.

It is now interesting to get insight into the H-bonding mechanism by looking at the electron density differences. A selection of illustrative dimers is shown in Fig. 27. The so-called "kebab-like" structure shows up^{100,65,94} between the hydrogens of the phenyl rings and the nitrogen of the carbonitrile group clearly indicating the fingerprint of the H-bond. Looking at dimers 5, 6, 8, 11, 12, 14, 19 and 20 one can notice a small excess of charge electron density (purple point) over the hydrogen adjacent to the two hydrogens involved in the H-bond. This is due to the H bond being formed not with one but with two H atoms which has a destabilizing effect on its energetics (note that stability of dimers starting from number 5 reduced abruptly by about 15.0 kJ/mol as compared to the dimers of the first group as is seen in Fig. 26). Equivalently, the character of the interaction between two monomers can be revealed by looking at

the NCI plots as demonstrated in Fig. 28(B). Besides the steric repulsion seen inside the benzene rings (red regions), a common pattern²⁵ associated with the H bonding (a combination of blue and green regions here) can be seen at precisely the same positions as shown by the density difference plot, Fig. 28(A). The green-blue colours indicate an intermediate strength of the H-bonding, which one would expect for the case of the (C-H)₂...N-C atomic arrangement. Since the two methods give equivalent results on the interaction between molecules, in all cases considered below only the density difference method will be used for simplicity. Note that both methods clearly show a local character for the bonding and hence, in agreement with the definition given in Introduction, can be characterised as H bonding interactions.

We find that dispersion interaction contributes significantly into the H-bonding interaction between molecules, amounting between 30 % and 50 % of the binding energy for strongly bound dimers (from 1 to 4). In the cases of weakly bound dimers the contribution of the dispersion interaction was found even higher, being the dominant contribution in many cases. We also looked at the dipole-dipole interaction between different dimers, but found this part of the electrostatic energy amounting only up to 10 % of the total binding energy for some C-C dimers. Although a more careful analysis is needed for understanding in detail the binding mechanism in all cases considered here using e.g. the methods discussed in Refs. 5,62, this kind of analysis, however, goes beyond the scope of this study, which main goal is to rationalize molecular assemblies observed by STM.

5.2.3 Ribbons

The next natural step in forming the structures that the monomers can build is by proposing simple linear-like conformations which we shall call ribbons. This type of polymers appears frequently in the experimental STM images of the low coverage phase of pTmDC molecules on the Ag(111) surface.⁸³ Using dimers as the basic building blocks, we have explored the energetics and optimal geometries of a number of these type of linear structures. In the optimization procedure, the coordinates of all the atoms in the unit cell containing a dimer were allowed to relax, while the cell parameters were maintained fixed in our model. Predominantly five arrangements emerged as the most favorable candidates for these ribbons, all shown in Fig. 29.

All these ribbons are formed by repetitions of dimers presenting two hydrogen bonds. For simplicity, only ribbons with two molecules in the one-dimensional unit cell were considered. The stability of the ribbons is expected to be greater per molecule compared to the corresponding dimer used to build it, as the number of H-bonds per molecule is greater in the ribbon. The ribbon TT_B is constructed by repetition of the dimer TT-P_{2b}, the ribbon TT_A is constructed from the dimer TT-P_{2a}, the ribbon TT_{Lin} from a dimer very similar to CT-Lin₂ in which both monomers are trans, the ribbon CC_A is constructed by repetition of the dimer CC-P_{2a}, and finally the ribbon CC_{Lin} is formed by repeating the dimer CC-Lin₂. Interestingly, unstable planar

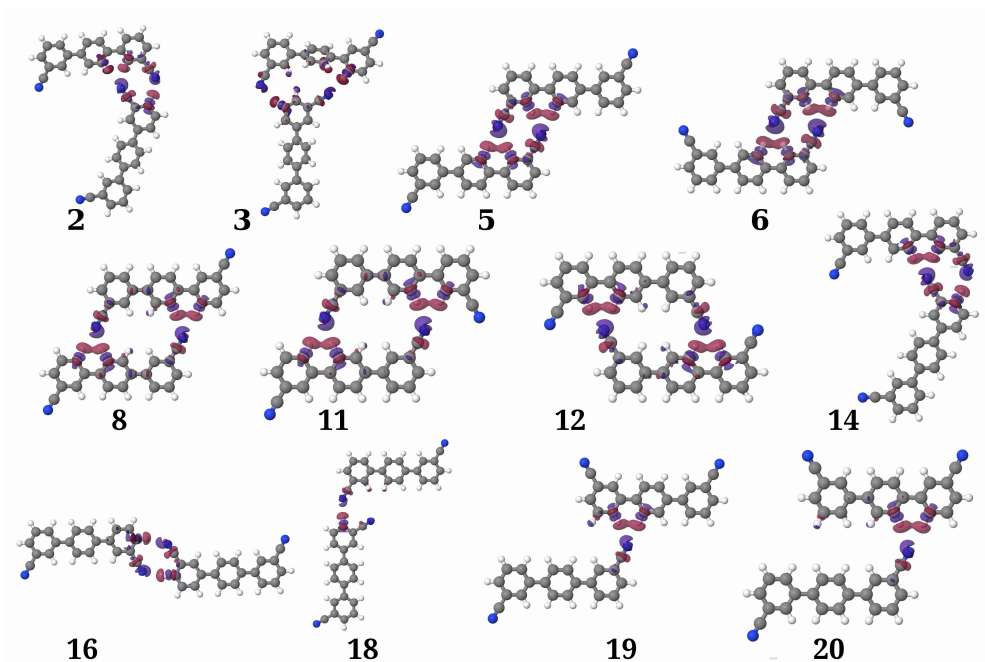


Figure 27: Electronic density difference maps of the most representative dimers with the hydrogen bonds distances being between 2.37 and 2.61 Å. The purple isosurface indicates an excess and the maroon a depletion of the electron density in the dimers compared to two isolated monomers. Isosurfaces are drawn at $\pm 0,0007$ electron/Å³.

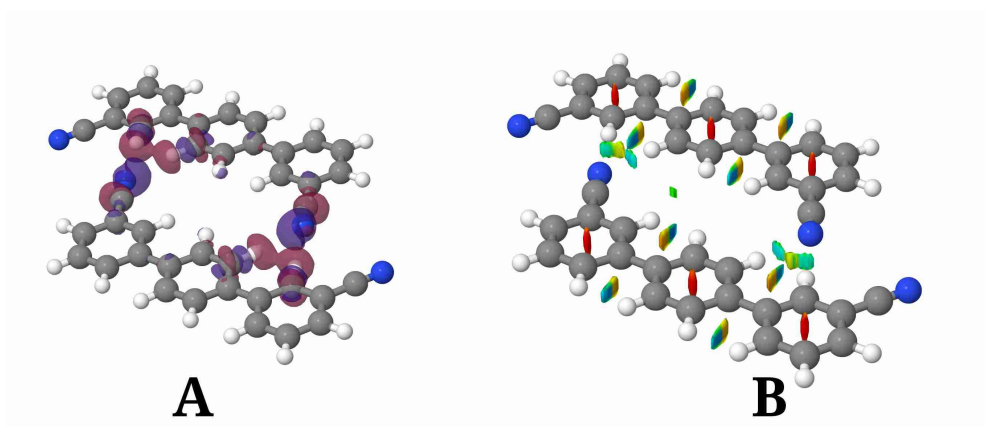


Figure 28: Comparison of the charge density difference (A) and NCI (B) plots for the dimer CC-P_{2b}. In (A) the same colours and the density value were used as in Fig. 27, while the value of $s = 0,5$ was used in (B) for the NCI plot (see Section Methods for the explanation of the colour scheme used),

linear-like dimers are able to form stable infinite linear chains. Moreover, those chains displaying linear H-bonds are clearly more stable than those with non linear H-bonds. This happens both for planar and non-planar conformations, although the non-planar conformation in each case is always more favorable than the planar one. This is demonstrated in Fig. 29, where the binding energies (per two molecules) are written in yellow and green for non-planar and planar conformations, respectively.

The linearity of these polymers is apparent, hence a longitudinal axis (LA) can be defined for each structure going symmetrically along the ribbon. Different widths of the ribbons can be observed, TT_B and TT_{Lin} being the widest and the thinnest conformations, respectively. Another visual parameter useful for the analysis of the STM images⁸³ is the directionality of the ribbon. Taking the backbone of the monomer as a reference direction, the angle of the LA of the ribbons varies from 0° (CC_A and CC_{Lin}) to 30° (TT_{Lin}), 45° (TT_A), and 60° (TT_B). Thus, different directionalities are expected for these linear chains. This is an interesting result in a broad agreement with the images observed in the experiments. The ribbon TT_A , being one of the two most stable structures, has been observed experimentally in the STM images.⁸³ The repeating unit of the third ribbon in stability, CC_A , has also been observed in STM images. Clearly, other structures have not been seen, which is likely due to adverse effects of the surface which are missing in this preliminary study.

Each ribbon conformation also presents different border shapes. The consideration of this feature may be useful if we analyze possibilities of the ribbons to form two-dimensional monolayers when the ribbons lie side-by-side. The TT_B border is almost straight, but TT_A and TT_{Lin} both present kinks. Chains of the cis isomers are of the zig-zag shape. A dense packing of the ribbons strengthened by (rather weak) dispersion interactions between them is possible in all cases. Experimentally, 2D monolayers made of TT_A ribbons has indeed been observed, though other possibilities (CC_A or TT_B) could fill the surface space as well.⁸³

5.2.4 Linkers

Looking at the STM images of Ref. 83, we are able to identify some pTmDC clusters that are associated with the changes in the directionality of the ribbons. These clusters can be understood as conformations of (mainly) three monomers of different chirality but with the same functional role, namely, that of connecting ribbons together. For this reason we shall name these structures linkers. In Fig. 30 we show molecular models for some of this type of observed arrangements of the pTmDC molecules on the silver surface.

Inspired by the STM images of the linkers, we developed a number of atomistic models for clusters of molecules which may serve as linkers connecting ribbons. Optimized configurations have been obtained for the isolated clusters following similar computational procedures as in the previous cases described above. The clusters we considered are shown in Fig. 31 inside a box-like frame. The experimentally seen lin-

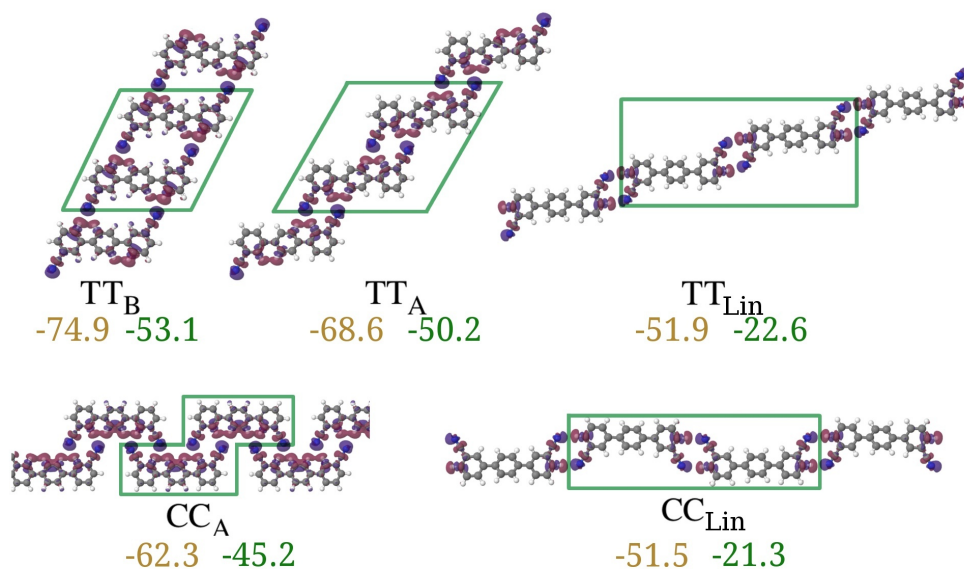


Figure 29: DFT relaxed considered ribbon conformations. The building-block motif is boxed in green. C or T letters denote cis or trans monomers. Notice that subscript A and B refer to chains formed by parallel dimers of kind P_{2a} and P_{2b} , respectively, and Lin for the linear one (see Fig. 26). Yellow and green numbers correspond to the binding energies (in kJ/mol) of the non-planar and planar geometries, respectively. Charge density differences are shown for each structure with the color scheme as in Fig. 27.

ker A in Fig. 30 has been modeled as a cluster CCT'-Lin, linker E was modeled as TCT'-Lin, while the triangular linker B as TTT-Tri. The cluster TCT-B serves as a model for the linker D or C in Fig. 30. Additional clusters CCC-Lin and CCC-Tri which apparently are absent on published STM images (but may as well exist on the surface) were also modeled. We also schematically show in this figure how ribbons may attach to our linkers. Note that the ribbons are shown only for illustration of the way the linkers work, they were not included in our actual calculations. In all cases we assumed that the linkers connect the ribbon TT_A from Fig. 29 as only this particular chain was clearly observed in the STM images in Ref. 83.

It is worthy of a remark that dimers also appear here as elementary building blocks; this can be easily identified in each of the different clusters gathered in Fig. 31. In particular, linkers CCC-Lin, TCT'-Lin, and CCT-Lin display binding mechanisms associated with $CC-P_{2a}$ and $CT-P_{2a}$ dimers. In the CCC-Tri linker, we can see three times the type of binding found in the dimer $CC-Tri_2$. In the TCT-B two different binding mechanisms are seen: $CT-P_{2a}$ and in the opposite end the $CT-Tri_2$. With respect to the linker TTT-Tri, we have not computed exactly the dimer involved in it because it will obviously be unstable, but the $TT-L_1$ dimer (which is unstable in its planar

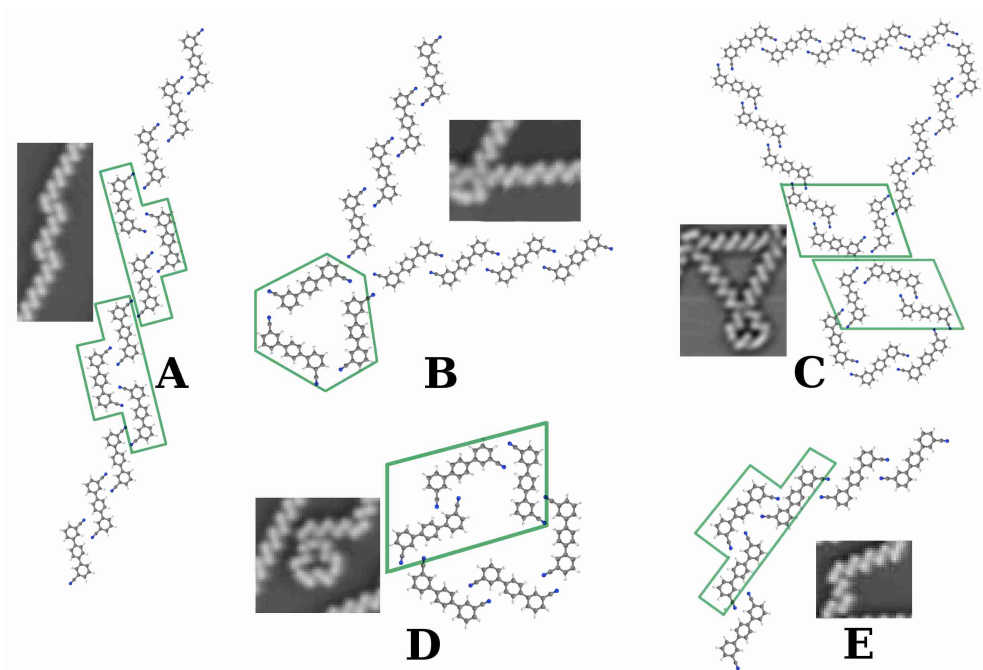


Figure 30: Some structures observed experimentally in STM images (adapted with permission from Ref. 83) and its proposed atomistic models constructed from the dimers building-blocks. Different linkers involved in the structure are placed in a green box-like frame.

form) does resemble the elementary building block used up in this arrangement. We see that in some cases, unstable dimers may form a linker structure which is overall stable.

The motifs shown in Fig. 31 also clearly illustrate how each of the linkers affects the directionality of the ribbons connected to it. It is clear that different arrangements are possible for the ribbons coming and leaving one particular linker cluster. The CCC-Lin can create an angle of 90° between two ribbons, one formed by L-trans monomers and the other by D-trans. The same effect happens with the linker TCT'-Lin, but in this case the trans isomers are directly involved in the cluster. In the case of CCT-Lin, the directionality of the ribbon (formed by only one trans isomer) is maintained, and the linker just creates a kink along the ribbon. Most of the times the cis monomer is the central part of these three linkers, primarily responsible for connecting the ribbons. These three linkers bifurcate the ribbon flow, whereas the other two possibilities, CCC-Tri and TTT-Tri, collected in Fig. 31, produce a trifurcation. The latter two linkers have a triangular shape, one formed by all cis monomers and another by all trans (L or D), respectively. For simplicity, we only show TTT-Tri in Fig. 31 formed by the D-trans, but another one based on the L-trans isomers is equivalent to this one.

Regarding the stability of these clusters, binding energies corresponding to both non-planar (yellow) and planar (green) geometries are shown in Fig. 31. All, except the planar TTT-Tri configuration, are very stable structures. The number of H-bonds in these linkers is an important parameter that roughly correlates with the binding energy, i.e. the binding energies of the linkers are approximately additive with respect to the binding energies of the dimers (where applicable). Thus, and using only non-planar values, CCC-Tri presents up to six H-bonds in the linker alone (-21.4 kcal/mol); TCT'-Lin (-69.9 kJ/mol), CCT-Lin (-67.3 kJ/mol), CCC-Lin (-63.6 kJ/mol) and TCT-B (-63.2 kJ/mol) show four H-bonds, while TTT-Tri (-20.5 kJ/mol) only with three H-bonds (none of them is linear). This is the only one with an unstable planar configuration.

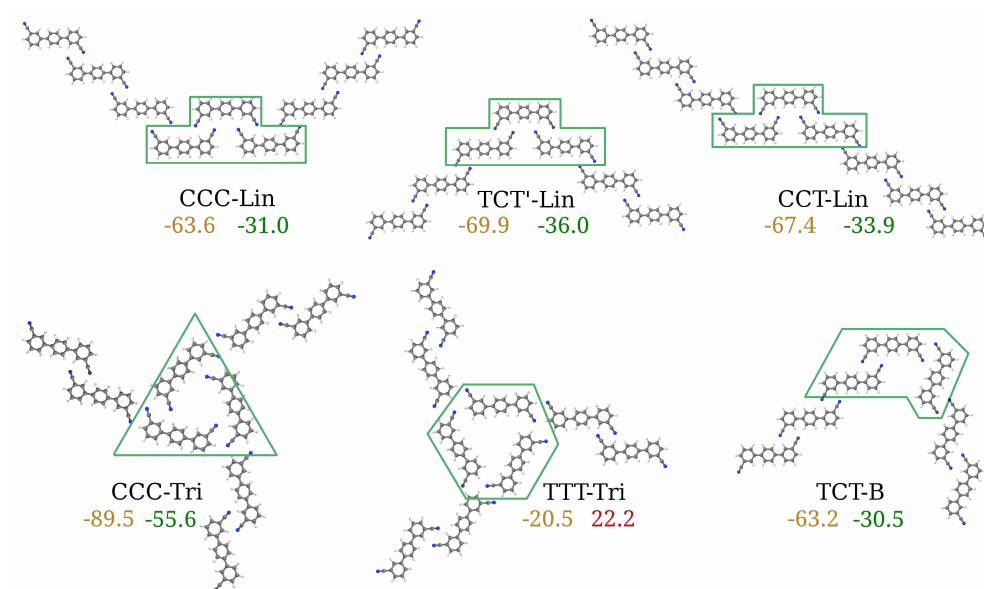


Figure 31: DFT relaxed geometries and binding energies (in kJ/mol) of several linkers investigated in this study. The actual systems computed were isolated clusters containing several molecules; they are indicated by a box-like green frame. In each case also a schematic is given of how ribbons may actually connect to the linkers; the molecules in the ribbons were not included in the calculations. Legend: the first three characters, either C or T, show which monomers are involved in the linker. Prime is used to note that trans isomers in the linker are stereoisomers. The index Lin is used when all monomers are parallel, while Tri is used if they form a triangle; finally, B designates the linker type when the features of both conformations (Lin and Tri) are present. Yellow numbers correspond to the binding energies of non-planar, while green for the relaxed planar conformations; red color is used for the unstable planar triangular structure.

As can be seen, all non-planar linkers are stable, especially CCC-Tri, TCT'-Lin, CCT'-Lin and CCC-Lin, and hence may be almost equally likely present on the sur-

face. However, note that their stability can be compromised by the molecule-surface interaction which is currently not considered.

6 | SELF-ASSEMBLY OF PTMDC ON SILVER SURFACE (111)

USING a toolkit of theoretical techniques comprising *ab initio* density functional theory calculations, the nudged elastic band method and kinetic Monte Carlo (KMC) modeling, we investigate in great detail how para-Terphenyl-meta-Dicarbonitrile (pTmDC) molecules diffuse and isomerize to self-assemble on the Ag (111) surface. We show that molecules “walk” on the surface via a pivoting mechanism moving each of its two “legs” one at a time. We then identify a peculiar “under-side” isomerization mechanism capable of changing the molecules chirality, and demonstrate that it is fundamental in understanding the growth of hydrogen bonding assemblies of ribbons, linkers, clusters and brickwall islands on the Ag (111) surface, as observed in recent scanning tunneling microscopy experiments (*ChemPhysChem* **11**, 1446 (2010)). The discovered underlying atomistic mechanism of self-assembly may be behind the growth of other hydrogen bonding structures of chiral molecules on metal surfaces.

6.1 METHODS

DFT calculations^{57,69} were carried out using the open source computer code CP2K.¹²³ It implements periodic boundary conditions and the hybrid Gaussian and plane wave method (GPW).⁷⁶ Goedecker-Teter-Hutter (GTH)⁴⁸ pseudopotentials were used. Perdew-Burke-Ernzerhof (PBE) generalized gradient exchange-correlation functional¹⁰⁶ was used with the dispersion correction to energy and forces due to Grimme’s DFT-D3 method.⁵¹ The optimized basis set m-DZVP¹²² was used for all atoms and a plane wave cutoff energy of 280 Ry. Geometries were relaxed until forces on atoms were less than 0.02 eV/Å. In all calculations (except those on adsorbed ribbons and islands) the corresponding simulation cells were chosen big enough to ensure that there are sufficient distances between images of adsorbed molecules and clusters to make the interaction between them negligible.

Binding energy of a complex $S + M_N$ obtained by placing N molecules on the surface is defined in the usual way as

$$E_{\text{bind}} = E_{S+M_N} - E_S^0 - \sum_{M=1}^N E_M^0,$$

where E_{S+M_N} is the DFT total energy of the complex $S + M_N$, E_S^0 is the energy of the relaxed surface, and E_M^0 are the energies of the individually relaxed molecules (C and/or T), respectively. Because a localized basis set is employed, the basis set superposition error (BSSE) is added to the binding energies, which is calculated by means of the (positive) counterpoise (CP) correction²⁰ method. When considering contributions to the binding energy between molecules in a cluster which is adsorbed on the surface, we also calculated the *cluster binding energy* (per molecule) using

$$E_{\text{Hb}} = \frac{1}{N} \left[E_{S+M_N} - \sum_{M=1}^N (\Delta E_M + E_M^0) - E_S^0 \right],$$

where $\Delta E_M = E_{S+M} - E_S^0 - E_M^0$ is the binding energy to the surface of an individual monomer M calculated at the geometry of the whole complex $S + M_N$. Finally, we also define a (positive) *deformation energy* $\Delta E_{\text{def}}^A = E_A - E_A^0$ for any component (surface and/or molecule) of the whole system, where E_A is the energy of the component A in the complex. This energy shows the cost for the component A to be in the complex.

All energy barriers were calculated by means of the Nudged Elastic Band (NEB) method.^{61,88} Both Improved Tangent NEB and the Climbing Image NEB calculations^{54,55} were employed, with the number of images varying between 7 and 9.

To illustrate the strength of H bonding interaction in a complex $S + M_N$ of N molecules on the surface, we used two methods. In the first one, we analyzed electronic density difference^{100,65,94} (EDD) defined as $\Delta\rho(\mathbf{r}) = \rho(\mathbf{r}) - \sum_A \rho_A(\mathbf{r})$, where ρ is the total density of the complex, while ρ_A is the density of the component A (either S or M) in the geometry of the complex. In the second method, we analyzed the topology of the electron density using the so-called (dimensionless) reduced density gradient^{59,25,26}

$$s(\mathbf{r}) = \frac{1}{2(3\pi^2)^{1/3}} \frac{|\nabla\rho(\mathbf{r})|}{\rho(\mathbf{r})^{4/3}}$$

This is specially designed to identify regions where non-covalent interactions (NCI) are dominant. In visualizing $s(\mathbf{r})$, the isosurfaces are colored on a blue-green-red color scale. With this color scheme, red indicates strong non-bonding (steric) repulsion, green indicates weak interaction, while blue detects strong attractive interaction as the H bonds.

6.2 RESULTS

6.2.1 Monomers on the silver surface

Knowledge of the energetics of monomers on the surface is mandatory for clear understanding of the self-assembly process. As possibilities of geometrical positions

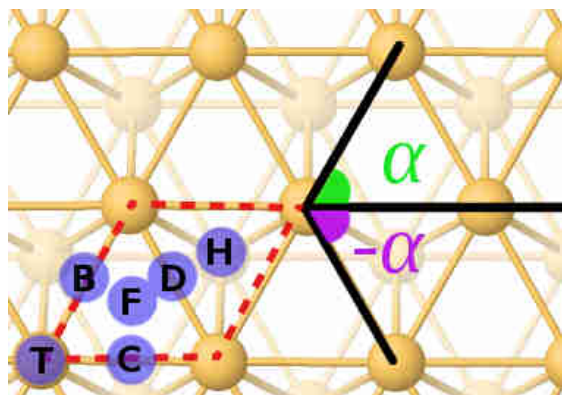


Figure 32: Docking sites on the Ag (111) surface. T label is used for top sites, B, C and D are used for the different bridge sites, and F and H are used for the fcc and hcp hollow sites respectively. Red dotted line indicates the primitive surface unit cell. The angle the backbone of the molecule makes with respect to one of the Ag-Ag surface symmetry directions (chosen as the horizontal axis in the picture) are considered positive if measured in the counterclockwise (green α) and negative if measured in the clockwise directions (purple $-\alpha$), respectively. Orange balls represent silver atoms.

of the monomers on the surface are enormous, we carried out a systematic exploration of the potential energy landscape to reveal all possible adsorption sites. We started by selecting six sites on the surface (see Fig. 32), where one N atom of the molecule was placed, and then, using the chosen N atom as a pivoting point, considered various orientations by rotating the molecular backbone prior to full geometry optimization. Altogether, 173 and 183 orientations of cis and trans isomers, respectively, were relaxed with our DFT method.

The most stable configurations found and their corresponding binding energies are presented in Figs. 33 and 34 for the cis and trans isomers, respectively. It is seen from these results that both isomers are strongly bound to the silver surface with binding energies as large as 200 kJ/mol, and hence both isomers are equally favorable. Careful inspection of the obtained geometries revealed that favorable geometries have at least two common features: (i) N atoms of the molecule prefer to be located near the top of Ag atoms, showing a weakly dative covalent bonding that we call a NAS (Nitrogen Atom Surface) interaction, and (ii) phenyl rings tend to avoid Ag atoms below their centers. We also find that there is some tendency for the carbonitrile groups to bend towards the surface, so that the molecule adopts a dome-like shape seen in Fig. 35. Thus, the mean distances to the surface of the carbon skeleton of the monomers is around 3.25 Å whereas that of the N atoms is only around 2.65 Å. The large number of adsorption geometries found with similar binding energies and the small variation in the molecule geometry with respect to the surface suggest that the corresponding potential energy surface (PES) is weakly corrugated.

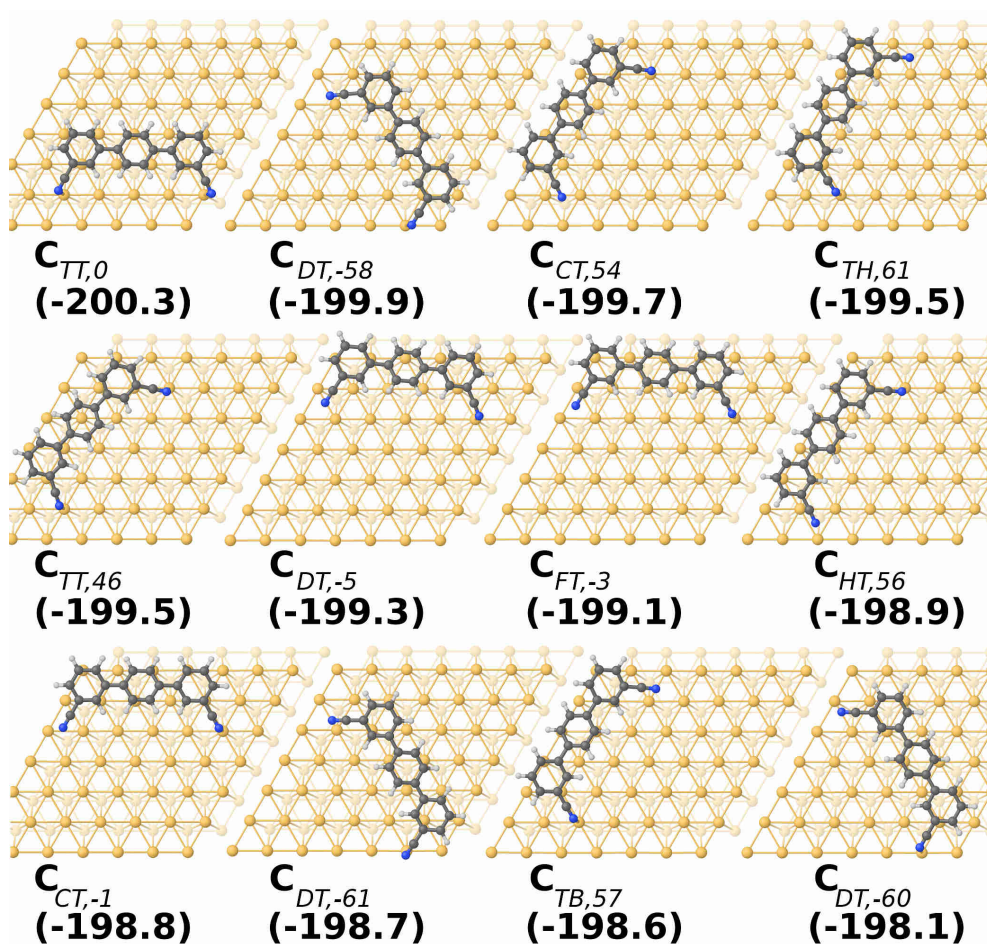


Figure 33: Twelve most stable cis conformers (C) on the surface found after the DFT geometry relaxation. The suggested nomenclature is meant to indicate the adsorption site and orientation of the molecule. The first subscript indicates the docking site of the left N atom, the second subscript indicates the docking site of the right N atom, and the number after the comma indicates the alpha angle (see Fig. 32). The corresponding binding energies (in kilojoules per mole) are also given underneath the symbol of the structure in round brackets. Orange, gray, white and blue balls correspond to Ag, C, H and N atoms, respectively.

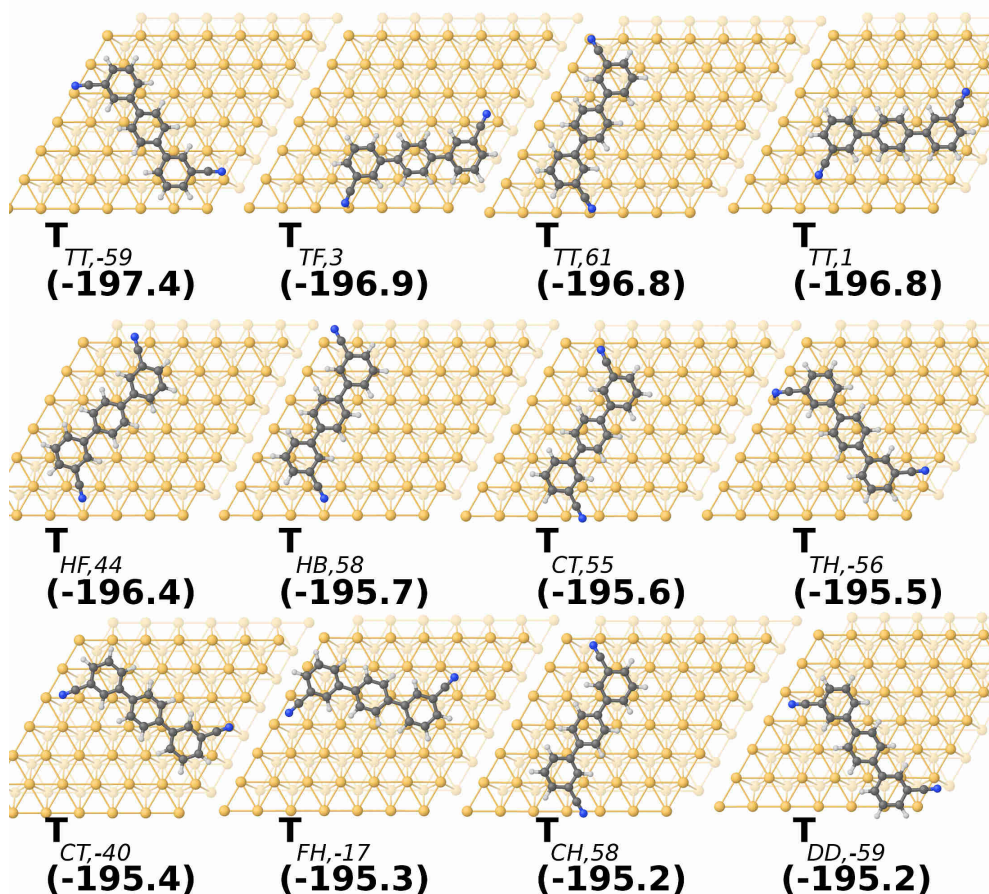


Figure 34: Twelve most stable trans conformers (T) on the surface found after the DFT geometry relaxation. The subscript of the nomenclature for each structure and the color code used are the same as in Fig. 33. When both N atoms align along a vertical line, then the first subscript refers to the bottom atom. The corresponding binding energies (in kilojoules per mole) are also given. Only L isomers are shown for clarity; the corresponding D isomers with identical binding energies are obtained by appropriate flipping of the molecules (not shown).

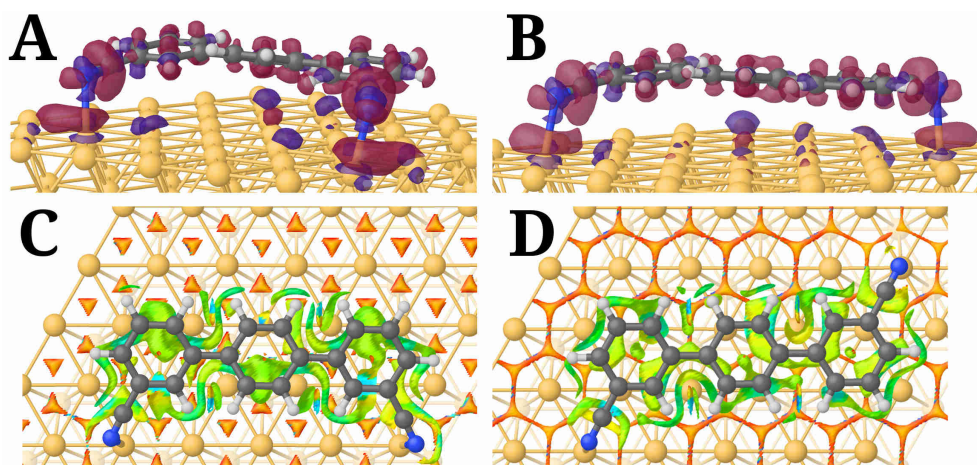


Figure 35: Comparison of the charge density difference (A,B) and NCI (C,D) plots for the cis $C_{TT,0}$ (A,C) and trans $T_{TT,1}$ (B,D) monomers adsorbed on the Ag(111) surface. In (A,B) the purple isosurface indicates an excess and the maroon depletion of the electron density, with the isosurfaces drawn at $\pm 0,0007$ electron/ \AA^3 . The value of $s = 0,5$ was used in (C,D) for the NCI plots, see Methods for the explanation of the color scheme used.

Dispersion is the essential attractive contribution to the binding energy in all of the most stable monomers showed in Fig. 33 and Fig. 34, so that dispersion is responsible to maintain the molecule bound to the surface. To investigate the nature of these interactions, we analyzed in detail the electron density for a number of adsorbed monomers using both the electron density difference^{100,65,94} (EDD) and the Non-Covalent Interaction (NCI)^{59,25,26} methods, which give complementary results. As an example, a comparison of the plots using the two methods is shown in Fig. 35 for one representative C and one T monomer. It is clearly seen that there is a considerable binding (as the charge density excess reveals) between N atoms and the surface Ag atoms (Fig. 35 A and B). This justify the preference of the molecule for certain docking sites where N atoms are on top of Ag atoms. The big green area, which represents the dispersion interactions between the molecule and the surface, depicted by the NCI analysis (Fig. 35 C and D), reveals the key role that dispersion plays in the binding mechanism, which is in agreement with the low corrugation of the PES and the large number of adsorption geometries found.

Further analysis based on integrating the charge density in planes parallel to the surface revealed that there is no charge transfer between the molecule and surface. This conclusion is also confirmed by the calculated projected density of states (PDOS) which is compared for a cis molecule $C_{TT,0}$ on the surface (see Fig. 33) with the PDOS calculated for the isolated molecule in Fig. 36. No energy levels of the $C_{TT,0}$ isomer stand around the Fermi level of the metal surface. Indeed, the HOMO and LUMO levels of the molecule are clearly positioned on the left and right of the Fermi energy

for the molecule on the surface, with small variations with respect to the isolated molecule.

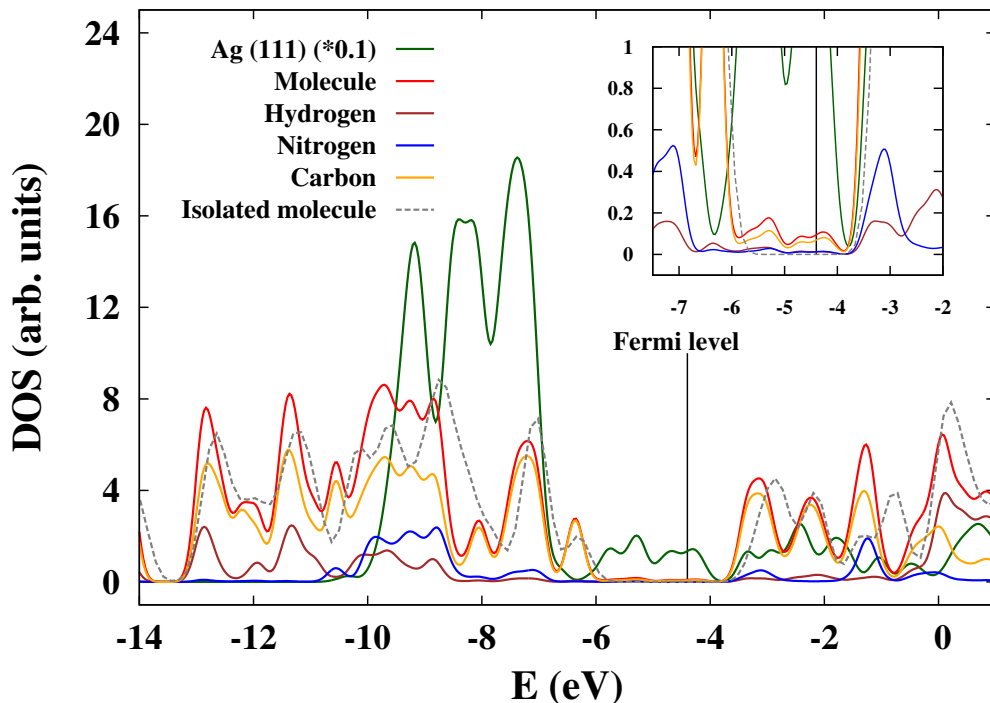


Figure 36: Comparison of PDOS for the cis structure $C_{TT,0}$ (solid lines) and the molecule in the gas phase (dashed line). The inset shows the region around the metal Fermi energy in more detail. Notice the negligible contribution of the monomer to the DOS in this region

It was suggested in the experimental study⁸³ that cis-to-trans isomerization plays an essential role in the self-assembly process of the pTmDC molecules on the Ag(111) surface. Therefore, using the NEB method we have considered the isomerization reaction for one monomer geometry adsorbed on the surface. The cis-to-trans isomerization transition can be modeled by rotating around the C-C bond connecting a benzonitrile group with the central phenyl ring. This can be done in two ways: in one the benzonitrile group rotates with its N atom going round away from the surface (the *upper-side* trajectory), while in the other the group proceeds near the surface (the *under-side* trajectory). Both paths were considered using a particular pair of isomers. The initial ($T_{TF,19}$) and final ($C_{TT,23}$) geometries and the transition states in both cases along with the computed minimum energy paths (MEP) are shown in Fig. 37. It is seen that the barrier for the C→T transition of around 38.6 kJ/mol for the under-side mechanism is by about 19.3 kJ/mol lower than for the upper-side mechanism which is easily explained by the fact that in the latter case one of the N-Ag interactions needs to be broken completely, while in the former case some bonding with the surface still re-

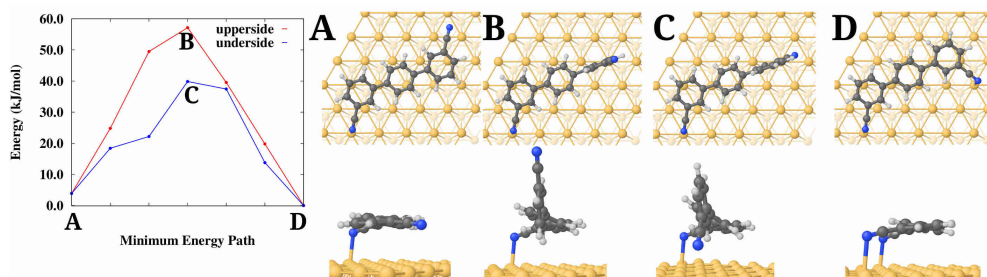


Figure 37: Cis-trans isomerization transition paths connecting the initial T (A) and final C (D) configurations via two possible mechanisms: (i) the upper-side with the transition state (B), and (ii) the under-side with the transitions state (C).

mains along the path. We also note that the barriers for the direct ($T \rightarrow C$) and reverse ($C \rightarrow T$) transitions differ by no more than 3.9 kJ/mol rendering both isomers on the surface almost equally possible, with the C isomer being marginally more favorable. Therefore, we expect C and T monomers being in almost equal amounts on the surface after first steps of deposition.

Diffusion of molecules on the surface is the next necessary prerequisite for understanding their ability to assemble into structures. Using some of the nearest stable geometries as initial and final states, and applying the NEB method to calculate the transition path between them, we have investigated several diffusion paths for both C and T monomers on the surface. Two basic mechanisms were considered: (i) *sliding transition* in which the molecule loses both its N interactions to the Ag anchoring sites on the surface to move to a new stable geometry, and (ii) a two steps *pivoting transition* whereby within each step one benzonitrile group remains bonded to the surface serving as a pivot for the other group, which rotates to a new stable position. In the latter mechanism one benzonitrile group serves as a pivot during the first, while another group during the second step. Because of the very large number of adsorption geometries of monomers on the surface, calculating transitions between all possible configurations is not feasible to consider in practice. Therefore, we selected only a number of reasonable possibilities between most stable structures. Examples of both types of transitions for C and T monomers together with the corresponding MEPs are shown in Figs. 38 and 39, respectively. As expected, the sliding transition requires about 2.1-3.5 kJ/mol higher barriers to overcome for both isomers than in the pivoting mechanism. This is because during sliding two molecule-surface interactions involving two N atoms have to be simultaneously broken, whereas in the pivoting transition two steps needed for the same displacement of the molecule require each only one of these interactions to be broken at a time. Hence rather small diffusion barriers are found ranging between 1.9-3.9 kJ/mol for C and 4.8-5.8 kJ/mol for T, depending on the particular initial and final geometries.

Concluding this Section, we find that dispersion is the main interaction that binds the molecule to the surface. From the large number of calculated adsorption geome-

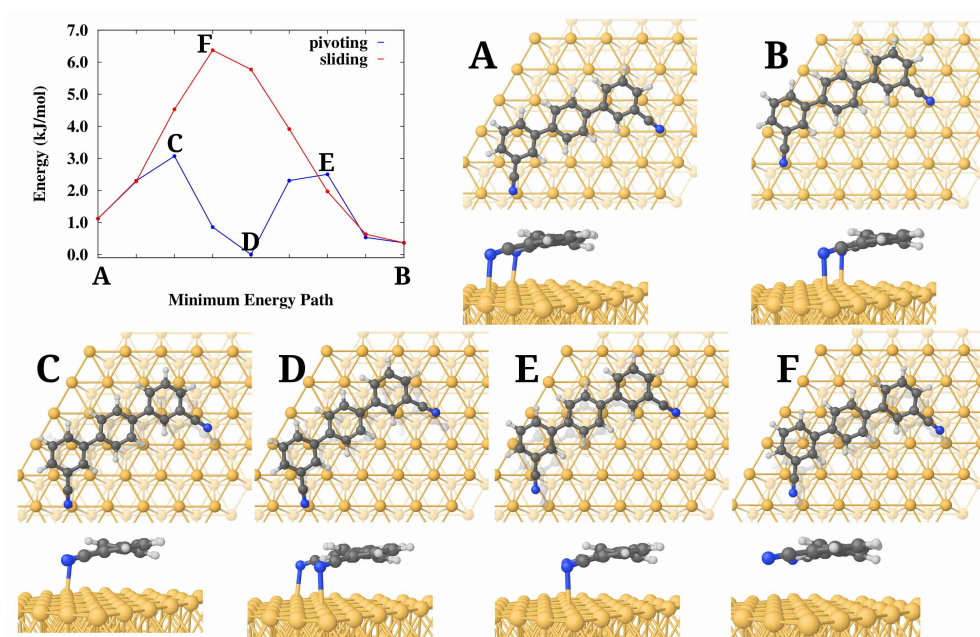


Figure 38: Diffusion paths for a C monomer on the Ag(111) surface. In the top-left panel the pivoting (blue) and sliding (red) MEP bands are shown labeled with the corresponding states shown in separate panels: initial and final (A and B), transition (C, F, E) and intermediate (D) states, as well as their geometries (top and perspective views). In the transition and intermediate states a ghost image of the molecule is superimposed showing its previous state.

tries and obtained small diffusion barriers we conclude that the PES of a pTmDC molecule on the Ag(111) surface is rather flat so that the molecule must be quite mobile at RT. The preferred sites are those where favorable NAS interactions between the Ag surface with the two N are formed. Thus, the molecule can be viewed as standing on two legs. Single molecules diffuse exploiting the pivoting mechanism and C and T isomers may undergo transformations into each other following an under-side trajectory with relatively high and equal rates.

6.2.2 Dimers on the silver surface

Next we shall consider pTmDC dimers on the silver surface. In total about 25 different dimers, including different orientations of the same dimers, were studied. A number of most stable dimer structures, fully relaxed with our DFT method, together with their total binding energies per molecule and H bond binding energies (in round and square brackets, respectively), are shown in Fig. 40. The total binding energies of the dimers range from 368.5 to 402.5 kJ/mol. The H bonding binding energies of dimers on the surface can be directly compared with those for the dimers in the gas

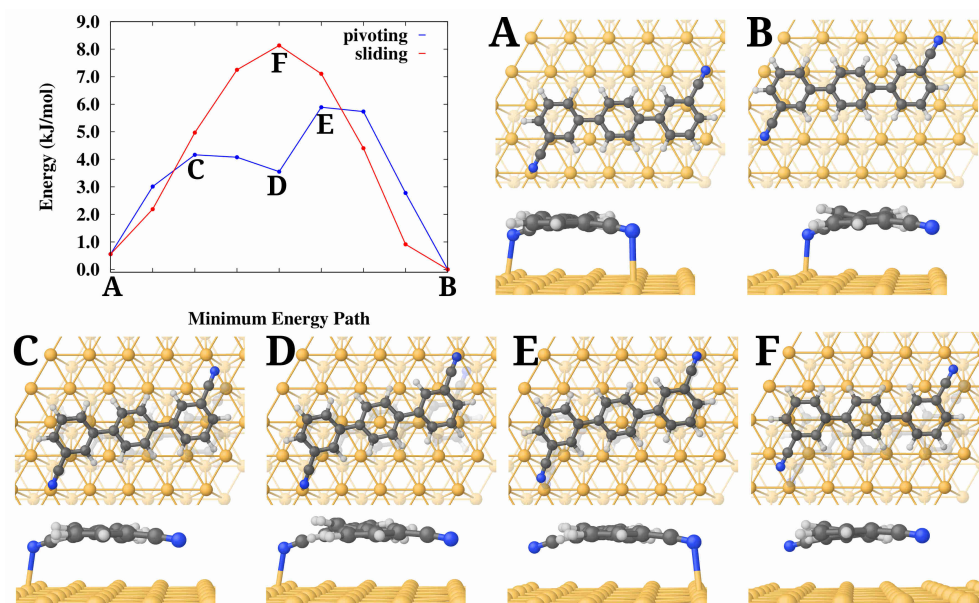


Figure 39: Diffusion paths for a T monomer on the Ag(111) surface. For the explanations, see the caption to Fig. 38

phase reported previously (see Ref. 1 and Chapter 5). The tendency in both phases is the same, but the H bond is up to 1.5 times stronger on the surface than in the gas phase. In fact, dimers with a single H bond and a planar geometry that are unstable in gas phase, become stable on surface with the central ring slightly rotated a dihedral angle around 12.5° .

Cis and trans monomers have a mean deformation energy of 6.4 and 12.9 kJ/mol, respectively, when they are bound to the surface, and this deformation energy increases to 13.0 and 14.0 kJ/mol when (monomers) are forming a dimer. On the other hand, the surface has a deformation energy of around 1.8 kJ/mol when a monomer is bound to it and increases to a mean value of 4.8 kJ/mol in the case of dimers. This suggests that it is easier for a trans conformer to form a dimer once it is deposited on the surface.

If we now compare the on-surface dimer total binding energies (around 385 kJ/mol) with binding energies of single monomers (around 192 kJ/mol), and binding energy in the gas phase dimers (around 29 kJ/mol), we see that these are not additive. This is because not all four N atoms of the dimers present NAS-type interactions; for instance, some of the N atoms are located above the Ag hollow sites and hence are less strongly bound to the surface. This is also reflected in the EDD plots (see Fig. 41).

Looking at the dimer geometries in more detail, we find that the effect of the surface manifests itself in mostly re-orienting the dimers on the surface in such a way as to best stabilize the structure; however, the relative orientation of the molecules in the dimers is very similar to that in the gas phase. We also find that only carbonitrile

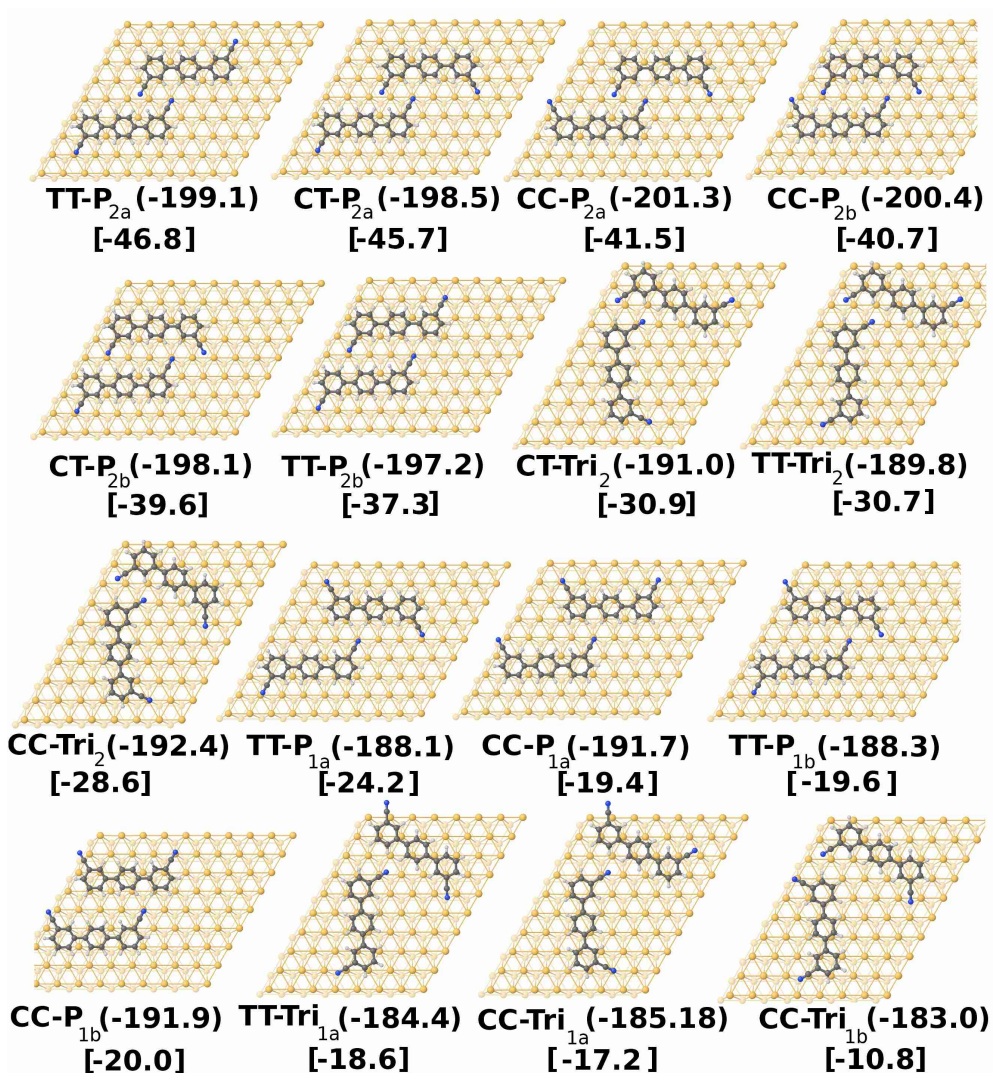


Figure 40: A selection of DFT relaxed dimers on the silver surface together with the corresponding total binding energies per molecule (in round brackets), and H bonding energies (in square brackets), all given in kJ/mol. The legend used to denote the dimers means: the first two characters are composed of either C or T corresponding to the cis or trans conformations of the constituent monomers; the next letters are either P or Tri referring to either parallel or triangular forms; the index 1 or 2 that follows corresponds to the number of hydrogen bonds in the dimer; finally, a subscript *a* or *b* is used to differentiate between similar structures.

groups at two ends of dimers remain bent towards the surface (showing NAS interactions similar to what CN-groups in the monomers do), while the CN-groups engaged in the H bonding are practically parallel to the surface, which is likely to be the main cause of the reduction of the binding energies from a mere sum of energies due to different interactions.

To analyze the nature of bonding between the molecules and of the molecules with the surface, we looked at electron density plots (see Fig. 41). It is seen that docking sites revealing NAS interactions are visible only for some of the N atoms, those which are located above the Ag atoms of the surface. This is consistent with the fact, mentioned above, that the relative interaction of each monomer in the dimers with the surface is somewhat weaker than that for isolated monomers. Looking at the EDD between two molecules in the dimer, Fig. 41 (B), we find it extremely similar to the one calculated for the same dimer in the gas phase¹ with the “kebab”-like structure characteristic for the H-bonding between the molecules clearly recognized. Note that the NCI method supports this result as well (Fig. 41 C to F). Detailed analysis confirms that binding between monomers in dimers on the surface can still be characterized in terms of the H-bonding with significant contribution coming from the dispersion interaction. It is seen by comparing panels E and F of the same Figure that the contribution of the dispersion interaction between molecules increases when the dimer is placed on the surface. Similar analysis has been conducted for other dimers as well, and in all cases qualitatively similar EDD were observed for the dimers in the gas phase and on the surface. This observation confirms that binding between monomers in dimers on the surface can still be characterized in terms of the H-bonding with significant contribution coming from the dispersion interaction, as discussed above and in our previous study¹. The H bond distances also follow the same tendency as in the gas phase; however, on the surface these distances become around 0.04 Å shorter for P geometries (with a distance around 2.44 Å for the bond where the carbonitrile groups and the H atoms lie along a line) and more than 0.10 Å shorter for Tri geometries, where the H bond is around 2.25 Å for the shortest non-linear H bond as in the CC-Tri₂ geometry. The mean distance of the molecule to the surface is 3.29 Å and 3.18 Å for the N atoms.

As the binding energies of dimers are in the region of 400 kJ/mol, we have not studied their diffusion as a whole, assuming that they are much less mobile than the monomers. However, from the point of view of investigating the growth of the molecular ribbons and linkers observed in,⁸³ it is essential to consider possible isomerization of molecules in dimers on the surface. The rationale for this is based on the following observation. Consider a dimer in which two molecules are connected with the double H-bonding, Fig. 42 (A). If one of the benzonitrile groups of a molecule facing the other molecule in a dimer rotates so that the corresponding monomer changes between cis and trans, the interaction between the monomers in the dimer would weaken and either of the molecules may easily diffuse out. Reversely, see Fig. 42 (B), a molecule may come closer to another, establish a single H bond, and then undergo an isomerization

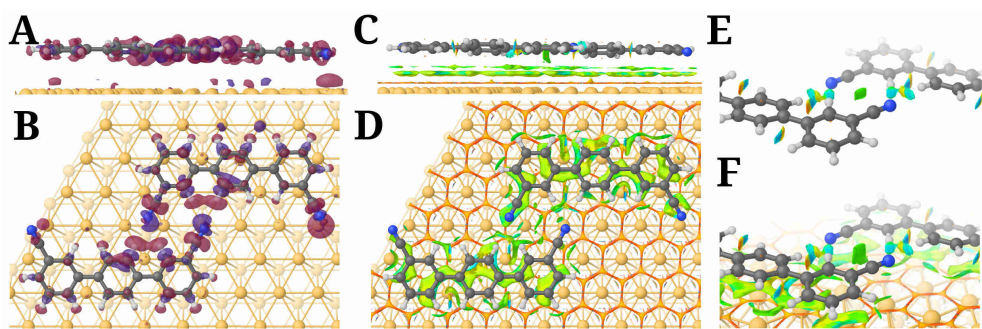


Figure 41: Electron density plots of the dimer $CC-P_{2\alpha}$ on the surface. EDD side (A) and top (B) views. NCI side (C) and top (D) views. NCI showing the H bonds and attractive dispersion interaction between the carbonitrile groups in a dimer without (E) and with (F) the surface. Note the bigger green area in (F) related with the dispersion interactions between carbonitrile groups. The same color scheme as in Fig. 35 is used.

reaction which would result in a double H bond between the two, providing the fundamental mechanism for dimer formation on the surface; this dimer may then serve as a nucleus for a further growth. The same type of reaction may also be responsible for the ribbons growth when a monomer comes to an already formed ribbon and then, upon the appropriate isomerization reaction, would attach to it.

For the isomerization reaction between C-T and C-C dimers we have studied both the under-side and upper-side mechanisms (Fig. 43). As expected, this calculation confirms that the upper-side mechanism requires larger energy barriers; hence for the isomerization reaction between T-T and T-C dimers only the under-side mechanism was studied shown in Fig. 44. In both cases the initial structures correspond to a $P_{2\alpha}$ like structure with the double H bond, while the final structure is the $P_{1\alpha}$ like with only a single bond. The essential result here is that the $P_{2\alpha}$ dimers are by at least 19.3 kJ/mol more favorable than the $P_{1\alpha}$ structures involving either neighboring T or C monomers. Therefore, the energy barrier of 61.7 kJ/mol required to break one H bond in the $P_{2\alpha}$ dimer and turning it into a $P_{1\alpha}$ dimer is by 19.3 kJ/mol larger than the barrier needed for the reverse reaction of turning a $P_{1\alpha}$ dimer into a more stable $P_{2\alpha}$ one. It follows from this consideration, that when two molecules come close to each other to form a favorable arrangement which may facilitate the formation of a proper dimer with a double H bond, then the appropriate isomerization reaction would favor such a formation yielding a lower system energy. Hence, if isomerization of monomers, as mentioned above, does not modify significantly the system energy, then the isomerization of molecules arranged next to each others, what we shall call an *assisted isomerization*, will result in a lower free energy of the system.

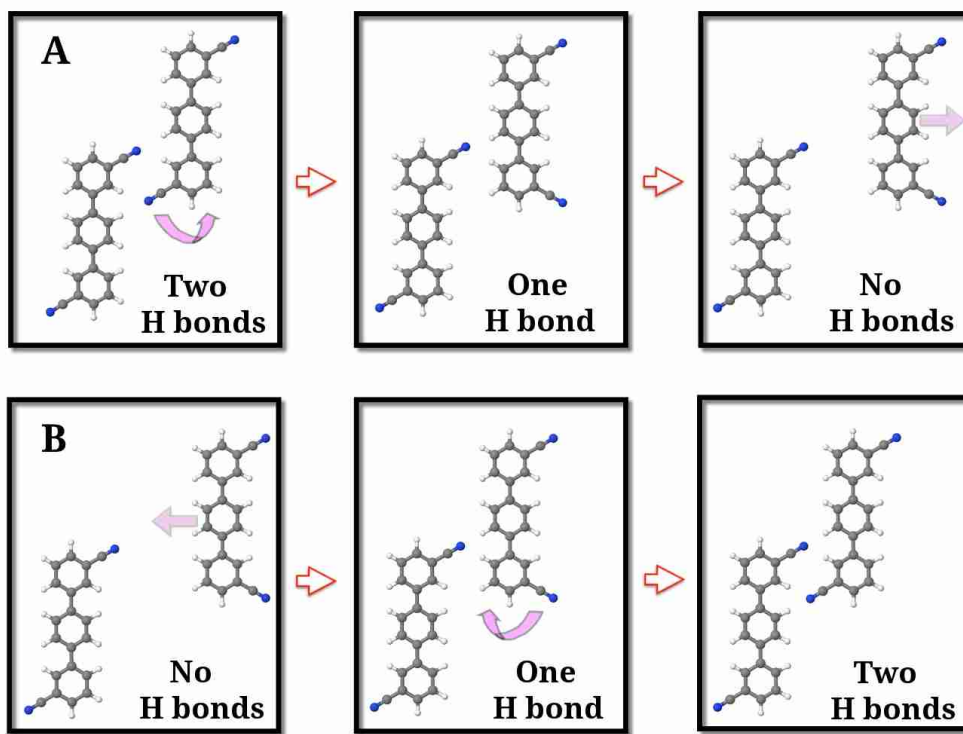


Figure 42: Schematics of the *assisted isomerization* reaction between two molecules on the surface: (A) the right molecule weakens its bonding and detaches from the left molecule increasing the system energy; (B) the right incoming molecule establishes a double H bond with the left molecule reducing the energy of the system.

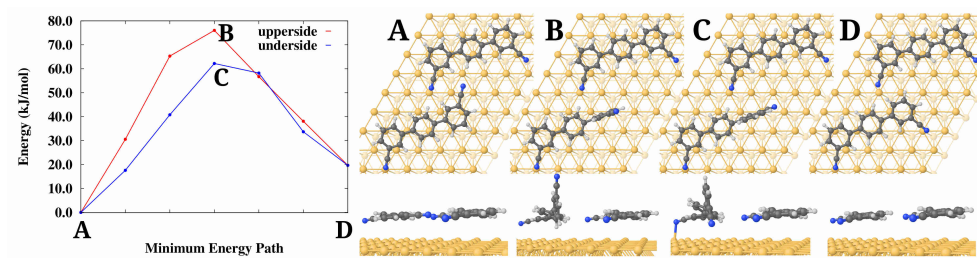


Figure 43: The MEP of cis-assisted isomerization and the NEB+DFT relaxed geometries of the initial (A), final (D), and transition states for the upper-side (B) and under-side (C) mechanisms.

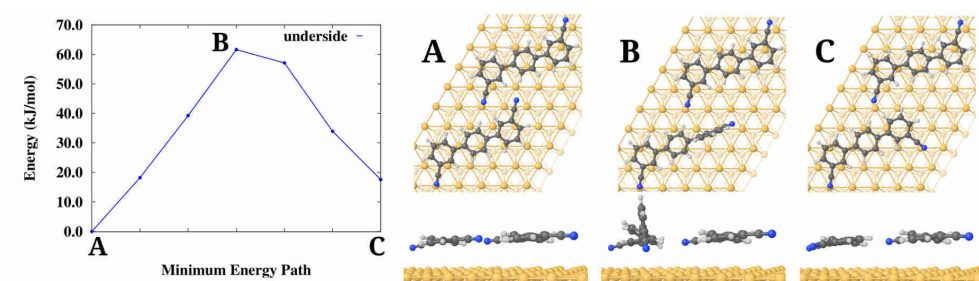


Figure 44: The MEP (left panel) and the initial (A), final (C) and transition state (B) geometries for the NEB+DFT relaxed isomerization transition between a T-T and a T-C dimers.

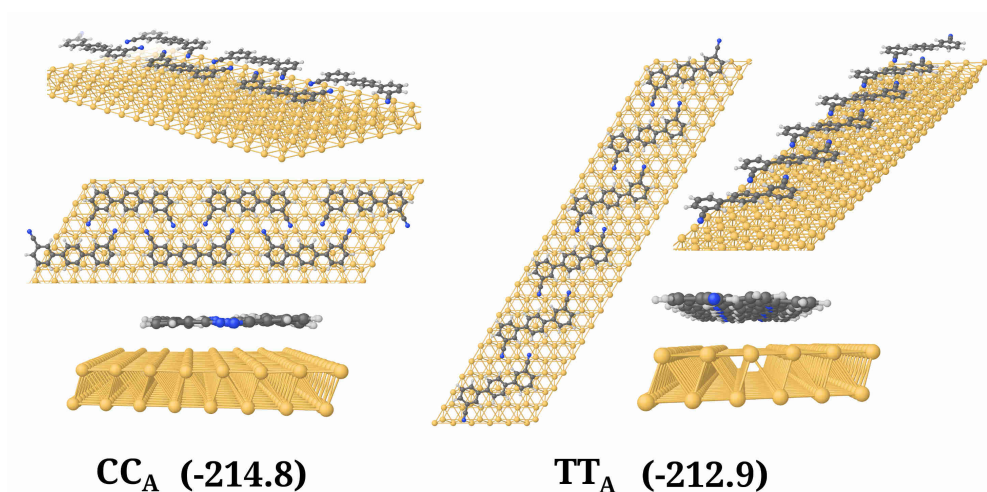


Figure 45: Relaxed geometries and corresponding binding energies (per molecule, in brackets and in kilojoules per mole) of the CC_A and TT_A ribbons on the silver surface.

6.2.3 Linkers and ribbons on the silver surface

Some of the ribbons and linkers considered previously in the gas phase¹ have also been relaxed on the surface using our DFT method to check their stability.

In the case of periodic ribbons, there is a question of their commensurability with the surface: larger surface cells may need to be taken to accommodate the sufficient number of primitive unit cells of the ribbon structure. In fact, different cells need to be considered to find the structure with the lowest Gibbs free energy. To avoid these rather tedious and expensive computations, we have chosen the smallest cell for the silver surface which accommodates the ribbons at the distances between molecules which are no more than 0.01 Å different from those found in the same ribbons in the gas phase.¹

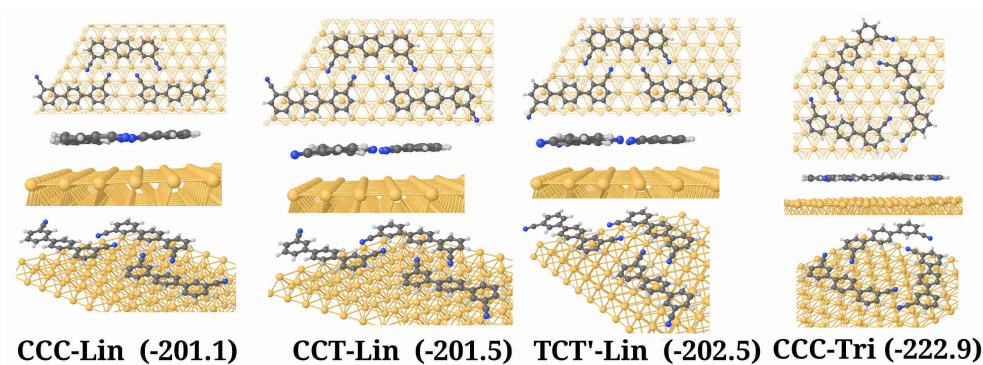


Figure 46: Relaxed geometries and corresponding binding energies (per molecule, in brackets, in kilojoules per mole) of several linker clusters on the silver surface.

The relaxed geometries of two types of ribbons, CC_A and TT_A , consisting of repeated C and T monomers respectively, are shown in Fig. 45. The molecules in the ribbons comprise a planar geometry with substantial binding energies (per molecule), also shown on the same Figure. The mean distance of the molecule to the surface is 3.3 Å and 3.2 Å for the N atom, due that the carbonitrile group is not bent towards the surface when is engaged in a H bond. The dihedral angle is about 10° which is very close to the value in gas phase. As ribbons have a higher binding energy per molecule than monomers and dimers, it is expected to have on the surface molecules aggregated rather than free molecules or forming dimers.

We have also considered a number of linker structures composed of 3 molecules which were also placed on the surface and relaxed with DFT. These are shown, together with their binding energies (per molecule) in Fig. 46. All the structures we considered are nearly planar. They are at 3.29 Å above the surface and the carbonitrile groups, involved or not in an H bond, become parallel to the surface.

We showed previously that in gas phase the linear H bond is stronger than the non linear.¹ The same happens on the surface as we can see comparing the H bond binding energies of the P-dimers with the Tri-dimers (Fig. 40). As the CCC-Tri linker has 3 linear and 3 non linear H bond, this linker is more stable than the linkers with only 4 linear H bond.

The calculations described in this section show that ribbons and linkers are stable on the surface and that their structures are very similar to the ones in the gas phase¹ confirming that the H-bonding plays the dominant role in the binding mechanism responsible for stability of the molecular aggregates on the silver surface.

6.2.4 Islands on the silver surface

It is known from experiment⁸³ that at large coverages the molecules form brickwall type islands. To understand the energetics of the most dense bi-dimensional phase, a

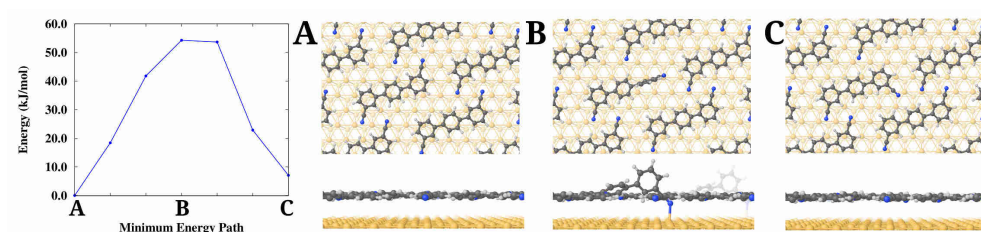


Figure 47: MEP (left panel) of the cis-trans isomerization of a monomer inside an island. Initial (A), transition (B), and final state (C) relaxed geometries (top and side views) obtained with the NEB+DFT method.

2D monolayer of molecules has also been studied. As in the case of the ribbons, we employed such orientation of the molecules with respect to the surface that allows to have a simultaneous periodicity in both organic and metallic lattices with the smallest unit cell of 4 molecules. The resulting binding energies per molecule are 206.7 kJ/mol for an all trans monolayer and 201.8 kJ/mol for a monolayer formed only by cis molecules. The optimized geometries reveal a nearly planar conformation with a dihedral angle lower than 15° between phenyl rings. The fully relaxed geometry for a T monolayer is shown in Fig. 47 (A). The mean length of the H bond is 2.6 Å and the molecules are at 3.37 Å above the surface. This fact shows that the larger the number of neighbors a molecule has, the higher the molecule is over the surface because the carbonitrile groups tends to participate in the H bonds, although the effect is small.

The T monolayer can be viewed as consisting of TT_A chains placed side-by-side. Since each molecule in the monolayer is double hydrogen bonded to two molecules from the neighboring chains, it would be interesting to investigate whether the molecules remain in their isomerization state at RT or can easily change between T and C states. To this end, we investigated the isomerization reaction for a monomer in the T monolayer and found a barrier of 54.2 kJ/mol for the $T \rightarrow C$ isomerization via underside mechanism, and 47.2 kJ/mol for the reverse reaction (Fig. 47). The relatively low barriers we find for the isomerization reaction in the monolayer imply that islands at RT are composed by a mixture of the three isomers inter-converting continuously one into the other. A typical STM image of a brickwall T monolayer from Ref. 83 is shown in Fig. 48. The superimposed molecular images correspond to the structure proposed by Marschall *et al.*⁸³ and consisting only of the T isomers. However, bright white areas on the other sides of the corresponding benzonitrile groups (some of these areas are circled) indicate that a portion of the time during the scan of these regions the group was directed the other way round.

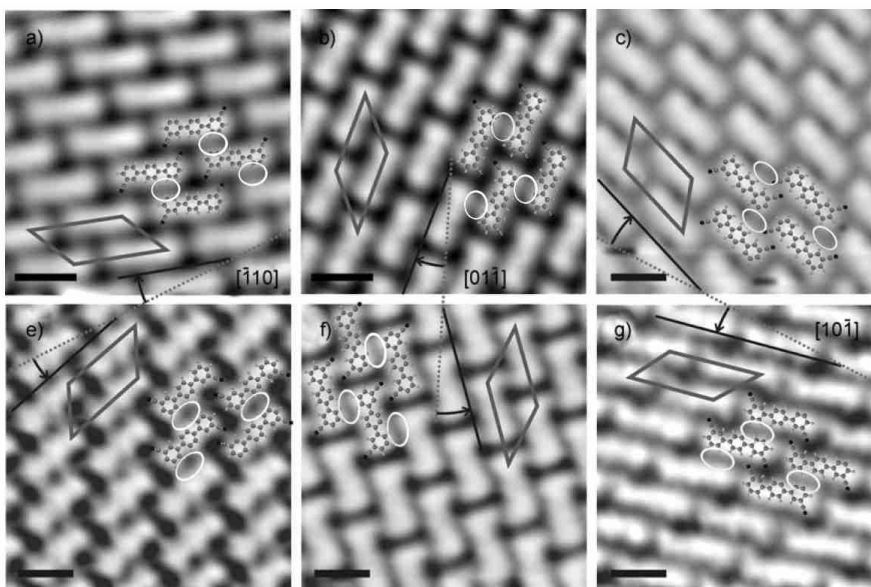


Figure 48: High resolution STM images (adapted with permission from Ref. 83) of pTmDC islands on the silver surface at room temperature. White circles indicate additional bright areas between chains.

6.3 KINETIC MONTE CARLO SIMULATION

To model the growth of the assemblies the pTmDC molecules may form on the silver surface, we performed extensive KMC simulations. Because of extremely large number of possible adsorption sites, which would require either introducing a fine grid or performing lattice-free KMC simulations, the problem was considerably simplified to make it tractable. This has been done by introducing two inter-penetrating hexagonal lattices, serving as a grid, and postulating that the molecules may only occupy the sides of the hexagons with their N atoms (or benzonitrile groups) placed on the corresponding vertices of the grid. When a molecule occupies a position on the grid (and there are three independent orientations), it may be in either of the four states, corresponding to two possible orientations of the benzonitrile groups corresponding to C or T isomers, see Fig. 49 (A). Each monomer can interact with its neighbors which may occupy four positions around it as shown in Fig. 49 (B), forming dimers of the kind $XY-P_{na}$, where X and Y can be either C or T and n can be 1 or 2 (see Fig. 40). Note that in real simulations only some of the four neighbors shown in Fig. 49 (B) may be present. For the sake of simplicity, in our KMC simulations we have not taken into account the weaker dimers $XY-Tri$ or $XY-P_{nb}$.

Since we find in our NEB calculations of diffusion of monomers that the main diffusion mechanism is pivoting, the molecules were allowed to move on the grid by using either of their ends as a pivot and rotating with the other end by $\pm 60^\circ$, Fig. 49 (C). Not

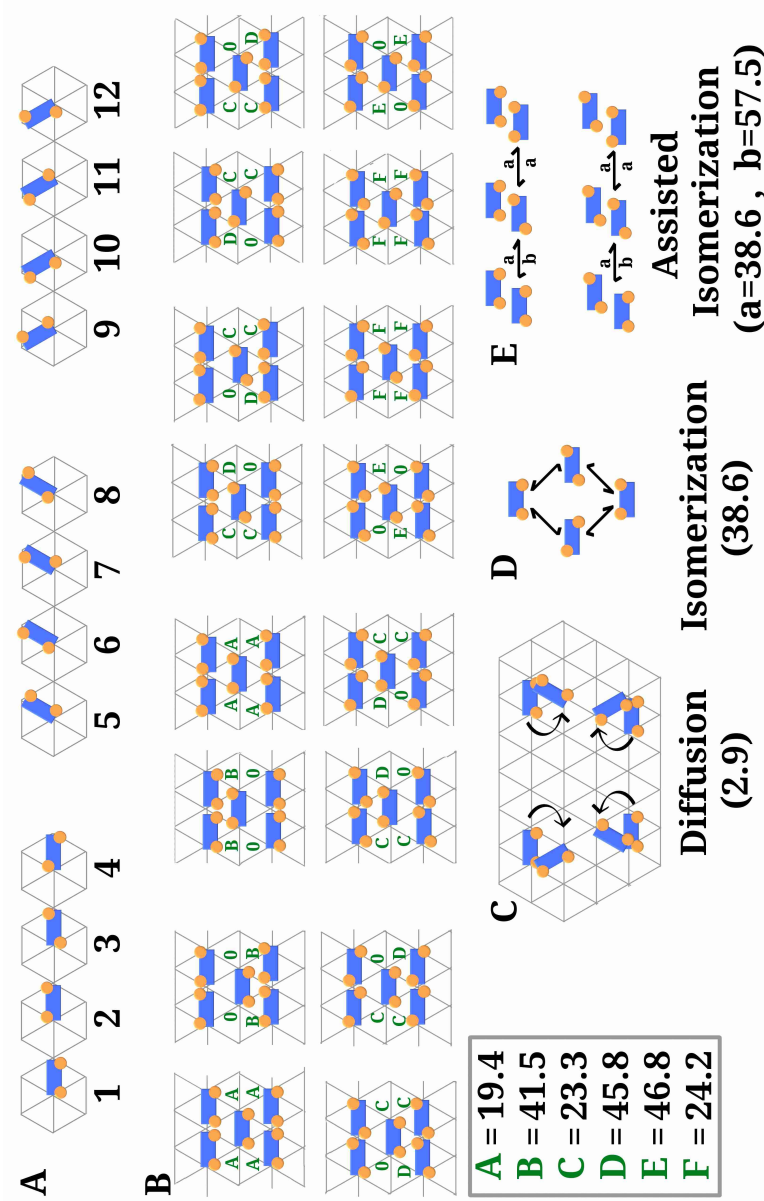


Figure 49: Schematic view of configurations, interactions and moves implemented in the KMC simulation. (A) All 12 possible non-equivalent states of a monomer on the surface. The central point of the hexagon is the net point occupied by the molecule. (B) Various arrangements for a monomer (placed in the center) with its four neighbors (only some may be present in a real simulation). Strength of the pair interactions is indicated with green labels (from A to F), which values were tuned according to our DFT results and are detailed in the light gray box (in kJ/mol). Only shown interactions for monomers 1 to 4. Two more sets of interactions exist by rotating the monomers by 60° (monomers 5 to 8) and 120° (monomers 9 to 12), that yields a total of 192 interactions. (C) The four diffusion mechanisms for a representative monomer. (D) Possible isomerization transformations for an isolated molecule and (E) the assisted isomerization transformations, where the barrier for the reaction “a” is the same as for an isolated monomer and “b” involves the breaking of one H bond. The energy barriers (in brackets) are given in kJ/mol. Blue rectangle represents the aromatic chain of the monomer, orange circles the carbonitrile groups, and the vertices of the hexagonal grid are the Ag atoms of the surface.

only the monomers may diffuse on the surfaces on their own, a molecule, if attached to a cluster, may diffuse out (detach from the cluster) to an empty position with the barrier which is calculated as a monomer diffusion barrier plus a sum of the interaction energies of the molecule with all its neighbors. Note that only monomers are allowed to diffuse on the surface, larger clusters (such as dimers, trimers, etc.) cannot move as a whole. By going through the isomerization transition $C \rightleftharpoons T$ the molecules do not change their orientation, but do change their state within the four possibilities shown in Fig. 49 (A). If a molecule is placed next to another, an assisted isomerization is allowed with the corresponding barriers depending on whether initially the molecules are connected by a double or single H bond, see Fig 49 (D and E). Finally, molecules are also allowed to desorb from the surface using their adsorption energy as the energy barrier for this transition. All the moves implemented in our KMC code and the corresponding energy barriers ΔE are schematically shown in Fig.49. Each “move” of the molecule on the grid is associated with the transition rate $r = \nu e^{-\Delta E/k_B T}$ based on the energy barrier ΔE we have calculated with DFT and the common prefactor $\nu = 10^{13} \text{ s}^{-1}$. Here k_B is the Boltzmann’s constant and T the absolute temperature.

In the simulations periodic boundary conditions were implemented with the cell comprising a 85×85 grid. The simulations were run in the following way. To speed up the simulations, either 4 or 5 molecules were initially deposited at random on the grid. These molecules were allowed to perform all possible moves described above. In addition, a deposition of a molecule onto the surface at an arbitrary empty position chosen at random is also allowed with a predefined deposition rate. The deposition is considered as a separate “move” which is attached to the list of all moves. At each KMC step a particular move (diffusion, isomerization, deposition or desorption) is chosen at random using the standard KMC algorithm.^{126,112,95} When a predefined coverage was reached, the deposition was ceased, while all other moves were allowed to continue to be executed until the desired number of KMC steps was reached. Each such simulation was run on average for over 225 million KMC steps using several seed values to accumulate statistics.

Various structures observed in experiment⁸³ were frequently seen in our KMC simulations, Fig. 50. Often we observed the molecules starting to condensate in small clusters (or islands), which are surrounded mainly by C monomers pointing its carbonitrile groups towards the interior of the cluster. When one of these molecules at the edges isomerizes to a T or leaves the cluster uncovering a T isomer, a chiral T chain can start growing from the cluster when an equal isomer binds to the first T monomer forming a $TT\text{-}P_{2\alpha}$ dimer. Then, in several cases the growth of a chain may be facilitated: (i) similar enantiomers can bind directly to enlarge the chain, (ii) a C monomer can bind to the chain forming a $CT\text{-}P_{2\alpha}$ dimer at the end of the chain, and after the isomerization of the free end of the C monomer to yield the T enantiomer, or (iii) a C monomer can form a $CT\text{-}P_{1\alpha}$ dimer at the end of the chain followed by the assisted isomerization mechanism yielding the required T enantiomer. Although these chains are relatively stable and can easily be formed, they can be destroyed at room

temperature unless are stabilized at both ends by clusters. During the growth of the chains, they can interconnect forming more complex patterns by means of the linkers.

Besides the straight growth, a chain may change its growth direction if a linker is created. This happens if a monomer binds to the chain end formed by a CT-P_{2α} dimer. Then if the new added monomer is: (i) a cis, then a CCT-Lin linker is created, or (ii) if it is a T' (the specular enantiomer of the isomer in the chain), a TCT'-Lin linker happens instead. In the former case a kink is created in the ribbon, which continues growing in the same direction (see Fig. 50 C). In the latter case the direction of growth is changed with molecules tending to aggregate in between both chiral ribbons forming small clusters (see Fig. 50 D). From a kink, a second ribbon adjacent to the main chain can start to grow as is shown in Fig. 50 (F).

As we said above, the borders of islands are mainly formed by C isomers. The growth of these islands is produced in several steps. Firstly, either a new C isomer reaches the borders by diffusion, or a T approaches to the border and then, by means of the assisted isomerization mechanism, becomes a C isomer. It can be stabilized when the monomers in the interior isomerize to create more H bonds with the new added monomer. Those monomers at the edges that are not stabilized by this mechanism are very mobile and can leave the cluster easily. This is in accordance with the experiment, according to which, at submonolayer coverages, supramolecular islands coexist with a disordered fluid phase of highly mobile molecules.⁸³

Appearance of long ribbons of molecules after thermal quenching is a characteristic feature in the observed experimental STM images.⁸³ We consistently observed formation of such features also in our KMC simulations, Fig. 50. We believe that the growth of long ribbons of trans species happens due to a delicate balance between the strength of the different H bonds and the isomerization barriers. While at room temperature the associated transition rates of breaking any H bond are similar, at lower temperature the rate of breaking a single H bond becomes relatively much larger than the rate for breaking a double H bond. Furthermore, isomerization of monomers involving the breaking of an H bond at the edges of the islands are much more difficult to occur than at the free end of the monomers at the ends of chains. This makes it more difficult to trap new monomers, by the mechanisms explained above, at the edges of the islands than at the ends of chains, favoring the growth of the chiral ribbons with a T isomer proportion increasing.

Other features observed experimentally⁸³ such as linkers, kinks, clusters and islands were also consistently observed in our KMC simulations, Fig. 50. We have also observed formation of islands when performing simulations at higher coverages. Snapshots of simulations for several coverages are displayed in Figs. 51-53

It was claimed by Marschall *et al.*⁸³ that the number of T isomers on the surface greatly surpassed that of the C isomers. We did not find this in our simulations: at room temperature all our simulations yield a slightly bigger proportion of C isomers with a mean value of 55.4 %, while the L-trans and D-trans isomers were found at 22.5 % and 22.1 %, respectively. At lower temperatures (assuming the same deposition

rate), the proportion of C isomers decreased to 42.7 %, whereas T isomers were found in increasing numbers (around 29.2 % for L-trans and 28.7 % for the D-trans).

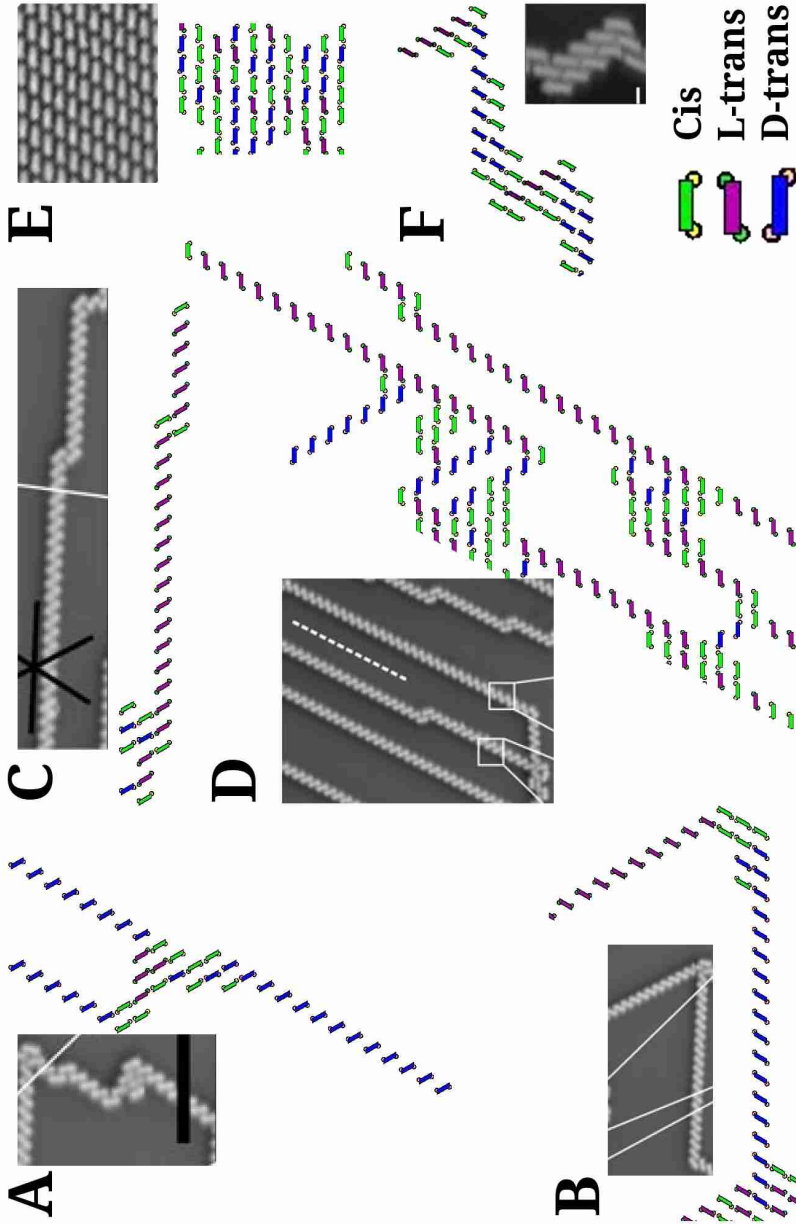


Figure 50: Sections of 85×85 KMC cells simulation with a 20% coverage and a 10^{-7} deposition rates compared with experimental results, adapted with permission from Ref. 83. Experimental STM high-resolution image was taken at 8 K on Ag(111) with a coverage of 0.1 ML. A, B and C STM images has been horizontally mirrored to facilitate the comparison with the simulation that was run at 175 K. A) Long quiral chain formed by L-trans with a TCC-Lin linker in the middle forming a kink. B) Long quiral chains formed by D-trans, with some molecules aggregated around a kink. CCC-Lin linker binds a long L-trans with a short D-trans chain. C) Two long chains of the two different stereoisomers bound by a double CCC-Lin linker. D) Long parallel chains with all kinds of linkers. E) A small piece of an island formed by a mixture of C and both T isomers. Green rectangles represent cis, blue D-trans, and magenta L-trans isomers.

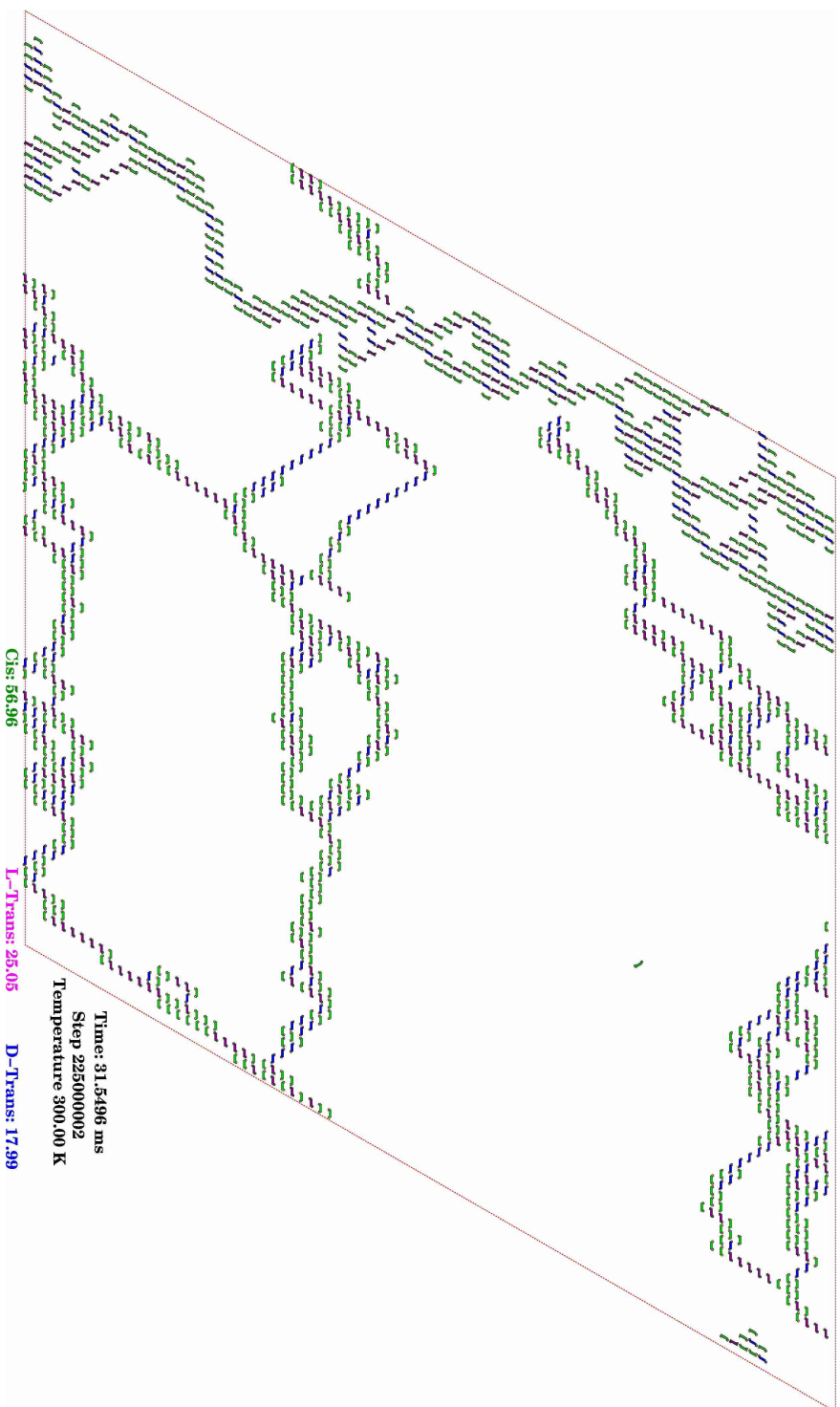


Figure 51: Snapshot of a KMC simulation at 300 K with the coverage of 20% in a 85×85 cell, and a deposition rate of 10^{-7} ps $^{-1}$. Green, purple and blue rectangles are cis, L-trans and D-trans monomers, respectively. Their proportions are given with the same color code at the bottom in the image. The KMC step number and the simulation time corresponding to the snapshot are also indicated.

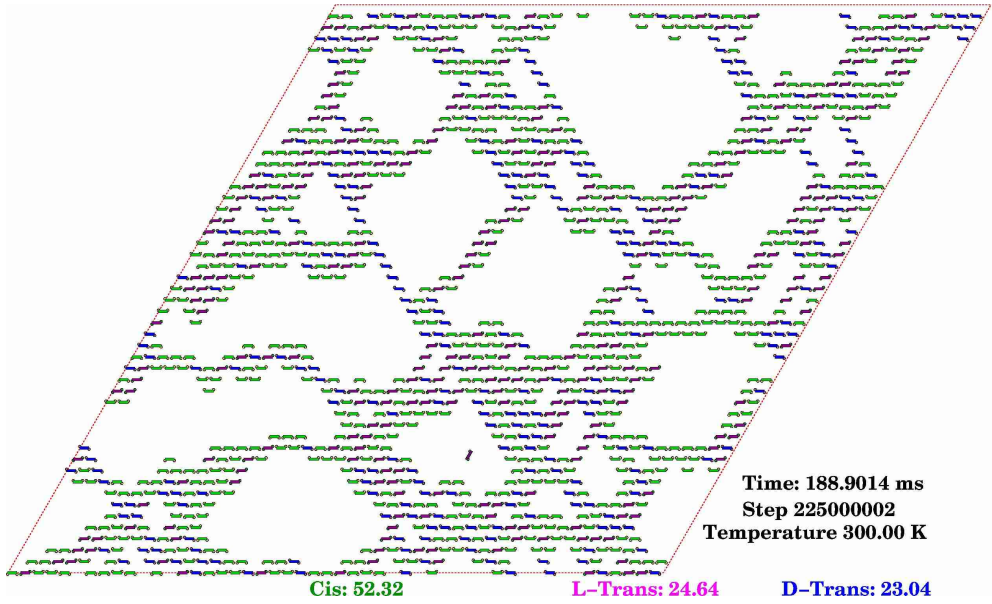


Figure 52: A snapshot of a KMC run corresponding to the 50x50 simulation cell for 300K, the coverage of 50 % and deposition rate of 10^{-7} ps $^{-1}$. The same color code as in Fig. 51 is used.

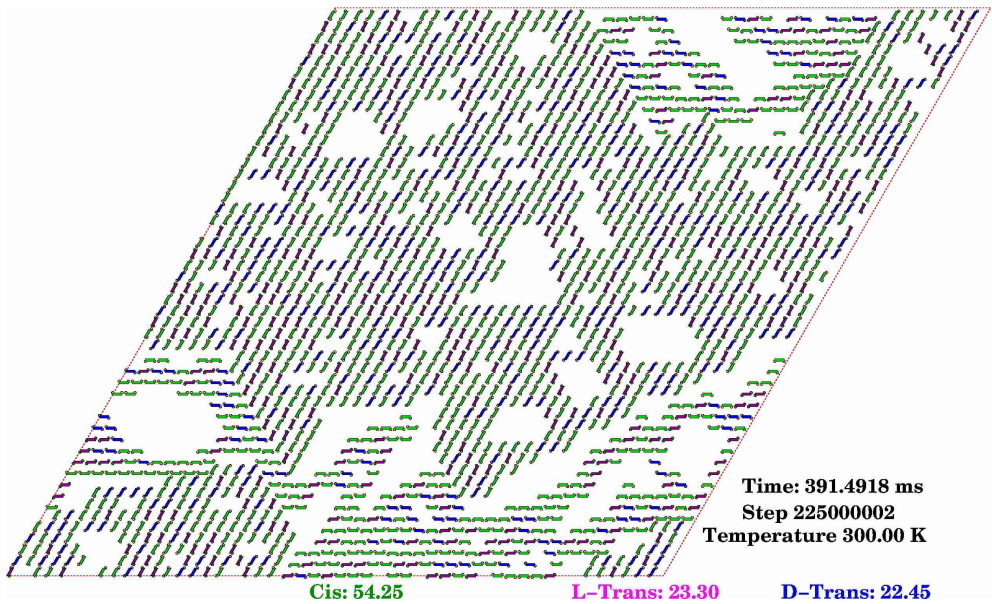


Figure 53: A snapshot of a KMC run corresponding to the 50x50 simulation cell for 300K, the coverage of 80 % and deposition rate of 10^{-7} ps $^{-1}$. The same color code as in Fig. 51 is used.

7 | CONCLUSIONS

7.1 THERMAL MODELS. THERMODYNAMICS OF BARIUM TUNGSTATE

The incorporation of thermal contributions in electronic structure calculations is a high demanding computational task. Therefore, it is necessary to develop and implement practical models able to simplify the calculations while preserving the underlying physics of the phenomena. One of these approaches is the Debye-Einsten model. In Chapter 2, we have first described the implementation of a Debye-Einstein-like model, using Fleche's equations, in the original GIBBS code and then, we have presented the re-implementation of this model, written in FORTRAN90, within the new GIBBS2 code. We have applied a Debye-like model and the new Debye-Einstein approach to study the thermodynamics and p-T phase diagram of a complex and interesting crystalline material, barium tungstate.

We have shown that zero point vibrational contributions have an effect in the static unit cell volume and bulk modulus of the same order as increasing temperature to 100-300 K. Overall, all our calculated thermodynamic properties of the two phases of barium tungstate show a good agreement with the experimental data, except the thermal expansion coefficient that presents some deviation with respect to values observed in the laboratory.

Our static data predict a transition pressure from the tetragonal to the monoclinic phase at 4.78 GPa. Zero point contributions increases this value to 5.6 GPa. We obtain a positive Clapeyron slope for this transition, *i. e.*, the transition pressure increases as temperature increases. Thanks to the experimental information of a region where the transition to the monoclinic phase is observed from metastable tetragonal structures, we can apply our thermal models to estimate values for the energetic barrier involved in the transformation. Our computed values are similar to those found for a similar transformation in zirconium silicate.

7.2 GRAPHITE

7.2.1 Non-Hydrostatic Stress

A thorough computational study of the mechanical response of graphite to hexagonal-like stresses has allowed us to derive equations of state parameters and to shed light

on the origin of frictional forces between graphite layers. Two interesting results are worth to be remarked from our computed EOS: (i) hydrostatic and uniaxial (σ_z) stresses behave very much the same as the unit cell structure is concerned, and (ii) the great resistance to compression of a graphite layer in graphite can be quantified through different moduli: $M_0^b=636$ GPa, $B_0^a=1310$ GPa, $b=12.5$ eV/Å². The EOS parameters also reveal that the most efficient way to store energy (enthalpy) in graphite is through biaxial stress load. In-plane C-C stretching modes ($E_{2g}(2)$ and E_{1u}) show almost the same high frequency values and similar pressure coefficients independent on the uniaxial z component. The interplay between the strong intra-layer C-C bonds and weak inter-layer interactions come into scene when one graphite layer is allowed to slide between other two fixed ones using a 3LG slab model with variable inter-layer separations. Calculated friction coefficients show low values (between 0.1 and 0.4) which are dependent on the displacement direction in agreement with experimental observations. It is the weakening of the intra-layer C-C bond across the path from the ABA to the AAA stacking, which is not compensated by the increasing in the dispersion forces between graphene layers, the responsible for the appearance of energy barriers and the associated frictional forces.

7.2.2 Static Friction

In chapter 4 we have demonstrated that combination of novel anvil cell experiments with Raman analysis in graphite/graphene over large sampling regions and high-stress values evidences shear stresses associated with frictional forces. These experiments can be successfully interpreted by means of quantum-mechanical calculations providing relevant microscopic information and realistic static friction parameters with a quality comparable to those obtained in dynamic FFM experiments. Overall, this kind of measurements, combined with computer simulations and atomistic models, open new avenues for routinely studying static friction phenomena on graphene and other layered materials of technological relevance, like boron nitride or molybdenum disulphide. Our results also demonstrates: (i) that adhesive (*i.e.* attractive) forces play a major role in the frictional behaviour of graphite and graphene in both static and dynamic³⁵ regimes, and (ii) that the inclusion of dispersive forces in atomic computer simulations, like that introduced here, is required to account for a realistic picture of friction at the atomic level.

7.3 SELF-ASSEMBLY

7.3.1 Gas Phase

In chapter 5 we considered various 2D structures the pTmDC molecules may form with each other in the gas phase. The main idea of this study was to understand, at

the atomic and molecular levels, what are the appropriate nanoscopic models for the structures these molecules form on the Ag(111) surface as observed in recent STM experiments.⁸³ By systematically going from the simplest assemblies consisting of just two molecules, we have built up more sophisticated structures including 1D ribbons and linkers connecting several ribbons, and developed, using *ab initio* DFT geometry relaxation, explicit atomistic models for them. We find that all of the assemblies observed in the STM images can be explained just by invoking H bonding interactions between the monomers.

Although the surface was not explicitly present in our calculations, its effect was effectively taken into account by considering 2D structures only. At the same time, one cannot underestimate the possible effect of the surface. For instance, the number of structures we find in our calculations is greater than is seen in the images, and this must be explained by the additional *directed* interaction of the molecules with the surface which makes some of the assemblies unfavorable when placed on the silver surface. In addition, orientation of the assemblies with respect to the surface cannot be explained without taking into account explicitly the interaction between them and the surface. These effects were shown in chapter 6

We have also considered in detail various forms of the monomers in the gas phase as this is important in understanding the distribution of molecules prior to their deposition on the surface. We concluded that there must be equal amounts of both C and T isomers in the gas phase, and hence when deposited on the surface one should expect 50 % cis and by 25 % of either L and D trans isomers.

7.3.2 On Surface

We considered in chapter 6 the kinetics of growth at small and intermediate coverages of assemblies of pTmDC molecules on the Ag(111) surface. We have used a toolkit of methods, from DFT modeling of adsorption geometries and NEB calculations of diffusion and isomerization energy barriers and mechanisms, to KMC modeling of the actual growth of assemblies. It was found that the dispersion interaction is the main contributor that binds the molecular assemblies to the surface with particularly favored adsorption sites through NAS interactions in which N atoms are placed above surface Ag atoms. This naturally leads to a slightly corrugated surface landscape for the molecules. Also, the preferred sites are those where phenyl rings avoid Ag atoms underneath. The molecule can be viewed as standing on two legs. The fact that the dispersion contribution dominates molecule-surface interactions leads to the molecules being quite mobile on the surface at RT and diffuse exploiting the pivoting mechanism when one “leg” serves as a pivot while another moves to the new available site. We also investigated possibilities of interconversion of C and T isomers into each other on the surface. We find that monomers may easily undergo transformations into each other following the under-side mechanism which ensures the lowest energy barrier;

moreover, the transformation occurs with equal rates implying equal amounts of both C and T monomers on the surface.

However, as molecules come closer to each other, they bind via a hydrogen bonding interaction forming dimers, chains, clusters and linkers. These structures were found to be almost identical to those found in our previous gas phase DFT calculations.¹ We find that H bonds are up to 1.5 times stronger on the surface than in the gas phase and this proves the dominant role the H bonding plays in binding the molecules together in the observed assemblies.⁸³ At the same time, we find that the growth is greatly facilitated by the assisted isomerization mechanism. Of course, lowering of the system free energy due to formation of H bonds between molecules is the main driving force behind the assembly formation. However, the assisted isomerization mechanism is the key mechanism of growth of linkers, islands and long ribbons. This is because it leads to maximizing the number of double H bonds between molecules. Hence, this specific mechanism is capable of explaining the structures observed in the experiment.⁸³

We also find in our KMC simulations that during the growth process chiral ribbons are created and destroyed at room temperature and can interconnect between themselves, creating more complex patterns by means of the linkers, where small clusters start to condensate. At the ends of the ribbons is a monomer with a free end that can isomerize easily facilitating further growth.

Importantly, no evidence was found in our theoretical investigation on the alleged chiral selectivity related to abundance of the T isomers upon the assembly as was suggested by Marschall *et al.*⁸³, the claim which was made entirely on analyzing the STM images. Instead, we find that both isomers are present almost in equal amounts. Moreover, islands are suggested to be not static: they are in a dynamic equilibrium whereby the three isomers (C and both T isomers) interconvert one into the other continuously at RT. However, the edges of islands are formed mainly by cis isomers.

We also find that at submonolayer coverages supramolecular islands coexist with a disordered fluid phase of highly mobile monomers as was also observed in the experiment.⁸³

We hope that this study sheds light on detailed mechanism of self-assembly of pTmDC molecules on the Ag(111) surface, demonstrating clearly, on the one hand, the role of their interaction with the surface which provides their high mobility via the pivoting mechanism, and, on the other, establishes importance of the H bonding interaction between molecules and of the assisted isomerization reaction which are the key for understanding the observed supramolecular assemblies. Our study also shows the importance of theoretical modeling in making conclusions concerning observed assemblies and the mechanisms responsible for their growth.

CONCLUSIONES

7.4 MODELOS TÉRMICOS. TERMODINÁMICA DEL WOLFRAMATO DE BARIO

La inclusión de efectos térmicos en los cálculos de estructura electrónica es una tarea computacionalmente cara. Por ello se hace necesario el desarrollo y la implementación de modelos que permitan una simplificación del cálculo conservando a su vez la física real subyacente, como es el caso del modelo de Debye-Einstein. En el capítulo 2 hemos descrito la implementación un modelo de Debye-Einstein, que hace uso de la aproximación de Fleche, en el código GIBBS y su posterior reimplementación en FORTRAN90 dentro del código de GIBBS2. Se han empleado los modelos térmicos de Debye y el nuevo modelo de Debye-Einstein para estudiar la termodinámica y el diagrama de fases p-T de un sólido complejo como el wolframato de bario. Demostramos que la inclusión de los efectos del punto cero tienen un mayor efecto en el volumen y en el módulo de bulk que el incremento de la temperatura desde los 0 K hasta 100 K o 300 K. Los resultados obtenidos comparan bien con los datos experimentales, salvo el coeficiente de expansión térmica que presenta mayores diferencias con los valores observados en el laboratorio.

Nuestros datos estáticos predicen una presión estática de transición de la fase tetragonal a la monoclinica a 4.78 GPa, y aumentando este valor hasta los 5.6 GPa al incluir los efectos térmicos del punto cero. Observamos que la pendiente de Clapeyron es positiva, con lo que la presión de transición va aumentando al aumentar la temperatura. Experimentalmente se encuentra una región donde la fase tetragonal es metaestable y sufre la transformación a la fase BaWO₄-II al aumentar la temperatura. Con nuestro modelo térmico hemos sido capaces de evaluar la altura de la barrera energética asociada a esta transformación obteniendo valores razonables del orden de los calculados para una transformación similar en el silicato de zirconio.

7.5 GRAFITO

7.5.1 Estrés No Hidrostático

Un completo estudio de la respuesta mecánica del grafito frente al estrés de simetría hexagonal nos ha permitido derivar los parámetros de la ecuación de estado y arrojar luz sobre el origen de las fuerzas de fricción entre láminas de grafito. Vale la pena remarcar dos resultados importantes de nuestra ecuación de estado (EOS): (i) el estrés hidrostático y el uniaxial (σ_z) se comportan de manera similar en cuanto a la estructu-

ra de la celda unidad se refiere, y (ii) la gran resistencia a la compresión de una lámina de grafito puede ser cuantificada por medio de dos *moduli* diferentes: $M_0^b=636$ GPa, $B_0^a=1310$ GPa, $b=12.5$ eV/Å². Los parámetros de la EOS revelan también que la forma más eficiente de almacenar energía (entalpía) en el grafito es a través de la carga de estrés biaxial. Los modos de tensión en el plano C-C ($E_{2g}(2)$ y E_{1u}) muestran prácticamente el mismo valor de frecuencia y similares coeficientes de presión, independientes del componente uniaxial z . La relación entre los enlaces fuertes C-C intra-capa y las interacciones débiles entre capas entran en escena cuando a una lámina de grafito se le permite deslizar entre otras dos fijas usando un modelo de 3 láminas de grafito (3LG por sus siglas en inglés) con una separación entre capas variable. Los coeficientes de fricción calculados muestran valores bajos (entre 0.1 y 0.4) que dependen de la dirección de desplazamiento de acuerdo con las observaciones experimentales. Es el debilitamiento del enlace C-C intra-capa a lo largo de la trayectoria desde el empaquetamiento ABA hasta el AAA, que no se ve compensado por el incremento de las fuerzas de dispersión entre las capas de grafeno, el responsable de la aparición de las barreras energéticas y las fuerzas asociadas de fricción.

7.5.2 Fricción Estática

En el capítulo 4 hemos demostrado que la combinación de nuevos experimentos de celda de yunque junto con análisis Raman en grafito/grafeno sobre grandes regiones de muestra y altos valores de estrés muestran evidencias de un estrés de cizalla asociado a fuerzas de fricción. Estos experimentos pueden ser satisfactoriamente interpretados por medio de cálculos mecánico-cuánticos aportando información microscópica relevante y parámetros de fricción estática realistas con una calidad comparable a los obtenidos mediante experimentos dinámicos de microscopía de fuerza de fricción (FFM). Sobre todo, este tipo de medidas combinadas con simulaciones computacionales y modelos atómicos, abren nuevas rutas para el estudio sistemático de fenómenos de fricción estática en grafeno y otros materiales laminados de relevancia tecnológica, como el nitruro de boro o el disulfuro de molibdeno. Nuestros resultados, además demuestran: (i) que la fuerza adhesiva (*i.e.* atractiva) juega un papel importante en la fricción tanto en el régimen estático como dinámico,³⁵ y (ii) que se requiere la inclusión de las fuerzas dispersivas en las simulaciones computacionales atómicas, como las introducidas en este trabajo, para describir la fricción de manera realista a nivel atómico.

7.6 AUTOENSAMBLADO

7.6.1 pTmDC en Fase Gas

En el capítulo 5 hemos considerado varias estructuras 2D que las moléculas de pTmDC pueden formar entre ellas en fase gas. La idea principal de este estudio ha sido la de entender, a un nivel atómico y molecular, cuáles son los modelos nanoscópicos apropiados para las estructuras que estas moléculas forman en la superficie (111) de plata, como ha sido observado en los experimentos de microscopía de efecto túnel (STM).⁸³ Sistemáticamente y comenzando desde el ensamblado más simple, consistente en solo dos moléculas, hemos construido estructuras más sofisticadas incluyendo cadenas monodimensionales (1D) y conectores que unen varias cadenas, y hemos desarrollado explícitos modelos atomísticos, usando relajaciones geométricas mediante DFT *ab initio*. Encontramos que todos los ensamblados observados en las imágenes de STM pueden ser explicados simplemente mediante interacciones de enlace de hidrógeno entre los monómeros.

Aunque la superficie no estuvo presente explícitamente en los cálculos, su efecto sin embargo sí que fue tenido en cuenta considerando únicamente estructuras 2D. Al mismo tiempo, no se puede subestimar los posibles efectos de la superficie. Por ejemplo, el número de estructuras que encontramos en nuestros cálculos es mayor que el observado en las imágenes, y esto puede ser explicado por la interacción *directora* adicional de las moléculas con la superficie que hace a algunos de los ensamblados desfavorables cuando son colocados sobre la superficie de plata. Además, la orientación de los ensamblados con respecto a la superficie no puede ser explicada sin tener en cuenta explícitamente la interacción entre ellos y la superficie. Estos efectos se mostraron en el capítulo 6.

Hemos considerado en detalle además varias formas de los monómeros en la fase gas ya que esto es importante para el entendimiento de la distribución de moléculas antes de su deposición sobre la superficie. Concluimos con que debe haber una cantidad igual de isómeros *cis* y *trans* en la fase gas, y por tanto al depositarse en la superficie cabría esperar que las proporciones sean 50 % *cis*, 25 % L-*trans* y 25 % D-*trans*.

7.6.2 pTmDC en Superficie Ag(111)

Hemos considerado en el capítulo 6 la cinética de crecimiento, a pequeños e intermedios recubrimientos, de agrupaciones de moléculas de pTmDC sobre la superficie Ag(111). Empleamos un conjunto de métodos, desde el modelado por DFT de las geometrías de adsorción y cálculos NEB de barreras energéticas y mecanismos de difusión e isomerización, a modelado por KMC del crecimiento real de los ensamblados. Encontramos que la interacción de dispersión es la contribución principal que une los ensamblados moleculares a la superficie con sitios de adsorción particularmente favorables a través de las interacciones NAS en las que los átomos de N se colocan sobre

los átomos de Ag de la superficie. Esto conduce de manera natural a una superficie de energía ligeramente corrugada para las moléculas. También, los sitios preferidos son aquellos donde los grupos fenilo no tienen átomos de Ag bajo su centro. Puede considerarse que la molécula se sujeta sobre dos piernas. El hecho de que la contribución de la dispersión domine las interacciones molécula-superficie conduce a que las moléculas sean bastante móviles sobre la superficie a temperatura ambiente y difundan empleando el mecanismo de pivotaje, en el que una de las “piernas” sirve como pivote mientras que la otra se mueve a un nuevo sitio disponible. Hemos investigado también las posibilidades de interconversión sobre la superficie entre los isómeros cis y trans. Encontramos que los monómeros pueden transformarse fácilmente el uno en el otro siguiendo un mecanismo de isomerización por el camino inferior (under-side mechanism) que garantiza la barrera energética más baja; además, las transformaciones ocurren al mismo ritmo, lo que implica una cantidad igual de monómeros cis y trans sobre la superficie.

Sin embargo, como las moléculas se acercan unas a otras, pueden unirse vía enlace de hidrógeno formando dímeros, cadenas, grupos y conectores. Estas estructuras resultaron ser prácticamente idénticas a las encontradas previamente en los cálculos DFT en fase gas.¹ Encontramos que los enlaces de H son hasta 1.5 veces más fuertes en la superficie que en la fase gas y esto prueba el papel dominante que juega el enlace de H al unir las moléculas en los ensamblados observados.⁸³ Al mismo tiempo, comprobamos que el crecimiento se ve facilitado por el mecanismo de isomerización asistida. Por supuesto, la disminución de la energía libre del sistema debido a la formación de enlaces de H entre las moléculas es la principal fuerza directriz detrás de la formación de ensamblados. Sin embargo, el mecanismo de isomerización asistida es el mecanismo clave en el crecimiento de conectores, islas y largas cadenas. Esto es porque maximiza el número de enlaces dobles de H entre moléculas. Por tanto, este mecanismo específico es capaz de explicar las estructuras observadas en el experimento.⁸³

También encontramos en las simulaciones de KMC que durante el proceso de crecimiento cadenas quirales son creadas y destruidas a temperatura ambiente y pueden interconectarse entre ellas, creando patrones más complejos por medio de los conectores, donde pequeños grupos de moléculas empiezan a condensar. Al final de las cadenas hay un monómero con uno de sus extremos libre que puede isomerizar fácilmente, favoreciendo así el crecimiento de la cadena.

En nuestra investigación teórica no hemos encontrado evidencias de la supuesta selectividad quiral relacionada con la abundancia de isómeros trans tras el ensamblado como fue sugerido por Marschall *et al.*⁸³, afirmación que fue hecha enteramente analizando las imágenes de STM. En vez de ello, encontramos que ambos isómeros están presentes en cantidades casi iguales. Además, las islas parecen no ser estáticas: ellas están en equilibrio dinámico donde los tres isómeros (cis y ambos trans) se interconvierten unos en otros continuamente a temperatura ambiente. Sin embargo, los bordes de las islas sí que están formados mayormente por isómeros cis.

Encontramos además que a recubrimientos inferiores al de la monocapa islas supramoleculares coexisten con una fase fluida desordenada de monómeros de alta movilidad como también ha sido observado en los experimentos.⁸³

Esperamos que este estudio arroje luz sobre el mecanismo detallado del autoensamblado de moléculas de pTmDC sobre una superficie Ag(111), demostrando claramente, por un lado, el papel de sus interacciones con la superficie que provee su gran movilidad mediante el mecanismo de pivotaje, y, por otro lado, establecer la importancia de la interacción de los enlaces de H entre las moléculas y la reacción de isomerización asistida que es la clave para la comprensión de los ensamblados supramoleculares observados. Este estudio también muestra la importancia del modelado teórico a la hora de sacar conclusiones relacionadas con los ensamblados observados y los mecanismos responsables de su crecimiento.



A continuación se presentan los artículos que conforman esta tesis, de los cuales han sido

- publicados:
 - GIBBS2: A new version of the quasiharmonic model code. II. Models for solid-state thermodynamics, features and implementation, Otero-de-la Roza, A., Abbasi-Pérez, D. and Luaña, V. *Computer Physics Communications*, vol. 182 (10), pp. 2232–2248.
 - Modeling graphite under stress: Equations of state, vibrational modes, and interlayer friction, Abbasi-Pérez, D., Menéndez, J., Recio, J., Otero-de-la Roza, A., del Corro, E., Taravillo, M., Baonza, V. and Marqués, M. (2014), *Phys. Rev. B*, vol. 90 (5), p. 054 105.
 - Building Motifs during Self-Assembly of para-Terphenyl-meta-dicarbonitrile on a Metal Surface: A Gas-Phase Study, Abbasi-Pérez, D., Recio, J. M. and Kantorovich, L. (2014), *J. Phys. Chem. C*, vol. 118, pp. 10 358-10 365.
- aceptados:
 - Role of Isomerization in Kinetics of Self-Assembly: p-Terphenyl-m-Dicarbonitrile on Ag(111) Surface, Abbasi-Pérez, D., Recio, J. M. and Kantorovich, L. (2015), *PCCP* (accepted, minor corrections).
- enviados:
 - Frictional forces in graphite under compression, E. del Corro, D. Abbasi-Pérez, M. Marqués, A. Otero-de-la-Roza, J. M. Menéndez, M. Taravillo, J. M. Recio, V. G. Baonza, *Phys. Rev. B*, (enviado)

Como indica la normativa, los artículos aceptados han de presentar el justificante de aceptación. A continuación se muestra el contenido del correo electrónico enviado por el editor de la revista *Phys. Chem. Chem. Phys.*, que certifica que el artículo ha sido considerado para su publicación.

Dear Mr Abbasi:

Manuscript ID CP-ART-01-2015-000220

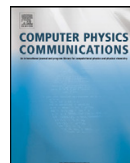
Title: Role of Isomerization in Kinetics of Self-Assembly: p-Terphenyl-m-Dicarbonitrile on Ag(111) Surface

I am pleased to inform you that your manuscript has been recommended for publication in Physical Chemistry Chemical Physics subject to revision in line with the attached reports. The manuscript may be subject to further peer review prior to reaching a final editorial decision.

[...]

Yours sincerely,

Dr Fiona Gillespie, MRSC, Publishing Editor Royal Society of Chemistry.



GIBBS2: A new version of the quasiharmonic model code. II. Models for solid-state thermodynamics, features and implementation ☆,☆☆

A. Otero-de-la-Roza^{*}, David Abbasi-Pérez, Víctor Luaña

Departamento de Química Física y Analítica, Facultad de Química, Universidad de Oviedo, 33006 Oviedo, Spain

ARTICLE INFO

Article history:

Received 3 March 2011

Received in revised form 2 May 2011

Accepted 10 May 2011

Available online 13 May 2011

Keywords:

Equations of state in solids

Equilibrium properties of solids

Data analysis

Treatment of noisy data

Discontinuous data

Thermal effects

ABSTRACT

In the second article of the series, we present the GIBBS2 code, a Fortran90 reimplementa- tion of the original GIBBS program [Comput. Phys. Commun. 158 (2004) 57] for the calculation of pressure- temperature dependent thermodynamic properties of solids under the quasiharmonic approximation. We have taken advantage of the detailed analysis carried out in the first paper to implement robust fitting techniques. In addition, new models to introduce temperature effects have been incorporated, from the simple Debye model contained in the original article to a full quasiharmonic model that requires the phonon density of states at each calculated volume. Other interesting novel features include the empirical energy corrections, that rectify systematic errors in the calculation of equilibrium volumes caused by the choice of the exchange-correlation functional, the electronic contributions to the free energy and the automatic computation of phase diagrams. Full documentation in the form of a user's guide and a complete set of tests and sample data are provided along with the source code.

Program summary

Program title: GIBBS2

Catalogue identifier: AEJL_v1_0

Program summary URL: http://cpc.cs.qub.ac.uk/summaries/AEJL_v1_0.html

Program obtainable from: CPC Program Library, Queen's University, Belfast, N. Ireland

Licensing provisions: GNU General Public License, v3

No. of lines in distributed program, including test data, etc.: 936 087

No. of bytes in distributed program, including test data, etc.: 8 596 671

Distribution format: tar.gz

Programming language: Fortran90

Computer: Any running Unix/Linux

Operating system: Unix, GNU/Linux

Classification: 7.8

External routines: Part of the minpack, pppack and slatec libraries (downloaded from www.netlib.org) are distributed along with the program.

Nature of problem: Given the static $E(V)$ curve, and possibly vibrational information such as the phonon density of states, calculate the equilibrium volume and thermodynamic properties of a solid at arbitrary temperatures and pressures in the framework of the quasiharmonic approximation.

Additional comments: A detailed analysis concerning the fitting of equations of state has been carried out in the first part of this article, and implemented in the code presented here.

Running time: The tests provided only take a few seconds to run.

© 2011 Elsevier B.V. All rights reserved.

[☆] This paper and its associated computer program are available via the Computer Physics Communications homepage on ScienceDirect (<http://www.sciencedirect.com/science/journal/00104655>).

^{☆☆} A contribution from the Malta-Consolider group (<http://www.malta-consolider.com/>).

^{*} Corresponding author.

E-mail addresses: alberto@carbono.quimica.uniovi.es (A. Otero-de-la-Roza), david@fluor.quimica.uniovi.es (D. Abbasi-Pérez), victor@carbono.quimica.uniovi.es (V. Luaña).

Table 1

Calculation parameters for magnesium oxide, diamond and fcc aluminum. The first field represents the number of volumes in the grid and E_{cut} is the plane-wave cutoff energy, in Ry. Next, we show the density of the electronic and vibrational meshes (Monkhorst–Pack), the electron configuration used to generate the pseudopotentials and the number of core electrons they represent.

	V	E_{cut}	k -point	q -point	El. config.	Core
MgO	174	80	$4 \times 4 \times 4$	$8 \times 8 \times 8$	Mg: $1s^2 2s^2 2p^6 3s^1$ O: $1s^2 2s^2 2p^5$	2 2
C	31	60	$6 \times 6 \times 6$	$6 \times 6 \times 6$	$1s^2 2s^2 2p^2$	2
Al	43	50	$16 \times 16 \times 16$	$6 \times 6 \times 6$	$1s^2 2s^2 2p^6 3s^2 3p^1$	10

1. Introduction

The first principles calculation of accurate equations of state (EOS), thermodynamic properties and phase diagrams is a very useful tool in a number of fields, including geophysics [1] and materials research [2,3]. One of the main advantages of the calculation of pressure and temperature dependent crystal properties is the easiness with which extreme conditions, unattainable by experimental means, can be modeled. Indeed, provided that there are no technical difficulties (e.g. pseudopotential transferability issues [4]), pressure effects can be accounted for simply by compression of the calculated crystal geometry to smaller volumes. The inclusion of temperature effects, primarily related to the vibrational degrees of freedom inside the crystal, is more delicate. There are essentially two mainstream ways of incorporating temperature in a theoretical calculation: molecular dynamics simulations [5,6] and the quasiharmonic approximation (QHA) [7]. The former is ideally suited for situations close to the classical limit, at temperatures close or including the melting temperature. The latter is based on the harmonic approximation and, as such, accurate only at temperatures of the order or below the Debye constant.

In this article, we present GIBBS2, a program that implements several varieties of the quasiharmonic approximation. The QHA has had in recent times a surge in popularity, thanks to the advent of very efficient methods of computing the vibrational dispersion relations of a crystal. In particular, the Density Functional Perturbation Theory [8] allows the calculation of phonon frequencies at a given crystal geometry using linear response theory. Nowadays, it is possible to undertake the prediction of equations of state and thermodynamic properties fully *ab initio* with breathtaking accuracy [9,10].

The GIBBS2 code is presented in this article as a successor of the highly popular GIBBS code [11,12], which has been completely rewritten from scratch. In the original GIBBS, emphasis was put on the calculation of thermodynamic properties from a minimal set of theoretical data, namely the static $E(V)$ curve, using a simplified Debye model to include temperature effects. In this new version, a number of models are implemented, with varying accuracy and input data requirements. The Debye model implemented in GIBBS is the least demanding and roughly the least accurate, requiring only the static energy curve, and possibly the Poisson ratio of the crystal. In the highest end of the accuracy scale, the full QHA has been implemented, requiring the user to input the phonon density of states (phDOS) or a mesh of phonon frequencies for each of the calculated crystal volumes. The different thermal models are discussed and compared in Section 3.

A detailed analysis of the fitting techniques to static energy *versus* volume data has been carried out in the preceding article of this series [13]. Equivalent methods have been included in GIBBS2. With them, it is possible to generate error bars for calculated thermodynamic properties at arbitrary pressures and temperatures. The details of the fitting procedures are given in Section 4.

A number of additional features have been implemented in GIBBS2, that are discussed in Section 5. These include the calculation of other contributions to the free energy of the solid, such as the electronic free energy in metals, the implementation of empirical energy corrections (EEC) to account for known systematic trends in the calculation of equilibrium volumes and the automatic determination of phase transitions and phase diagrams.

In Section 6, we discuss the structure of the code, its installation, usage and a complete input and output. The user interface of the original GIBBS has been made much easier to use, including the possibility of treating several crystal phases on the same run.

2. Computational details

In the following sections, we use three simple solids to discuss the features of GIBBS2: magnesium oxide, diamond and fcc aluminum. The calculations were carried out using a plane-wave plus pseudopotentials approach together with DFPT, as implemented in the Quantum ESPRESSO package [14]. Ultrasoft pseudopotentials for all the atoms were generated using the USPP program by D. Vanderbilt [15]. The phDOS was calculated for every volume point on a grid. The exchange-correlation functionals used were LDA and the PBE version of GGA. The calculation details are shown in Table 1.

3. Thermal models

3.1. Introduction

The function controlling the geometry and phase stability of a solid under a given pressure and temperature is the non-equilibrium Gibbs free energy,

$$G^*(\boldsymbol{x}, V; p, T) = E_{\text{sta}}(\boldsymbol{x}, V) + pV + F_{\text{vib}}^*(\boldsymbol{x}, V; T) + F_{\text{el}}^*(\boldsymbol{x}, V; T) + \dots \quad (1)$$

where E_{sta} is the static energy (obtained directly from the *ab initio* calculation) and F_{vib}^* is the non-equilibrium vibrational Helmholtz free energy. The crystal structure is completely determined by the volume V , and a number of coordinates, including atomic positions and cell parameters, which we label collectively as \boldsymbol{x} . More free energy terms are used to represent additional degrees of freedom in the solid: electronic (F_{el}^*), magnetic, configurational, defects, etc.

The central result related to G^* is the following: at a given pressure (p) and temperature (T), the equilibrium geometry is achieved by minimizing G^* with respect to the remaining variables:

$$G(p, T) = \min_{\mathbf{x}, V} G^*(\mathbf{x}, V; p, T), \quad (2)$$

which yields equilibrium internal coordinates, $\mathbf{x}(p, T)$, and volume, $V(p, T)$, as well as the equilibrium Gibbs function $G(p, T)$. Because of the difficulty of calculating G^* for the whole potential energy surface, a usual approach is restricting the internal variables to those resulting of a minimization of the static energy at any given volume:

$$\mathbf{x}_{\text{opt}}(V) \quad \text{from} \quad E_{\text{sta}}(V) = \min_{\mathbf{x}} E_{\text{sta}}(\mathbf{x}, V), \quad (3)$$

that transforms Eq. (1) into:

$$G^*(V; p, T) = E_{\text{sta}}(\mathbf{x}_{\text{opt}}, V) + pV + F_{\text{vib}}^*(\mathbf{x}_{\text{opt}}, V; T) + \dots \quad (4)$$

Minimization of the above equation with respect to volume yields the mechanical equilibrium condition:

$$\frac{\partial G^*}{\partial V} = 0 = -p_{\text{sta}} + p - p_{\text{th}} \quad (5)$$

where $p_{\text{sta}} = -dE_{\text{sta}}/dV$ is the static pressure, $p_{\text{th}} = -\partial F_{\text{vib}}^*/\partial V$ is the thermal pressure and p is the applied external pressure.

Using \mathbf{x}_{opt} , instead of $\mathbf{x}(p, T)$, in the context of the QHA leads to what other authors have called the statically constrained QHA [16]. This approximation implies assuming that the effect of temperature is expressed through a thermal pressure instead of a thermal stress tensor, and that the free atomic coordinates are determined by the cell volume alone. The consistent computation of $\mathbf{x}(p, T)$ requires the knowledge of portions of the multidimensional potential energy surface and its associated vibrational properties. This approach is, in general, exceedingly expensive. Note that, because of Neumann's principle, thermal stress in cubic crystals is isotropic, so the test cases we present are free from the static constrain error.

3.2. The quasiharmonic approximation

In the harmonic model, the vibrations in a crystal are treated as a gas of $3nN$ non-interacting phonons with volume independent frequencies ω_j , where n is the number of atoms per primitive cell and N the number of cells in the macroscopic solid. The complete lack of anharmonicity in this model leads to well known unphysical behavior [17]: zero thermal expansion, infinite thermal conductivity, ... The simplest way of accounting for anharmonic effects is assuming the harmonic approximation at any given crystal geometry, even if it does not correspond to the equilibrium structure: the quasiharmonic approximation (QHA). Plenty of examples of the success of QHA in the prediction of thermodynamic properties and phase stability of solids can be found in the literature [18–21].

In QHA, the non-equilibrium Helmholtz free energy is (atomic units are used throughout the article):

$$F_{\text{vib}}^*(\mathbf{x}, V; T) = \sum_{j=1}^{3nN} \left[\frac{\omega_j}{2} + k_B T \ln(1 - e^{-\omega_j/k_B T}) \right], \quad (6)$$

$$F^*(\mathbf{x}, V; T) = E_{\text{sta}}(\mathbf{x}, V) + F_{\text{vib}}^*(\mathbf{x}, V; T), \quad (7)$$

where the vibrational frequencies ω_j depend on the crystal geometry (\mathbf{x}, V) . The considered solid is periodic with n atoms per primitive cell and a total of N cells, hence the limit of the summation. It is usual practice to measure extensive thermodynamic quantities per unit cell (F_{vib}^*/N in the equation above). Also, it is not possible to calculate a sampling of the vibrational frequencies comparable to the number of cells of a finite crystal. Instead, a relatively fine sampling of the first Brillouin zone is used, and it is assumed that each reciprocal space point represents a certain volume. This amounts to choosing a frequency normalization so that

$$3n = \sum_j \omega'_j, \quad (8)$$

and

$$\frac{F_{\text{vib}}^*}{N} = \sum_j \left[\frac{\omega'_j}{2} + k_B T \ln(1 - e^{-\omega'_j/k_B T}) \right], \quad (9)$$

where the index j runs over the number of calculated frequencies. In the following, we will drop the primes of the vibrational frequencies and we will assume that extensive quantities are calculated per primitive cell.

Summations over frequencies such as in Eq. (6) can be calculated by integration using the pDOS:

$$g(\omega) = \frac{dG}{d\omega}; \quad G(\omega) = \int_0^\omega \sum_{j=1}^{3nN} \delta(\omega - \omega_j) d\omega, \quad (10)$$

$$F_{\text{vib}}^* = \int_0^\infty \left[\frac{\omega}{2} + k_B T \ln(1 - e^{-\omega/k_B T}) \right] g(\omega) d\omega. \quad (11)$$

The normalization condition (Eq. (8)) transforms into:

$$3n = \int_0^\infty g(\omega) d\omega, \quad (12)$$

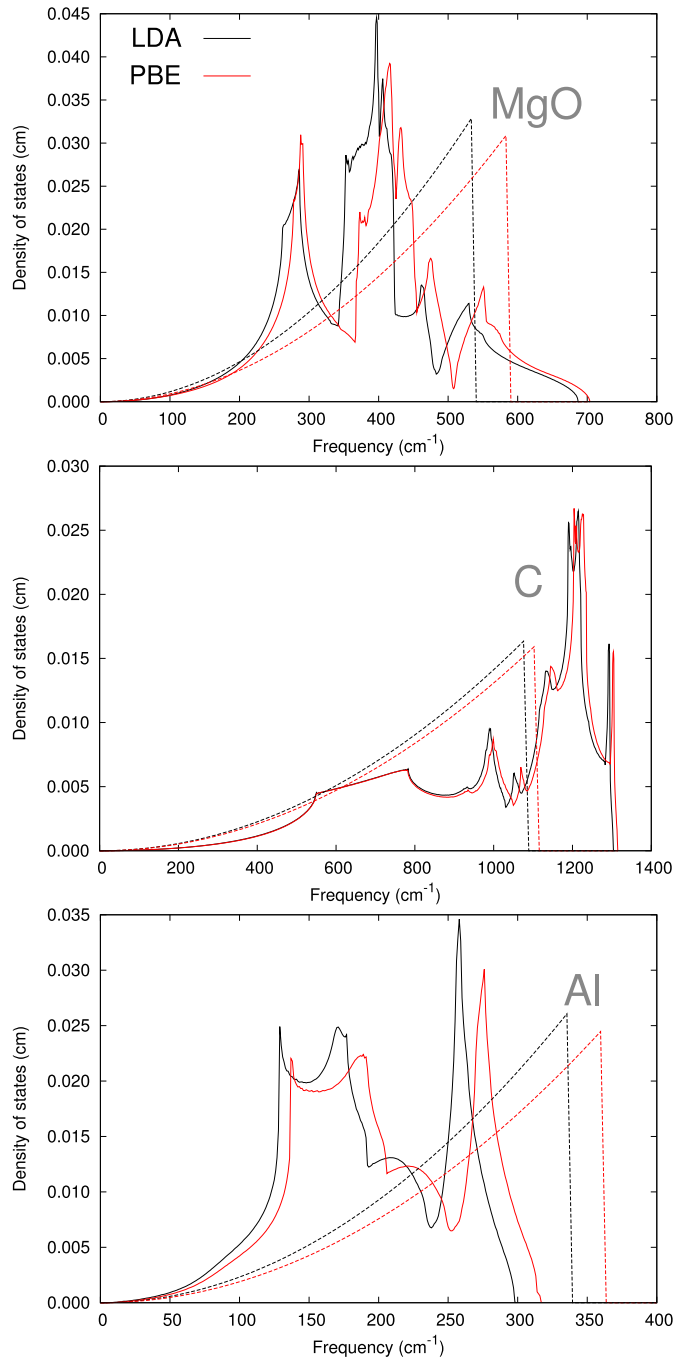


Fig. 1. Phonon density of states of MgO, diamond (C) and fcc Al, calculated using DFPT, with LDA (black) and PBE (red) exchange–correlation functionals at the experimental volumes. The phDOS used in the Debye–Slater model (see Section 3.3) are represented with dashed lines. (For interpretation of the references to color in this figure legend, the reader is referred to the web version of this article.)

so that extensive quantities are, again, calculated per primitive cell. The two approaches—using the ω_j calculated on a grid or the phDOS—have been incorporated into `GIBBS2`, and yield equivalent results.

Fig. 1 shows the calculated phDOS for MgO, diamond and fcc aluminum. Aluminum contains only one atom per primitive cell, and so its dispersion relations are composed exclusively of the acoustic branches. MgO and diamond have 2 atoms per cell, so there are 3

optic and 3 acoustic branches in the dispersion diagram. The pDOS of diamond stretches to higher frequencies, because of the stiffness of the carbon-carbon covalent bond. The LDA and PBE pDOS show comparable features, and can be brought to almost coincidence by scaling. This is important, because it is the same effect observed when the volume is changed, indicating that the discrepancy between both functionals can be corrected by an appropriate modification of the equilibrium volume.

In a typical QHA calculation, the user inputs a volume grid together with the static energy $E(V)$ resulting from the minimization of the internal coordinates \mathbf{x} . In addition, either the frequencies or the phonon density of states at each volume are also provided. With this information, `GIBBS2` loops over a list of user-controlled pressure–temperature pairs. For the chosen temperature, three quantities are calculated on the input volume grid: the static energy, the non-equilibrium Helmholtz free energy and the entropy, and fitted using the techniques described in the previous article [13] and summarized in the next section. The fit to F^* is used to find the equilibrium volume, $V(p, T)$, according to Eq. (5), where $p_{\text{sta}} + p_{\text{th}}$ is obtained as a $-\partial F^*/\partial V$. It is interesting to note that, should the vibrational frequencies be given in the input, the thermal pressure can also be calculated as:

$$p_{\text{th}} = -\frac{\partial F_{\text{vib}}^*}{\partial V} = -\sum_j \left[\frac{\omega_j \gamma_j}{2V} + \frac{\omega_j \gamma_j / V}{e^{\omega_j/k_B T} - 1} \right], \quad (13)$$

where $\gamma_j = -\partial \ln \omega_j / \partial \ln V$ are the mode gammas. This approach is, however, less general, because the mode gamma information is lost if only the $g(\omega; V)$ are given, and also less efficient, because it involves the fitting of each volume dependent frequency $\omega_j(V)$.

Once the equilibrium volumes are known, a number of thermodynamic properties are derived directly from F^* (Eq. (7)). Namely, the equilibrium entropy (S), Helmholtz free energy (F), Gibbs free energy (G), internal energy (U), constant-volume heat capacity (C_V) and isothermal bulk modulus (B_T):

$$F = F^*(V(p, T), T), \quad (14)$$

$$S = S(V(p, T), T) = -\left(\frac{\partial F}{\partial T}\right)_V = \sum_j \left[-k_B \ln(1 - e^{-\omega_j/k_B T}) + \frac{\omega_j}{T} \frac{1}{e^{\omega_j/k_B T} - 1} \right], \quad (15)$$

$$U = U(V(p, T), T) = F + TS = E_{\text{sta}} + \sum_j \frac{\omega_j}{2} + \sum_j \frac{\omega_j}{e^{-\omega_j/k_B T} - 1}, \quad (16)$$

$$G = U + pV - TS, \quad (17)$$

$$C_V = C_V(V(p, T), T) = \left(\frac{\partial U}{\partial T}\right)_V = \sum_j C_{v,j} = \sum_j k_B \left(\frac{\omega_j}{k_B T}\right)^2 \frac{e^{-\omega_j/k_B T}}{(e^{-\omega_j/k_B T} - 1)^2}, \quad (18)$$

$$B_T = -V \left(\frac{\partial p}{\partial V}\right)_T = V \left(\frac{\partial^2 F}{\partial V^2}\right)_T. \quad (19)$$

A second set of properties depend on the thermodynamic Grüneisen ratio:

$$\gamma_{\text{th}} = \frac{\alpha B_T V}{C_V}, \quad (20)$$

where α is the volumetric thermal expansion coefficient. In the quasiharmonic approximation, it can be computed using:

$$\gamma_{\text{qha}} = \frac{\sum_j \gamma_j C_{v,j}}{C_V}. \quad (21)$$

However, as in the calculation of p_{th} , it is preferable to avoid the computation of mode gammas. In this case, we use the thermodynamic relation:

$$\alpha B_T = \left(\frac{\partial S}{\partial V}\right)_T = \left(\frac{\partial p}{\partial T}\right)_V, \quad (22)$$

so we can use the volume derivative of $-TS$ to compute γ_{th} :

$$\gamma_{\text{th}} = -\frac{V}{C_V T} \left(\frac{\partial(-TS)}{\partial V}\right)_T. \quad (23)$$

Once the Grüneisen ratio is known, the thermal expansion coefficient, constant-heat capacity (C_p) and adiabatic bulk modulus (B_S) follow:

$$\alpha = -\frac{1}{V} \left(\frac{\partial V}{\partial T}\right)_p = \frac{\gamma_{\text{th}} C_V}{V B_T}, \quad (24)$$

$$C_p = \left(\frac{\partial H}{\partial T}\right)_p = C_V (1 + \gamma_{\text{th}} \alpha T), \quad (25)$$

$$B_S = -V \left(\frac{\partial p}{\partial V}\right)_S = V \left(\frac{\partial^2 U}{\partial V^2}\right)_S = B_T (1 + \gamma_{\text{th}} \alpha T). \quad (26)$$

We mention two technical issues regarding the use of the above formulas. First, the calculation of thermodynamic properties at $V(p, T)$ requires $g(\omega; V(p, T))$ or $\omega_j(V(p, T))$, that must be interpolated from the $g(\omega; V)$ or $\omega_j(V)$, known only on the volume grid. `GIBBS2`

implements two strategies for the interpolation: linear and cubic splines. For the cases we explored, the results are not significantly affected by this choice.

Second, the calculation of γ_{th} at very low temperatures is tricky. If Eq. (23) is used, γ_{th} is calculated using a fit to entropy values that approach zero when $T \rightarrow 0$, for any volume. If Eq. (21) is used instead, the quotient is dominated by the lowest frequency modes, i.e. the acoustic branch at gamma that, again, cannot be calculated by fitting. The practical solution implemented in GIBBS2 involves extrapolating the results at very low but not zero temperatures.

3.3. The Debye–Slater model

Even with its intrinsic limitations, the QHA has recently achieved a great deal of success in the prediction of equations of state and thermodynamic properties. However, in spite of the mentioned advances, computing the full vibrational spectra of a crystal on a grid of volumes is still a complex and computationally expensive task. For this reason, simplified models for $g(\omega; V)$ are useful, as they can serve as tools for rapid exploration of the thermal properties of a solid.

A simple and popular [22–24] model of the crystal vibrations dates back to the original work by P. Debye in 1912 [25]. The model correctly describes the low and high temperature limits of the constant volume heat capacity. The basis for the model is the observation that, at low temperatures, only low frequency (long wavelength) modes contribute to the heat capacity. These wavelengths are large compared to interatomic spacings, so they see the solid as a continuum, with two transversal and one longitudinal direction dependent sound velocities. The phonon density of states approximated by the Debye model is built by treating all phonons as stationary waves in a unstructured solid, and reads:

$$g_{\text{Debye}}(\omega) = \begin{cases} \frac{9n\omega^2}{\omega_D^3} & \text{if } \omega < \omega_D, \\ 0 & \text{if } \omega \geq \omega_D, \end{cases} \quad (27)$$

where ω_D is the Debye frequency, directly related to the Debye temperature:

$$\Theta_D = \frac{\omega_D}{k_B} = \frac{1}{k_B} \left(\frac{6\pi^2 n}{V} \right)^{1/3} v_0. \quad (28)$$

In the quasiharmonic Debye model, Θ_D is a function of volume, and the Grüneisen ratio is:

$$\gamma_D = - \frac{\partial \ln \Theta_D}{\partial \ln V}. \quad (29)$$

Inserting g_{Debye} into the quasiharmonic formulas yields:

$$F = E_{\text{sta}} + \frac{9}{8}nk_B\Theta_D + 3nk_B T \ln(1 - e^{-\Theta_D/T}) - nk_B T D(\Theta_D/T), \quad (30)$$

$$S = -3nk_B \ln(1 - e^{-\Theta_D/T}) + 4nk_B D(\Theta_D/T), \quad (31)$$

$$U = E_{\text{sta}} + \frac{9}{8}nk_B\Theta_D + 3nk_B T D(\Theta_D/T), \quad (32)$$

$$C_v = 12nk_B D(\Theta_D/T) - \frac{9nk_B\Theta_D/T}{e^{\Theta_D/T} - 1}, \quad (33)$$

$$p_{\text{th}} = \frac{\gamma_D}{V} \left[\frac{9}{8}nk_B\Theta_D + 3nk_B T D\left(\frac{\Theta_D}{T}\right) \right] = \frac{\gamma_D U_{\text{vib}}}{V}, \quad (34)$$

where D is the Debye integral:

$$D(x) = \frac{3}{x^3} \int_0^x \frac{y^3 e^{-y}}{1 - e^{-y}} dy \quad (35)$$

and $U_{\text{vib}} = U - E_{\text{sta}}$ is the vibrational free energy. Incidentally, Eq. (34) is known as the Mie–Grüneisen equation of state, valid for models where all mode gammas are assigned the same value. In the case of the Debye model, $\gamma_j = \gamma_D$ for all j .

There are a number of ways of calculating the $\Theta_D(V)$ function. Ideally, one would obtain it from the average velocities $v_0(V)$, which in turn can be computed from the transversal and longitudinal velocities using:

$$\frac{3}{v_0^3} = \frac{1}{4\pi} \int d\Omega \left(\frac{2}{v_t^3(\Omega)} + \frac{1}{v_l^3(\Omega)} \right). \quad (36)$$

However, obtaining the sound velocities requires the calculation of the elastic constants at every volume of the grid, defeating the simplicity purpose of the approximate model.

A reasonable approximation to $\Theta_D(V)$ was originally proposed by Slater [26], implemented in the original GIBBS program [11], and explored in M.A. Blanco’s PhD thesis [12]. The Debye temperature is calculated assuming an isotropic solid and $B_S \approx B_{\text{sta}}$:

$$\Theta_D = \frac{1}{k_B} (6\pi^2 V^{1/2} n)^{1/3} f(\sigma) \sqrt{\frac{B_{\text{sta}}}{M}}, \quad (37)$$

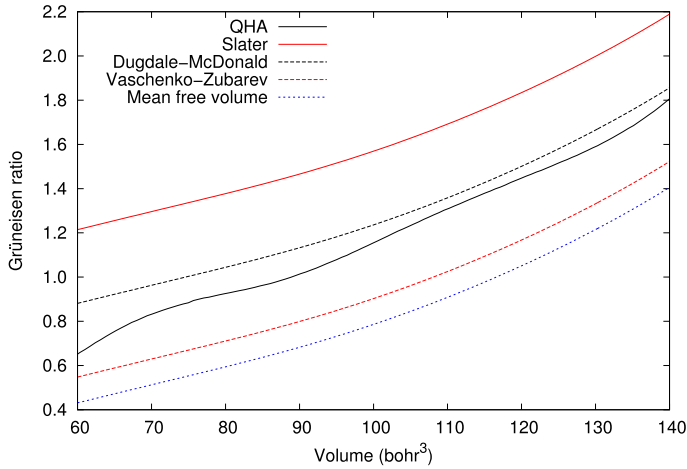


Fig. 2. Different approximations to the Grüneisen ratio are represented against cell volume for magnesium oxide. The curve labeled QHA corresponds to a full quasiharmonic calculation.

where M is the molecular mass per primitive cell, and B_{sta} and σ are the static bulk modulus and Poisson ratio at the equilibrium geometry. The $f(\sigma)$ function is:

$$f(\sigma) = \left\{ 3 \left[2 \left(\frac{2}{3} \frac{(1+\sigma)}{(1-2\sigma)} \right)^{3/2} + \left(\frac{1}{3} \frac{(1+\sigma)}{(1-\sigma)} \right)^{3/2} \right]^{-1} \right\}^{1/3} \quad (38)$$

In Fig. 1, the approximated $g(\omega)$ of the Debye–Slater model are represented along with the calculated phDOS at the experimental volume. For the crudeness of the model, the extent and steepness of the parabola being determined solely using the static energy, the match is quite remarkable. Indeed, as we will see below, the leading error in this model is not in the approximated $g(\omega)$ but in the treatment of the quasiharmonicity.

The Poisson ratio can be calculated *ab initio* or taken as experimental input. A reasonable approximation, and the default value in GIBBS2 is $\sigma = 1/4$, corresponding to a Cauchy solid.

Using Eq. (37) leads to a Grüneisen ratio:

$$\gamma_{th} = \gamma_S = -\frac{1}{6} + \frac{1}{2} \frac{dB_{sta}}{dp}, \quad (39)$$

where B_{sta} is the static bulk modulus. This expression is known in the literature as the Slater gamma [27,28].

3.4. The Debye–Grüneisen model

Fig. 2 shows the Grüneisen ratio in the Slater approximation, calculated using the full QHA and the experimental result. Even for a system as simple as MgO, γ_S differs from the experimental or from the reference QHA result by a non-negligible factor. The cause of this discrepancy was pointed out by Slater [26]: in Eq. (29), the Poisson ratio is assumed to be invariant with volume. Therefore, quasiharmonicity is not properly introduced in the Debye–Slater model.

In the Debye–Grüneisen model [29], $\Theta_D(V)$ is calculated at the static equilibrium volume V_0 using Eq. (29). Then, an approximate Grüneisen ratio is chosen to be of the form:

$$\gamma = a + b \frac{dB_{sta}}{dp} = a - b \frac{d \ln B_{sta}}{d \ln V}, \quad (40)$$

that is consistent with some approximate γ_{th} proposed in the literature [27,28], including the expressions by Dugdale–McDonald ($a = -1/2$, $b = 1/2$), Vaschenko–Zubarev ($a = -5/6$, $b = 1/2$), and the mean free volume gamma ($a = -0.95$, $b = 1/2$). The Slater gamma is also represented by Eq. (40) with $a = -1/6$ and $b = 1/2$.

It is easy to prove that, assuming a γ_{th} of the form above is equivalent to setting the volume variation of the Debye temperature to:

$$\Theta_D(V) = \Theta_D(V_0) \frac{(B_{sta}/B_0)^b}{(V/V_0)^a}, \quad (41)$$

where V_0 and B_0 are the static equilibrium volume and bulk modulus respectively. Therefore, by using Eq. (41) to calculate $\Theta_D(V)$ at arbitrary volumes introduces a new volume dependence of the Poisson ratio, fixing to some extent the problems in the treatment of the quasiharmonicity.

Indeed, Fig. 2 shows that approximate γ_{th} improve the agreement with the QHA result with respect to γ_S . It is important to note that the amount of theoretical data required is the same as in the Debye–Slater model: the static $E(V)$ and possibly the Poisson ratio at the equilibrium geometry.

3.5. The Debye–Einstein model

The shortcomings of the Debye model are apparent in molecular and loosely packed systems. In these solids, there is a large number of optic branches, that are incorrectly treated as acoustic in the Debye model. Therefore, it comes as no surprise that mixed acoustic/optic approximations to $g(\omega)$ are very popular within the mineralogist community [30,31]. The simplest approach, implemented in GIBBS2, consists of using single frequencies to represent each of the $3n - 3$ optic branches [31], and renormalizing the Debye temperature to the 3 acoustic branches:

$$g_{DE}(\omega) = \begin{cases} \frac{9n\omega^2}{\omega_{DE}^3} & \text{if } \omega < \omega_{DE}, \\ \sum_{j=1}^{3n-3} \delta(\omega - \omega_j) & \text{if } \omega \geq \omega_{DE}, \end{cases} \quad (42)$$

where the normalization condition (Eq. (12)) yields a Debye–Einstein characteristic temperature (Θ_{DE}) related to the plain Debye model (Θ_D) by:

$$\Theta_{DE} = \frac{\Theta_D}{n^{1/3}} = \frac{6\pi^2}{V} v_0. \quad (43)$$

In GIBBS2, Θ_D is calculated as in the Debye–Slater model, resulting in a new Debye temperature that is correctly independent of the number of atoms in the cell.

Using Eq. (42) in the QHA expressions yields thermodynamic properties that average acoustic and optic terms:

$$F = E_{sta} + \underbrace{\frac{9}{8}k_B\Theta_{DE} + 3nk_B T \ln(1 - e^{-\Theta_{DE}/T}) - nk_B T D(\Theta_{DE}/T)}_{F_{ac}} + \underbrace{\sum_{j=1}^{3n-3} \frac{\omega_j}{2} + k_B T \ln(1 - e^{-\omega_j/k_B T})}_{F_{op}}, \quad (44)$$

$$S = \underbrace{-3nk_B \ln(1 - e^{-\Theta_{DE}/T}) + 4nk_B D(\Theta_{DE}/T)}_{S_{ac}} + \underbrace{\sum_{j=1}^{3n-3} -k_B \ln(1 - e^{-x_j}) - \frac{\omega_j}{T} \frac{1}{e^{x_j} - 1}}_{S_{op}}, \quad (45)$$

$$U = E_{sta} + k_B T \underbrace{\left[\frac{9}{8}x_{DE} + D(x_{DE}) \right]}_{U_{ac}} + k_B T \underbrace{\sum_{j=1}^{3n-3} \left[\frac{x_j}{2} + \frac{x_j}{1 - e^{-x_j}} \right]}_{U_{op}}, \quad (46)$$

$$C_v = \underbrace{12nk_B D(\Theta_{DE}/T) - \frac{9nk_B \Theta_{DE}/T}{e^{\Theta_{DE}/T} - 1}}_{C_{v,ac}} + \underbrace{nk_B \sum_{j=1}^{3n-3} \frac{(\omega_j/T)^2 e^{\omega_j/T}}{(e^{\omega_j/T} - 1)^2}}_{C_{v,op}}. \quad (47)$$

The Grüneisen ratio is calculated as:

$$\gamma_{th} = \frac{\gamma_S C_{v,ac} + \gamma_{op} C_{v,op}}{C_v}, \quad (48)$$

$$\gamma_{op} = \frac{9B_{sta}(dB_{sta}/dp - 1) + 2p_{sta}}{6(3B_{sta} - 2p_{sta})}, \quad (49)$$

and the thermal pressure is:

$$p_{th} = \underbrace{\frac{\gamma_S}{V} \left[\frac{9}{8}nk_B \Theta_{DE} + 3nk_B T D(\Theta_D/T) \right]}_{p_{ac}} + \underbrace{\frac{\gamma_{op}}{V} \sum_{j=1}^{3n-3} \left(\frac{\omega_j}{2} + \frac{\omega_j}{e^{\omega_j/k_B T} - 1} \right)}_{p_{op}} \\ = \frac{U_{ac}\gamma_S}{V} + \frac{U_{op}\gamma_{op}}{V}. \quad (50)$$

The implementation in GIBBS2 follows that of Fleche [31], where the frequencies at the Γ point calculated, $\omega_i(\Gamma)$ are used as representatives of the whole branch. The input required is further reduced by using only the $\omega_i(\Gamma)$ calculated at the static equilibrium structure and setting the volume evolution of these frequencies to:

$$\omega_i(\Gamma) = \omega_i^0(\Gamma) \left(\frac{V}{V_0} \right)^{1/6} \left(\frac{B_{sta}}{B_0} \right)^{1/2} \left(1 - \frac{2}{3} \frac{p_{sta}}{B_{sta}} \right)^{1/2}, \quad (51)$$

where $\omega_i^0(\Gamma)$ are the frequencies at Γ corresponding to the equilibrium, p_{sta} and B_{sta} are the static pressure and bulk modulus and V_0 and B_0 are the static equilibrium volume and bulk modulus.

To summarize this section, we have added to the GIBBS2 code the possibility of using four models. In increasing order of complexity and accuracy: Debye–Slater, Debye–Grüneisen, Debye–Einstein and the full QHA.

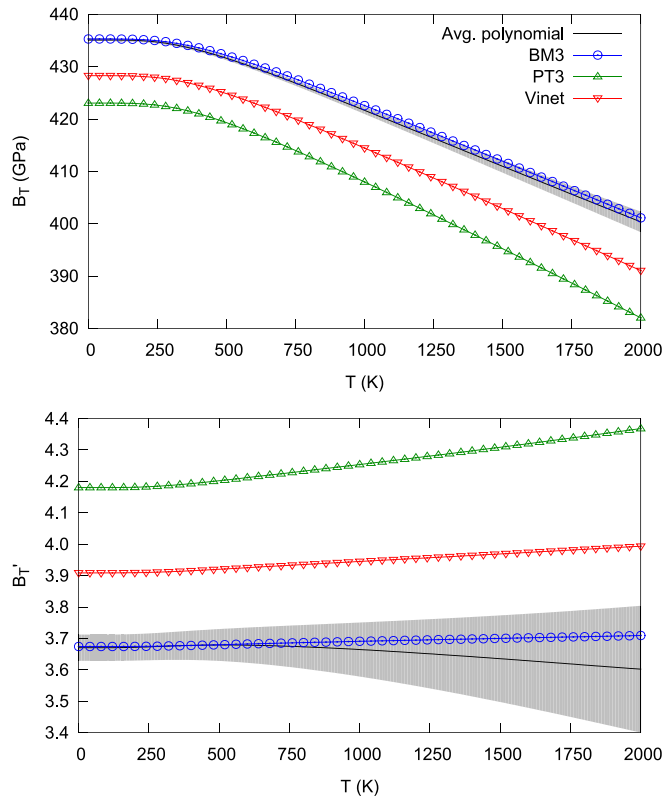


Fig. 3. Isothermal bulk modulus (top) and its pressure derivative (bottom) for diamond, calculated using different equations of state. The shaded area represents the error bar calculated for the average polynomial.

4. Energy fitting

In the previous article [13], we exhaustively explored how different equations of state yield diverging properties when fitted to the same static $E(V)$ dataset. We discussed how an average of strain polynomials can not only render more accurate equilibrium volume, bulk modulus, ... but also offer an insight into the quality of the fit. As an additional benefit, the process of polynomial averaging allows the calculation of error bars for the properties, that are sensitive to the quality of the input data.

The same fitting techniques and EOS expressions as in the ASTURFIT package [13] have been implemented in GIBBS2, including a number of traditional EOS as well as strain polynomials and their averages. The former are fitted using a non-linear minimization algorithm, while for the latter we use the robust linear polynomial fitting methods. Namely, the common EOS subject to non-linear fit in GIBBS2 are:

- (1) Birch–Murnaghan (BM) family: non-linear fits up to fourth order.
- (2) Poirier–Tarantola (PT) family: non-linear fits up to fifth order.
- (3) Murnaghan EOS.
- (4) Anton–Schmidt EOS.
- (5) Vinet EOS.
- (6) Holzapfel's AP2 EOS.

The BM and PT families can be fit as polynomials to arbitrary order using the Eulerian and natural strains respectively. Additional strain choices are: Lagrangian, infinitesimal, V/V_0 , $(V/V_0)^{1/3}$ and the simple volume strain (V).

The implementation in GIBBS2 extends the results of Ref. [13], to the fitting of $F^*(V; T)$ and $-TS(V; T)$ at any given temperature T . Applying the same statistical methods, it is possible to compute error bars to the calculated thermodynamic properties.

A sample of the diverging results obtained by using different equations of state in diamond is shown in Fig. 3. The third-order Poirier–Tarantola and Vinet EOS, which are routinely used in the literature, diverge from the polynomial average result by several times the calculated error bar. For instance, the isothermal bulk modulus predicted by the popular Vinet EOS is off the average polynomial result by 6.78 GPa, a non-negligible amount. The third-order Birch–Murnaghan result is within the error bar limits, but experience with other systems suggests that the good behavior of this particular EOS is accidental. It was already discussed in Ref. [13] that the precision of the calculated properties degrades when these depend on higher-order derivatives of the energy. Fig. 3 shows a similar trend, even when thermal effects are incorporated. The error bars are comparatively much larger for B_T' than for B_T .

5. Additional capabilities of GIBBS2

5.1. Empirical energy corrections

The accuracy of the thermodynamic properties calculated by GIBBS2 is determined by the quality of the underlying energy and vibrational data. In most cases, these data are obtained as a result of a DFT calculation, and the main source of uncertainty is invariably the exchange–correlation functional.

The errors introduced by the functional are systematic, and well studied in the literature. For instance, the accuracy of the calculated thermodynamic properties is greatly improved if a correction is applied to shift the static $E(V)$ curve in a way that the model reproduces the experimental volume and, optionally, the bulk modulus at ambient conditions. We have called empirical energy corrections (EEC) to such energy scalings, and will be explained in detail elsewhere.

Three different corrections to the static energy implemented in GIBBS2:

(1) The PSHIFT EEC:

$$\tilde{E}_{\text{sta}}(V) = E_{\text{sta}}(V) + \Delta pV. \quad (52)$$

(2) The APBAF EEC:

$$\tilde{E}_{\text{sta}}(V) = E_{\text{sta}}(V) + \frac{\alpha}{V}. \quad (53)$$

(3) The BPSCAL EEC:

$$\tilde{E}_{\text{sta}}(V) = E_{\text{sta}}(V_0) + \frac{B_{\text{exp}}V_{\text{exp}}}{B_0V_0} \left[E_{\text{sta}}\left(V \frac{V_0}{V_{\text{exp}}}\right) - E_{\text{sta}}(V_0) \right]. \quad (54)$$

The value of the free parameters Δp , α , V_{exp} and B_{exp} in the three EECs above are chosen so that the experimental room temperature equilibrium volume is reproduced and, in the case of BPSCAL, also the experimental bulk modulus.

Fig. 4 illustrates the systematic trends caused by the choice of the exchange–correlation functional. It is well known that solids calculated using LDA tend to be overbound: volumes are too small and bulk moduli too large. Contrarily, PBE tends to underbind. This very effect is displayed in the above figure for magnesium oxide. Using the BPSCAL correction, volumes and bulk moduli are brought to a far better agreement with experimental results than the bare DFT results. In addition, the limit of validity of the harmonic approximation, that breaks down at high temperature, is pushed to higher temperatures, especially for the PBE functional.

5.2. Electronic contributions to the free energy

Apart from the vibrational, some solids possess additional degrees of freedom that contribute to the free energy. For instance, in a metal, electrons are free to traverse the solid because the band structure contains electronic levels at energies arbitrarily close to the Fermi level. There is an electronic contribution F_{el}^* to the F^* that is usually small compared to F_{vib}^* , except at very low temperatures.

The electronic contribution has been implemented in GIBBS2 in three ways:

- (1) The Sommerfeld model of free and independent electrons.
- (2) The Sommerfeld model, but the density of states at the Fermi level is obtained from a first principles calculation.
- (3) The user supplies polynomial fits to $F_{\text{el}}^*(T)$ and $-TS_{\text{el}}(T)$, calculated using the finite-temperature DFT formalism [39].

The expressions for the free energy and entropy for a free electron model are:

$$S_{\text{el}} = C_{v,\text{el}} = \frac{\pi^2}{3} N(\varepsilon_F) k_B^2 T, \quad (55)$$

$$F_{\text{el}} = -U_{\text{el}} = \frac{TS_{\text{el}}}{2}, \quad (56)$$

where $N(\varepsilon_F)$ is the density of states at the Fermi level, that in the Sommerfeld model reads:

$$N(\varepsilon_F) = \frac{3}{2} \frac{n_{\text{elec}}}{\varepsilon_F}, \quad (57)$$

with n_{elec} the number of valence electrons.

Fig. 5 represents the electronic contributions to the entropy and free energy versus volume. The results of the first principles calculation agree very well with the free electron model, consistent with the fact that elemental fcc aluminum is a characteristic free-electron-like metal. Also, the free energy and entropy contributions are 3–4 orders of magnitude smaller than the vibrational terms, and they do not modify in an appreciable way the calculated thermodynamic properties. Because of the exceedingly small value of the electronic energy compared to the static energy, a certain degree of noise when information from the *ab initio* calculation is obtained, even when a very fine \mathbf{k} -point mesh is used. In Fig. 5, for instance, a $52 \times 52 \times 52$ Monkhorst–Pack grid was used.

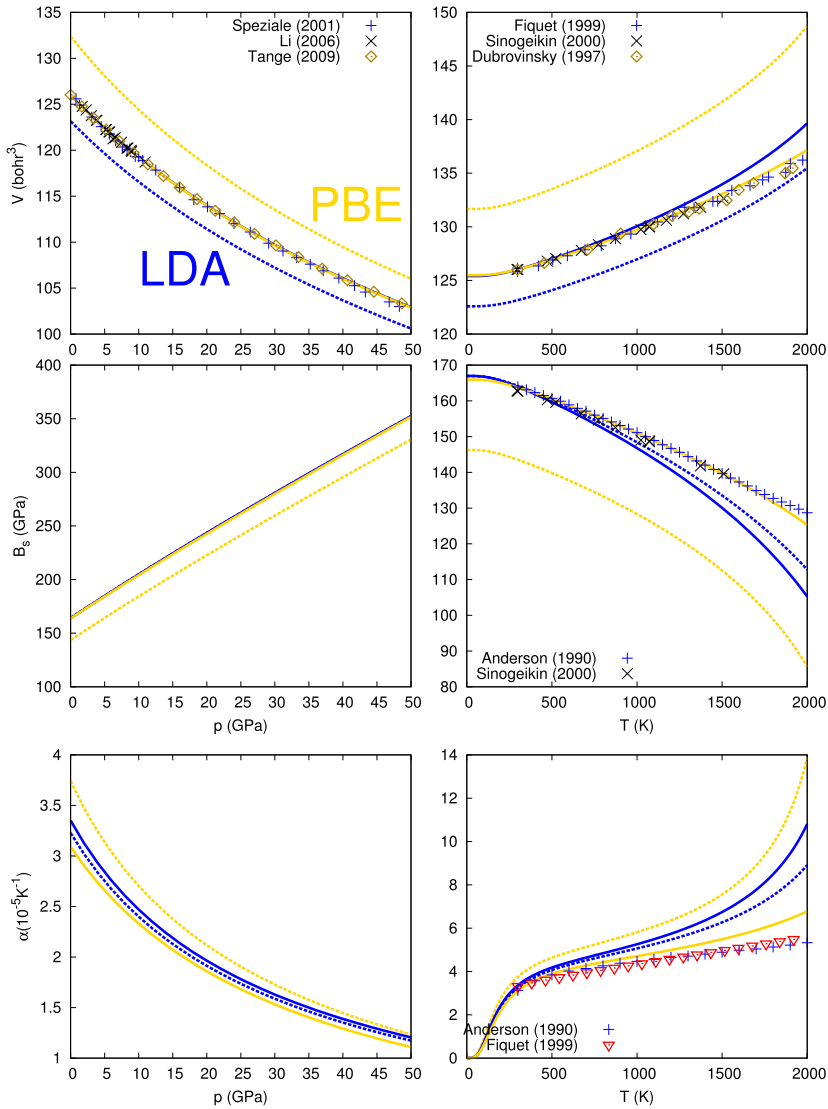


Fig. 4. Calculated pressure and temperature dependence of the volume (top), adiabatic bulk modulus (middle) and thermal expansion coefficient (bottom) of the B1 phase of MgO, compared to experimental data. Dotted lines represent uncorrected results for the LDA (blue) and PBE (gold) exchange correlation functionals. BRSCAT-corrected results are shown as full lines. The experimental data correspond to Refs. [32–38] and are labeled using the first author and the year. (For interpretation of the references to color in this figure legend, the reader is referred to the web version of this article.)

5.3. Automatic computation of phase diagrams

Different phases of a solid correspond to different local minima and attraction basins of the potential energy surface. A corollary of the principle stated in Eq. (2) is that, given a pressure and a temperature, the thermodynamically stable phase is that with lowest $G(p, T)$.

In the original GIBBS program, only one $E(V)$ curve and, therefore, only one phase could be treated in a single run. GIBBS2 has been generalized to introduce the possibility of computing the $G(p, T)$ of different phases and detecting the most stable. In addition, transition pressures at any temperature, phase transition volume and G changes and phase diagrams are automatically computed in a simple and straightforward way.

6. The GIBBS2 distribution

6.1. Structure of the source code

GIBBS2 is written in Fortran90. The driver routine is the `gibbs2.f90` file, which accesses functions and subroutines contained in ancillary modules (described below). The source code is contained in the `src/` directory of the GIBBS2 distribution. The sequence of tasks

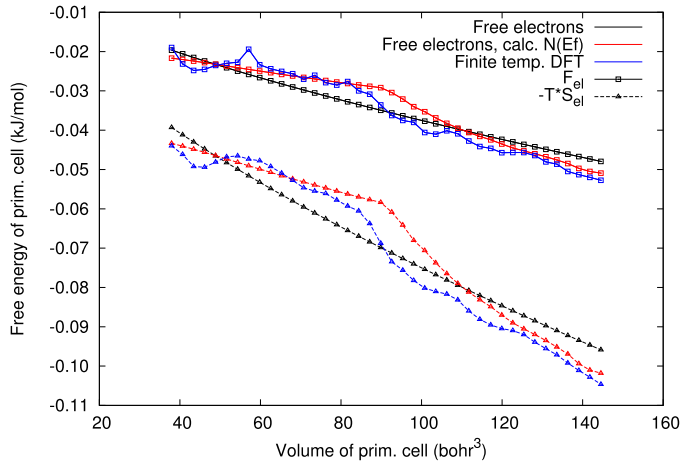


Fig. 5. Electronic Helmholtz free energy and $-TS_{el}$ is represented against cell volume for fcc Al at room temperature. Note the energy scale is in kJ/mol.

in the main routine are:

- (1) Read and parse the input file and any auxiliary file. GIBBS2 accepts a single input file, typically with extension `ing`. The input file contains the source $E(V)$ and vibrational data (or a pointer to the files where it can be found), the pressure and temperature list where the properties are calculated and, optionally, keywords controlling the kind of calculation to be run.
- (2) Once the reading is finished, the information of each phase is initialized: input units are converted to atomic units, phonon DOS or frequencies are renormalized, ...
- (3) The empirical energy corrections are applied, if requested.
- (4) The static energy is fitted against the volume, and a detailed account of the static equation of state and the static equilibrium properties is reported.
- (5) If more than one phase is defined in input, the static transition pressures are calculated.
- (6) Once the static computation is finished, the program checks whether any of the phases has an associated thermal model. If they do, then GIBBS2 runs over the temperature-pressure pair list defined by the user, computing the thermodynamic properties at each pair.
- (7) Finally, transition pressures at the input temperatures are calculated and reported.

A description of the modules used by `gibbs2.f90` follows. The list is ordered, with the most basic modules first:

param.f90 Contains mathematical and physical constants, enumerates and basic variables and subroutines.

tools.f90 Self-contained subroutines and functions that perform well-defined tasks: input/output, timer, error signaling, string manipulation, memory management, sorting, and mathematical operations.

evfunc.f90 Definitions of the strains and equations of state. The main functions of this module are the `fvn` that, given the information of a fit and a volume calculate the n th derivative of the energy.

fit.f90 Routines for the fitting of energy versus volume curves, possibly with a shifting constant pressure.

varbas.f90 Basic thermodynamic subroutines and variables. The large `phase` user-defined type, containing the description of a phase, is defined here. Provides subroutines for reading and parsing external files and for phase initialization.

gnuplot_templates.f90 A small module defining subroutines for the generation of gnuplot files.

eos.f90 A module containing a single driver routine for static energy fits.

debye.f90 Calculation of thermodynamic properties at a given temperature, for all the defined thermal models.

topcalc.f90 Highest level routines, called directly by the main program.

setvariables.f90 A single subroutine that manipulates GIBBS2 SET options according to the user's input.

In addition, parts of external libraries (obtained from www.netlib.org) have been included, namely:

- The routine `dgam.f` for the computation of the incomplete Gamma function (used in the AP2 equation of state).
- The spline library `pppack`.
- Part of the `minpack` library for the non-linear minimization of functions using a Levenberg–Marquardt algorithm.
- The `slatec` library for the polynomial fits.

6.2. Documentation and tests

The GIBBS2 distribution comes with full documentation and tests. The user's guide can be found in the `doc/` subdirectory, either in plain text, or a compiled pdf file. The tests are located in the `tests/` directory. There are 6 tests that try to extensively display the features of `gibbs2`. These tests access first principles data for the same test cases used in this article: magnesium oxide (phases B1 and B2), fcc aluminum and diamond; calculated using LDA and PBE, under the conditions described in Section 2.

6.3. Installation

To compile GIBBS2, simply enter the `src/` directory and modify the `Makefile.inc` file to point to a Fortran90 compiler (the default compiler is `gfortran`). Then, a `make` command builds the program, that can be linked to the user's `bin/`.

7. Test case

7.1. Sample input

A simple input that compares the results of several thermal models in MgO follows. Each thermal model corresponds to one phase, so transition pressures between phases are not computed (`set notrans` option). The number of atoms per primitive cell (2) and the mass of the cell in atomic mass units (40.3044) are needed for the Debye-like models. The pressure/temperature list contains pressures from 0 up to 250 GPa, in steps of 1 GPa, at room temperature (−1). Each thermal model uses the same static $E(V)$ data source, in the file `mgo.res`. The calculated three non-zero equilibrium geometry frequencies at Γ are indicated for the Debye–Einstein model.

```
# MgO
set notrans
mm 40.3044
vfree 2
pressure 0 1 250
temperature -1

phase debye file ../dat/mgo_pbe/mgo.res tmodel debye \
    units energy ry freq cm-1 \
    prefix ../dat/mgo_pbe/
phase debgrun file ../dat/mgo_pbe/mgo.res tmodel debye_gruneisen dm \
    units energy ry freq cm-1 \
    prefix ../dat/mgo_pbe/
phase debeins file ../dat/mgo_pbe/mgo.res tmodel debye_einstein \
    units energy ry freq cm-1 \
    prefix ../dat/mgo_pbe/

freqg0 debeins
402.9580 402.9580 701.1656
endfreqg0
phase qha file ../dat/mgo_pbe/mgo.res tmodel qha \
    units energy ry freq cm-1 \
    prefix ../dat/mgo_pbe/

end
```

The input is saved to `test.ing` and run using:

```
gibbs2 test.ing test.out
```

The execution time is less than 6 seconds.

7.2. Sample output

The file `test.out` is the main output of GIBBS2. A summarized version follows. Ellipsis are denoted by the `[...]` symbols.

GIBBS2: (p,t) thermodynamics of solids.

```
A. Otero-de-la-Roza, V. Lua-na and D. Abbasi.
See doc/gibbs2.txt for details on the proper citation of \
this software.
```

* Input

```
Title:
Output file (lu= 2): stdout
Units: output is in atomic units, except where noted.
Number of atoms per primitive cell: 2
Molecular mass (amu): 40.30440000
Infinite V energy (hy): 0.000000000000E+00
Number of phases: 4
Phase 1: debye
Phase 2: debgrun
Phase 3: debeins
Phase 4: qha
```

```

Polynomial fit mode: slatec
Polynomial weight mode: gibbs2
Max. polynomial degree: 12

COMMENT(phase_checkconvex): Found 4 inflection points in (E,V) \
of phase debye
Near (E,V) point number ** : 153.0874653
Near (E,V) point number ** : 153.7787188
Near (E,V) point number ** : 154.4699723
Near (E,V) point number ** : 155.1612257
[...]
* Pressure range examined
Min_phases{p_max} (GPa): 1801.897
Pressure range (GPa): 0.000 -> 250.000
Number of p points: 251

* Phase information after initial setup
+ Phase 1 (debye)
Number of volume points: 174
Number of vfree units (Z): 1.000
p(V) input data? F
Pressure range (GPa): -20.406 -> 1801.897
Number of interpolated fields : 0
Input units:
  Volume : bohr^3
  Energy : Ry
  Pressure : GPa
  Frequency : cm^(-1)
  DOS energy : Hartree
Output units are atomic units (Hy), except where noted.
First/last volume (bohr^3): \
  4.000000000000E+01 1.600000000000E+02
First/last energy (Hy): \
  -7.256282263500E+01 -7.362748155500E+01
Poisson ratio (sigma): 0.250000
Poisson function, f(sigma): 0.859949
Correction of static energy: no correction
Energy fit mode: 130100
S(V) fit mode: 130100
ThetaD(V) fit mode: 130100
omega(V) fit mode: 130506
Number of fixed fit parameters: 0
Static equilibrium volume (bohr^3): 130.0791903025
Static equilibrium energy (Hy): -73.6398334037
Static equilibrium energy (kJ/mol): -193341.3531454799
Static bulk modulus (GPa): 150.495329
Static EOS fit, error RMS (Hy): 4.9714060E-06
Static EOS fit, max|error| (Hy): 1.2153275E-05
r2 of the fit: 9.99999306879E-01
Akaike information criterion: -3.324033510862E+03
Bayesian information (Schwarz) criterion: -3.279806736673E+03
Temperature model: Debye, Td from static B(V).
All data points are ACTIVE for dynamic calculations
WARNING(phase_popinfo): Max. pressure ( 1801.897) exceeds 500.000

Fit to static E(V) data:
# Copy in file : test.eos_static
# Lines beginning with 'e' contain fit error estimation.
# p(GPa) E (Hy) V(bohr^3) V/V0 \
  p_fit(GPa) B(GPa) Bp Bpp(GPa-1)
0.0000 -7.363983340E+01 130.0792 1.0000000 \
  0.0000 150.4953 4.1284098 -2.6643E-02
e 0.0000 6.942853822E-06 0.0050 0.0000383 \
  0.0000 0.2632 0.0091035 2.2082E-03
[...]
249.0000 -7.285510749E+01 75.5707 0.5809595 \

```

```

      249.0000   962.7513   2.9588830  -1.2099E-03
e   249.0000   1.907348633E-06   0.0017   0.0000129 \
      0.0000   0.1030   0.0027031   2.0426E-05
      250.0000  -7.285254022E+01   75.4924   0.5803573 \
      250.0000   965.7095   2.9576756  -1.2049E-03
e   250.0000   1.907348633E-06   0.0017   0.0000129 \
      0.0000   0.1037   0.0026941   2.0693E-05
# Polynomial fit to strain:
# Degree : 12
# p(x) = a_0 + a_1 * f(V) + ... + a_n * f(V)^n
# a_00 = -7.363982856743E+01
# a_01 =  7.631351488211E-03
# a_02 =  3.010947421871E+00
# a_03 =  3.875836351843E-01
# a_04 =  6.716613773129E-03
# a_05 = -7.466501037307E+00
# a_06 =  3.413490981977E+01
# a_07 = -6.053735322551E+01
# a_08 = -6.024159002718E+01
# a_09 =  4.906434420653E+02
# a_10 = -9.524557855687E+02
# a_11 =  8.498976616667E+02
# a_12 = -2.994128654586E+02
# V_scal (bohr^3) =  1.295848475056E+02
# p_scal (GPa) =      0.000000000000

# Composition of the average polynomial and equilibrium static properties:
# n      weight   V(bohr^3)      E(Hy)      B(GPa)   \
      Bp      Bpp(GPa-1)
   2     0.0000000   130.7640  -7.363998E+01  149.6773 \
      4.0000000   -2.5982E-02
[...]
  12     0.1192278   130.0865  -7.363983E+01  150.1951 \
      4.1237206   -2.3010E-02
--average pol.--   130.0792  -7.363983E+01  150.4953 \
      4.1284098   -2.6643E-02
--dir. average--   130.0792  -7.363983E+01  150.4953 \
      4.1284076   -2.6636E-02
---std. dev.---    0.0050    6.942854E-06    0.2632 \
      0.0091035   2.2082E-03

+ Phase 2 (debgrun)
[...]
+ Phase 3 (debeins)
[...]
+ Phase 4 (qha)
[...]

* Input and fitted static energy
Writing file : test.efit

Writing file : test_efit.aux

Writing file : test_efit.gnu

* Plotting static DeltaH

Writing file : test_dH.aux

Writing file : test_dH.gnu

* Computed Debye temperatures from static data
+ Phase debye
# ThetaD at static eq. volume:      792.05
# V(bohr^3)  Tdebye(K)  Tdebye_slater(K)
   40.0000   3810.55   3810.55

```



```
[...]
 159.3087    512.28    512.28
 160.0000    506.81    506.81
[...]
```

* Temperature range examined
 Min_{DebyeT} (K): 198.767
 Temperature range (K): 298.150 -> 298.150
 Number of T points: 1

* Calculated temperature effects
 Writing file : test.eos

+ Phase debye
 + Phase debgrun
 + Phase debeins
 + Phase qha

Writing file: test_all_p.gnu

GIBBS2 ended successfully (5 WARNINGS, 4 COMMENTS)

Acknowledgements

The development of this code has been done under financial support from the Spanish Ministerio de Ciencia y Tecnología and the ERDF of the European Union (project No. CTQ2006-02976). A.O.R. is indebted to the Spanish Ministerio de Educación for a FPU grant. D.A. acknowledges financial support by the Spanish government under project No. MAT2006-13548-C02-02. The authors belong to the MALTA group (CSD2007-0045 project, MEC Consolider Ingenio 2010 program).

References

- [1] R.M. Wentzcovitch, Y.G. Yu, Z. Wu, Thermodynamic properties and phase relations in mantle minerals investigated by first principles quasiharmonic theory, in: *Theoretical and Computational Methods in Mineral Physics: Geophysical Applications*, in: *Reviews in Mineralogy & Geochemistry*, vol. 71, Mineral. Soc. Amer., Chantilly, VA, 2010, pp. 59–98.
- [2] D. Errandonea, C. Ferrer-Roca, D. Martínez-García, A. Segura, O. Gomis, A. Muñoz, P. Rodríguez-Hernández, J. López-Solano, S. Alconchel, F. Sapina, High-pressure x-ray diffraction and ab initio study of Ni₂Mo₃N, Pd₂Mo₃N, Pt₂Mo₃N, Co₃Mo₃N, and Fe₃Mo₃N: Two families of ultra-incompressible bimetallic interstitial nitrides, *Phys. Rev. B* 82 (2010) 174105.
- [3] B. Alling, E.I. Isaev, A. Flink, L. Hultman, I.A. Abrikosov, Metastability of fcc-related Si–N phases, *Phys. Rev. B* 78 (2008) 132103.
- [4] D. Porezag, M.R. Pederson, A.Y. Liu, Importance of nonlinear core corrections for density-functional based pseudopotential calculations, *Phys. Rev. B* 60 (1999) 14132–14139.
- [5] D. Marx, J. Hutter, *Ab Initio Molecular Dynamics: Basic Theory and Advanced Methods*, Cambridge University Press, 2009.
- [6] M. Allen, D. Tildesley, *Computer Simulation of Liquids*, Clarendon Press, 1989.
- [7] M. Born, K. Huang, *Dynamical Theory of Crystal Lattices*, Oxford University Press, USA, 1988.
- [8] S. Baroni, S. de Gironcoli, A. Dal Corso, P. Giannozzi, Phonons and related crystal properties from density-functional perturbation theory, *Rev. Mod. Phys.* 73 (2001) 515–562.
- [9] B.B. Karki, R.M. Wentzcovitch, S. De Gironcoli, S. Baroni, First-principles determination of elastic anisotropy and wave velocities of MgO at lower mantle conditions, *Science* 286 (1999) 1705.
- [10] Z.Q. Wu, R.M. Wentzcovitch, K. Umemoto, B.S. Li, K. Hirose, J.C. Zheng, Pressure–volume–temperature relations in MgO: An ultrahigh pressure–temperature scale for planetary sciences applications, *J. Geophys. Res.* 113 (2008) B06204.
- [11] M.A. Blanco, E. Francisco, V. Luaña, GIBBS: isothermal–isobaric thermodynamics of solids from energy curves using a quasi-harmonic Debye model, *Comput. Phys. Commun.* 158 (2004) 57–72, source code distributed by the CPC program library: <http://cpc.cs.qub.ac.uk/summaries/ADS5>.
- [12] M. Álvarez Blanco, *Métodos cuánticos locales para la simulación de materiales iónicos*. Fundamentos, algoritmos y aplicaciones, Tesis doctoral, Universidad de Oviedo, Julio 1997.
- [13] A. Otero-de-la-Roza, V. Luaña, GIBBS2: A new version of the quasi-harmonic model code. I. Robust treatment of the static data, *Comput. Phys. Commun.* 182 (8) (2011) 1708–1720.
- [14] P. Giannozzi, S. Baroni, N. Bonini, M. Calandra, R. Car, C. Cavazzoni, D. Ceresoli, G.L. Chiarotti, M. Cococcioni, I. Dabo, A. Dal Corso, S. de Gironcoli, S. Fabris, G. Fratesi, R. Gebauer, U. Gerstmann, C. Gougoussis, A. Kokalj, M. Lazzeri, L. Martin-Samos, N. Marzari, F. Mauri, R. Mazzarello, S. Paolini, A. Pasquarello, L. Paulatto, C. Sbraccia, S. Scandolo, G. Sclauzero, A.P. Seitsonen, A. Smogunov, P. Umari, R.M. Wentzcovitch, QUANTUM ESPRESSO: a modular and open-source software project for quantum simulations of materials, *J. Phys. Condens. Matter* 21 (2009) 395502, <http://www.quantum-espresso.org>.
- [15] D. Vanderbilt, Soft self-consistent pseudopotentials in a generalized eigenvalue formalism, *Phys. Rev. B* 41 (1990) 7892–7895.
- [16] P. Carrier, R. Wentzcovitch, J. Tsuchiya, First-principles prediction of crystal structures at high temperatures using the quasiharmonic approximation, *Phys. Rev. B* 76 (2007) 64116.
- [17] N.W. Ashcroft, N.D. Mermin, *Solid State Physics*, Thomson Learning Inc., 1976.
- [18] X.-J. Chen, C. Zhang, Y. Meng, R.-Q. Zhang, H.-Q. Lin, V.V. Struzhkin, H.-K. Mao, β -tin \rightarrow Imma \rightarrow sh phase transitions of germanium, *Phys. Rev. Lett.* 106 (2011) 135520.
- [19] K. Umemoto, R.M. Wentzcovitch, S. Saito, T. Miyake, Body-centered tetragonal C-4: a viable sp³ carbon allotrope, *Phys. Rev. Lett.* 104 (2010) 125504.
- [20] B.C. Wood, N. Marzari, Dynamics and thermodynamics of a novel phase of NaAlH₄, *Phys. Rev. Lett.* 103 (2009) 185901.
- [21] A.R. Oganov, J. Chen, C. Gatti, Y. Ma, Y. Ma, C.W. Glass, Z. Liu, T. Yu, O.O. Kurakevych, V.L. Solozhenko, Ionic high-pressure form of elemental boron, *Nature* 457 (2009) 863–867.
- [22] X.-R. Chen, Z.-Y. Zeng, Z.-L. Liu, L.-C. Cai, F.-Q. Jing, Elastic anisotropy of epsilon-Fe under conditions at the Earth's inner core, *Phys. Rev. B* 83 (2011) 132102.
- [23] L. Deng, X. Liu, H. Liu, J. Dong, High-pressure phase relations in the composition of albite NaAlSi₃O₈ constrained by an ab initio and quasi-harmonic Debye model, and their implications, *Earth Planet. Sci. Lett.* 298 (2010) 427–433.
- [24] D. Errandonea, R.S. Kumar, L. Gracia, A. Beltran, S.N. Achary, A.K. Tyagi, Experimental and theoretical investigation of ThGeO₄ at high pressure, *Phys. Rev. B* 80 (2009) 094101.
- [25] P. Debye, Concerning the theory of specific heat, *Ann. Phys.* 39 (1912) 789–839.

- [26] J. Slater, *Introduction to Chemical Physics*, McGraw-Hill, 1939.
- [27] J. Poirier, *Introduction to the Physics of the Earth's Interior*, Cambridge University Press, 2000.
- [28] L. Vocadlo, J. Poirer, G. Price, Gruneisen parameters and isothermal equations of state, *Am. Mineralog.* 85 (2000) 390.
- [29] V.L. Moruzzi, J.F. Janak, K. Schwarz, Calculated thermal properties of metals, *Phys. Rev. B* 37 (1988) 790–799.
- [30] S.W. Kieffer, Thermodynamics and lattice vibrations of minerals: 3. Lattice dynamics and an approximation for minerals with application to simple substances and framework silicates, *Rev. Geophys.* 17 (1979) 35–59.
- [31] J.L. Fleche, Thermodynamical functions for crystals with large unit cells such as zircon, cofinite, fluorapatite, and iodoapatite from ab initio calculations, *Phys. Rev. B* 65 (2002) 245116.
- [32] S. Speziale, C.S. Zha, T.S. Duffy, R.J. Hemley, H.K. Mao, Quasi-hydrostatic compression of magnesium oxide to 52 GPa: Implications for the pressure–volume–temperature equation of state, *J. Geophys. Res.* 106 (2001) 515–528.
- [33] B. Li, K. Woody, J. Kung, Elasticity of MgO to 11 GPa with an independent absolute pressure scale: Implications for pressure calibration, *J. Geophys. Res.* 111 (2006) B11206.
- [34] Y. Tange, Y. Nishihara, T. Tsuchiya, Unified analyses for PVT equation of state of MgO: A solution for pressure-scale problems in high PT experiments, *J. Geophys. Res.* 114 (2009) B03208.
- [35] G. Fiquet, D. Andraut, J.P. Iti, P. Gillet, P. Richet, X-ray diffraction of periclase in a laser-heated diamond-anvil cell, *Phys. Earth Planet. Int.* 95 (1996) 1–17.
- [36] S.V. Sinogeikin, J.M. Jackson, B. O'Neill, J.W. Palko, J.D. Bass, Compact high-temperature cell for Brillouin scattering measurements, *Rev. Sci. Instrum.* 71 (2000) 201–206.
- [37] L.S. Dubrovinsky, S.K. Saxena, Thermal expansion of periclase (MgO) and tungsten (W) to melting temperatures, *Phys. Chem. Minerals* 24 (1997) 547–550.
- [38] O. Anderson, K. Zou, Thermodynamic functions and properties of MgO at high compression and high temperature, *J. Phys. Chem. Ref. Data* 19 (1990) 69–83.
- [39] N.D. Mermin, Thermal properties of the inhomogeneous electron gas, *Phys. Rev.* 137 (1965) A1441–A1443.

Modeling graphite under stress: Equations of state, vibrational modes, and interlayer friction

D. Abbasi-Pérez, J. M. Menéndez, and J. M. Recio*

MALTA-Consolider Team and Departamento de Química Física y Analítica, Universidad de Oviedo, E-33006 Oviedo, Spain

A. Otero-de-la-Roza†

MALTA-Consolider Team and School of Natural Sciences, University of California, Merced, California 95343, USA

E. del Corro, M. Taravillo, and V. G. Baonza

MALTA-Consolider Team and Departamento de Química Física I, Universidad Complutense de Madrid, E-28040 Madrid, Spain

M. Marqués

MALTA-Consolider Team and Departamento de Física Teórica, Universidad de Valladolid, E-47011 Valladolid, Spain

(Received 8 January 2014; revised manuscript received 19 July 2014; published 11 August 2014)

Extensive two- and three-dimensional periodic first-principles simulations have been carried out to investigate the mechanical response of graphite to hydrostatic and nonhydrostatic stress conditions. Our results show a clear analogy between uniaxial (σ_z) stress and hydrostatic pressure as far as structural changes in the unit cell are concerned. For intralayer C-C distances and in-plane graphite vibrational frequencies, the similarity with hydrostatic conditions is however found under biaxial ($\sigma_x = \sigma_y$) stresses. The calculated uniaxial equation of state is further used to investigate sliding mechanisms of a graphite layer in graphite at different interlayer separations, thus providing insight at an atomic level on the origin of the low static friction coefficient of graphite.

DOI: [10.1103/PhysRevB.90.054105](https://doi.org/10.1103/PhysRevB.90.054105)

PACS number(s): 71.15.Nc, 62.50.-p, 68.35.-p, 78.30.-j

I. INTRODUCTION

Hydrostatic and nonhydrostatic stress conditions open avenues for new synthetic routes and unknown phase transformations, and for novel applications of materials with otherwise undisclosed properties [1,2]. Many interesting challenges appear related to all these new phenomena induced by general stress conditions, demanding fundamental research on both the experimental and theoretical fronts. In anvil cell experiments, it is well known that the maximum pressure that can be reached under hydrostatic conditions depends on the specific transmitting medium [3]. Propolenko *et al.* observed the crucial effect of nonhydrostaticity in the phase diagram of silica after carrying out a number of diamond anvil cell experiments without transmitting fluid [4]. More recently, our measurements on highly oriented pyrolytic graphite (HOPG) show that a direct examination of the material response to nonhydrostatic stresses is possible, in principle, combining micro-Raman spectroscopy with a careful experimental setup of the cell in which the sample is directly placed between the anvils, without gasket and pressure transmitting media [5,6].

First-principles calculations constitute efficient tools to assist these experiments, should we provide a thorough insight on the chemistry and physics of the phenomena. As an illustrative example, Liang *et al.* were able to clarify the experimental controversy on high dense phases of silica “by invoking the important role of nonhydrostatic stresses” through molecular dynamics simulations [7]. Under general stress conditions, specific thermodynamic potentials have to be introduced for a global searching of the equilibrium stable structures [8,9].

Two different computational strategies are worth noting. Since one of the main interests from the calculations is the determination of the relationship between stress (σ) and strain (ϵ) tensors, one possibility is the calculation of the equilibrium ϵ components under a given σ tensor. Inversely, and more frequently in standard methodologies, the components of σ are evaluated for different values of the strain tensor, which are given in this second strategy as input data to the computational package. Both schemes have to yield the same ϵ - σ information within the uncertainty of the numerical procedure.

The importance of graphite demands extensive studies concerning its response to hydrostatic and nonhydrostatic stresses, and, at the same time, constitutes a paradigmatic system to check how computational simulations perform under these general stress conditions. In contrast with the hydrostatic regime where graphite has been thoroughly investigated (see, for example, recent computational works by Savini *et al.* [10] and Colonna *et al.* [11]), there are not explicit calculations of graphite under nonhydrostatic conditions. Simulations that preserve the hexagonal space group of graphite are in principle enough to cover structural and spectroscopic (IR and Raman) observations carried out on HOPG [5,6,12,13]. In addition, simulations of graphite under specific biaxial stresses can be used to evaluate its resistance to reduce the surface area of a two-dimensional (2D) graphite layer. Interestingly, the formal analogy with the well-known bulk scenario allows us the definition of equivalent equation of state parameters for 2D- and one-dimensional (1D)-like stresses. Furthermore, regarding uniaxial stresses, knowledge of the decrease of graphite interlayer separations under compression provides one of the two ingredients (the normal force) to evaluate the friction coefficient between two graphite layers. The second ingredient (the friction force) can be determined from the energetic profile of one graphite layer sliding between other two graphite layers.

*Corresponding author: jmrecio@uniovi.es

†Present address: National Institute for Nanotechnology, National Research Council of Canada, Edmonton, Alberta, Canada T6G 2M9.

In this paper, we aim to contribute to the understanding of the mechanical response of HOPG under general hexagonal-like stress conditions. Structural, vibrational, and electronic structure calculations mimicking uniaxial, biaxial, and triaxial stresses have been carried out to determine: (i) 1D, 2D, and three-dimensional (3D) equation of state (EOS) parameters of graphite, and (ii) pressure coefficients for in-plane vibrational modes at the center of the Brillouin zone. These results will provide information to propose equivalences between hydrostatic and nonhydrostatic conditions depending on the specific property of graphite under study. In addition, slab periodic models have been considered to explore the sliding landscape potential energy of a graphite layer at different directions and displacements in bulk graphite. Our goal is to describe friction phenomena in graphite (not graphene) and, therefore, we considered one graphite layer confined between other two at interlayer distances following the computed uniaxial equation of state of graphite. These simulations allow us not only to evaluate friction forces and the static friction coefficient of graphite, but also to get insight at an atomic level into the sliding paths that minimize the friction between graphite layers. As far as we know, our study provides for the first time computational results of the behavior of graphite under nonhydrostatic conditions.

We divide the paper in four more sections. The next one gathers the thermodynamic potentials used for tri-, bi- and uniaxial calculations. Section III presents the computational details for 3D and 2D simulations. Section IV contains the main results and the discussion of our investigation split in two subsections. The first one deals with bulklike properties including EOS and vibrational modes at different stress conditions. The second one presents results from slab models to investigate the atomic origin of the frictional forces and the friction coefficient between graphite layers. The last section summarizes the main conclusions of this study.

II. THERMODYNAMIC POTENTIALS UNDER HEXAGONAL-LIKE STRESS CONDITIONS

The relevant thermodynamic potential in a closed system of a single pure substance with mechanical work under general stress conditions (see, for example, Ref. [8]) can be written as follows [9]:

$$\phi = E - V_0\sigma\epsilon - TS, \quad (1)$$

where E is the internal energy of the system (in our case only the energy of the electronic ground state), V_0 is the equilibrium volume at free stress conditions, and σ and ϵ are the stress and strain tensors, respectively. The entropic term (TS) will not be discussed here as we will consider the athermal ($T = 0$) limit with negligible vibrational zero point contributions. All the quantities are per formula unit which means that they are per one single carbon atom.

In our work on graphite, only stress conditions that keep the hexagonal space group of the lattice will be taken into account. In the notation with $i = 4, 5, 6$ standing for nondiagonal elements of the stress tensor, the previous requisite means that only $\sigma_1, \sigma_2,$ and σ_3 can be nonzero. Besides, it is required that $\sigma_1 = \sigma_2$. In the same way, only the diagonal

elements of the strain tensor will participate in the expressions below.

In this study, the role played by the thermodynamic potential is, in principle, restricted to that of a function able to yield the equilibrium strain components of the crystal at arbitrary sets of σ_i values, provided the hexagonal symmetry is maintained. An operative definition of this thermodynamic potential at zero temperature introduces the explicit dependence on the unit cell lattice parameters through the configurational vector \vec{x} :

$$\phi(\vec{x}; \sigma) = E(\vec{x}) - V_0 \sum_{i=1}^3 \sigma_i \epsilon_i, \quad (2)$$

being $V_0 = \frac{\sqrt{3}}{8} a_0^2 c_0$ the zero stress volume per formula unit (one carbon atom), and a_0 and c_0 the corresponding length parameters of the unit cell. For a given set of σ_i values, the equilibrium lattice parameters (\vec{x}_e) are those that minimize the thermodynamic potential ϕ . Stresses acting on the unit cell generate compression and have negative values, whereas tensile stresses are positive. In this way, we shall call $\sigma_x = -\sigma_1$, $\sigma_y = -\sigma_2$, and $\sigma_z = -\sigma_3$, and all positive (negative) values for these Cartesian components of σ represent compression (tensile) forces acting on the corresponding unit cell surface of the crystal.

We will discuss results coming from three different stress conditions. The first one is a triaxial stress (σ_t) consisting of the particular biaxial stress (σ_b) in the a - b plane where $\sigma_b = \sigma_x = \sigma_y$, and a nonzero value for σ_z , along the c axis of graphite. If we have the same value for the three stress components then the hydrostatic pressure (p) case is recovered. The thermodynamic potential is easily derived from Eq. (2):

$$\begin{aligned} \phi_t(\vec{x}; \sigma) = E(\vec{x}) + \frac{\sqrt{3}}{4} \sigma_b a a_0 c_0 \\ + \frac{\sqrt{3}}{8} \sigma_z c a_0^2 - (2V_0 \sigma_b + V_0 \sigma_z). \end{aligned} \quad (3)$$

The second one concerns the biaxial stress $\sigma_b = \sigma_x = \sigma_y$, with $\sigma_z = 0$. The thermodynamic potential reduces to

$$\phi_b(\vec{x}; \sigma) = E(\vec{x}) + \frac{\sqrt{3}}{4} \sigma_b a a_0 c_0 - 2V_0 \sigma_b. \quad (4)$$

The last condition is the uniaxial stress (σ_u) along the z axis. The corresponding expression is

$$\phi_u(\vec{x}; \sigma) = E(\vec{x}) + \frac{\sqrt{3}}{8} \sigma_z c a_0^2 - V_0 \sigma_z, \quad (5)$$

where we keep the symbol σ_z for σ_u to emphasize that the uniaxial stress is applied along the direction perpendicular to the graphite layers. The terms involving V_0 are constant for given σ_i values, and do not affect the minimization process, i.e., the same equilibrium \vec{x}_e parameters are obtained if we discard these terms from the potential function. We can define a generalized enthalpy (H_n , subscript ‘‘n’’ refers to nonhydrostatic) to account, respectively, for triaxial (t), biaxial (b), and uniaxial (u) stress conditions just deleting the constant

contributions in these equations:

$$H_t(\vec{x}; \sigma) = E(\vec{x}) + \frac{\sqrt{3}}{4} \sigma_b a a_0 c_0 + \frac{\sqrt{3}}{8} \sigma_z c a_0^2, \quad (6)$$

$$H_b(\vec{x}; \sigma) = E(\vec{x}) + \frac{\sqrt{3}}{4} \sigma_b a a_0 c_0, \quad (7)$$

$$H_u(\vec{x}; \sigma) = E(\vec{x}) + \frac{\sqrt{3}}{8} \sigma_z c a_0^2. \quad (8)$$

These expressions allow us to discuss the relative stability of different structures under the same nonhydrostatic conditions [14] (not considered here), and also for comparing the magnitude of the effects introduced by different types of stress.

To end this section, it is interesting to bring the attention to the two different equivalent computational strategies that can be carried out to determine the ϵ - σ relationship. The first one evaluates the energy of the system at selected strains, usually in a regular grid of a and c . At each of these strained lattices the corresponding set of σ_i values is computed. The second one

searches for the minimum of the thermodynamic potential (or better the enthalpy) at selected σ_i values using the equations presented here. Both schemes have been followed in this work and have shown to yield same results within the error bars of the calculations.

III. COMPUTATIONAL DETAILS FOR 3D AND 2D PERIODIC MODELS OF GRAPHITE

First-principles total energy calculations for bulk graphite and trilayer graphite (3LG) were performed within the density-functional theory (DFT) formalism with a plane-wave pseudopotential approach. Simulations in bulk graphite were performed using both QUANTUM ESPRESSO [15] and the Vienna *ab initio* simulation package (VASP) [16] with the Perdew-Burke-Ernzerhof (PBE) generalized gradient exchange-correlation functional [17]. As shown below, same results were obtained (see Sec. IV) within the accuracy of the computational packages. In QUANTUM ESPRESSO we use an RRKJ ultrasoft

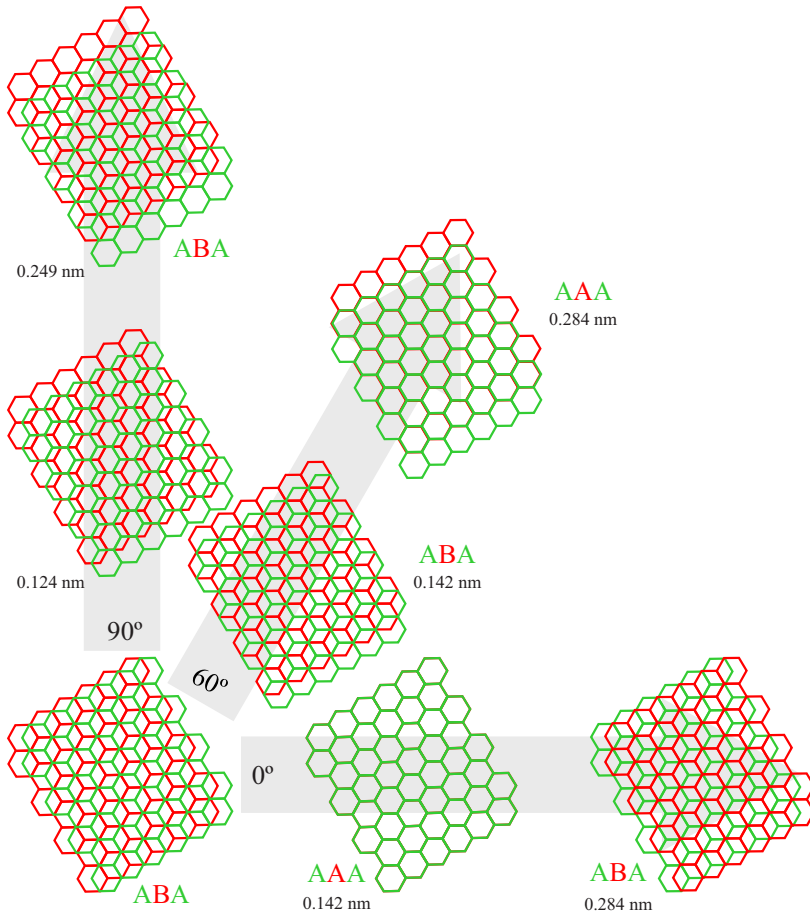


FIG. 1. (Color online) Trilayer system with the central layer B (in red) sliding two different displacements s (indicated for each direction) at 0, 60, and 90 degrees.

pseudopotential [18]. A cutoff energy of 816 eV and a $24 \times 24 \times 12$ k grid were considered in these calculations. In VASP, we follow the standard projector augmented wave all-electron description of the electron-ion-core interaction. Brillouin-zone integrals were also approximated using the Monkhorst-Pack method [19], and the energies converged to 1 meV with respect to k -point density ($16 \times 16 \times 8$ k meshes) and the plane-wave cutoff (600 eV). In both cases, the Grimme's correction [20] was included to account for the dispersion interactions. Γ -point phonon frequencies were calculated within the DFT perturbation theory implemented in the QUANTUM ESPRESSO code [15]. The total energies required in the calculation of the phonons were obtained with the same computational parameters specified above.

For the 3LG calculations, we consider a periodic slab model consisting of three graphite layers with an initial ABA stacking representing the Bernal-type configuration of stable bulk graphite. With this model, we carry out a number of computer simulations directed to study friction in graphite. For this reason, in each of these calculations the coordinates of all the atoms in layer A are required to be fixed. One of the two nonequivalent carbon atoms of layer B, originally at (0,0,0), is displaced to a different pair of x and y coordinates, thus defining the sliding (s) and the direction (Θ) of displacement. Along with the z coordinate of this atom, the coordinates of the second nonequivalent carbon atom of layer B are unconstrained and therefore the C-C distance in this layer is treated as a free parameter. Nevertheless, we found negligible departures from both the initial $z = 0$ value and the bulk C-C intralayer equilibrium distance (1.42 Å). By changing the position of the first (singular) carbon atom of layer B, and the subsequent optimization of the position of the second carbon atom, we simulate how layer B slides between the two fixed A layers. We used tetr [21] to displace the central layer (B) a distance up to 4.2672 Å in steps of 0.0889 Å at different sliding directions from 0 to 110 degrees. By repeating these calculations using the same sliding parameters and different fixed interlayer distances, we obtain a number of potential energy surfaces, each of them corresponding to a σ_z stress value derived from the linear EOS calculated in our bulk graphite simulations (see below). Therefore, it has to be understood that fixing the positions of atoms in A layers is not an approximation but a requirement of our model to mimic friction in graphite. Figure 1 shows a finite representation of the 3LG slab model for three different angles and two sliding displacements.

IV. RESULTS AND DISCUSSION

A. Bulk graphite under hydrostatic and nonhydrostatic conditions

In order to calculate 1D, 2D, and 3D EOS parameters for graphite, we chose a bidimensional strain grid by sampling 11 points in both, the a (from 2.40 to 2.50 Å) and c (5.72 to 6.77 Å) unit cell lengths. At each grid node, we calculated the stress obtaining an energy mapping with respect to a (nonuniform) stress grid, with limits -20.4 to 35.6 GPa in σ_b and -1.5 to 12.7 GPa in σ_z . These results are partially plotted in two contour maps in Fig. 2, where we have restricted the map window to

positive stress values not higher than 15 GPa. Following the $\sigma_b = 0$, $\sigma_z = 0$, and $\sigma_z = \sigma_b$ lines, the response of graphite unit cell parameters under, respectively, uniaxial, biaxial, and hydrostatic conditions can be derived. Given the simplicity of the isoline patterns in both plots, it can be straightforwardly concluded that graphite shows a largely anisotropic behavior, with hydrostatic conditions similar to biaxial and uniaxial stress regarding, respectively, $a = b$ and c distortions. Since the effect of the biaxial stress on $a = b$ is shown to be almost negligible in the considered range, we can reasonably state that hydrostatic and uniaxial (σ_z) conditions on graphite behave very much the same as far as structural strains are concerned.

The comparison of our results with a number of experimental and computational investigations is available for hydrostatic conditions. We refer to the recent papers of Savini *et al.* [10] and Colonna *et al.* [11] since they contain detailed and specific data of the lattice parameters of graphite under hydrostatic pressure including a critical comparison of several measured and calculated data. Our calculated reductions of c , a , and V under hydrostatic pressure are in very good agreement with this general analysis. To give some numbers from our calculations, and in common with the experimental and theoretical data reported in Refs. [10] and [11], the reduction of a and c is close to 1% and 12%, respectively, when hydrostatic pressure reaches 10 GPa. In the same pressure range, volume is reduced less than 14%. Overall, these results illustrate that c is the easy axis under compression, as expected for this layered compound.

A quantitative account of the results under hydrostatic and nonhydrostatic conditions is given below (see Table I) in terms of equation of state parameters. The same formal expressions resembling the isotropic bulk modulus are used:

$$M_0^z = - \left[c \frac{\partial \sigma_z}{\partial c} \right]_{0,T}, \quad M_0^b = - \left[S \frac{\partial \sigma_b}{\partial S} \right]_{0,T},$$

$$B_0 = - \left[V \frac{\partial p}{\partial V} \right]_{0,T}, \quad (9)$$

where “0” means that the evaluation of the corresponding property is at the equilibrium free stress configuration, and the 1D, 2D, and 3D structural parameters are, respectively, the unit cell parameter c , the C-hexagon area in the a - b plane S , and the graphite unit cell volume V . Note that as a result of the definitions in Eq. (9), these three parameters have the same units (GPa in our case), and s and V refer to one C atom.

Results in Table I confirm the conclusions derived from the bidimensional plots of Fig. 2. Uniaxial and hydrostatic parameters show similar values (around 64 and 58 GPa, respectively) because the easiest direction to compress the crystal (the c axis) is almost the only contribution to the bulk volumetric compressibility. Colonna *et al.* [11] calculate an athermal B_0 value of 36.3 GPa with $B'_0 = 9.85$, and report experimental values [22] of B_0 and B'_0 of 37 GPa and 14, respectively. Correlation between the two EOS parameters (B_0 and B'_0) can explain in part the discrepancy with our calculated value of B_0 since in standard EOS fittings it is known that as B'_0 increases B_0 decreases. Notice that our value for B'_0 (3.2) is almost one-third of the reported value by Colonna *et al.* The same applies to M_0^z when comparing with

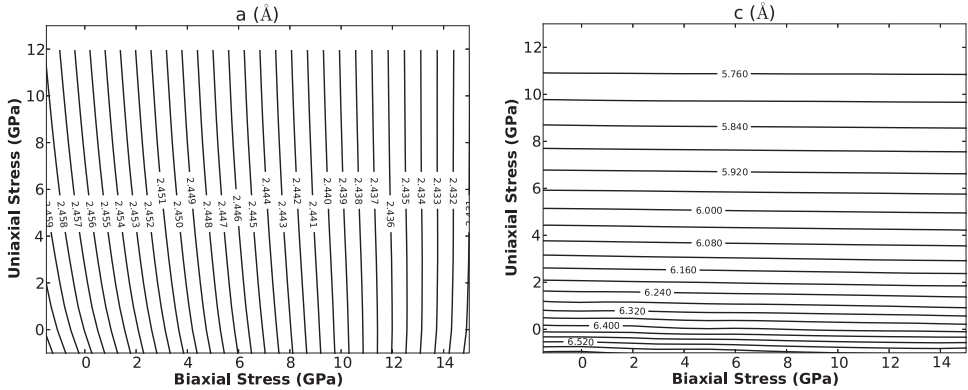


FIG. 2. Isolines of the $a = b$ (left) and c (right) lattice parameters of graphite under uniaxial ($\sigma_x = \sigma_y$) and biaxial ($\sigma_x = \sigma_y$) conditions. Results for triaxialities (including hydrostatic) can also be inferred from this plot (see text).

the experimental data of Hanfland *et al.* [12]. We speculate that another contribution to our greater values for B_0 and M_0^z can also be due to an overestimation of the weak dispersion forces between graphite layers described by the Grimme correction.

The calculated EOS parameter for the surface bulk moduli, $M_0^b = 636.3$ GPa, is conspicuous. This indicates the great resistance to compression of intralayer C-C bonds in graphite. From our discussion above, and also from comparisons between elastic constants in monolayer and bilayer graphene with bulk graphite [23], this value might be similar to other reported values for graphene. The comparison with graphene and few-layer graphene is not straightforward because our calculations aim to simulate the response of bulk graphite to biaxial stresses. Different experimental and theoretical values have been reported (from 500 to 1000 GPa for the Young's modulus, 700 GPa for M_0^b with a zero pressure first derivative of 1) depending on the thickness of the graphene sample and other factors (see, for example, Refs. [24–26]). However, the evaluation of the linear bulk modulus [$B_0^a = -(a \frac{dP}{da})_{0,T}$] describing the variation of the lattice parameter a in graphite as a function of the hydrostatic pressure provides an unequivocal way to compare our data with other calculated and experimental values. Either under hydrostatic or biaxial conditions, our calculations yield B_0^a close to 1300 GPa to be compared with a measured value of 1250 ± 70 GPa [12] or with computed values of 1240 GPa and 1171 GPa (see

Refs. [10], [23], respectively) evaluated from the relationship between elastic constants and B_0^a . In all cases, the agreement is quite satisfactory.

We have checked the alternative scheme indicated in Sec. II to compute the ϵ - σ relationship, that of minimizing the enthalpy of graphite at different stress conditions according to the expressions in Eqs. (6)–(8). In Fig. 3 (left), we illustrate how the enthalpy changes with c for different σ_z values. The minima of these curves give us the equilibrium c_e - σ_z relationship. These values reproduce the 1D EOS parameters collected in Table I and will be used below in the computation of frictional coefficients. It can be seen that lower c_e values are obtained as σ_z increases, in quantitative agreement with the results obtained using the first strategy illustrated in the contour map of Fig. 2 (left). But, perhaps more important, is to see how the enthalpy at the respective equilibrium configuration increases with σ_z [see Fig. 3 (left)]. This particular σ_z -enthalpy set of values is reproduced in the enthalpy surface plotted in Fig. 3 (right). In this plot, we can quickly recognize that the weak interactions along the easily compressible axis (c) lead to a lower increase in enthalpy than when the strong C-C bonds in the graphene layer are stretched as σ_b is applied. For the same stress (say 10 GPa), the increase in enthalpy is more than twice under σ_b than under σ_z .

Moreover, from this plot [Fig. 3 (right)], and using the relationship between σ_b and a , we can follow Zakharchenko *et al.* [27] to evaluate a 2D bulk modulus b defined by

$$\Delta E = 2b(\Delta a)^2, \quad (10)$$

where ΔE refers to the increase in the internal energy (elastic energy) due to the biaxial stress that produces an isotropic deformation ($\Delta a = \Delta b$) in the a - b plane. We have obtained a very good parabolic fitting of ΔE with respect to Δa (σ_b up to 15 GPa), and a 2D b value of $12.5 \text{ eV}/\text{\AA}^2$ in good agreement with calculated values of Zakharchenko *et al.* [27]. Notice here that $\frac{\text{energy}}{\text{area}}$ units instead of pressure are used for this b parameter.

Once uniaxial, biaxial, and triaxial (including hydrostatic) EOS parameters have been determined, we proceed to the evaluation of zone center graphite vibrational modes in all

TABLE I. Equation of state parameters of graphite under uniaxial, biaxial, and hydrostatic conditions according to our calculations. X refers to the corresponding 1D, 2D, and 3D unit cell property under uniaxial, biaxial, and hydrostatic stress, respectively. The 0 superscript refers to the free stress state. Units of \AA and GPa are used.

	X_0	$M_0 = -[X \frac{d\sigma_x}{dX}]_0$	M_0^z
Uniaxial	$c_0 = 6.430$	64.3	4.1
Biaxial	$S_0 = 5.248$	636.3	5.2
Hydrostatic	$V_0 = 33.743$	57.9	3.2

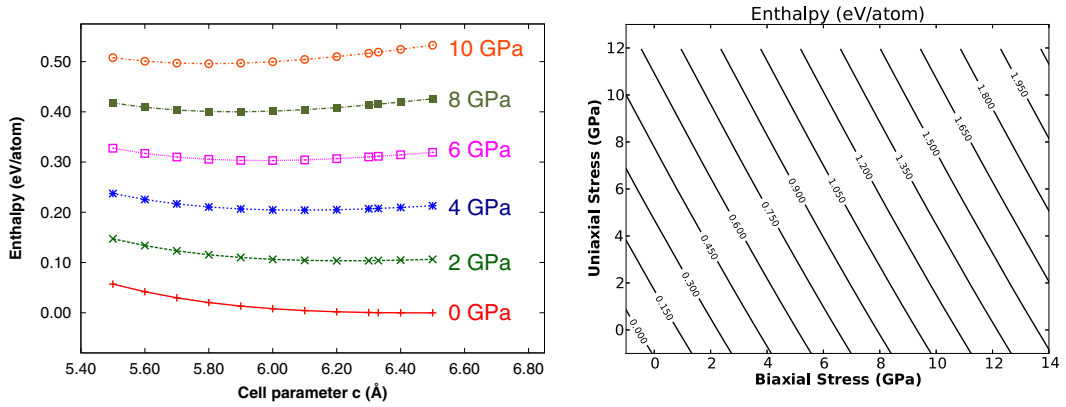


FIG. 3. (Color online) Enthalpy vs c for different uniaxial (σ_z) stresses (left). Isolines of the enthalpy potential of graphite (right) corresponding to uniaxial (σ_z) and biaxial ($\sigma_x = \sigma_y$) conditions. Results for triaxialities (including hydrostatic) can also be inferred from this plot (see text).

the nodes of our a - c grid. Γ -point vibrational modes can be divided in three groups: (i) $E_{2g}(1)$ and $E_{2g}(2)$ Raman active modes, (ii) E_{1u} and A_{2u} IR active modes, and (iii) $B_{2g}(1)$ and $B_{2g}(2)$ optically inactive modes. E -like modes represent different in-plane atomic displacements, whereas

nondegenerate modes display out-of-plane atomic movements (see Fig. 4 and Fig. S1 in Supplemental Material [28]). All of them have been evaluated in all the nodes of our a - c grid.

In particular, we are interested in stress effects on the in-plane C-C symmetric stretching [$E_{2g}(2)$] mode and

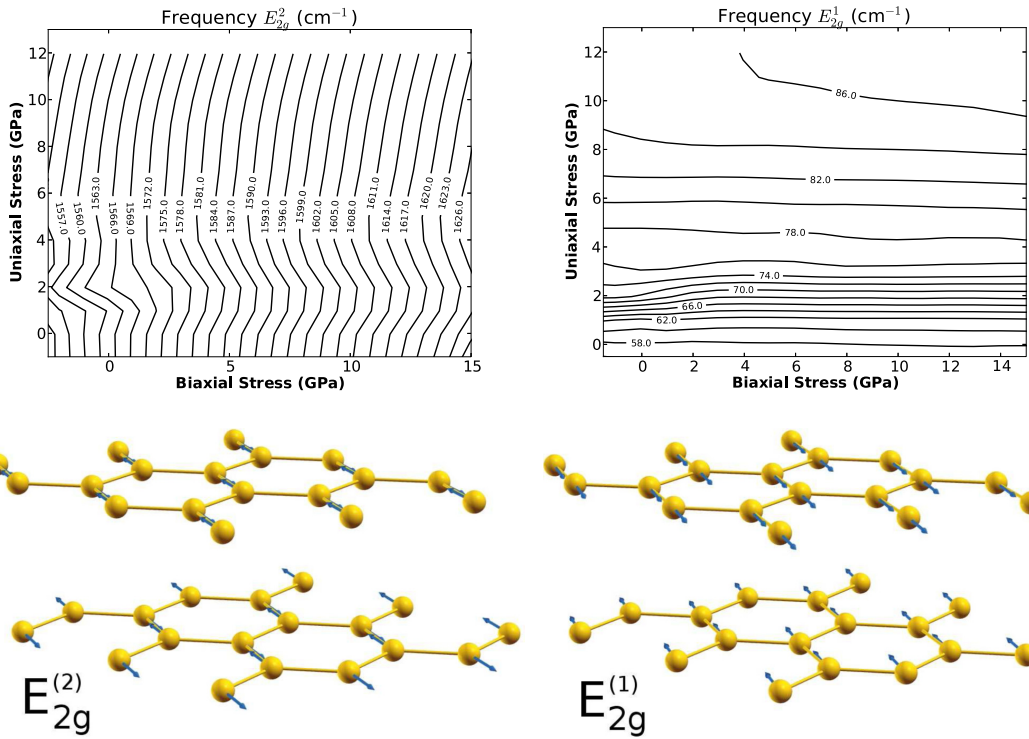


FIG. 4. (Color online) Frequency contour maps (top) and atomic displacements (bottom) of the vibrational modes $E_{2g}(2)$ (left) and $E_{2g}(1)$ (right) of graphite under uniaxial (σ_z) and biaxial ($\sigma_x = \sigma_y$) conditions. Results for triaxialities (including hydrostatic) can also be inferred from this plot (see text).

on the one related to the relative displacement (rigid shear movement) of consecutive graphite layers [$E_{2g}(1)$]. Calculated frequencies for the rest of the vibrational modes can be found in Fig. S1 of the Supplemental Material. Experimental frequencies of $E_{2g}(1)$ and $E_{2g}(2)$ modes under hydrostatic conditions have been reported by Hanfland *et al.* [12]. Similar to the results for the lattice parameters and the enthalpy, contour maps illustrate here how the frequencies of these modes change with σ_z and σ_b (see Fig. 4). Our calculated values for $E_{2g}(2)$ are in good agreement with the experimental data both in absolute and relative (Grüneisen parameters) terms. At $p = 10$ GPa, we compute an increase of $\omega(E_{2g}(2))$ around 43 cm^{-1} from its zero pressure value, 1561 cm^{-1} (1579 cm^{-1} is the experimental value of Hanfland *et al.* [12]). This is in agreement with the initial pressure coefficient [$4.8(5) \text{ cm}^{-1}/\text{GPa}$] and the sublinear increase with pressure of this mode reported by Hanfland *et al.* [12]. From the plot of Fig. 4 (left), it is interesting to remark that the effect of σ_z is almost completely negligible. For example, differences in this frequency at 10 GPa between hydrostatic and biaxial conditions are lower than 4 cm^{-1} . This is the expected result for a genuine in-plane vibrational mode involving the stretching of C-C chemical bonds, and work is in progress to exploit this result in the analysis of nonhydrostatic experiments [29]. Besides, we have found a very similar behavior for the antisymmetric stretching E_{1u} mode associated with intralayer C-C bonds. The calculated zero pressure value is 1580 cm^{-1} (1588 cm^{-1} is the experimental value reported by Nemanich *et al.* [30]), and the blue shift induced by 10 GPa is almost 50 cm^{-1} , slightly greater than in the case of the $E_{2g}(2)$ mode. The same negligible dependence on σ_z has been obtained for this mode, thus revealing the equivalent role that biaxial and hydrostatic conditions play in these high frequency in-plane vibrational modes (contour maps for this E_{1u} and the rest of the modes are collected in Fig. S1 of the Supplemental Material).

Concerning $E_{2g}(1)$, our calculated zero pressure value (58 cm^{-1}) is 14 cm^{-1} above the experimental value of Hanfland *et al.* [12], probably reflecting again some overestimation in our description of the interlayer interaction. This low frequency mode can be linked to frictional forces between graphite layers. Notice that all C atoms in each graphite layer move in the same direction, and no changes of intralayer

C-C bonds are explicitly involved in this mode [see Fig. 4 (right)]. Here, we check the ability of a harmonic model to account for an estimation of the force constant (k) involved in the relative (opposed directions) displacements of alternate layers associated with this mode. The estimated force constant using the zero pressure calculated frequency is around 1.2 N/m (0.7 N/m using the experimental value), whereas at 10 GPa [$\omega[E_{2g}(1)] \simeq 86 \text{ cm}^{-1}$] k increases up to 2.6 N/m . These values will be compared with direct simulations of graphite layer displacements in the next subsection, and constitute upper limits to force constants due to the strong anharmonicity associated with this mode [12,31]. To end up with our discussion, it is to be emphasized that the contour map displayed in Fig. 4 (right) shows a negligible effect of the biaxial stress on this mode, but a clear dependence on σ_z which illustrates the link of this mode with frictional forces between graphite layers.

B. Graphite slabs under uniaxial conditions

Using our 3LG model, we have computed potential energy surfaces (PES, Z axis) as functions of the sliding displacement of the B graphite layer s (Y axis), and the angle Θ (X axis), for interlayer separations corresponding to σ_z values, as dictated by the 1D EOS (Fig. 5 displays PES for $\sigma_z = 0$ and 16 GPa). The absolute maxima in these plots correspond to the AAA arrangement of the trilayer, which can be found for all the analyzed angles (except 30° and 90°) provided we do not limit the amount of displacement of the singular atom in layer B. Illustrative animations of the interplay between energetic profiles and displacement paths are available as movies Mov1 (at 0°), Mov2 (at 60°), and Mov3 (at 90°) in the Supplemental Material (see Fig. S2).

Intra- and interlayer interactions in graphite have been studied many times (see, for example, Refs. [32] and [33], and references therein). They allow us to explain the preference of graphite for the Bernal-type ABA stacking and the existence of maxima at AAA configurations. Other different stackings also have been investigated due to the increased interest in graphene and in the so-called few-layer graphites or few-layer graphenes (FLG) (see Refs. [10,23,34–36], and references therein). In all these works it is revealed that the strong

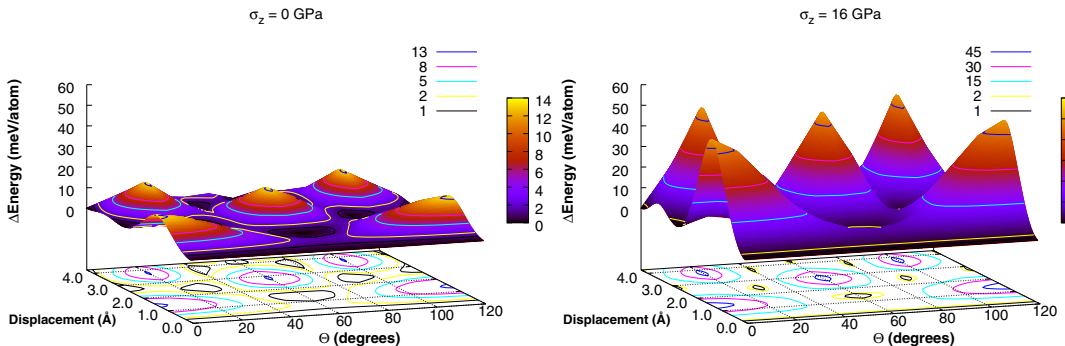


FIG. 5. (Color online) Potential energy surface of the three-slab model of graphite under zero stress (left) and $\sigma_z = 16$ GPa (right) conditions. Displacements (s) and directions (Θ) ranged by the middle layer start in the ABA configuration.

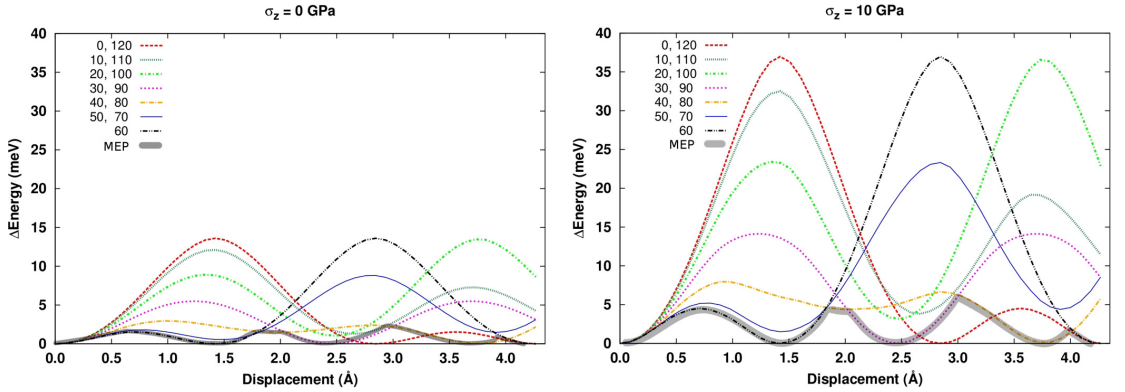


FIG. 6. (Color online) Energy differences relative to the equilibrium energy of 3LG as a function of the sliding displacement of the B central layer s at an interlayer distance of 3.25 \AA ($\sigma_z = 0 \text{ GPa}$, left) and at an interlayer distance of 2.91 \AA ($\sigma_z = 10 \text{ GPa}$, right). Different lines mean selected directions at the labeled angles. The solid (colored) wide line represents the minimum energy sliding path for the B layer following different angles.

in-plane C-C covalent bonds contrast with the weak interlayer dispersion forces leading to an “essentially two-dimensional character of graphite” [37,38]. The dispersion forces do not come from the σ -type intralayer chemical bonds, but from the π electron density above and below the plane. As de Andres *et al.* [39] have shown in 2LG, the AA stacking facilitates the formation of C-C interlayer bonds breaking the planar geometry and weakening the intralayer C-C bonding network. In our 3LG system resembling a graphite slab, although the planar geometry is kept as we move from the ABA to the AAA stacking, the dispersion (attractive) forces between layers are enhanced at the expense of weakening intralayer C-C bonds leading to the energy maxima at AAA configurations. In this way, we found an increase in energy at these maxima of 13.5 meV/atom with respect to the ABA stacking when the interlayer distance is kept at the calculated equilibrium value of graphite (3.27 \AA). A value of 8.9 meV/atom was obtained by Reguzzoni *et al.* [36] for two-layer graphene with optimized interlayer separations of 3.37 \AA (AB stacking) and 3.59 \AA (AA stacking). In spite of this and other similarities (see, for example, a thorough computational study by Guo *et al.* [35]), we would like to emphasize that our 3LG model is introduced here to analyze friction forces and the friction coefficient only for graphite and, therefore, it does not intend to simulate friction phenomena in graphene. That is why interlayer separations are kept fixed following the uniaxial (σ_z -c) EOS in each calculation of the PES.

By comparing the energy surfaces at different interlayer distances, we clearly observe that, while the topology of the energy surfaces remains unaltered, the energy required to displace layer B along a given direction increases when the adjacent layers become closer (equivalent to an increase of σ_z). Notice that this enhancement of the potential corrugation as σ_z increases is in agreement with the results of a subsequent theoretical work of Reguzzoni *et al.* [40]

Our theoretical results could be analyzed for the case in which the graphite layers could displace without restriction on the angular direction, which is the situation that resembles

previous FFM experiments found in the literature where graphite is revealed as superlubricant [41,42]. For this purpose we must take into account that the graphite layers can move with a given direction for a certain distance and change, if possible, their sliding direction when they find an energetic barrier; giving rise to potential energetic curves as those shown in Fig. 6 (see also movie Mov4 and Fig. S2 in the Supplemental Material). Once again, the effect of stress is to increase these energetic barriers but keep the whole topology unaltered.

From these potential energy surfaces we are able to calculate the force felt by the B layer when it moves along a given direction as

$$F = -\frac{\partial E}{\partial s}. \quad (11)$$

We evaluate forces along displacement paths $s = 1.5 \text{ \AA}$ and $s = 4.2 \text{ \AA}$ long at different sliding directions and interlayer distances from equilibrium to 2.8 \AA . As before, we can convert these interlayer distances into σ_z using the uniaxial equation of state obtained in our calculations in bulk graphite. The corresponding range of σ_z goes from 0 up to 16 GPa. The maximum forces obtained for the 1.5 \AA displacement paths correspond with the forces required to initiate the motion (static friction force), whereas those for the longer displacements are for maintaining the surfaces in the subsequent relative motion. These results lead to the curves shown in Fig. 7.

It is to be noted that the maximum force, F_{\max} , obtained at the 0 degree sliding direction for a displacement value (s_{\max}) is just at the middle of the path between the starting position and the position corresponding to the first maximum in the energy profile. The ratio $\frac{F_{\max}}{s_{\max}}$ is a rough estimation of the force constant associated with $\omega[E_{2g}(1)]$. Although the calculated values using this ratio at 0 GPa (0.4 N/m) and 10 GPa (0.9 N/m) are lower than the values assuming harmonic frequencies (see above), it is remarkable to see that they are of the same order of magnitude and show a very similar increase with pressure. Inversely, from the force constant calculated with this ratio, it

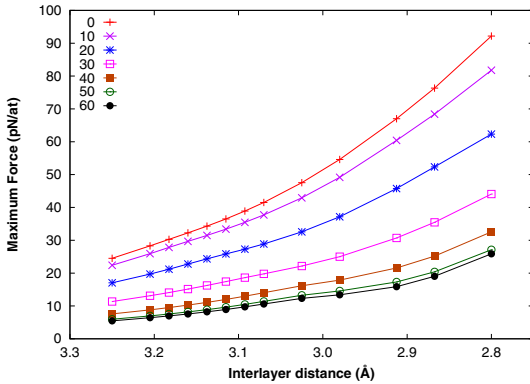


FIG. 7. (Color online) Friction forces between graphite layers vs σ_z for displacement directions from 0 to 60 degrees.

is also possible to estimate the associated harmonic frequency resulting in 32 cm^{-1} at 0 GPa and 51 cm^{-1} at 10 GPa. These values are also lower than the experimental ones (around 45 cm^{-1} and 70 cm^{-1} , respectively) [12], but again of the same order and with very similar pressure coefficient. The whole analysis reveals that this low frequency Raman mode is a good indicator of the frictional forces between graphene layers in graphite. In this respect, it is interesting to notice that this low frequency mode has been recently measured in graphene [43], although the effect of stress on it has not been determined yet.

Now, we transform the calculated frictional forces into stress (σ_{friction} , in GPa) using

$$\frac{1 \text{ pN}}{S_{\text{atom}}} = 0.0383 \text{ GPa}, \quad (12)$$

which is obtained by considering the surface of a C atom, $S_{\text{atom}} = 2.61 \text{ \AA}^2$, calculated as the half of the area of a hexagon of 1.42 \AA side (C-C bonding equilibrium distance in graphite). For example, the calculated minimum and maximum values of σ_{friction} at zero pressure are 1.1 GPa and 4.2 GPa obtained at sliding directions of 60 and 0 degrees, respectively.

From σ_z and σ_{friction} values, the static friction coefficient (μ_S , adimensional) can be straightforwardly calculated along with its load dependence using $\mu_S = (\frac{d\sigma_{\text{friction}}}{d\sigma_z})_{\sigma_z}$. As expected, μ_S strongly depends on the sliding directions, with values ranging between 0.1 and 0.4, in excellent agreement with the accepted experimental values [41]. As regards the comparison with other experimental results, it must be pointed out that, in spite of the obvious differences, 30 and 90 degrees sliding directions (without AAA stacking) can be seen as analogous to the incommensurate situation examined by Dienwiebel *et al.* [42] for angle rotations other than 0 and 60 degrees. Notice that angles for sliding directions (our work) and rotations (Ref. [42]) are not directly comparable. It is satisfactory to see that in both cases (30 and 90 degrees sliding directions in our calculations and incommensurate rotation angles in the experiments) a low friction behavior is obtained. It could be argued that we also obtain low friction static coefficients for other sliding directions (40, 50, 60 degrees). However, only low dynamic friction coefficients can be obtained for

the 30- and 90-degree sliding directions according to our calculations, since for the rest of the sliding directions the AAA stacking (pronounced friction) is sooner or later achieved. Verhoeven *et al.* [44] perform more realistic simulations of Dienwiebel *et al.* experiments calculating friction forces between a graphite flake on a rigid graphite substrate. They conclude that the friction forces do not depend much on the pulling direction since the flake follows in all cases a minimum energy path which is quite analogous to the one calculated and discussed in this article. It is also interesting to note the strong decrease in μ_S observed with increasing σ_z . Using an average $\bar{\mu}_S$ parameter that accounts for all the sliding directions, our calculations lead to $\bar{\mu}_S$ values of 0.223, 0.203, and 0.167 for $\sigma_z = 0, 2, \text{ and } 10 \text{ GPa}$, respectively. This means that the barrier between the regimes of static and dynamic friction in graphite gradually fades under compression.

In terms of microscopic interactions, the existence of frictional forces between graphite layers comes from the loss of π -type interactions within the C-C intralayer honeycomb pattern. This energetic loss is not compensated by the new dispersion forces connecting graphite layers in the AAA stacking. Those sliding directions where this AAA stacking is not achieved prevent the weakening of the strong C-C intralayer bonds and facilitates layer displacements leading to lower frictional forces. As normal forces (σ_z) increase, the result of the interplay between intra- and interlayer interactions induced by the sliding of the graphite layer show an enhanced effect of the weakening of intralayer C-C bonds. This trend tends to saturate probably because interlayer interactions start to be competitive. This conjecture could be confirmed by analyzing the changes in the electron density, as Reguzzoni *et al.* have done in a two-layer graphene model, where they observe a charge transfer from the interlayer region toward the near-layer regions.

V. CONCLUSIONS

A thorough computational study of the mechanical response of graphite to hexagonal-like stresses has allowed us to derive equations of state parameters and to shed light on the origin of frictional forces between graphite layers. Two interesting results are worth noting from our computed EOS: (i) hydrostatic and uniaxial (σ_z) stresses behave very much the same as the unit cell structure is concerned, and (ii) the great resistance to compression of a graphite layer in graphite can be quantified through different moduli: $M_0^b = 636 \text{ GPa}$, $B_0^a = 1310 \text{ GPa}$, $b = 12.5 \text{ eV/\AA}^2$. The EOS parameters also reveal that the most efficient way to store energy (enthalpy) in graphite is through biaxial stress load. In-plane C-C stretching modes [$E_{2g}(2)$ and E_{1u}] show almost the same high frequency values and similar pressure coefficients independent on the uniaxial z component. The interplay between the strong intralayer C-C bonds and weak interlayer interactions come into play when one graphite layer is allowed to slide between other two fixed ones using a 3LG slab model with variable interlayer separations. Calculated friction coefficients show low values (between 0.1 and 0.4) which are dependent on the displacement direction in agreement with experimental observations. It is the weakening of the intralayer C-C bond across the path from the ABA to the AAA stacking, which is not compensated by the increase in the dispersion forces

between graphene layers, that is responsible for the appearance of energy barriers and the associated frictional forces.

ACKNOWLEDGMENTS

Financial support from the Asturias FICYT Agency (Project No. SV-13-ECOMP-12), the Spanish MICINN and FEDER programs under Projects No. CTQ2012-35899-C02-

01 and No. CTQ2012-35899-C02-02, Comunidad de Madrid and European Union through the S2009/PPQ-1551 program, and the Spanish MALTA-Consolider Ingenio-2010 program under Project No. CSD2007-00045 are gratefully acknowledged. D.A.P. thanks the Spanish MICINN for an FPI postgraduate grant. M.M. thanks the Principado de Asturias FICYT program for a postdoctoral grant.

-
- [1] W. B. Holzapfel, *Rep. Prog. Phys.* **59**, 29 (1996).
- [2] J. Zhao, R. J. Angel, and N. L. Ross, *J. Appl. Cryst.* **43**, 743 (2010).
- [3] S. Klotz, J. C. Chervin, P. Munsch, and G. Le Marchand, *J. Phys. D: Appl. Phys.* **42**, 075413 (2009).
- [4] V. B. Prokopenko, L. S. Dubrovinsky, V. Dmitriev, and H. P. Weber, *J. Alloys Comp.* **327**, 87 (2001).
- [5] E. del Corro, M. Taravillo, J. González, and V. G. Baonza, *Carbon* **49**, 973 (2011).
- [6] E. del Corro, A. Otero-de-la-Roza, M. Taravillo, and V. G. Baonza, *Carbon* **50**, 4600 (2012).
- [7] Y. Liang, C. R. Miranda, and S. Scandolo, *Phys. Rev. Lett.* **99**, 215504 (2007).
- [8] D. C. Wallace, *Thermodynamics of Crystals* (Wiley, New York, 1972).
- [9] R. F. Tinder, *Tensor Properties of Solids: Phenomenological Development of the Tensor Properties of Crystals* (Morgan and Claypool Publishers Series, San Rafael, 2008).
- [10] G. Savini, Y. J. Dappe, S. Oberg, J.-C. Charlier, M. I. Katsnelson, and A. Fasolino, *Carbon* **49**, 62 (2011).
- [11] F. Colonna, A. Fasolino, and E. J. Meijer, *Carbon* **49**, 364 (2011).
- [12] M. Hanfland, H. Beister, and K. Syassen, *Phys. Rev. B* **39**, 12598 (1989).
- [13] A. F. Goncharov, *High Press. Res.* **8**, 607 (1992).
- [14] K. Sarasamak, A. J. Kulkarni, M. Zhou, and S. Limpijumngong, *Phys. Rev. B* **77**, 024104 (2008).
- [15] P. Giannozzi, S. Baroni, N. Bonini, M. Calandra *et al.*, *J. Phys.: Condens. Matter* **21**, 395502 (2009).
- [16] G. Kresse and J. Furthmüller, *Phys. Rev. B* **54**, 11169 (1996).
- [17] J. P. Perdew, K. Burke, and M. Ernzerhof, *Phys. Rev. Lett.* **77**, 3865 (1996).
- [18] A. M. Rappe, K. M. Rabe, E. Kaxiras, and J. D. Joannopoulos, *Phys. Rev. B* **41**, 1227 (1990).
- [19] H. J. Monkhorst and J. D. Pack, *Phys. Rev. B* **13**, 5188 (1976).
- [20] S. Grimme, *J. Comput. Chem.* **27**, 1787 (2006).
- [21] L. N. Kantorovich, <http://www.emmp.ucl.ac.uk/lev/codes/lev00/index.html>.
- [22] Y. X. Zhao and I. L. Spain, *Phys. Rev. B* **40**, 993 (1989).
- [23] P. L. de Andres, F. Guinea, and M. I. Katsnelson, *Phys. Rev. B* **86**, 245409 (2012).
- [24] C. Lee, X. Wei, J. W. Kysar, and J. Hone, *Science* **321**, 385 (2008).
- [25] I. W. Frank, D. M. Taenenbaum, A. M. van der Zande, and P. L. McEuen, *J. Vac. Sci. Technol. B* **25**, 2558 (2007).
- [26] S. Reich, C. Thomsen, and P. Ordejón, *Phys. Rev. B* **65**, 153407 (2002).
- [27] K. V. Zakharченко, M. I. Katsnelson, and A. Fasolino, *Phys. Rev. Lett.* **102**, 046808 (2009).
- [28] See Supplemental Material at <http://link.aps.org/supplemental/10.1103/PhysRevB.90.054105> for atomic displacements and frequencies for the rest of the vibrational modes, and illustrative animations of energy profiles for different displacement paths including the minimum energy path.
- [29] E. del Corro *et al.* (unpublished).
- [30] R. J. Nemanich, G. Lucovsky, and S. A. Solin, *Solid State Comm.* **23**, 117 (1977).
- [31] D. P. DiVincenzo, E. J. Mele, and N. A. W. Holzwarth, *Phys. Rev. B* **27**, 2458 (1983).
- [32] A. Vanossi, N. Manini, M. Urbakh, S. Zapperi, and E. Tosatti, *Rev. Mod. Phys.* **85**, 529 (2013).
- [33] M. Birowska, K. Milowska, and J. A. Majewski, *Acta Phys. Pol. A* **120**, 845 (2011).
- [34] S. Latil and L. Henrard, *Phys. Rev. Lett.* **97**, 036803 (2006).
- [35] Y. Guo, W. Guo, and C. Chen, *Phys. Rev. B* **76**, 155429 (2007).
- [36] M. Reguzzoni, A. Fasolino, E. Molinari, and M. C. Righi, *J. Phys. Chem. C* **116**, 21104 (2012).
- [37] J. C. Charlier, X. Gonze, and J. P. Michenaud, *Phys. Rev. B* **43**, 4579 (1991).
- [38] J. C. Charlier, J. P. Michenaud, and X. Gonze, *Phys. Rev. B* **46**, 4531 (1992).
- [39] P. L. de Andres, R. Ramírez, and J. A. Vergés, *Phys. Rev. B* **77**, 045403 (2008).
- [40] M. Reguzzoni, A. Fasolino, E. Molinari, and M. C. Righi, *Phys. Rev. B* **86**, 245434 (2012).
- [41] D. Maugis, *Contact, Adhesion and Rupture of Elastic Solids*, (Springer-Verlag, Berlin, 2000).
- [42] M. Dienwiebel, G. S. Verhoeven, N. Pradeep, J. W. M. Frenken, J. A. Heimberg, and H. W. Zandbergen, *Phys. Rev. Lett.* **92**, 126101 (2004).
- [43] P. H. Tan, W. P. Han, W. J. Zhao, Z. H. Wu, K. Chang, H. Wang, Y. F. Wang, N. Bonini, N. Marzari, N. Pugno, G. Savini, A. Lombardo, and A. C. Ferrari, *Nature Materials* **11**, 294 (2012).
- [44] G. S. Verhoeven, M. Dienwiebel, and J. W. M. Frenken, *Phys. Rev. B* **70**, 165418 (2004).

Frictional forces in graphite under compression

E. del Corro^{1,2}, D. Abbasi-Pérez^{1,3}, M. Marqués^{1,3}, A. Otero-de-la-Roza^{1,3,4}, J. M. Menéndez^{1,3}, M. Taravillo^{1,2}, J. M. Recio^{1,3}, V. G. Baonza^{1,2}

¹ *MALTA-Consolider Team, Spain*

² *Departamento de Química Física I, Universidad Complutense de Madrid, E-28040 Madrid, Spain*

³ *Departamento de Química Física y Analítica, Universidad de Oviedo, E-33006 Oviedo, Spain*

⁴ *School of Natural Sciences, University of California, Merced, CA95343, USA.*

ABSTRACT

The technological importance of graphite as a solid lubricant, along with the significant scientific interest of graphene, has stimulated numerous investigations on friction in carbon based materials. However, at the atomic level, there is still some room for improving our knowledge about the nature of the interactions involved in these phenomena. Here, a deep interpretative analysis of results from a novel experimental strategy is carried out to obtain the force that a graphene sheet must overcome for achieving relative motion in graphite at varying stress loads. The experiments are performed by compressing oriented graphite specimens between two opposed anvils. A detailed stress analysis is fully monitored by Raman spectroscopy. The corrugation energy landscape and the static friction parameters calculated in our previous computer simulations on a tri-layer graphene model are used to assist in interpreting the anvil cell Raman experiments. We find a consistent picture between theory and experiment that reveals how the static friction between loaded graphene sheets follows a Hertzian law with attractive forces.

PACS number(s): 62.50.-p, 81.05.uf, 68.35.Af, 78.30.-j

I. INTRODUCTION

Graphite is among the best solid lubricants, but it is also known that graphite behaves as a poor lubricant in vacuum.¹ Such a diverse behaviour makes graphite a target model in many frictional/tribological studies at both macroscopic² and atomic^{3,4,5} levels. Graphite also was the first system studied in the seminal work by Mate et al.,⁶ when the friction force microscope (FFM) was developed. Nowadays graphene has emerged into the scene of frictional studies^{7,8,9} and many works have been focused on understanding the underlying mechanisms of friction in graphite^{10,11} and graphene.¹² For instance, novel terms like superlubricity^{13,14} have been coined to refer to the near-zero friction force observed between a graphite substrate and a graphite flake in an incommensurate configuration.

Typical FFM results consist of a periodic variation of the lateral force with the sliding distance, reflecting a characteristic stick-slip motion pattern.¹⁵ In stick-slip phenomena, static friction determines the force to be overcome during the stick phase, before the slip takes place at the interface. Key parameters are the static and kinetic friction coefficients, μ_S and μ_K , respectively, which are related to the force required to initiate motion between two contacting surfaces and the force to maintain the surfaces in the subsequent relative motion.² Such dynamic experiments have been successfully interpreted in terms of analytical models,^{16,17} like the Prandtl-Tomlinson, Frenkel-Kontorova or a combination of both,¹⁸ and, with the advancement of computational capabilities, first principles calculations now play a major role to understand atomic-scale interactions.⁴

FFM studies also present some drawbacks and limitations, since conventional experiments involve one small surface (usually a tip) and application of relatively low loads. As a consequence, there is still little information about static friction between

large contact surfaces and at large loads, aspects for which clear understanding at the atomic level is yet to be achieved.

Our investigation aims to complete the fundamental knowledge of friction phenomena by examining the static regime emerging when both large loads and large contact surfaces meet simultaneously, conditions which are difficult to achieve in FFM experiments. Again, graphite is particularly suited for our purposes, since a perfect specimen presents an ideal ABA commensurate configuration due to its highly symmetrical layered structure. Graphite can therefore be regarded as a model for studying interlocking single asperity problems¹⁹ at the atomic scale, in the classical Bowden and Tabor's view.²⁰ In this article we face this challenge by following an experimental approach which is radically different to those existing in the literature. By squeezing highly oriented pyrolytic graphite (HOPG) specimens between two opposed anvils, we are able to estimate the ensuing static friction forces opposed to the displacement of the graphene layers in graphite. These rather unconventional experiments in anvil devices are monitored by micro-Raman spectroscopy, which is among the most powerful techniques to probe carbon materials.^{21,22} It provides direct access to the stress distribution of both anvils (see Ref. [23]) and samples,²² and is especially suited for anvil devices.²⁴

An important effort in our investigation concerns the interpretative capability provided by our recent computer simulations on graphite under different non-hydrostatic stresses.²⁵ These calculations were performed using density-functional theory (DFT) including corrections to account for dispersion effects (DFT-D2²⁶), which are known to yield reliable results for graphite.²⁷ We obtained the 2D energy landscape (*i.e.* the corrugation potential) and studied the misfit angle dependence of static friction.²⁵ The load dependence of these quantities was evaluated by varying the interlayer distances of

a tri-layer graphene model, exceeding the stress range covered in our current experiments. Here, these simulations are exploited to carry out a deep interpretative analysis of the experimental data. The whole analysis allows us to assess our measurements and to check the validity under large loads of Hertzian-like contact models including adhesive contacts.²⁸

The rest of the paper contains three more sections. Next, we briefly describe the details of the experimental procedures concerning the anvil cell device and the collection of the Raman spectra. A summary of our previous computational modelling is also included. Section III contains the results and the discussion. It is split into two subsections dealing, respectively, with (i) the analysis of stress effects on the sample, and (ii) friction models and the determination of graphite static friction coefficients. In the last section, the most relevant findings and conclusions are summarized along with some emphasis on the general approach followed in this investigation.

II. EXPERIMENTAL AND COMPUTATIONAL DETAILS

A. Experiments

The general characteristics of the anvil device used here have been described elsewhere.²⁹⁻³¹ Silicon carbide (6H-SiC) anvils were obtained as loose gem-quality moissanite stones with standard brilliant cut. The opposed anvil device mounts two gems with culets cut perpendicular to the *c*-axis and polished to optical quality; culet dimensions are optimized for achieving the maximum stress projected in each experiment (about 400 μm in diameter for stresses less than 10 GPa). Since no gasket is used in our experiments, the opposed culets need to be properly aligned by interferometry before compressing the sample in order to prevent breakage of the anvils

and non-uniform stresses during the experiments. It is to be noted that special care has been taken to avoid alignments problems that could bias the resulting measurements. When a sample is compressed in such fashion, the load exerted by the anvil along the c -axis of graphite (σ_{load}) generates a biaxial stress profile across the sample.³² For this reason, Raman spectra were collected at different locations of the sample.

Raman measurements are performed using a Jobin-Yvon HR460 monochromator equipped with 600 and 2400 grooves/mm holographic gratings and a liquid-nitrogen cooled charge-coupled detector (CCD). Raman spectra were excited using the 532.0 nm line of a Spectra Physics solid-state laser. Excitation power is optimized for maximizing signal to noise ratios, while avoiding undesired heating effects on the sample. These specifications, along with a continuous calibration of the system using a standard neon discharge lamp, provide spectral resolutions between 1 and 4 cm^{-1} , depending on the grating configuration. We use a 10x Mitutoyo infinity-corrected microscope objective coupled to a Navitar 10x zoom to collect the backscattered radiation from the sample. Confocal conditions are achieved by combining spatial filtering and appropriate CCD binning. This gives access to sampling regions between 2 and 20 μm , which largely exceeds the sampling sizes available in FFM setups. Combination of a Newport XYZ precision stage with digital Mitutoyo actuators provides spatial resolutions close to 1 μm .

B. Computer Simulations

Two types of simulations were performed in our recent theoretical study on graphite.²⁵ Firstly, we optimized the structural parameters and evaluated the vibrational frequencies at the center of the Brillouin zone of bulk graphite under different uniaxial, biaxial and triaxial stresses preserving its hexagonal symmetry. Secondly, a periodic and infinite

three layer graphene (3LG) model was built following the Bernal-type ABA stacking. First-principles total energy calculations for both type of simulations were performed within the density-functional theory (DFT) formalism with a plane-wave pseudopotential approach. Simulations in bulk graphite were performed using both Quantum ESPRESSO³³ and the Vienna *ab initio* simulation package (VASP)³⁴ with the Perdew-Burke-Ernzerhof (PBE) generalized gradient exchange-correlation functional.³⁵ Same results within the accuracy of the two computational packages were obtained.²⁵ In Quantum ESPRESSO, we use a RRKJ ultra-soft pseudopotential.³⁶ In VASP, we follow the standard projector augmented wave all-electron description of the electron-ion-core interaction. In both cases, the Grimme's correction²⁶ was included in order to account for the dispersion interactions. Other computational details can be found in Ref. 25.

In our 3LG model, we displaced the central layer (B) up to 0.42672 nm in 0.00889 nm steps along selected sliding directions from 0 to 120 degrees at intervals of 10 degrees, and the difference in energy was evaluated at each step; these calculations were repeated at 13 decreasing interlayer distances from 0.325 nm to 0.280 nm. In all cases, a DFT-D2²⁶ approach was included to account for the weak dispersion forces between graphene layers. The basic characteristics of both experiments and calculations are schematized in Fig. 1.

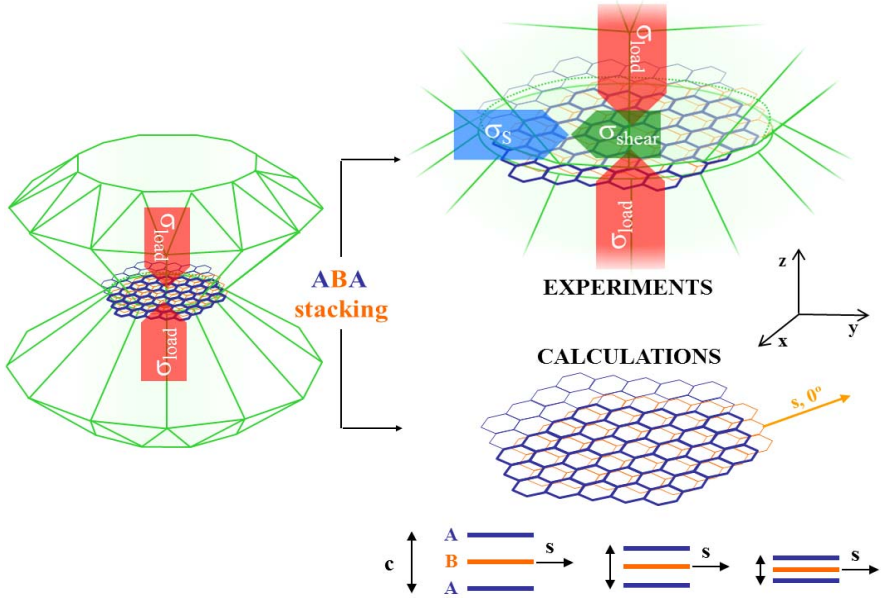


FIG. 1. (Color online) Scheme of our experimental and theoretical strategies. Graphite specimens are directly compressed between the culets of two moissanite anvils. The different stress components acting on the sample are indicated by arrows with size approximately proportional to their relative values. On a tri-layer slab model with an initial ABA structure we displaced the central layer (B) at different sliding directions and for selected interlayer distances.

III. RESULTS AND DISCUSSION

A. Stress Analysis

The value of σ_{load} can be accurately determined at the anvil/sample interface by measuring the Raman spectrum at the anvil culet, as confirmed by the exhaustive study of the stress behaviour of moissanite.²³ For these purposes, one LO phonon overtone of moissanite (2LO) exhibits some desirable features: a) it is a sharp feature, so its

frequency can be accurately determined in a second derivative analysis (Fig. 2b), b) being an overtone, its stress slope ($7.8 \text{ cm}^{-1}\cdot\text{GPa}^{-1}$) almost doubles those of the fundamentals, thus improving the accuracy in the calculation of σ_{load} from the relationship $\sigma_{load} \text{ (GPa)} = \Delta\omega_{2LO} \text{ (cm}^{-1})/7.8$, where $\Delta\omega_{2LO}$ is the frequency shift of the 2LO band with respect to its frequency at room conditions (1712 cm^{-1}), and c) this feature is close to the G band of graphite (1580 cm^{-1}), so both bands can be simultaneously measured in the same spectral window (Fig. 2a). This allowed us to obtain the specific value of σ_{load} supported by each sampling region and to include the effect of the spatial loading distribution in our analysis.

In order to make our study comparable to existing FFM experiments, stress ought to be converted into force ($1 \text{ GPa} = 1 \text{ nN}\cdot\text{nm}^{-2}$). Previous FFM studies in the low-load regime reached equivalent pressures of about 1.4 (Ref. [6]) and 0.5 GPa (Ref. [37]), so our experiments (*ca.* 4 GPa) should be regarded as moderate-to-large in terms of applied load. We shall consider here only the results recorded in those sampling regions with no defects or small concentration of defects, which essentially corresponds to measurements at the center of the anvils, where maximum load stress is attained in each run. This was confirmed by the negligible intensity of the so-called D-band^{38,39} in each Raman spectrum of graphite used in our analysis.

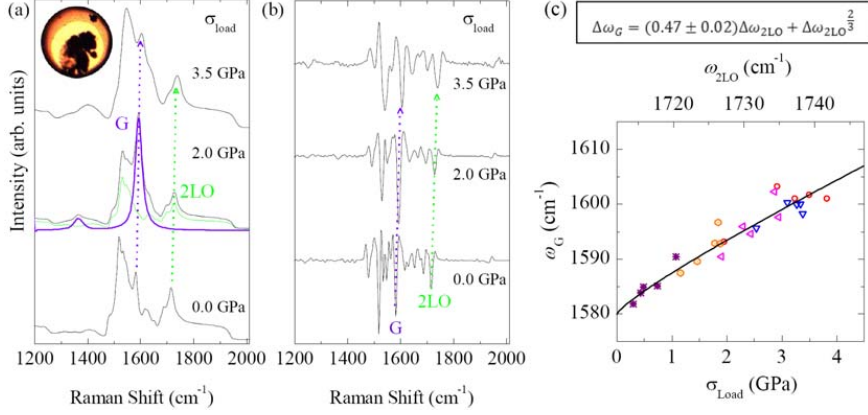


FIG. 2. (Color online) (a) Raman spectra containing superimposed contributions from the front anvil and the sample at selected loading stresses. Both contributions are plotted separately for moissanite (green) and graphite (blue-violet). The inset shows a photograph of the graphite sample (in black) between the moissanite anvils in the pressure cell. (b) Second derivative analysis of the collected spectra providing unambiguous separation of ω_G of graphite and ω_{2LO} of moissanite. (c) Dependence of ω_G with σ_{load} , as measured by the ω_{2LO} of moissanite (upper axis). Different symbols stand for different experimental runs. The black solid line represents the fitting function shown on top to account for the sub-linear dependence of ω_G with σ_{load} .

The Raman spectrum of graphite has been extensively studied and analysed under different stress conditions, both hydrostatic⁴⁰ and non-hydrostatic,^{29,30, 41, 42} using conventional gasketed anvil cells. A general observation is that the frequency of the G band, which originates from an in-plane vibration of E_{2g} symmetry, increases when compressive in-plane stresses are present. Thus, it was somewhat unexpected that in our experiments ω_G increases (Figs. 2a and c) when the stress was applied perpendicular to the basal plane of graphite with no gasket between the anvils. As a matter of fact, our

theoretical calculations predicted negligible changes on ω_G with uniaxial stress (Fig. 3b). Thus, our experiments reveal that, when graphite is squeezed between two opposed anvils, in addition to σ_{load} , other in-plane stress components appear on the sample. As we shall conclude later, the main in-plane stress component acting on the graphene layers derives from friction forces against sliding (σ_S in Fig. 1), resulting from locking confinement of the sample between the anvils (despite the absence of gasket between them).

Our calculations indicate that, when graphite is loaded along the c -axis, the interlayer distance strongly decreases while the lattice parameter a remains essentially constant (as shown in Fig. 3a, within the experimental stress range (σ_{load} : 0-4 GPa), a decreases in 0.13%). Despite the intrinsic interest of this result within the framework of auxetics,⁴³ it agrees with the fact that the c_{13} elastic constant of graphite is essentially null at room pressure,⁴⁴ becoming slightly negative under high stress. This also means that if the stress tensor includes only c -axis contributions, the shift observed in ω_G should be negligible or, at most, slightly negative (Fig. 3b), in clear contrast to the experimental results of Fig. 2c. Our calculations also demonstrate that a blue-shift in ω_G is only expected when the stress is applied within the graphene planes, in our case, biaxial stress. Interestingly, our calculated stress coefficient for ω_G (4.6 $\text{cm}^{-1}/\text{GPa}$) is in close agreement with that found in hydrostatic experiments,⁴⁰ as confirmed in Fig. 3c, thus explaining why both hydrostatic and biaxial experiments on graphite and graphene yield similar mode Grüneisen parameters for this band.³⁰

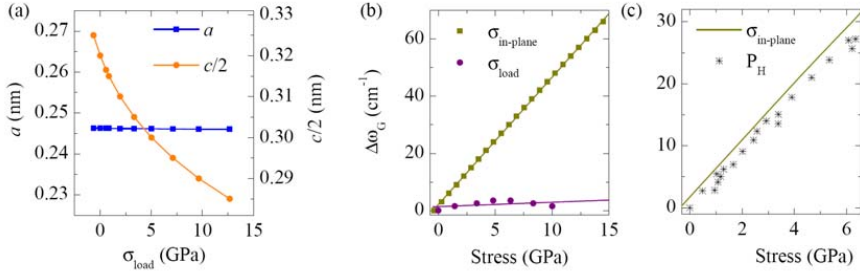


FIG. 3. (Color online) (a) Calculated lattice parameters, a and c , of graphite as function of the stress applied along the normal direction to graphene layers (σ_{load}), ($c/2$) corresponds to the interlayer distance between two graphene sheets. (b) Calculated Raman shift of the G band of graphite (referred to ω_G at zero pressure) as function of different stress components. (c) Comparison of calculated $\Delta\omega_G$ values under biaxial stress (solid line) and hydrostatic pressure (P_H) experiments (symbols) from Ref. [40].

Overall, the analysis of the experimental data in the light of our previous theoretical results confirms the hypothesis that when graphite is squeezed along the c -axis, compressive in-plane biaxial stress components are present. One may speculate that the largest in-plane contribution is due to frictional stress, but in order to determine its relative value, we must quantify other possible stress contributions during the experiments. Let us begin analysing the possible contributions concerning the graphite-anvil interface. Unlike graphite, moissanite exhibits positive c_{13} values (52 ± 9 GPa),⁴⁵ so shear stresses (σ_{shear}) may be transferred from the anvil to the sample, since the anvil is also non-uniformly stressed along the axial direction. Thus, an additional contribution to be considered concerns shear components from the center towards the border of the anvil culet (σ_{shear} in Fig. 1). Neglecting such contributions would result in an erroneous determination of the pure friction stress, σ_S , making it necessary to perform a detailed

analysis of the anvils response to stress in our particular experimental configuration. A recent procedure²³ to analyse the stress distribution of the anvils has been used to estimate the correlation between load and shear stress in moissanite: $\sigma_{shear} \approx 0.6\sigma_{load}$. This result is in excellent agreement with similar analyses in diamond along the [111] direction,⁴⁶ and agrees with the fact that both diamond and moissanite exhibit comparable ν_{13} Poisson ratios. In any case, the relevant conclusion is that the total stress acting on the sample in the in-plane direction, $\sigma_{in-plane}$, contains contributions from both friction and shear. Since $\sigma_{in-plane}$ can be estimated from existing correlations between ω_G and the applied stress,⁴⁰ the friction contribution can be calculated simply as $\sigma_S = \sigma_{in-plane} - \sigma_{shear}$. This contribution represents the average stress supported by about 90 graphene layers (considering the penetrability of the 532 nm radiation in graphite samples); being unlikely to discern between the behaviour of the first graphene layer, in direct contact with the anvil, and that of the rest of layers.

B. Friction Analysis

In order to check whether σ_S can be related to the microscopic sliding friction force between graphene layers, a deep analysis of our previous computer simulations in 3LG models²⁵ is carried out. We recover in Fig. 4a the energetic profiles of a graphene layer inside graphite sliding along different directions at zero stress. In Fig. 4b such profiles along the 0° direction at decreasing interlayer distances up to 0.280 nm (about 12.5 GPa) are displayed. The effect of the in-plane stress components has been evaluated and almost negligible variations were observed in the sliding distance, s , at which the energetic barriers appear. Along all the sliding directions considered, the 3GL model reaches the AAA configuration at sufficiently large distances, with the exception of the 30° and 90° ones. When applying load stress (i.e. decreasing the interlayer distances),

the energetic barriers just raise their height, but their location remain unaltered, as observed in Fig. 4b.

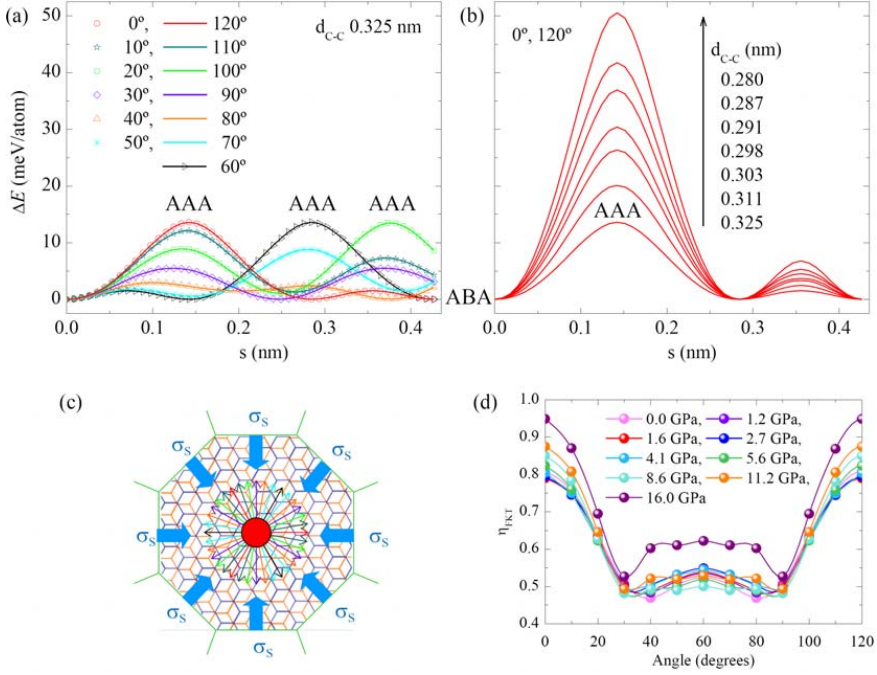


FIG. 4. (Color online) Calculated energy differences relative to the equilibrium energy of tri-layer graphene as a function of the sliding distance of the B central layer, s , (a) for selected sliding angles at an interlayer distance of 0.325 nm and (b) for the 0° direction at selected interlayer distances. (c) Rendering of the load (red) and friction (blue) forces acting on the graphite samples squeezed between the opposed anvils. As the sample is loaded, graphene layers tend to displace in all directions (colored arrows), but the confinement of the sample induces friction stresses opposed to the relative motion of the graphene layers. (d) Friction parameter in the 2D-FKT model (calculated with Eq. (1) at different load stresses) as a function of the sliding angle.

Our calculations predict that, if incommensurate displacements are allowed between graphene layers, the relative orientations of the layers must change according to the path of minimum energy, which, interestingly, does not change with the applied load (see Ref. 25). A similar behaviour was found in studies of a tip movement over the FCC(111) surface using a 2D Prandtl-Tomlinson model.¹⁷ Although we are interested here on the early stages of movement between the graphene sheets, the previous discussion demonstrates that this kind of computer simulations can be successfully used to analyse dynamic friction problems. The corrugation energy profiles in Fig. 4 resembles the potential of a 2D Frenkel-Kontorova-Tomlinson (FKT) model,¹⁷ where different one-dimensional FKT-like potentials appear depending of the sliding angle, with an angle periodicity of 120 degrees. From these profiles it is also possible to analyse the dimensionless parameter, η_{FKT} , which gives the boundary values for stick-slip processes included in the FKT model:¹¹

$$\eta_{FKT} = 2\pi^2 \frac{\Delta E_{1/2}}{ks^2}, \quad (1)$$

where $\Delta E_{1/2}$ and s are half the height and the sliding distance of the first energy barrier found along a given sliding direction, respectively, and k is the harmonic elastic constant that is obtained as the second derivative of the energy profile at the equilibrium position (ABA configuration).

In Figure 4d we plot η_{FKT} as a function of the sliding directions at different interlayer distances (*i.e.* different values of σ_{load}). We find that the preferred sliding directions are $(30+60n)$ degrees, where n represents an integer, whereas those directions at $(120n)$ degrees are the less favourable ones. Once again, the characteristics of the sliding directions are the same regardless the interlayer distance considered, since load does not change the ABA configuration. It is interesting to note that the value of η_{FKT} does not

show significant changes with load below 10 GPa. At higher stress (between 10-15 GPa) η_{FKT} increases, regardless the sliding direction considered, so it can be understood that, beyond that point, graphene sheets literally stuck each other with little chances to displace in any direction. Interestingly, within the same stress range (*ca.* 15-20 GPa) a cold-compression phase transition from graphite to a super-hard phase is now under debate,⁴⁷ so one would speculate that nucleation of the new phase might start when interlocking takes place between adjacent graphene sheets. This result opens new avenues for understanding the relationship between large friction forces and other phenomena under extreme stress conditions.

In any case, the important improvement against classical FKT analytical models¹⁷ is that our DFT calculations provide direct access to numerical values of the corrugation energy and, through the first derivative of the energy with respect to the sliding distance, to the friction force. As described in detailed in Ref. 25, from the results of Fig. 4a, and others similar at interlayer distances between 0.325 nm and 0.280 nm, σ_S can be calculated using the maximum force required to initiate motion between adjacent layers, so the analysis can be restricted to sliding distances below the first maximum in each energy curve. In addition, we can convert interlayer distances into σ_{load} using the equation of state we obtained in bulk graphite.²⁵ The results are plotted in Fig. 5a. These results allow us to compare both experimental and calculated friction forces and to give a global discussion of our study on the basis of existing contact mechanical models.⁴⁸ The main results are summarized in Figs. 5b and 6. The sub-linear variation observed in Fig. 5a, regardless the sliding angle considered, suggests using a Hertzian-like law⁴⁸ to fit the results, in the line of previous studies of different carbon materials under relatively low loads:³⁷

$$\sigma_S = \sigma_0 (\sigma_{load} - \sigma_R)^H. \quad (2)$$

In Eq. (2), σ_0 , σ_R and H are characteristic parameters of a Hertzian model including attractive forces, and it is analogous to the “*Hertz plus-offset model*” proposed by Schwarz *et al.*³⁷ We are dealing with a microscopic interpretation in terms of interactions involving the electronic density of the graphite layers, and it is not our aim to claim that the simulated behaviour obey equation (2). However, we think that it is worth to use the *Hertz plus-offset model* in our analysis since our data are well described with the above equation. In our case, we considered H as an adjustable parameter in order to evaluate whether graphite follows a purely Hertzian behaviour (σ_s scales as $\sigma_{load}^{2/3}$) or not at the atomic level. The parameters σ_0 , σ_R and H obtained from the fit are plotted in Fig. 6, where an evident angular dependence of each parameter is observed, thus reflecting the importance of the shape shown by the corrugation energy. Figure 6 also shows how these parameters change when the friction regime develops from static (black symbols) into dynamic (red symbols). The evolution of H in Fig. 6 reveals that, according to our calculations, loaded graphite tends to follow a Hertzian-like law only in the dynamic regime, in agreement with the low-loading experiments.³⁷

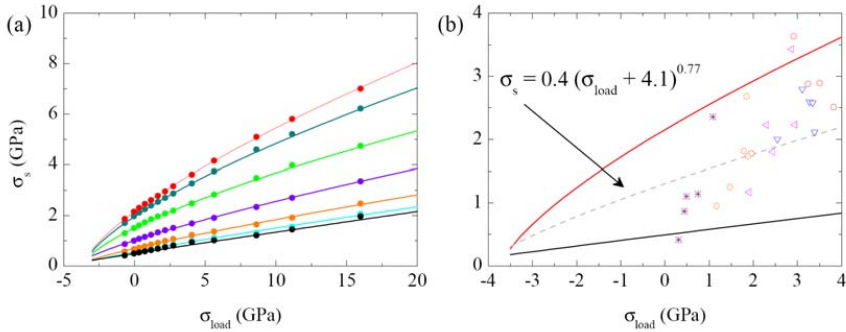


FIG. 5. (Color online) (a) Calculated static friction stress along selected sliding directions as a function of σ_{load} ; symbols stand for different sliding directions using the same color definitions of Fig. 4a; lines are fits to Eq. (2). These results correspond to the maximum stresses found along the selected sliding directions before reaching the first

energy maximum in Fig. 4a. (b) Comparison of the calculated static friction stress from (a) with the experimental values derived from Fig. 2c. The dashed line represents Eq. (2) using averaged values of the characteristics parameters shown in Fig 6; continuous lines represent the limiting values (sliding directions of 0° and 60°) plotted in (a).

.What is perhaps even more interesting from a fundamental point of view is the analysis of the parameter σ_R , which indirectly measures the effect of attractive forces included in more sophisticated models.⁴⁹ Thus, according to its definition in Eq. (2), σ_R also represents the negative (rupture) stress needed to separate two graphene sheets and gives an indirect measure of the exfoliation energy of graphene. In the field of equations of state (EOS), the same concept stands for the so-called spinodal stress,⁵⁰ which is intimately related to Born's stability conditions.⁵¹ To analyse this, we shall consider the linear, one-dimensional Murnaghan's equation,⁵² which takes the following form for the c -axis length in graphite:⁴⁰

$$\left(\frac{c}{c_0}\right) = \left(\frac{\beta'}{\beta_0} \sigma_{load} + 1\right)^{\frac{1}{\beta'}} \quad (3)$$

where c_0 is the length of the c -axis at zero stress, β_0 is the linear stiffness coefficient at zero stress and β' its first stress derivative. Thus, σ_R can be simply calculated as $\sigma_R = -(\beta_0/\beta')$ from known values of β_0 and β' . Using the results $\beta_0 = 35.7$ GPa and $\beta' = 10.8$ reported by Hanfland *et al.*⁴⁰ from EOS measurements using X-ray diffraction experiments in bulk graphite, the estimated value of σ_R is -3.3 GPa. This value is in good agreement with the average value of $\sigma_R = (-4.1 \pm 0.5)$ GPa, obtained from the analysis included in Fig. 6, and with the value of $\sigma_R = (-4.3 \pm 0.3)$ GPa, obtained with the parameters $\beta_0 = (50 \pm 1)$ GPa and $\beta' = 11.5 \pm 0.5$ from the fitting of (c/c_0) results of Fig. 3a to Eq. (3).

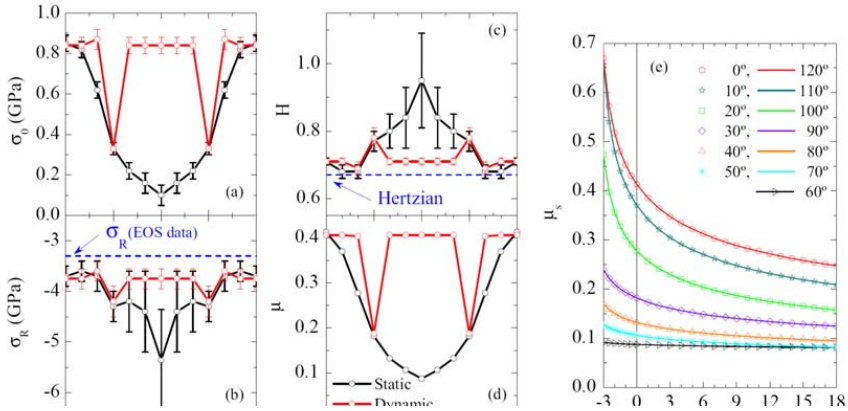


FIG. 6. (Color online) (a to c) Parameters in the Hertzian model with attractive forces, Eq. (2), in the static (black) and dynamic (red) regimes. The static results derive directly from the results plotted in Fig 5a, while dynamic results are obtained from the maximum stress found at large, formally infinite, sliding distances. (d) Friction coefficient at zero load as a function of the angle of the selected sliding directions for the static and dynamic regimes. (e) Static friction coefficient calculated along selected sliding directions as a function of σ_{load} , obtained from the derivative of σ_S , with respect to σ_{load} (Fig. 5a), using the parameters of Eq. (2).

Figure 6 also provides the appropriate framework to compare them with the experimental results given in Fig. 5b. Performing such a comparison demands transforming calculated friction forces (pN/atom) into stress (GPa) by dividing the calculated friction force by the effective surface occupied by a carbon atom (0.0261 nm^2). This effective surface has been obtained by considering an initial equilibrium carbon-carbon bond-length of 0.142 nm in the hexagonal lattice of graphene. Although experimental results show a large dispersion, they are nicely bounded by the limiting values (0° and 60° sliding directions) of the calculated static friction stress shown in Fig.

5a. This confirms that the Raman measurements average the static friction contributions across large interaction areas along all sliding directions. The dispersion in the experimental data observed in Fig. 5b is very likely related to the generation of defects in the initially perfect commensurate ABA structure of bulk graphite. Notice that in each run the experimental results tends to increase as the average stress increases, which indicates that shear components generate some concentration of defects (not very large though, according to the small intensity of the D band²² observed around 1350 cm^{-1} in the Raman spectrum of graphite, see Fig. 2a). Our experimental results thus suggest that, as the concentration of defects increases, the static friction also increases, in agreement with recent dynamic friction experiments in graphene.⁵³ However, it is striking that the average friction stress measured in each run nicely fits the average curve shown in Fig. 5b, which has been obtained by averaging the characteristic parameters shown in Fig. 6a to c.

Finally, the results of Fig. 5 can also be used to estimate boundary values for the static friction coefficient μ_S and its load dependence, Figs. 6d and 6e. Notice that the static friction coefficient is defined as the derivative of the load stress with respect to the load, and, therefore, it is a finite value at zero load stress, where a non-negligible static friction stress (the *offset* in the Hertzian model) is present. As expected, μ_S also strongly depends on the sliding direction, with values ranging between 0.1 and 0.4, in excellent agreement with the accepted experimental values.²⁸ It is also noticeable that μ_S remains nearly constant around 0.18 along the 30 and 90 degrees directions, in close agreement with the low friction regime observed in FFM studies.¹⁴ Another interesting issue concerns the strong decrease in μ_S observed with increasing σ_{load} , which means that the barrier between the regimes of static and dynamic friction in graphite gradually fades under compression.

IV. CONCLUSIONS

In summary, we have demonstrated that combination of novel anvil cell experiments with Raman analysis in graphite/graphene over large sampling regions and high-stress values evidences shear stresses associated with frictional forces. These experiments can be successfully interpreted by means of quantum-mechanical calculations providing relevant microscopic information and realistic static friction parameters with a quality comparable to those obtained in dynamic FFM experiments. Overall, this kind of measurements, combined with computer simulations and atomistic models, open new avenues for routinely studying static friction phenomena on graphene and other layered materials of technological relevance, like boron nitride or molybdenum disulphide. Our results also demonstrates: (i) that adhesive (*i.e.* attractive) forces play a major role in the frictional behaviour of graphite and graphene in both static and dynamic⁴ regimes, and (ii) that the inclusion of dispersive forces in atomic computer simulations, like that introduced here, is required to account for a realistic picture of friction at the atomic level.

Acknowledgements

We thank Prof. J. González (U. Cantabria) for useful discussions. This work was supported by the MICINN through the MALTA Consolider Project CSD2007-00045. Further financial support was obtained from MINECO through projects CTQ2009-14596-C02 and CTQ2012-38599-C02 and Comunidad de Madrid and EU through the S2009/PPQ-1551 program. E.C. was granted with a MICINN-FPU fellowship, which is also acknowledged.

References

- ¹ R. H. Savage, *J. Appl. Phys.* **19**, 1 (1948).
- ² B. Bhushan, *Introduction to tribology* (Wiley, 2002).
- ³ B. Bhushan, J. N. Israelachvili, U. Landman, *Nature* **374**, 607 (1995).
- ⁴ Z. Deng, A. Smolyanitsky, Q. Li, X-Q. Feng, R. J. Cannara, *Nature Mater.* **11**, 1032 (2012).
- ⁵ Y. Mo, K. Turner, I. Szlufarska, *Nature* **457**, 1116 (2009).
- ⁶ C. M. Mate, G. M. McClelland, R. Erlandsson, S. Chiang, *Phys. Rev. Lett.* **59**, 1942 (1987).
- ⁷ C. G. Lee, Q. Li, W. Kalb, X.-Z. Liu, H. Berger, R.W. Carpick, J. Hone, *Science* **328**, 76 (2010).
- ⁸ Filleter, T.; McChesney, J. L.; Bostwick, A.; Rotenberg, E.; Emtsev, K. V.; Seyller, Th.; Horn, K.; Bennewitz, R. *Phys. Rev. Lett.* **2009**, *102*, 086102.
- ⁹ A. L. Kitt, Z. Qi, S. Remi, H. S. Park, A. K. Swan, B. B. Goldberg, *Nano Lett.* **13**, 2605 (2013).
- ¹⁰ Z. Liu, J. Yang, F. Grey, J. Z. Liu, Y. Liu, Y. Wang, Y. Yang, Y. Cheng, Q. Zheng, *Phys. Rev. Lett.* **108**, 205503 (2012).
- ¹¹ A. Socoliuc, R. Bennewitz, E. Gnecco, E. Meyer, *Phys. Rev. Lett.* **92**, 134301 (2004).
- ¹² A. Smolyanitsky, J. P. Killgore, *Phys. Rev. B* **86**, 125432 (2012).
- ¹³ M. Hirano, K. Shinjo, *Phys. Rev. B* **41**, 11837 (1990).
- ¹⁴ M. Dienwiebel, G. S. Verhoeven, N. Pradeep, J. W. M. Frenken, J. A. Heimberg, H. W. Zandbergen, *Phys. Rev Lett.* **92**, 126101 (2004).
- ¹⁵ F. P. Bowden, L. Leben, *Nature* **141**, 691 (1938).
- ¹⁶ M. H. Müser, M. Urbakh, M. O. Robbins, *Adv. Chem. Phys.* **126**, 187 (2003).
- ¹⁷ Y. Dong, A. Vadakkepatt, A. Martini, *Tribol. Lett.* **44**, 367 (2011).
- ¹⁸ M. Weiss, F.-J. Elmer, *Phys. Rev. B* **53**, 7539 (1996).

- ¹⁹ M. Mishra, P. Egberts, R. Bennewitz, I. Szlufarska, *Phys. Rev. B* **86**, 045452 (2012).
- ²⁰ F. P. Bowden, D. Tabor, *The friction and lubrication of solids* (Oxford, 1954).
- ²¹ Y. Wang, D. C. Alsmeyer, R. L. McCreery, *Chem. Mater.* **2**, 557 (1990).
- ²² L. M. Malard, M. A. Pimenta, G. Dresselhaus, M. S. Dresselhaus, *Phys. Rep.* **473**, 51 (2009).
- ²³ E. Del Corro, J. G. Izquierdo, J. González, M. Taravillo, V. G. Baonza, *J. Raman Spectrosc.* **44**, 758 (2013).
- ²⁴ J. R. Ferraro, *Vibrational Spectroscopy at High External Pressures. Handbook of Vibrational Spectroscopy* (Wiley, 2006).
- ²⁵ D. Abbasi-Pérez, A. Otero-de-la-Roza, E. del Corro, M. Marqués, J. M. Menéndez, M. Taravillo, V. G. Baonza, J. M. Recio, *Phys. Rev. B* **90**, 054105 (2014).
- ²⁶ S. Grimme, *J. Comp. Chem.* **27**, 1787 (2006).
- ²⁷ T. Bucko, J. Hafner, S. Lebegue, J. G. Angyan, *J. Phys. Chem. A* **114**, 11814 (2010).
- ²⁸ D. Maugis, *Contact, Adhesion and Rupture of Elastic Solids* (Springer-Verlag, 2000).
- ²⁹ E. del Corro, M. Taravillo, V. G. Baonza, *Phys. Rev. B* **85**, 033407 (2012).
- ³⁰ E. del Corro, A. Otero-de la Roza, M. Taravillo, V. G. Baonza, *Carbon* **50**, 4600 (2012).
- ³¹ V. G. Baonza, M. Taravillo, A. Arencibia, M. Cáceres, J. Núñez, *J. Raman Spectrosc.* **34**, 264 (2003).
- ³² E. Del Corro, J. González, M. Taravillo, E. Flahaut, V. G. Baonza, *Nano Lett.* **8**, 2215 (2008).
- ³³ P. Giannozzi, S. Baroni, N. Bonini, M. Calandra, et al., *J. Phys.: Condens. Matter* **21**, 395502 (2009).
- ³⁴ G. Kresse, J. Furthmuller, *Phys. Rev. B* **54**, 11169 (1996).
- ³⁵ J. P. Perdew, K. Burke, M. Ernzerhof, *Phys. Rev. Lett.* **77**, 3865 (1996).

- ³⁶ A. M. Rappe, K. M. Rabe, E. Kaxiras, and J. D. Joannopoulos, Phys. Rev. B **41**, 1227 (1990).
- ³⁷ U. D. Schwarz, O. Zwörner, P. Köster, R. Wiesendanger, Phys. Rev. B **56**, 6987 (1997).
- ³⁸ R.J. Nemanich, S. A. Solin, Phys. Rev. B **20**, 392 (1979).
- ³⁹ E. del Corro, M. Taravillo, J. González, V. G. Baonza, Carbon **49**, 973 (2011).
- ⁴⁰ M. Hanfland, H. Beister, K. Syassen, Phys. Rev. B **39**, 12598 (1989).
- ⁴¹ A. F. Goncharov, High Press. Res. **8**, 607 (1992).
- ⁴² M. Peña-Álvarez, E. del Corro, V. G. Baonza, M. Taravillo, J. Phys. Chem. C. DOI: 10.1021/jp505730v.
- ⁴³ R. H. Baughman, Nature **425**, 667 (2003).
- ⁴⁴ A. Bosak, M. Krisch, M. Mohr, J. Maultzsch, C. Thomsen, Phys. Rev. B **75**, 153408 (2007).
- ⁴⁵ K. Kamitani, M. Grimsditch, J. C.; Nipko, C. K. Loong, M. Okada, I. Kimura, J. Appl. Phys. **82**, 3152 (1997).
- ⁴⁶ Y. Akahama, H. Kawamura, J. Appl. Phys. **98**, 083523 (2005).
- ⁴⁷ S. E. Boulfelfel, A. R. Oganov, S. Leoni, Sci. Rep. **2**, 471 (2012).
- ⁴⁸ K. L. Johnson, *Contact Mechanics* (Cambridge University Press, 1985).
- ⁴⁹ D. Maugis, J. Colloid Interface Sci. **150**, 243 (1992).
- ⁵⁰ E. Francisco, M. Bermejo, V. G. Baonza, L. Gerward, J. M. Recio, Phys. Rev. B **67**, 064110 (2003).
- ⁵¹ M. I. Born, Proc. Camb. Phil. Soc. **36**, 160 (1940).
- ⁵² F. D. Murnaghan, Proc. Natl. Acad. Sci. **30**, 244 (1944).
- ⁵³ X. Liu, T. H. Metcalf, J. T. Robinson, B. H. Houston, F. Scarpa, Nano Lett. **12**, 1013 (2012).

Building Motifs during Self-Assembly of *para*-Terphenyl-*meta*-dicarbonitrile on a Metal Surface: A Gas-Phase Study

D. Abbasi-Pérez,[†] J. M. Recio,^{*,†} and L. Kantorovich[‡][†]Departamento de Química Física y Analítica, Facultad de Química, Universidad de Oviedo, Julian Clavería, 8, 33006 Oviedo, Spain[‡]Physics Department, King's College London, Strand, London WC2R 2LS, United Kingdom

ABSTRACT: Various structural motifs such as 1D ribbons and their interconnections were recently seen in scanning tunneling microscopy experiments when *para*-terphenyl-*meta*-dicarbonitrile (pTmDC) molecules were deposited on the Ag(111) surface (Marschall, M.; et al. *ChemPhysChem* 2010, 11, 1446). By using ab initio density functional theory calculations, we systematically study the main building blocks that the two isomers of the pTmDC molecules can form in the gas phase, going from dimers to more complex structures involving trimers, chains, and various linkers. We show that the hydrogen bonding plays a decisive role in the formation of the different experimentally observed structures. We have also found that the energy barriers for the isomerization transition for a single molecule in the gas phase are always lower than 9.6 kJ/mol, proving that there must be equal amounts of both isomers on the surface initially at deposition.



INTRODUCTION

Self-assembly of organic molecules on crystal surfaces is an essential tool in fabricating nanodevices.^{1–3} Because of its directionality and significant binding strength, hydrogen bonding between molecules has been widely exploited in building surface molecular assemblies. Detailed knowledge of the interaction between molecules is crucial in identifying the basic building units, thus providing a simple route in understanding of the self-assembled motifs.^{4,5} Obviously, how these motifs are organized is also influenced by the nature (chemical versus physical) of the molecule–surface interaction.

In a recent experimental study,⁶ deposition of [1,1';4',1'']-terphenyl-3,3'-dicarbonitrile (also known as *para*-terphenyl-*meta*-dicarbonitrile or pTmDC in short) molecules on the Ag(111) surface was investigated by scanning tunneling microscopy (STM). In the gas phase, these molecules may exist in cis and trans forms (isomers), shown in Figure 1. Although the cis isomer is achiral, trans isomer is, however, prochiral; that is, depending on which side the molecule gets adsorbed on the surface, two possibilities exist denoted L- and D-trans. Correspondingly, both trans species form equivalent structures that are mirror reflections of each other.

Using STM, it was found that at low deposition the molecules form 1D ribbons that intrinsically intercross by means of various linkers. It was proposed that in all of these structures the molecules bind to each other via double hydrogen bonds. Moreover, it was suggested based on high-resolution STM images that ribbons are constructed exclusively from trans isomers and only a small amount of cis isomers can be found on the surface, mostly in linkers.

By employing ab initio density functional theory (DFT) calculations, we investigate in this paper theoretically possible structures that the pTmDC molecules may form with each other. Our main goals are: (i) to provide a rational explanation

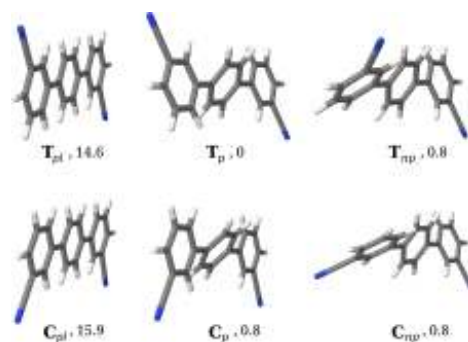


Figure 1. DFT relaxed geometries found for different conformers of the pTmDC molecule. Legends: C, cis; T, trans; subscript pl, planar; p, parallel; and np, nonparallel. (See definitions in the text.) Numbers next to the labels are relative energies in kilojoules per mole. Blue ends represent the N atoms, white ends represent H atoms, and gray color corresponds to C atoms.

at an atomic level of the experimentally observed structures of pTmDC molecules on the Ag(111) surface and (ii) to demonstrate the dominant role that the hydrogen bond plays in holding these molecules together. It was stated that there is a broad range of H bonds that depend on the particular species participating and the specific atomic environment, all united by a “pronounced local aspect”.⁷ Following this criterion, we believe that the binding between the molecules studied here corresponds to an attractive interaction between a nitrile group

Received: December 15, 2013

Revised: February 18, 2014

Published: March 10, 2014

of one monomer and one or two H atoms from a benzonitrile ring of the other and can be characterized as an H bond bearing in mind that contribution of the dispersion interaction (as will be shown later on) is essential. If we are to believe that H bonding is the main binding mechanism of intermolecular interactions, then dimers would serve as the elementary building blocks in forming various structures on the surface. Both points will be demonstrated in this contribution.

In all of the calculations reported in this paper, we do not explicitly simulate the surface when studying various molecular structures; all computations have been done in the molecular gas phase with the role of the surface being implicit: only structures that have 2D character were examined. This is a rational computational strategy, which enabled us to consider at a moderate cost relatively large molecular assemblies needed for direct comparison with those seen in experimental images and hence evaluate the role played exclusively by the H bonding between molecules in forming these assemblies. The complete modeling of the phenomena including the role of the surface is currently being undertaken and will be reported separately.

The plan of the paper is as follows. In the next section our computational procedure is briefly described. Results are presented and discussed in four different subsections: Monomers, Dimers, Ribbons, and Linkers. The paper is finished with the main conclusions of our work.

METHODS

Calculations have been carried out in the framework of the DFT^{8,9} using the open source computer code CP2K/QUICKSTEP.¹⁰ It implements the hybrid Gaussian and plane-wave method (GPW)¹¹ whereby atom-centered Gaussian-type functions are used to describe the Kohn–Sham wave functions; however, an on-the-fly conversion is made to a plane-wave basis set to calculate efficiently the electrostatic energy. Atomic cores are represented using Goedecker–Teter–Hutter (GTH)¹² pseudopotentials. We used the Perdew–Burke–Ernzerhof (PBE) generalized gradient exchange–correlation functional,¹³ whereas the Grimme’s DFT-D3 method¹⁴ was employed for taking into account the dispersion forces. We have chosen the optimized basis set m-DZVP¹⁵ for all atoms and a plane-wave cutoff energy of 280 Ry. Geometries were relaxed until forces on atoms became < 0.02 eV/Å. All calculations have been done using periodic boundary conditions, and in the cases of the calculations on individual clusters of molecules, we ensured that units cells big enough so as to make the interaction between neighboring clusters negligible were considered. It was suggested in a detailed study based on systematic quantum-chemistry calculations that DFT-based methods perform reasonably well for H-bonded systems.¹⁶

Binding energy of a complex ABC... obtained by combining species A, B, C, and so on together is defined as

$$E_{\text{bind}} = E_{\text{ABC...}} - E_A^0 - E_B^0 - E_C^0 - \dots$$

where $E_{\text{ABC...}}$ is the DFT total energy of the complex and E_A^0 , E_B^0 , and so on are the energies of the individually relaxed species A, B, and so on, respectively. However, as we employed a localized basis set, we need to consider the basis-set superposition error (BSSE) for computing the actual binding energy of the complex. It was calculated by means of the (positive) counterpoise (CP) correction¹⁷ being added to the previous expression for the binding energy. The latter requires

calculating species A, B, and so on individually in an extended basis set comprised of orbitals of each respective species and the “ghost” orbitals of other species.

For accessing the energy barriers involved in the cis–trans isomerization process of a monomer, we computed the minimum energy path (MEP) between all stable configurations by means of the nudged elastic band (NEB)^{18,19} method. Both improved tangent NEB and the climbing image NEB calculations^{20,21} were employed, as discussed later.

To illustrate the strength of H bonds, we used two methods. In the first one, we analyzed charge-density differences in various structures. These were calculated by subtracting from the electron density $\rho(\mathbf{r})$ of the combined system the densities of the corresponding parts calculated at the geometry of the combined system. In the second method, we analyzed the topology of the electron density using the so-called (dimensionless) reduced density gradient^{22–24}

$$s(\mathbf{r}) = \frac{1}{2(3\pi^2)^{1/3}} \frac{|\nabla\rho(\mathbf{r})|}{\rho(\mathbf{r})^{4/3}}$$

which is specially designed to identify regions where non-covalent interactions (NCIs) play a dominant role. In visualizing $s(\mathbf{r})$, the isosurfaces are colored on a blue–green–red scale according to the values of $\text{sign}(\lambda_2)\rho(\mathbf{r})$, whose values range between –0.02 and 0.02. Here λ_2 is the middle eigenvalue of the Hessian matrix of the density. With this color scheme, red indicates strong nonbonding (steric) repulsion, green indicates weak interaction, and blue detects strong attractive interaction, for example, the H bonding.

RESULTS

Monomers. We start by discussing structures and energetics of the pTmDC monomers. After an exhaustive search of possible atomic equilibrium configurations, we obtained six stable conformations that can be grouped in three sets, each including the cis (C) and trans (T) isomers, plotted in Figure 1. The set with higher energies (denoted with a subindex pl) contains planar geometries in which all atoms are within a plane. The other two sets contain nonplanar conformations. We call parallel (labeled with p) those conformations that have the atoms of only the two end benzonitrile rings being in the same plane, whereas the nonparallel configurations (labeled with np) refer to monomer conformations where all three rings are in three different planes. In these two nonplanar sets, the dihedral angles between rings lay in the range of 32–40°. Differences between the energies of all p and np structures, including both C and T isomers, are almost negligible, while the planar geometries lie ~14.6 kJ/mol higher in energy, that is, are much less favorable. Detailed energetic information about all found stable gas-phase structures is collected in Figure 1. Our results clearly illustrate that isolated monomers in the gas phase are preferably nonplanar and that they could be with equal likelihood in either T or C geometry because both isomers are almost indistinguishable in energy.

We have also calculated dipole moments of the molecules. These for the parallel and nonparallel geometries were found to be 7.9 and 6.5 D for C and 0.3 and 4.4 D for T, respectively.

Because it was claimed that the number of cis molecules on the surface is significantly reduced after evaporation and assembly,⁶ it is essential to understand whether indeed cis to trans isomerization does not happen in the gas phase prior to the molecules to adsorb on the surface. Therefore, to obtain a

deeper understanding of the isomerization mechanism and to estimate the energetic cost involved in this process, we carried out NEB calculations. Starting from the C_p conformation, we calculated the MEP for one end ring of the molecule being rotated by 360° along its backbone passing through three other possible conformers C_{np} , T_p , and T_{np} until the same initial conformation C_p is reached again. We divided the isomerization path in four steps, each step corresponding to the path between two nearest stable geometries. Within each step, we created 8 replicas (including the two fully relaxed structures at the ends) and computed 11 improved tangent NEB steps before moving to the climbing image NEB calculation.^{20,21} The energetic profile along this rotation, including schematic views of the relevant intermediate conformations, is shown in Figure 2. In

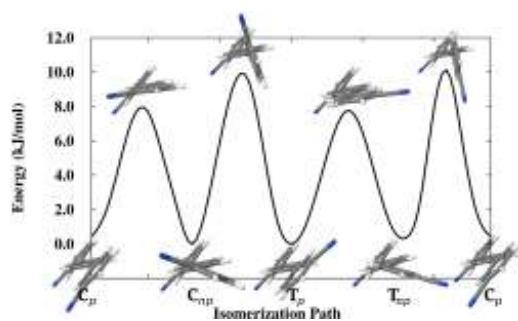


Figure 2. DFT calculated MEP of the isomerization process considered by rotating one end ring of the molecule by 360° around its backbone using the NEB method. Colors as in Figure 1. Reading the graph from left to right, the obtained geometries correspond to a clockwise rotation of the front ring. Correspondingly, each conformer has two possible paths for isomerization into another one following one of the two possible directions.

this way, we obtain all possible isomerization paths for transforming one conformer into any other stable conformer following either a clockwise or anticlockwise rotation of the ring. As we can see, planar conformations never happen along the isomerization path. If the $C_p \rightarrow C_{np}$ and $T_p \rightarrow T_{np}$ transitions can be attributed to steric hindrance, the other two transitions are most likely to do with peculiar restructuring of the occupied molecular orbitals resulting from the transition between the two isomers.

The highest barrier, ΔE , obtained for the transformation between C and T isomers is ~ 9.6 kJ/mol. This corresponds, at room temperature, to the rate of $\sim 10^{11}$ isomerizations per second. This very high rate means that the isomerization process occurs very easily at room temperature. Using this result, we can conclude that the four nonplanar isomers are almost equally favorable in the gas phase, and their expected population will be approximately the same. In other words, one should assume that there will be equal amounts of the C and T gas-phase isomers prior to their adsorption on the silver surface. Hence, upon deposition, there must be 50% of cis and 25% of each of the trans isomers.

Dimers. As will be shown later on, a rational explanation of the pTmDC structures experimentally observed on the Ag(111) surface can be provided assuming that the hydrogen bonding (H bonding) plays the dominant role in holding the molecules together. Because the H bonding is highly direc-

tional, it seems very reasonable to think about dimers as the most elementary building blocks of the many pTmDC motifs experimentally found on top of this surface. Thus, the next logical step is to fully characterize all possible dimers two molecules may form.

Therefore, we performed full geometry optimization of a large sample of different dimer configurations. In Figure 3, we show the relaxed geometries, along with the corresponding binding energies, for 20 dimers found (more were tried but found unstable; not shown). We have tried to be exhaustive in our search by mimicking, as much as possible, all patterns found in the experimental STM images (see figures 3–5 in ref 6) as well as many other possibilities, and no more stable dimer conformations were found.

By looking at the results presented in Figure 3, we can classify all dimers in three main groups according to their binding energies. The first one contains dimers CT- Tri_{2np} , CC- Tri_{2np} , TT- T_2 , TT- Lin_2 (numbers 1–4); the second group includes TT- P_{2a} , CC- P_{2a} , CT- P_{2a} , TT- P_{2b} , TT- Lin_1 , CC- Lin_1 , CT- P_{2b} , CC- P_{2b} , TT- Tri_2 , CC- Tri_2 , CT- Tri_2 (5–15); and the rest of the dimers form the last group. The first group consists of stable nonplanar monomers bonded by two hydrogen bonds, only one of them presenting a linear C–N–H arrangement. The binding energies in the first group are all around -29.0 kJ/mol with a minimum distance between monomers being ~ 2.4 Å (measured by the shortest distance between atoms of the two molecules). The dimers of the second group have binding energies between -2.1 and -11.7 kJ/mol. Here minimum distances between monomers are within the 2.37 to 2.41 Å range, similar to the dimers in set one. This group is mainly formed (dimers 5–8 and 11–15) by planar monomers bonded by two hydrogen bonds. Dimers 9 and 10 are bound by a single H bond but are nonplanar, which gives them an extra stability. The two H bonds of the most stable planar conformations in this group (dimers 5–8, 11, and 12) are both linear (in the sense that the three atoms involved align along a line), while the other three planar conformations (dimers 13–15) display one linear and one nonlinear H bond. Dimers 5–8 and 11 and 12 present similar arrangements of the two molecules, with dimers 5–7 being found to be slightly more stable. This presumably may be due to lack of steric repulsion of the hydrogens that are between the hydrogen bonds; we shall return to this point later. Differences in energies between the dimers 8, 11, and 12 are due to the specific isomers forming the dimers: T–T is slightly more stable than T–C, and the latter is more stable than C–C, but differences are almost negligible. With respect to the third group, these dimers have positive binding energies, and distances between monomers are bigger than 2.41 Å. In dimers 16 and 17, monomers are bonded by two nonlinear H bonds. Dimer 18 has lower energy than 19 and 20, even though it presents nonlinear H bond because it does not have this steric repulsion effect.

We note that despite being unstable, dimers of the last group are worth discussing because these conformations may be involved in the self-assembly process of the pTmDC molecules on the silver surface. Moreover, simple rearrangements may lead these dimers to other stable configurations. For example, if we compare dimer 19, which is unstable, with dimer 5, which is the most favorable conformation within the planar dimer set, we see that a cis–trans isomerization of one of the monomers can convert one structure (19) into the other (5). The same happens between dimers 20 and 8. Another interesting example

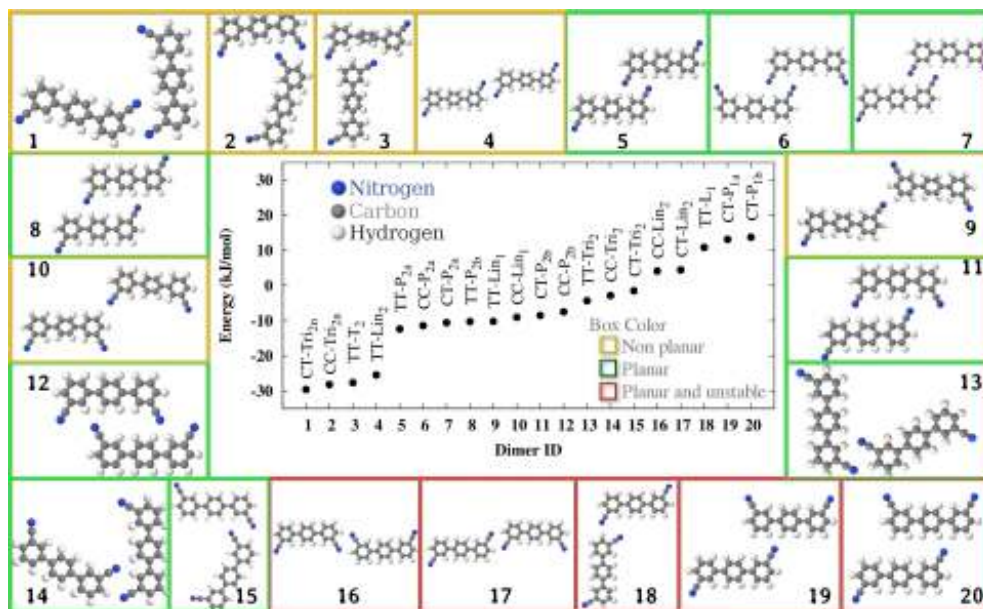


Figure 3. DFT calculated binding energies (in kilojoules per mole, the central panel) and relaxed geometries of dimers considered here. The legend used to denote the dimers means: the first two characters are composed of either C or T corresponding to the cis or trans conformations of the constituent monomers; the next letter is either L, T, P, Tri, or Lin and refers to L-like, T-like, parallel, triangular, or linear forms, respectively; the index 1 or 2 that follows corresponds to the number of hydrogen bonds in the dimer; finally, a n subscript is used for nonplanar triangular dimers, and a subscript a or b is used to differentiate between similar parallel structures. All dimers are numbered from 1 to 20, and their binding energies are shown in the plot in the center of the Figure. Around the energy plot, all 20 relaxed structures are shown. Yellow and green frames are used to indicate stable nonplanar and planar geometries, respectively, while the red frame is used for unstable planar structures found.

is the formation of the ribbon from the unstable dimer 16, which yields a stable chain. (See the Ribbons section below.)

Finishing with the energetics and geometry analysis of the dimers, several general conclusions can be made, and most of them are chemically intuitive. First, nonplanar structures are clearly more stable than the planar ones. Second, the greater the number of H bonds, the more stable the structure is. Third, linear H bonds when the three atoms involved in it (C, N, H) are arranged along a line are generally stronger than when they are not, that is, when the H bond is nonlinear. Finally, a rather small destabilization comes from steric repulsion between H atoms not involved in the H bonds but which are close to them. In addition, there is also a small preference for the T isomers to form a dimer as compared with C isomers.

It is now interesting to get insight into the H bonding mechanism by looking at the electron density differences. A selection of illustrative dimers is shown in Figure 4. The so-called “kebab-like” structure shows up^{25–27} between the hydrogens of the phenyl rings and the nitrogen of the carbonitrile group, clearly indicating the fingerprint of the H bond. Looking at dimers 5, 6, 8, 11, 12, 14, 19, and 20, one can notice a small excess of charge electron density (purple point) over the hydrogen adjacent to the two hydrogens involved in the H bond. This is due to the H bond being formed not with one but with two H atoms, which has a destabilizing effect on its energetics. (Note that stability of dimers starting from number 5 reduced abruptly by ~ 15.0 kJ/mol as compared with the dimers of the first group, as is seen in Figure 3.) Equivalently, the character of the interaction between two

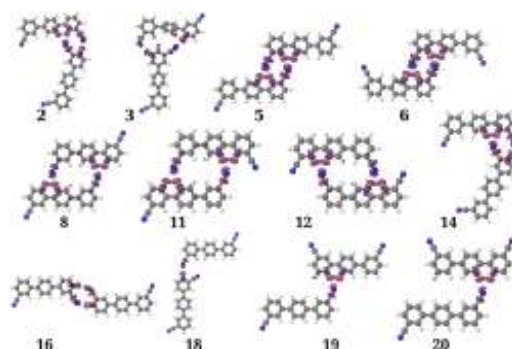


Figure 4. Electronic density difference maps of the most representative dimers with the hydrogen bond distances being between 2.37 and 2.61 Å. The purple isosurface indicates an excess and maroon indicates a depletion of the electron density in the dimers compared with two isolated monomers. Isosurfaces are drawn at ± 0.0007 electron/Å³.

monomers can be revealed by looking at the NCI plots, as demonstrated in Figure 5B. Besides the steric repulsion seen inside the benzene rings (red regions), a common pattern²³ associated with the H bonding (a combination of blue and green regions here) can be seen at precisely the same positions, as shown by the density difference plot, Figure 5A. The green–blue colors indicate an intermediate strength of the H bonding, which one would expect for the case of the (C–H)₂⋯N–C

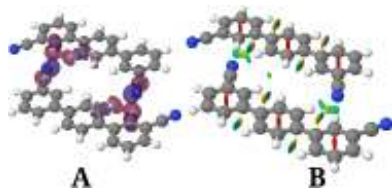


Figure 5. Comparison of the charge density difference (A) and NCI (B) plots for the dimer $CC\text{-}P_{2b}$. In panel A, the same colors and the density value were used as in Figure 4, while the value of $s = 0.5$ was used in panel B for the NCI plot. (See the Methods section for the explanation of the color scheme used.)

atomic arrangement. Because the two methods give equivalent results on the interaction between molecules, in all cases considered later only the density difference method will be used for simplicity. Note that both methods clearly show a local character for the bonding and hence, in agreement with the definition given in Introduction, can be characterized as H-bonding interactions.

We find that dispersion interaction contributes significantly into the H-bonding interaction between molecules, amounting to between 30 and 50% of the binding energy for strongly bound dimers (from 1 to 4). In the cases of weakly bound dimers, the contribution of the dispersion interaction was found to be even higher, which is the dominant contribution in many cases. We also looked at the dipole–dipole interaction between different dimers but found this part of the electrostatic energy amounting only up to 10% of the total binding energy for some C–C dimers. Although a more careful analysis is needed for understanding in detail the binding mechanism in all cases considered here using, for example, the methods discussed in refs 7 and 16, this kind of analysis goes beyond the scope of this study, the main goal of which is to rationalize molecular assemblies observed by STM.

Ribbons. The next natural step in forming the structures that the monomers can build is by proposing simple linear-like conformations, which we shall call ribbons. This type of polymers appears frequently in the experimental STM images of the low-coverage phase of pTmDC molecules on the Ag(111) surface.⁶ Using dimers as the basic building blocks, we have explored the energetics and optimal geometries of a number of these type of linear structures. In the optimization procedure, the coordinates of all atoms in the unit cell containing a dimer were allowed to relax, while the cell parameters were maintained fixed in our model. Predominantly five arrangements emerged as the most favorable candidates for these ribbons, all shown in Figure 6.

All of these ribbons are formed by repetitions of dimers presenting two hydrogen bonds. For simplicity, only ribbons with two molecules in the 1D unit cell were considered. The stability of the ribbons is expected to be greater per molecule compared with the corresponding dimer used to build it, as the number of H bonds per molecule is greater in the ribbon. The ribbon TT_B is constructed by repetition of the dimer $TT\text{-}P_{2b}$, the ribbon TT_A is constructed from the dimer $TT\text{-}P_{2a}$, the ribbon TT_{Lin} is constructed from a dimer very similar to $CT\text{-}Lin_2$ in which both monomers are trans, the ribbon CC_A is constructed by repetition of the dimer $CC\text{-}P_{2a}$, and finally the ribbon CC_{Lin} is formed by repeating the dimer $CC\text{-}Lin_2$. Interestingly, unstable planar linear-like dimers are able to form stable infinite linear chains. Moreover, those chains displaying

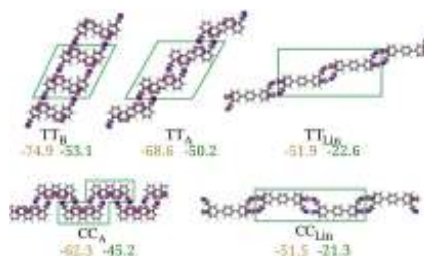


Figure 6. DFT relaxed considered ribbon conformations. The building-block motif is boxed in green. C or T letters denote cis or trans monomers. Notice that subscripts A and B refer to chains formed by parallel dimers of kind P_{2a} and P_{2b} , respectively, and Lin for the linear one. (See Figure 3.) Yellow and green numbers correspond to the binding energies (in kilojoules per mole) of the nonplanar and planar geometries, respectively. Charge density differences are shown for each structure with the color scheme as in Figure 4

linear H bonds are clearly more stable than those with nonlinear H bonds. This happens for both planar and nonplanar conformations, although the nonplanar conformation in each case is always more favorable than the planar one. This is demonstrated in Figure 6, where the binding energies (per two molecules) are written in yellow and green for nonplanar and planar conformations, respectively.

The linearity of these polymers is apparent, and hence a longitudinal axis (LA) can be defined for each structure going symmetrically along the ribbon. Different widths of the ribbons can be observed, with TT_B and TT_{Lin} being the widest and the thinnest conformations, respectively. Another visual parameter useful for the analysis of the STM images⁶ is the directionality of the ribbon. Taking the backbone of the monomer as a reference direction, the angle of the LA of the ribbons varies from 0° (CC_A and CC_{Lin}) to 30° (TT_{Lin}), 45° (TT_A), and 60° (TT_B). Thus, different directionalities are expected for these linear chains. This is an interesting result in a broad agreement with the images observed in the experiments. The ribbon TT_A is one of the two most stable structures and has been observed experimentally in the STM images.⁶ The repeating unit of the third ribbon in stability, CC_A , has also been observed in STM images. Clearly, other structures have not been seen, which is likely due to adverse effects of the surface that are missing in this preliminary study.

Each ribbon conformation also presents different border shapes. The consideration of this feature may be useful if we analyze possibilities of the ribbons to form 2D monolayers when the ribbons lie side-by-side. The TT_B border is almost straight, but TT_A and TT_{Lin} both present kinks. Chains of the cis isomers are of the zigzag shape. A dense packing of the ribbons strengthened by (rather weak) dispersion interactions between them is possible in all cases. Experimentally, 2D monolayers made of TT_A ribbons have indeed been observed, although other possibilities (CC_A or TT_B) could fill the surface space as well.⁶

Linkers. Looking at the STM images of ref 6, we are able to identify some pTmDC clusters that are associated with the changes in the directionality of the ribbons. These clusters can be understood as conformations of (mainly) three monomers of different chirality but with the same functional role, namely, that of connecting ribbons together. For this reason, we shall name these structures linkers. In Figure 7, we show molecular

models for some of this type of observed arrangements of the pTmDC molecules on the silver surface.

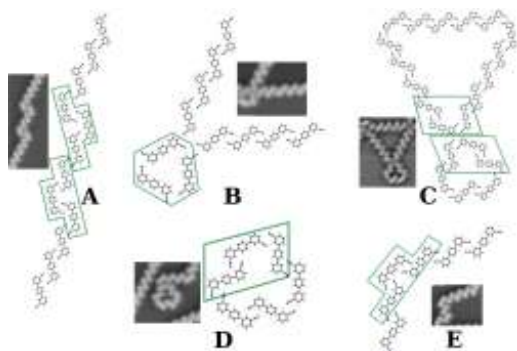


Figure 7. Some structures observed experimentally in STM images (adapted with permission from ref 6) and their proposed atomistic models constructed from the dimer building blocks. Different linkers involved in the structure are placed in a green box-like frame.

Inspired by the STM images of the linkers, we developed a number of atomistic models for clusters of molecules that may serve as linkers connecting ribbons. Optimized configurations have been obtained for the isolated clusters following similar computational procedures as in the previous cases previously described. The clusters we considered are shown in Figure 8 inside a box-like frame. The experimentally seen linker A in Figure 7 has been modeled as a cluster CCT-Lin, linker E was modeled as TCT'-Lin, while the triangular linker B was modeled as TTT-Tri. The cluster TCT-B serves as a model for

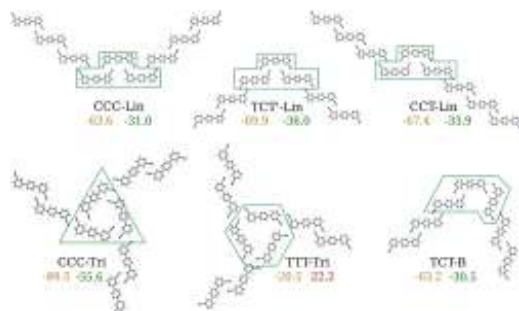


Figure 8. DFT relaxed geometries and binding energies (in kilojoules per mole) of several linkers investigated in this study. The actual systems computed were isolated clusters containing several molecules; they are indicated by a box-like green frame. In each case, schematics are also given of how ribbons may actually connect to the linkers; the molecules in the ribbons were not included in the calculations. Legend: the first three characters, either C or T, show which monomers are involved in the linker. Prime is used to note that trans isomers in the linker are stereoisomers. The index Lin is used when all monomers are parallel, while Tri is used if they form a triangle; finally, B designates the linker type when the features of both conformations (Lin and Tri) are present. Yellow numbers correspond to the binding energies of nonplanar, while green is used for the relaxed planar conformations and red is used for the unstable planar triangular structure.

the linker D or C in Figure 7. Additional clusters CCC-Lin and CCC-Tri that apparently are absent on published STM images (but may as well exist on the surface) were also modeled. We also schematically show in this Figure how ribbons may attach to our linkers. Note that the ribbons are shown only for illustration of the way the linkers work; they were not included in our actual calculations. In all cases, we assumed that the linkers connect the ribbon TT_A from Figure 6, as only this particular chain was clearly observed in the STM images in ref 6.

It is worth to remark that dimers also appear here as elementary building blocks; this can be easily identified in each of the different clusters gathered in Figure 8. In particular, linkers CCC-Lin, TCT'-Lin, and CCT-Lin display binding mechanisms associated with CC- P_{2a} and CT- P_{2a} dimers. In the CCC-Tri linker, we can see three times the type of binding found in the dimer CC-Tri₂. In the TCT-B, two different binding mechanisms are seen: CT- P_{2a} and in the opposite end the CT-Tri₂. With respect to the linker TTT-Tri, we have not computed exactly the dimer involved in it because it will obviously be unstable, but the TT-L₁ dimer (which is unstable in its planar form) does resemble the elementary building block used up in this arrangement. We see that in some cases unstable dimers may form a linker structure that is overall stable.

The motifs shown in Figure 8 also clearly illustrate how each of the linkers affects the directionality of the ribbons connected to it. It is clear that different arrangements are possible for the ribbons coming and leaving one particular linker cluster. The CCC-Lin can create an angle of 90° between two ribbons, one formed by L-trans monomers and the other by D-trans. The same effect happens with the linker TCT'-Lin, but in this case the trans isomers are directly involved in the cluster. In the case of CCT-Lin, the directionality of the ribbon (formed by only one trans isomer) is maintained, and the linker just creates a kink along the ribbon. Most of the times the cis monomer is the central part of these three linkers, primarily responsible for connecting the ribbons. These three linkers bifurcate the ribbon flow, whereas the other two possibilities, CCC-Tri and TTT-Tri, collected in Figure 8, produce a trifurcation. The latter two linkers have a triangular shape, one formed by all cis monomers and another by all trans (L or D), respectively. For simplicity, we show only TTT-Tri in Figure 8 formed by the D-trans, but another one based on the L-trans isomers is equivalent to this one.

Regarding the stability of these clusters, binding energies corresponding to both nonplanar (yellow) and planar (green) geometries are shown in Figure 8. All, except the planar TTT-Tri configuration, are very stable structures. The number of H bonds in these linkers is an important parameter that roughly correlates with the binding energy; that is, the binding energies of the linkers are approximately additive with respect to the binding energies of the dimers (where applicable). Thus, and using only nonplanar values, CCC-Tri presents up to six H bonds in the linker alone (-21.4 kcal/mol); TCT'-Lin (-69.9 kJ/mol), CCT-Lin (-67.3 kJ/mol), CCC-Lin (-63.6 kJ/mol), and TCT-B (-63.2 kJ/mol) show four H bonds, while TTT-Tri (-20.5 kJ/mol) only shows three H bonds (none of them is linear). This is the only one with an unstable planar configuration.

As can be seen, all nonplanar linkers are stable, especially CCC-Tri, TCT'-Lin, CCT-Lin, and hence may be almost equally likely present on the surface. However, note

that their stability can be compromised by the molecule–surface interaction, which is currently not considered.

CONCLUSIONS

We considered various 2D structures the pTmDC molecules may form with each other in the gas phase. The main idea of this study was to understand, at the atomic and molecular levels, the appropriate nanoscopic models for the structures these molecules form on the Ag(111) surface as observed in recent STM experiments.⁶ By systematically going from the simplest assemblies consisting of just two molecules, we have built up more sophisticated structures including 1D ribbons and linkers connecting several ribbons and developed, using ab initio DFT geometry relaxation, explicit atomistic models for them. We find that all of the assemblies observed in the STM images can be explained just by invoking H bonding interactions between the monomers.

Although the surface was not explicitly present in our calculations, its effect was effectively taken into account by considering 2D structures only. At the same time, one cannot underestimate the possible effect of the surface. For instance, the number of structures we find in our calculations is greater than is seen in the images, and this must be explained by the additional *directed* interaction of the molecules with the surface, which makes some of the assemblies unfavorable when placed on the silver surface. In addition, orientation of the assemblies with respect to the surface cannot be explained without taking into account explicitly the interaction between them and the surface. We are currently working on these issues, and the results of our study will be published elsewhere in due course.

We have also considered in detail various forms of the monomers in the gas phase as this is important in understanding the distribution of molecules prior to their deposition on the surface. We concluded that there must be equal amounts of both C and T isomers in the gas phase, and hence when deposited on the surface one should expect 50% cis and 25% of either L and D trans isomers.

We hope that this study provides an additional insight into the self-assembly of pTmDC molecules on the silver surface and supports an observation made in ref 6 based on their STM observations that the H bonding must play the dominant role in the formation of the structures. We also indicated the important role of the molecule–surface interaction in the assembly mechanism at play, which is the matter of our current investigation.

AUTHOR INFORMATION

Corresponding Author

*E-mail: jmrecio@uniovi.es.

Notes

The authors declare no competing financial interest.

ACKNOWLEDGMENTS

D.A.-P. and J.M.R. acknowledge support by the Spanish MINECO and the ERDF of the European Union (project no. CTQ2012-38599-C02) and Principado de Asturias FICYT (project SV-PA-13-ECOEMP-12). We belong to the MALTA Team (CSD2007-0045 project, MEC Consolider Ingenio 2010 program). D.A.-P. thanks the now extinct Spanish MICINN for an FPI grant.

REFERENCES

- (1) Barth, J. V.; Costantini, G.; Kern, K. Engineering Atomic and Molecular Nanostructures at Surfaces. *Nature* **2005**, *437*, 671–679.
- (2) Bandyopadhyay, A.; Pati, R.; Sahu, S.; Peper, F.; Fujita, D. Massively Parallel computing on an Organic Molecular Layer. *Nat. Phys.* **2010**, *6*, 369–375.
- (3) Mura, M.; Silly, F.; Burlakov, V.; Castell, M. R.; Briggs, G. A. D.; Kantorovich, L. N. Formation Mechanism for a Hybrid Supramolecular Network Involving Cooperative Interactions. *Phys. Rev. Lett.* **2012**, *108*, 176103.
- (4) Otero, R.; Lukas, M.; Kelly, R. E. A.; Xu, W.; Lagsgaard, E.; Stensgaard, I.; Kantorovich, L. N.; Besenbacher, F. Elementary Structural Motifs in a Random Network of Cytosine Adsorbed on a Gold(111) Surface. *Science* **2008**, *319*, 312–315.
- (5) Kelly, R. E. A.; Lukas, M.; Kantorovich, L. N.; Otero, R.; Xu, W.; Mura, M.; Lagsgaard, E.; Stensgaard, I.; Besenbacher, F. Understanding the Disorder of the DNA Base Cytosine on the Au(111) Surface. *J. Chem. Phys.* **2008**, *129*, 184707.
- (6) Marschall, M.; Reichert, J.; Seufert, K.; Auwärter, W.; Klappenberger, F.; Weber-Bargioni, A.; Klyatskaya, S.; Zoppellaro, G.; Nefedov, A.; Strunskus, T.; et al. Supramolecular Organization and Chiral Resolution of p-Terphenyl-m-Dicarbonitrile on the Ag(111) Surface. *ChemPhysChem* **2010**, *11*, 1446–1451.
- (7) Arras, E.; Seitsonen, A. P.; Klappenberger, F.; Barth, J. V. Nature of the Attractive Interaction Between Proton Acceptors and Organic Ring Systems. *Phys. Chem. Chem. Phys.* **2012**, *14*, 15995.
- (8) Hohenberg, P.; Kohn, W. Inhomogeneous Electron Gas. *Phys. Rev.* **1964**, *136*, B864–B871.
- (9) Kohn, W.; Sham, L. J. Self-Consistent Equations Including Exchange and Correlation Effects. *Phys. Rev.* **1965**, *140*, A1133–A1138.
- (10) VandeVondele, J.; Krack, M.; Mohamed, F.; Parrinello, M.; Chassaing, T.; Hutter, J. Quickstep: Fast and Accurate Density Functional Calculations Using a Mixed Gaussian and Plane Waves Approach. *Comput. Phys. Commun.* **2005**, *167*, 103–128.
- (11) Lippert, G.; Jurg, H.; Parrinello, M. A Hybrid Gaussian and Plane Wave Density Functional Scheme. *Mol. Phys.* **1997**, *92*, 477–488.
- (12) Goedecker, S.; Teter, M.; Hutter, J. Separable Dual-Space Gaussian Pseudopotentials. *Phys. Rev. B* **1996**, *54*, 1703–1710.
- (13) Perdew, J. P.; Burke, K.; Ernzerhof, M. Generalized Gradient Approximation Made Simple. *Phys. Rev. Lett.* **1996**, *77*, 3865–3868.
- (14) Grimme, S.; Antony, J.; Ehrlich, S.; Krieg, H. A consistent and accurate ab initio parametrization of density functional dispersion correction (DFT-D) for the 94 elements H–Pu. *J. Chem. Phys.* **2010**, *132*, 154104.
- (15) VandeVondele, J.; Hutter, J. Gaussian Basis Sets for Accurate Calculations on Molecular Systems in Gas and Condensed Phases. *J. Chem. Phys.* **2007**, *127*, 114105.
- (16) Jurecka, P.; Sponer, J.; Cerny, J.; Hobza, P. Benchmark Database of Accurate (MP2 and CCSD(T) Complete Basis Set Limit) Interaction Energies of Small Model Complexes, DNA Base Pairs, and Amino Acid Pairs. *Phys. Chem. Chem. Phys.* **2006**, *8*, 1985.
- (17) Boys, S.; Bernardi, F. The Calculation of Small Molecular Interactions by the Differences of Separate Total Energies. Some Procedures with Reduced Errors. *Mol. Phys.* **1970**, *19*, 553.
- (18) Jónsson, H.; Mills, G.; Jacobsen, K. W. Nudged Elastic Band Method for Finding Minimum Energy Paths of Transitions. In *Classical and Quantum Dynamics in Condensed Phase Simulations*; Berne, B. J., Cicchetti, G., Coker, D. F., Eds.; World Scientific: Singapore, 1998.
- (19) Mills, G.; Jónsson, H.; Schenter, G. K. Reversible Work Transition State Theory: Application to Dissociative Adsorption of Hydrogen. *Surf. Sci.* **1995**, *324*, 305–337.
- (20) Henkelman, G.; Jónsson, H. Improved Tangent Estimate in the Nudged Elastic Band Method for Finding Minimum Energy Paths and Saddle Points. *J. Chem. Phys.* **2000**, *113*, 9978–9985.

(21) Henkelman, G.; Uberuaga, B. P.; Jónsson, H. A Climbing Image Nudged Elastic Band Method for Finding Saddle Points and Minimum Energy Paths. *J. Chem. Phys.* **2000**, *113*, 9901–9904.

(22) Johnson, E. R.; Keinan, S.; Mori-Sánchez, P.; Contreras-García, J.; Cohen, A. J.; Yang, W. Revealing Noncovalent Interactions. *J. Am. Chem. Soc.* **2010**, *132*, 6498–6506.

(23) Contreras-García, J.; Yang, W.; Johnson, E. R. Analysis of Hydrogen-Bond Interaction Potentials from the Electron Density: Integration of Noncovalent Interaction Regions. *J. Phys. Chem. A* **2011**, *115*, 12983–12990.

(24) Contreras-García, J.; Calatayud, M.; Piquemal, J.-P.; Recio, J. M. Ionic Interactions: Comparative Topological Approach. *Comput. Theor. Chem.* **2012**, *998*, 193–201.

(25) Otero, R.; Schock, M.; Molina, L. M.; Legsgaard, E.; Stensgaard, L.; Hammer, B.; Besenbacher, F. Guanine Quartet Networks Stabilized by Cooperative Hydrogen Bonds. *Angew. Chem., Int. Ed.* **2005**, *44*, 2270.

(26) Kelly, R. E. A.; Kantorovich, L. Planar Nucleic Acid Base Superstructures. *J. Mater. Chem.* **2006**, *16*, 1894–1905.

(27) Mura, M.; Gulans, A.; Thonhauser, T.; Kantorovich, L. Role of Van der Waals Interaction in Forming Molecule-Metal Junctions: Flat Organic Molecules on the Au(111) Surface. *Phys. Chem. Chem. Phys.* **2010**, *12*, 4759–4767.



PCCP

Role of Isomerization in Kinetics of Self-Assembly: p-Terphenyl-m-Dicarbonitrile on Ag(111) Surface

Journal:	<i>Physical Chemistry Chemical Physics</i>
Manuscript ID:	CP-ART-01-2015-000220
Article Type:	Paper
Date Submitted by the Author:	14-Jan-2015
Complete List of Authors:	Abbasi, David; Universidad de Oviedo, Physical and Analytical Chemistry Muniz, Jose; Universidad de Oviedo, Departamento de Química Física y Analítica Kantorovich, Lev; King's College London, Physics

SCHOLARONE[®]
Manuscripts

PCCP Guidelines for Referees

Physical Chemistry Chemical Physics (PCCP) is a high quality journal with a large international readership from many communities

Only very important, insightful and high-quality work should be recommended for publication in PCCP.



To be accepted in PCCP - a manuscript must report:

- Very high quality, reproducible new work
- **Important new physical insights** of significant general interest
- A novel, stand-alone contribution

Routine or incremental work should not be recommended for publication. Purely synthetic work is not suitable for PCCP

If you rate the article as 'routine' yet recommend acceptance, please give specific reasons in your report.

Less than 50% of articles sent for peer review are recommended for publication in PCCP. The current PCCP Impact Factor is **4.20**.

PCCP is proud to be a leading journal. We thank you very much for your help in evaluating this manuscript. Your advice as a referee is greatly appreciated.

With our best wishes,

Anna Simpson (pccp@rsc.org)
Managing Editor, PCCP

Prof Daniella Goldfarb
Chair, PCCP Editorial Board

General Guidance (For further details, see the RSC's [Refereeing Procedure and Policy](#))

Referees have the responsibility to treat the manuscript as confidential. Please be aware of our [Ethical Guidelines](#) which contain full information on the responsibilities of referees and authors.

When preparing your report, please:

- Comment on the originality, importance, impact and scientific reliability of the work;
- State clearly whether you would like to see the paper accepted or rejected and give detailed comments (with references) that will both help the Editor to make a decision on the paper and the authors to improve it;

Please inform the Editor if:

- There is a conflict of interest;
- There is a significant part of the work which you cannot referee with confidence;
- If the work, or a significant part of the work, has previously been published, including online publication, or if the work represents part of an unduly fragmented investigation.

When submitting your report, please:

- Provide your report rapidly and within the specified deadline, or inform the Editor immediately if you cannot do so.
- We welcome suggestions of alternative referees.

Role of Isomerization in Kinetics of Self-Assembly: p-Terphenyl-m-Dicarbonitrile on Ag(111) Surface

David Abbasi-Pérez and J. Manuel Recio

MALTA-Consolider Team and Departamento de Química Física y Analítica, Facultad de Química,
Universidad de Oviedo, 33006 Oviedo, Spain

Lev Kantorovich*

Physics Department, King's College London, Strand, London, WC2R 2LS, United Kingdom
lev.kantorovitch@kcl.ac.uk

Abstract

Using a toolkit of theoretical techniques comprising *ab initio* density functional theory calculations, the nudged elastic band method and kinetic Monte Carlo (KMC) modeling, we investigate in great detail how para-Terphenyl-meta-Dicarbonitrile (pTmDC) molecules diffuse and isomerize to self-assemble on the Ag(111) surface. We show that molecules “walk” on the surface via a pivoting mechanism moving each of its two “legs” one at a time. We then identify a peculiar “under-side” isomerization mechanism capable of changing the molecules chirality, and demonstrate that it is fundamental in understanding the growth of hydrogen bonding assemblies of ribbons, linkers, clusters and brickwall islands on the Ag(111) surface, as observed in recent scanning tunneling microscopy experiments (*ChemPhysChem* **11**, 1446 (2010)). The discovered underlying atomistic mechanism of self-assembly may be behind the growth of other hydrogen bonding structures of chiral molecules on metal surfaces.

Introduction

One route of building sophisticated nanodevices is to explore natural ability of many organic molecules to self-assemble on crystal surfaces into structures of various complexity varying from small clusters to ribbons and islands.^{1–3} The structures the molecules form on surfaces are a result of a complex interplay between molecule-molecule and molecule-surface interactions, and knowing these may help in understanding many assemblies observed.⁴ However, in order to be able to manipulate the growth of molecules into desired geometries on surfaces, i.e. steer the assembly along a predefined direction to form structures most suitable for the given application, one needs to understand the mechanism of growth of the structures in detail. The latter knowledge cannot be gained just by understanding why the molecules bind to themselves and to the surface, i.e. their ability to form dimers, trimers, and bigger clusters; it requires comprehensive simulations of *kinetics of growth* which in turn necessitates understanding of diffusion mechanism, rates of transformations between different states of molecules on the surface (e.g. between various isomers) and the corresponding rates of formation of clusters of molecules and their decomposition. By means of scanning tunneling microscopy (STM) it is possible to get access to detailed information on how the molecules are organized on the surface and identify the essential building blocks predominant in the self-assembly process. However, time evolution of growth is less accessible to STM based techniques (unless the growth happens much slower than the available scan speeds), and hence theoretical investigation of the factors determining the growth becomes extremely important.

In a recent experimental study,⁵ deposition of [1,1';4',1'']-terphenyl-3,3''-dicarbonitrile (also known as para-Terphenyl-meta-Dicarbonitrile or pTmDC in short) molecules on the Ag(111) surface was investigated by STM. In the gas phase the molecules may exist either in *cis* (C) or *trans* (T) forms (isomers) shown in Fig. 1. When evaporated on the silver surface the two isomers can be clearly imaged with STM at room temperature (RT) both appearing in a similar rectangular form. Though the *cis* isomer is achiral, *trans* isomer is however prochiral, i.e. depending on which side the molecule gets adsorbed on the surface, two possibilities exist denoted L- and D-*trans*, Fig. 1.

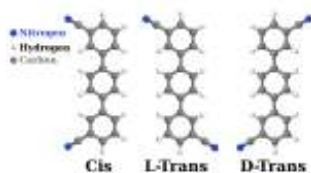


Figure 1 Cis and trans isomers of pTmDC .

Using STM, it was found⁵ that at low coverages upon thermal quenching the molecules form one-dimensional (1D) ribbons which cross with and connect to each other via a number of linkers which molecular arrangement has been resolved. At higher coverages two-dimensional (2D) islands are formed instead. When evaporated on the surface, both cis and trans isomers are expected to be present; however, intriguingly, it was claimed that mostly trans isomers were found in abundance on the surface (e.g. in ribbons) after the self-assembly takes place at either small or large coverage with cis isomers appearing only in small amounts, mostly in linkers and at the ends of the ribbons. Note that it was assumed⁵ that in all these structures the molecules bind to each other via double hydrogen bonds. The STM images revealed that both trans species form equivalent structures which are mirror reflections of each other.

In our preceding work⁶ various possible assemblies of the pTmDC molecules were studied in the gas phase using *ab initio* density functional theory (DFT) method, assuming that the role of the surface was to constrain the molecular structures in two dimensions. This method allowed to consider large molecular structures at reasonable computational expense, including many that were resolved in the experimental STM images. The hypothesis⁵ that the binding mechanism holding the molecules together on the surface is based on hydrogen (or H) bonding was also broadly confirmed, although it was found that dispersion interaction plays a significant role in the binding, especially for weak dimers. It was also established that in the gas phase there are very small barriers between cis and trans isomers, confirming that, as expected, there must be equal amounts of the two conformers during their evaporation on the surface. Hence, upon deposition, there must be 50% of cis and by 25% of each of the trans isomers.

Here we go further and consider the silver surface explicitly; moreover, we present a detailed *ab initio* density functional theory (DFT) based theoretical study of the *kinetic processes* responsible for the growth of the observed structures on the Ag(111) surface. Our main aim is to provide the driving mechanism(s) of self-assembly of pTmDC molecules on this surface at small and up to intermediate coverages. This includes detailed determination of the transition paths involved in the cis-to-trans isomerization, molecular diffusion, binding and decomposition of molecular structures, followed by extensive kinetics modeling of molecular assemblies themselves based on Kinetic Monte Carlo (KMC) technique. This comprehensive and complementary toolkit of theoretical methods is essential to build up a detailed understanding of the growth mechanism for the observed assemblies and to verify the claim⁵ stated above about the observed chiral selectivity. The corresponding energy barriers for the transitions incorporated in the KMC simulations were all calculated using Nudged Elastic Band (NEB)^{7,8} method and DFT.

Methods

DFT calculations were carried out using the CP2K code.⁹ It implements periodic boundary conditions and the hybrid Gaussian and plane wave method (GPW).¹⁰ Goedecker-Teter-Hutter (GTH)¹¹ pseudopotentials were used as well as Perdew-Burke-Ernzerhof (PBE) generalized gradient exchange-correlation functional¹² with the dispersion correction to energy and forces due to Grimme's DFT-D3 method.¹³ The optimized m-DZVP basis set¹⁴ was used for all atoms and a plane wave cutoff energy of 280 Ry. Geometries were relaxed until forces on atoms were less than 0.02 eV/Å. In all calculations (except for those with adsorbed infinite ribbons and islands) the corresponding simulation cells were chosen big enough to ensure that there are sufficient distances between images of adsorbed molecules and clusters to make the interaction between them negligible.

Binding energy of a complex $S + M_N$ obtained by placing N molecules M on the surface S is defined in the usual way as

$$E_{bind} = E_{S+M_N} - E_S^0 - \sum_{M=1}^N E_M^0,$$

where E_{S+M_N} is the DFT total energy of the complex $S + M_N$, E_S^0 is the energy of the individually relaxed surface, and E_M^0 are the energies of the individually relaxed molecules (C and/or T). Because a localized basis set is employed, the basis set superposition error (BSSE) is added to the binding energies, which is calculated by means of the (positive) counterpoise (CP) correction¹⁵ method. When considering contributions to the binding energy between molecules in a cluster which is adsorbed on the surface, we also calculated the *cluster binding energy* using

$$E_{Hb} = \left[E_{S+M_N} - \sum_{M=1}^N (\Delta E_M + E_M^0) - E_S^0 \right],$$

where $\Delta E_M = E_{S+M} - E_S^0 - E_M^0$ is the binding energy to the surface of an individual monomer M calculated at the geometry of the whole complex $S + M_N$. The energy E_{Hb} has the meaning of a mean H bonding energy between molecules on the surface.

All energy barriers were calculated by means of the Nudged Elastic Band (NEB) method.^{7,8} Both Improved Tangent NEB and the Climbing Image NEB calculations^{16,17} were employed, with the number of images varying between 7 and 9.

To illustrate the strength of H bonding interaction in a complex $S + M_N$ of N molecules on the surface, we used two methods. In the first one, we analyzed electronic density difference¹⁸⁻²⁰ (EDD) defined as $\Delta\rho(\mathbf{r}) = \rho(\mathbf{r}) - \sum_A \rho_A(\mathbf{r})$, where ρ is the total density of the complex, while ρ_A is the density of the component A (either S or M) considered in the geometry of the complex. In the second method, we analyzed the topology of the electron density using the so-called (dimensionless) reduced density gradient,²¹⁻²³ when the following quantity is analyzed:

$$s(\mathbf{r}) = \frac{1}{2(3\pi^2)^{1/3}} \frac{|\nabla\rho(\mathbf{r})|}{\rho(\mathbf{r})^{4/3}}$$

This is specially designed to identify regions where non-covalent interactions (NCI) are dominant. In visualizing $s(\mathbf{r})$, the iso-surfaces are colored on a blue-green-red color scale. With this color scheme, red indicates strong non-bonding (steric) repulsion, green indicates weak interaction such as dispersion, while blue detects strong attractive interaction such as the H bonds.

Results

Monomers on the silver surface

Knowledge of the energetics of monomers on the surface is mandatory for clear understanding of the self-assembly process. As possibilities of geometrical positions of the monomers on the surface are enormous, we carried out a systematic exploration of the potential energy landscape to reveal all possible adsorption sites (see the Supplementary Information for details). Altogether, 173 and 183 orientations of cis and trans isomers, respectively, were relaxed with our DFT method.

The most stable configurations found and their corresponding binding energies are presented in Fig. 2 for the cis and trans isomers (more relaxed geometries are shown in Figs. S2 and S3 in the Supplementary Information). It is seen from these results that both isomers are strongly bound to the silver surface with binding energies as large as 200 kJ/mol, and hence both isomers are equally favorable. Careful inspection of the obtained geometries revealed that favorable geometries have at least two common features: (i) N atoms of the molecule prefer to be located near the top of Ag atoms, showing a weakly dative covalent bonding that we call a NAS (Nitrogen Atom Surface) interaction, and (ii) phenyl rings tend to avoid Ag atoms below their centers. We also find that there is some tendency for the carbonitrile groups to bend towards the surface, so that the molecule adopts a dome-like shape seen in Fig. 3. Thus, the mean distances to the surface of the carbon skeleton of the monomers is around 3.25 Å, whereas that of the N atoms is only around 2.65 Å (see the Supplementary Information for further details). The large number of adsorption geometries found with similar binding energies and the small variation in the molecule geometry with respect to the surface suggest that the corresponding potential energy surface (PES) is weakly corrugated.

Dispersion is the essential attractive contribution to the binding energy in all stable monomers including those shown in Fig. 2. To investigate the nature of the interaction of the molecule to the surface, we analyzed in detail the electron density for a number of adsorbed monomers using both the electron density difference (EDD)¹⁸⁻²⁰ and the Non-Covalent Interaction (NCI)²¹⁻²³ methods, which give complementary results. As an example, a comparison of the plots using the two methods is shown in Fig. 3 for one representative C and one T monomer. It is clearly seen that there is a considerable binding (as the charge density excess reveals) between N atoms and the surface Ag atoms (Fig. 3 A and B). This NAS interaction justifies the preference of the molecule for certain docking sites where N atoms are on top of Ag atoms. The big green area depicted by the NCI analysis

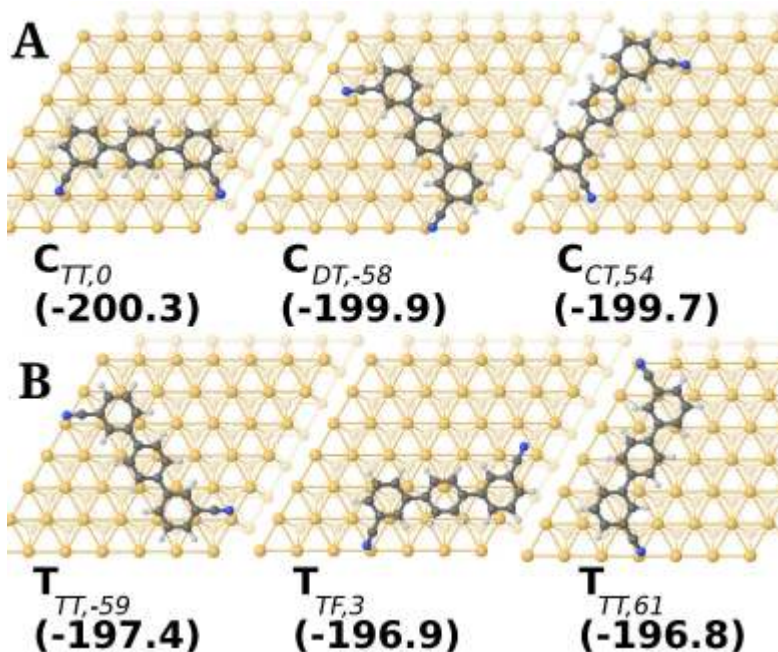


Figure 2 Three most stable (A) cis C and (B) trans T conformers on the surface found after the DFT geometry relaxation. The suggested nomenclature is meant to indicate the adsorption site and orientation of the molecule: the first subscript indicates the docking site of the left N atom, the second subscript indicates the docking site of the right N atom, and the number after the comma indicates the alpha angle (see Fig. S1 in the Supplementary Information). When both N atoms align along a vertical line, then the first subscript refers to the bottom atom. The corresponding binding energies (in kJ/mol) are also given. Only L-trans isomers are shown for clarity; the corresponding D-trans isomers with identical binding energies are obtained by appropriate flipping of the molecules (not shown).

(Fig. 3 C and D), which represents the dispersion interactions between the molecule and the surface, reveals the key role that dispersion plays in the binding mechanism, which is in agreement with the low corrugation of the PES and the large number of adsorption geometries found. Further analysis based on integrating the charge density in planes parallel to the surface revealed that there is no perceptible charge transfer between the molecule and surface. This conclusion is also confirmed by the calculated projected density of states, see Fig. S4 in the Supplementary Information.

It was suggested in the experimental study⁵ that cis-to-trans isomerization plays an essential role in the self-assembly process of the pTmDC molecules on the Ag(111) surface. Therefore, using the NEB method we have considered the isomerization reaction for one monomer geometry adsorbed on the surface. The cis-to-trans isomerization transition can be modeled by rotating around the C-C bond connecting a benzonitrile group with the central phenyl ring. This can be done in two ways: in one the benzonitrile group rotates with its N atom going round away from the surface (the *upper-side* trajectory), while in the other the group proceeds near the surface (the *under-side* trajectory). Both paths were considered using a particular pair of isomers. The initial ($T_{TF,19}$) and final ($C_{TT,23}$) geometries and the transition states in both cases along with the computed minimum energy paths (MEP) are shown in Fig. 4. It is seen that the barrier for the C→T transition of around 38.6 kJ/mol for the under-side mechanism is by about 19.3 kJ/mol lower than for the upper-side mechanism which is easily explained by the fact that in the latter case one of the N-Ag interactions needs to be broken completely, while in the former case some bonding with the surface still remains along the path. We also note that the barriers for the direct (T→C) and reverse (C→T) transitions differ by no more than 3.9 kJ/mol rendering both isomers on the surface almost equally possible, with the C isomer being marginally more favorable. Therefore, we expect C and T monomers being in almost equal amounts on the surface after first steps of deposition.

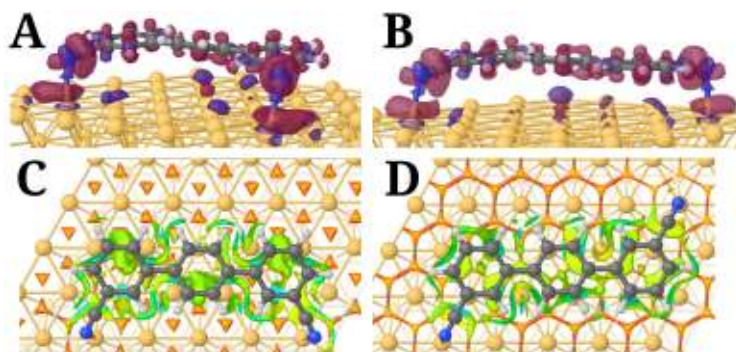


Figure 3 Comparison of the electron density difference (A,B) and NCI (C,D) plots for the cis $C_{TT,0}$ (A,C) and trans $T_{TT,1}$ (B,D) monomers adsorbed on the Ag(111) surface. In (A,B) the purple isosurface indicates an excess and the maroon depletion of the electron density, with the isosurfaces drawn at ± 0.0007 electron/ \AA^3 . The value of $s = 0.5$ was used in (C,D) for the NCI plots, see Methods for the explanation of the color scheme used.

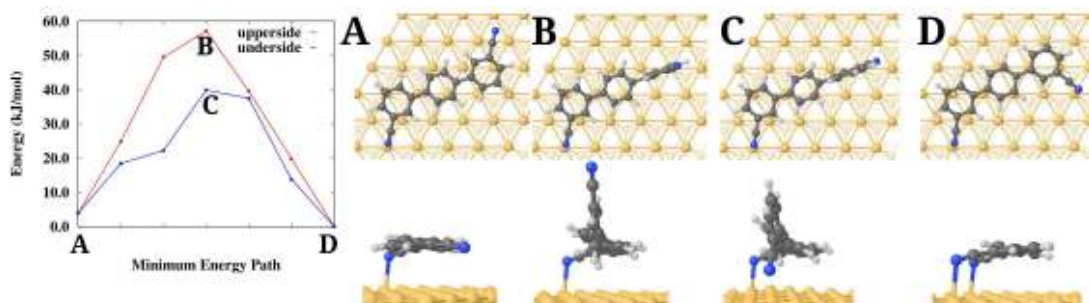


Figure 4 Cis-trans isomerization transition paths connecting the initial T (A) and final C (D) configurations via two possible mechanisms: (i) the upper-side with the transition state (B), and (ii) the under-side with the transitions state (C).

Diffusion of molecules on the surface is the next necessary prerequisite for understanding their ability to assemble into structures. Using some of the nearest stable geometries as initial and final states, and applying the NEB method to calculate the transition path between them, we have investigated several diffusion paths for both C and T monomers on the surface. Two basic mechanisms were considered: (i) *sliding transition* in which the molecule loses both its N interactions to the Ag anchoring sites on the surface to move to a new stable geometry, and (ii) a two steps *pivoting transition* whereby within each step one benzonitrile group remains bonded to the surface serving as a pivot for the other group, which rotates to a new stable position. In the latter mechanism one benzonitrile group serves as a pivot during the first, while another group during the second step. Because of the very large number of adsorption geometries of monomers on the surface, calculating transitions between all possible configurations is not feasible to consider in practice. Therefore, we selected only a number of reasonable possibilities between most stable structures. Examples of both types of transitions for a C monomer together with the corresponding MEPs are shown in Figs. 5 (for a T monomer see Fig. S5 in the Supplementary Information). As expected, the sliding transition requires about 2.1-3.5 kJ/mol higher barriers to overcome for both isomers than in the pivoting mechanism. This is because during sliding two molecule-surface interactions involving two N atoms have to be simultaneously broken, whereas in the pivoting transition two steps needed for the same displacement of the molecule require each only one of these interactions to be broken at a time. Hence rather small diffusion barriers are found ranging between 1.9-3.9 kJ/mol for C and 4.8-5.8 kJ/mol for T, depending on the particular initial and final geometries.

Concluding this Section, we find that dispersion is the main interaction that binds the molecule to the surface. From the

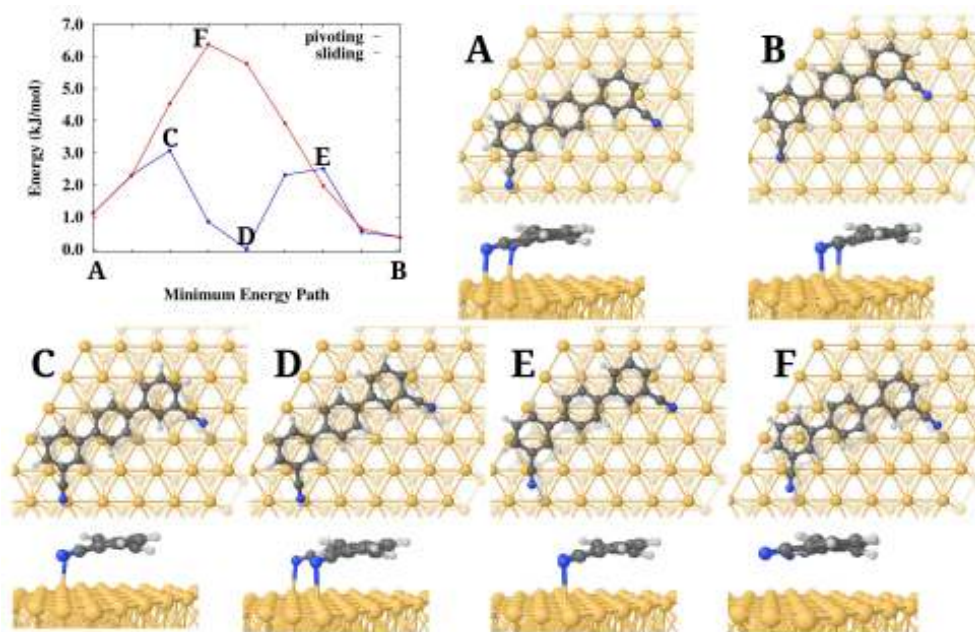


Figure 5 Diffusion paths for a C monomer on the Ag(111) surface. In the top-left panel the pivoting (blue) and sliding (red) MEP bands are shown labeled with the corresponding states shown in separate panels: initial and final (A and B), transition (C, F, E) and intermediate (D) states, as well as their geometries (top and perspective views). In the transition and intermediate states a ghost image of the molecule is superimposed showing its previous state.

large number of calculated adsorption geometries and obtained small diffusion barriers we conclude that the PES of a pTmDC molecule on the Ag(111) surface is rather flat so that the molecule must be quite mobile at RT. The preferred sites are those where favorable NAS interactions between the Ag surface with the two N are formed. Thus, the molecule can be viewed as standing on two legs. Single molecules diffuse exploiting the pivoting mechanism and C and T isomers may undergo transformations into each other following an under-side trajectory with relatively high and equal rates.

Dimers on the silver surface

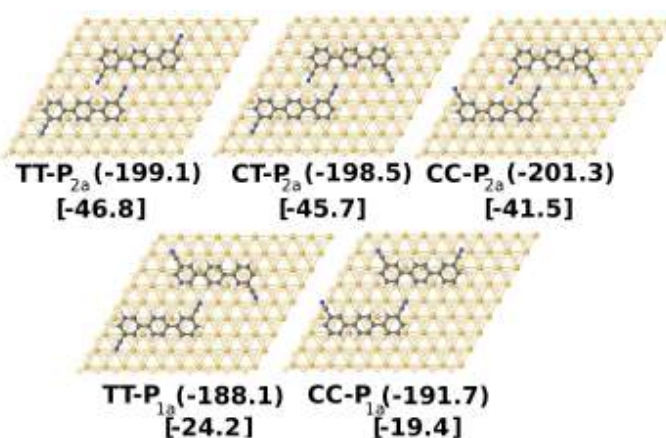


Figure 6 A selection of DFT relaxed dimers on the silver surface together with the corresponding total binding energies per molecule (in round brackets), and H bonding energies (in square brackets), all given in kJ/mol. The legend used to denote the dimers means: the first two characters are composed of either C or T corresponding to the cis or trans conformations of the constituent monomers; the next letter P refers to the parallel form; the index 1 or 2 that follows corresponds to the number of hydrogen bonds in the dimer; finally, a subscript *a* or *b* is used to differentiate between similar structures. More dimers structures are shown in Fig. S6 of the Supplementary Information.

Next we shall consider pTmDC dimers on the silver surface. In total about 25 different dimers, including different orientations of the same dimers, were studied. A number of the most stable dimer structures, fully relaxed with our DFT method, together with their total binding energies per molecule and H bond binding energies (in round and square brackets, respectively) are shown in Fig. 6. The total binding energies of the dimers range from 368.5 to 402.5 kJ/mol and follow the same tendency as in the gas phase⁶ (see also the Supplementary Information).

If we now compare the on-surface dimer total binding energies (around 385 kJ/mol) with binding energies of single monomers (around 192 kJ/mol), and binding energy in the gas phase dimers (around 29 kJ/mol), we see that these are not additive. This is because not all four N atoms of the dimers present NAS-type interactions; for instance, some of the N atoms are located above the Ag hollow sites and hence are less strongly bound to the surface. This is also reflected in the EDD plots (see Fig. S7 in the Supplementary Information).

Looking at the dimer geometries in more detail, we find that the effect of the surface manifests itself in mostly re-orienting the dimers on the surface in such a way as to best stabilize the structure; however, the relative orientation of the molecules in the dimers is very similar to that in the gas phase. We also find that only carbonitrile groups at two ends of dimers remain bent towards the surface (showing NAS interactions similar to what CN-groups in the monomers do), while the CN-groups engaged in the H bonding are practically parallel to the surface, which is likely to be the main cause of the reduction of the binding energies from a mere sum of energies due to different interactions.

To analyze the nature of bonding between the molecules and of the molecules with the surface, we looked at electron density plots (see Fig. S7 in the Supplementary Information). It is seen that docking sites revealing NAS interactions are visible only for some of the N atoms, those which are located above the Ag atoms of the surface. This is consistent with the fact, mentioned above, that the relative interaction of each monomer in the dimers with the surface is somewhat weaker than that for isolated

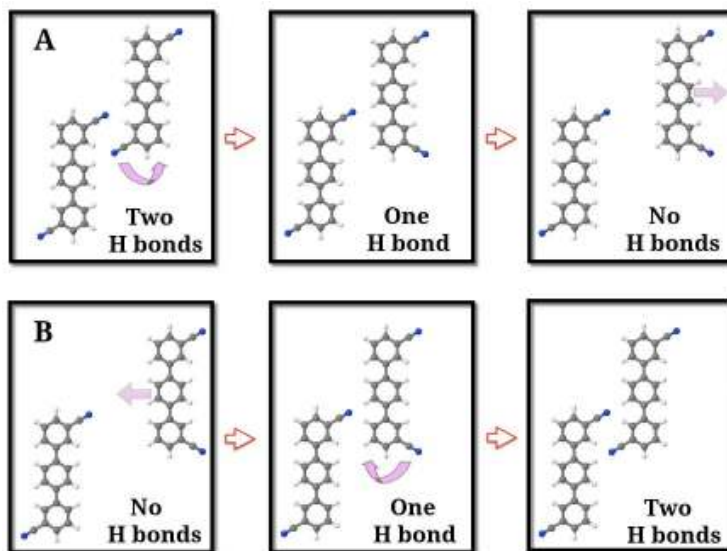


Figure 7 Schematics of the *assisted isomerization* reaction between two molecules on the surface: (A) the right molecule weakens its bonding and detaches from the left molecule increasing the system energy; (B) the right incoming molecule establishes a double H bond with the left molecule reducing the energy of the system.

monomers. Looking at the EDD between two molecules in the dimer, Fig. S7 (B), we find it extremely similar to the one calculated for the same dimer in the gas phase⁶ with the “kebab”-like structure characteristic for the H-bonding between the molecules clearly recognized. Note that the NCI method supports this result as well (Fig. S7, C to F). Detailed analysis confirms that binding between monomers in dimers on the surface can still be characterized in terms of the H-bonding with significant contribution coming from the dispersion interaction (see the Supplementary Information).

As the binding energies of dimers are in the region of 400 kJ/mol, we have not studied their diffusion as a whole, assuming that they are much less mobile than the monomers. However, from the point of view of investigating the growth of the molecular ribbons and linkers observed in,⁵ it is essential to consider possible isomerization of molecules in dimers on the surface. The rationale for this is based on the following observation. Consider a dimer in which two molecules are connected with the double H-bonding, Fig. 7 (A). If one of the benzonitrile groups of a molecule facing the other molecule in a dimer rotates so that the corresponding monomer changes between *cis* and *trans*, the interaction between the monomers in the dimer would weaken and either of the molecules may easily diffuse out. Reversely, see Fig. 7 (B), a molecule may come closer to another, establish a single H bond, and then undergo an isomerization reaction which would result in a double H bond between the two, providing the fundamental mechanism for dimer formation on the surface; this dimer may then serve as a nucleus for a further growth. The same type of reaction may also be responsible for the ribbons growth when a monomer comes to an already formed ribbon and then, upon the appropriate isomerization reaction, would attach to it.

For the isomerization reaction between C-T and C-C dimers we have studied both the under-side and upper-side mechanisms (Fig. 8). As expected, this calculation confirms that the upper-side mechanism requires larger energy barriers; hence for the isomerization reaction between T-T and T-C dimers only the under-side mechanism was studied shown in Fig. S8 of the Supplementary Information. In both cases the initial structures correspond to a P_{2a} like structure with the double H bond, while the final structure is the P_{1a} like with only a single bond. The essential result here is that the P_{2a} dimers are by at least 19.3 kJ/mol more favorable than the P_{1a} structures involving either neighboring T or C monomers. Therefore, the energy barrier of 61.7 kJ/mol required to break one H bond in the P_{2a} dimer and turning it into a P_{1a} dimer is by 19.3 kJ/mol larger than the barrier needed for the reverse reaction of turning a P_{1a} dimer into a more stable P_{2a} one. It follows from this consideration, that when two molecules come close to each other to form a favorable arrangement which may facilitate the formation of a proper

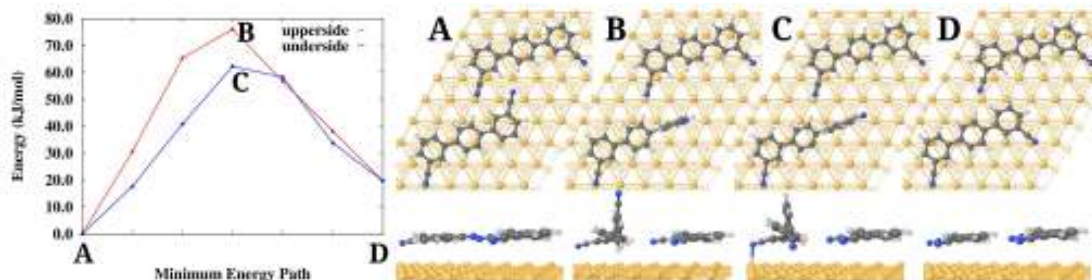


Figure 8 The MEP (the left panel) and the corresponding NEB+DFT relaxed geometries of the initial (A), final (D), and transition states for the upper-side (B) and under-side (C) mechanisms of the cis-assisted isomerization reaction between C-T and C-C dimers.

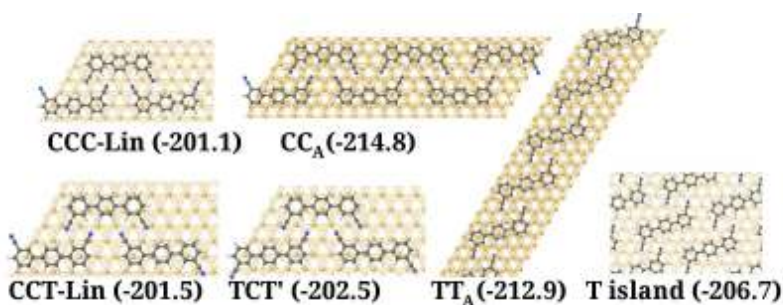


Figure 9 Relaxed geometries and corresponding binding energies (per molecule, in brackets, in kJ/mol) of several linker clusters (CCC-Lin, CCT-Lin and TCT'-Lin), ribbons (CC_A and TT_A) and the T monolayer on the silver surface (top views).

dimer with a double H bond, then the appropriate isomerization reaction would favor such a formation yielding a lower system energy. Hence, if isomerization of monomers, as mentioned above, does not modify significantly the system energy, then the isomerization of molecules arranged next to each others, what we shall call an *assisted isomerization*, will result in a lower free energy of the system.

Linkers and ribbons on the silver surface

Some of the ribbons and linkers considered previously in the gas phase⁶ have also been relaxed on the surface using our DFT method to check their stability.

In the case of periodic ribbons, there is a question of their commensurability with the surface: larger surface cells may need to be taken to accommodate the sufficient number of primitive unit cells of the ribbon structure. In fact, different cells need to be considered to find the structure with the lowest Gibbs free energy. To avoid these rather tedious and expensive computations, we have chosen the smallest cell for the silver surface which accommodates the ribbons at the distances between molecules which are no more than 0.01 Å different from those found in the same ribbons in the gas phase.⁶

The relaxed geometries of two types of ribbons, CC_A and TT_A , consisting of repeated C and T monomers respectively, are shown in Fig. 9 (see also Supplementary Information). The molecules in the ribbons comprise a planar geometry with substantial binding energies (per molecule), also shown in the same Figure. As ribbons have a higher binding energy per molecule than monomers and dimers, it is expected to find molecules aggregated on the surface rather than free molecules or dimers.

We have also considered a number of linker structures composed of 3 molecules which were also placed on the surface and relaxed with DFT. These are shown, together with their binding energies (per molecule) in Fig. 9 (see also Supplementary

Information). All the structures we considered are nearly planar.

The calculations described in this section show that ribbons and linkers are stable on the surface and that their structures are very similar to the ones in the gas phase⁶ confirming that the H-bonding plays the dominant role in the binding mechanism responsible for stability of the molecular aggregates on the silver surface.

Islands on the silver surface

It is known from experiment⁵ that at large coverages the molecules form brickwall type islands. To understand the energetics of the most dense bi-dimensional phase, a 2D monolayer of molecules has also been studied. As in the case of the ribbons, we employed such orientation of the molecules with respect to the surface that allows to have a simultaneous periodicity in both organic and metallic lattices with the smallest unit cell of 4 molecules. The resulting binding energies per molecule are 206.7 kJ/mol for an all trans monolayer and 201.8 kJ/mol for a monolayer formed only by cis molecules. The optimized geometries reveal a nearly planar conformation with a dihedral angle lower than 15° between phenyl rings. The fully relaxed geometry for a T monolayer is shown in Fig. 9. The mean length of the H bond is 2.6 Å and the molecules are at 3.37 Å above the surface. This fact shows that the larger the number of neighbors a molecule has, the higher the molecule is over the surface because the carbonitrile groups tends to participate in the H bonds, although the effect is small.

The T monolayer can be viewed as consisting of TT_A chains placed side-by-side. Since each molecule in the monolayer is double hydrogen bonded to two molecules from the neighboring chains, it would be interesting to investigate whether the molecules remain in their isomerization state at RT or can easily change between T and C states. To this end, we investigated the isomerization reaction for a monomer in the T monolayer and found a barrier of 54.2 kJ/mol for the T→C isomerization via under-side mechanism, and 47.2 kJ/mol for the reverse reaction (Fig. S11 in the Supplementary Information). The relatively low barriers we find for the isomerization reaction in the monolayer imply that islands at RT are composed by a mixture of the three isomers inter-converting continuously one into the other. Actually, in the STM images of the islands⁵ one can see bright bridges between many molecules on both sides of them (see Fig. S12 in the Supplementary Information) implying that indeed these molecules do change their isomerization state frequently on the time scale of the STM scan.

Kinetic Monte Carlo simulations

To model the growth of the assemblies the pTmDC molecules may form on the silver surface, we performed extensive KMC simulations. Because of extremely large number of possible adsorption sites, which would require either introducing a fine grid or performing lattice-free KMC simulations, the problem was considerably simplified to make it tractable. This has been done by introducing two inter-penetrating hexagonal lattices, serving as a grid, and postulating that the molecules may only occupy the sides of the hexagons with their N atoms (or benzonitrile groups) placed on the corresponding vertices of the grid. When a molecule occupies a position on the grid (and there are three independent orientations), it may be in either of the four states, corresponding to two possible orientations of the benzonitrile groups corresponding to C or T isomers, see Fig. 10 (A). Each monomer can interact with its neighbors which may occupy four positions around it as shown in Fig. 10 (B), forming dimers of the kind XY-P_{na}, where X and Y can be either C or T and *n* can be 1 or 2 (see Fig. 6). Note that in real simulations only some of the four neighbors shown in Fig. 10 (B) may be present. For the sake of simplicity, in our KMC simulations we have not taken into account the weaker dimers XY-Tri or XY-P_{nb}.

Since we find in our NEB calculations of diffusion of monomers that the main diffusion mechanism is pivoting, the molecules were allowed to move on the grid by using either of their ends as a pivot and rotating with the other end by ±60°, Fig. 10 (C). Not only the monomers may diffuse on the surfaces on their own, a molecule, if attached to a cluster, may diffuse out (detach from the cluster) to an empty position with the barrier which is calculated as a monomer diffusion barrier plus a sum of the interaction energies of the molecule with all its neighbors. Note that only monomers are allowed to diffuse on the surface, larger clusters (such as dimers, trimers, etc.) cannot move as a whole. By going through the isomerization transition C \rightleftharpoons T the molecules do not change their orientation, but do change their state within the four possibilities shown in Fig. 10 (A). If a molecule is placed next to another, an assisted isomerization is allowed with the corresponding barriers depending on whether initially the molecules are connected by a double or single H bond, see Fig 10 (D and E). Finally, molecules are also allowed to desorb from the surface using their adsorption energy as the energy barrier for this transition. All the moves implemented in our KMC code and the corresponding energy barriers ΔE are schematically shown in Fig.10. Each “move” of the molecule on the grid is associated

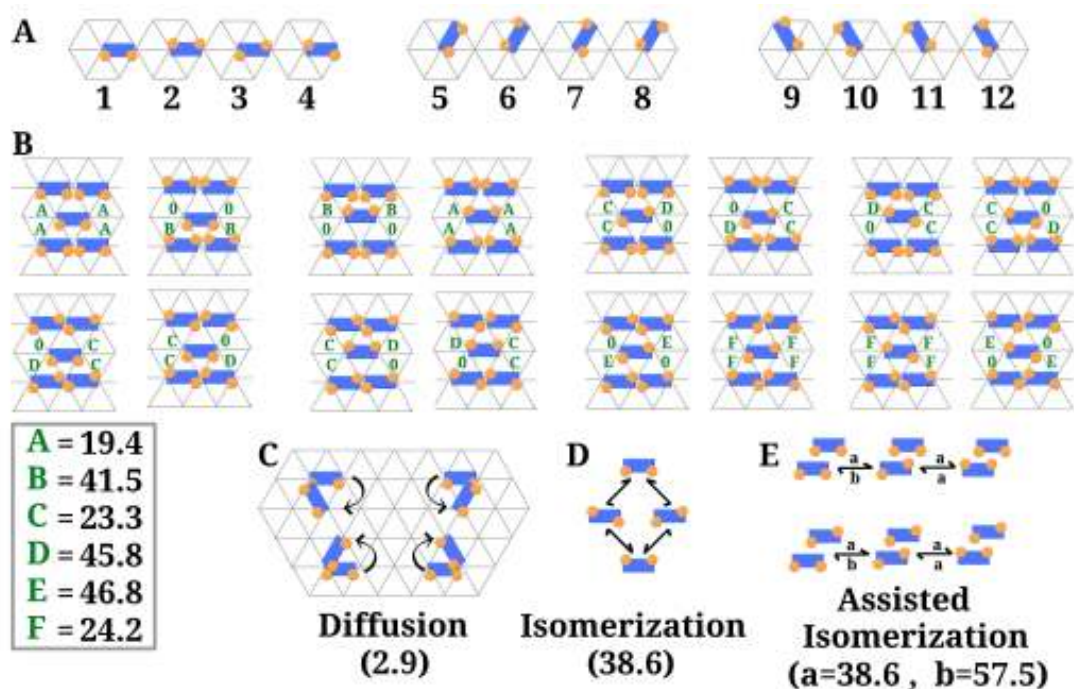


Figure 10 Schematic view of configurations, interactions and moves implemented in the KMC simulation. (A) All 12 possible non-equivalent states of a monomer on the surface. The central point of the hexagon is the net point occupied by the molecule. (B) Various arrangements for a monomer (placed in the center) with its four neighbors (only some may be present in a real simulation). Strength of the pair interactions is indicated with green labels (from A to F), which values were tuned according to our DFT results and are detailed in the light gray box (in kJ/mol). Only shown interactions for monomers 1 to 4. Two more sets of interactions exist by rotating the monomers by 60° (monomers 5 to 8) and 120° (monomers 9 to 12), that yields a total of 192 interactions. (C) The four diffusion mechanisms for a representative monomer. (D) Possible isomerization transformations for an isolated molecule and (E) the assisted isomerization transformations, where the barrier for the reaction “a” is the same as for an isolated monomer and “b” involves the breaking of one H bond. The energy barriers (in brackets) are given in kJ/mol. Blue rectangle represents the aromatic chain of the monomer, orange circles the carbonitrile groups, and the vertices of the hexagonal grid are the Ag atoms of the surface.

with the transition rate $r = \nu e^{-\Delta E/k_B T}$ based on the energy barrier ΔE we have calculated with DFT and the common prefactor $\nu = 10^{13} \text{ s}^{-1}$. Here k_B is the Boltzmann's constant and T the absolute temperature.

In the simulations periodic boundary conditions were implemented with the cell comprising a 85×85 grid. The simulations were run in the following way. To speed up the simulations, either 4 or 5 molecules were initially deposited at random on the grid. These molecules were allowed to perform all possible moves described above. In addition, a deposition of a molecule onto the surface at an arbitrary empty position chosen at random is also allowed with a predefined deposition rate. The deposition is considered as a separate "move" which is attached to the list of all moves. At each KMC step a particular move (diffusion, isomerization, deposition or desorption) is chosen at random using the standard KMC algorithm.^{3,24,25} When a predefined coverage was reached, the deposition was ceased, while all other moves were allowed to continue to be executed until the desired number of KMC steps was reached. Each such simulation was run on average for over 225 million KMC steps using several seed values to accumulate statistics.

Various structures observed in experiment⁵ were frequently seen in our KMC simulations, Fig. 11. Often we observed the molecules starting to condensate in small clusters (or islands), which are surrounded mainly by C monomers pointing its carbonitrile groups towards the interior of the cluster. When one of these molecules at the edges isomerizes to a T or leaves the cluster uncovering a T isomer, a chiral T chain can start growing from the cluster when an equal isomer binds to the first T monomer forming a TT-P_{2a} dimer. Then, in several cases the growth of a chain may be facilitated: (i) similar enantiomers can bind directly to enlarge the chain, (ii) a C monomer can bind to the chain forming a CT-P_{2a} dimer at the end of the chain, and after the isomerization of the free end of the C monomer to yield the T enantiomer, or (iii) a C monomer can form a CT-P_{1a} dimer at the end of the chain followed by the assisted isomerization mechanism yielding the required T enantiomer. Although these chains are relatively stable and can easily be formed, they can be destroyed at room temperature unless are stabilized at both ends by clusters. During the growth of the chains, they can interconnect forming more complex patterns by means of the linkers.

Besides the straight growth, a chain may change its growth direction if a linker is created. This happens if a monomer binds to the chain end formed by a CT-P_{2a} dimer. Then if the new added monomer is: (i) a cis, then a CCT-Lin linker is created, or (ii) if it is a T' (the specular enantiomer of the isomer in the chain), a TCT'-Lin linker happens instead. In the former case a kink is created in the ribbon, which continues growing in the same direction (see Fig. 11 C). In the latter case the direction of growth is changed with molecules tending to aggregate in between both chiral ribbons forming small clusters (see Fig. 11 D). From a kink, a second ribbon adjacent to the main chain can start to grow as is shown in Fig. 11 (F).

As we said above, the borders of islands are mainly formed by C isomers. The growth of these islands is produced in several steps. Firstly, either a new C isomer reaches the borders by diffusion, or a T approaches to the border and then, by means of the assisted isomerization mechanism, becomes a C isomer. It can be stabilized when the monomers in the interior isomerize to create more H bonds with the new added monomer. Those monomers at the edges that are not stabilized by this mechanism are very mobile and can leave the cluster easily. This is in accordance with the experiment, according to which, at submonolayer coverages, supramolecular islands coexist with a disordered fluid phase of highly mobile molecules.⁵

Appearance of long ribbons of molecules after thermal quenching is a characteristic feature in the observed experimental STM images.⁵ We consistently observed formation of such features also in our KMC simulations, Fig. 11. We believe that the growth of long ribbons of trans species happens due to a delicate balance between the strength of the different H bonds and the isomerization barriers. While at room temperature the associated transition rates of breaking any H bond are similar, at lower temperature the rate of breaking a single H bond becomes relatively much larger than the rate for breaking a double H bond. Furthermore, isomerization of monomers involving the breaking of an H bond at the edges of the islands are much more difficult to occur than at the free end of the monomers at the ends of chains. This makes it more difficult to trap new monomers, by the mechanisms explained above, at the edges of the islands than at the ends of chains, favoring the growth of the chiral ribbons with a T isomer proportion increasing.

Other features observed experimentally⁵ such as linkers, kinks, clusters and islands were also consistently observed in our KMC simulations, Fig. 11. We have also observed formation of islands when performing simulations at higher coverages (see details in the Supplementary Information).

It was claimed in⁵ that the number of T isomers on the surface greatly surpassed that of the C isomers. We did not find this in our simulations: at room temperature all our simulations yield a slightly bigger proportion of C isomers with a mean value of 55.4%, while the L-trans and D-trans isomers were found at 22.5% and 22.1%, respectively. At lower temperatures (assuming the same deposition rate), the proportion of C isomers decreased to 42.7%, whereas T isomers were found in increasing numbers (around 29.2% for L-trans and 28.7% for the D-trans).

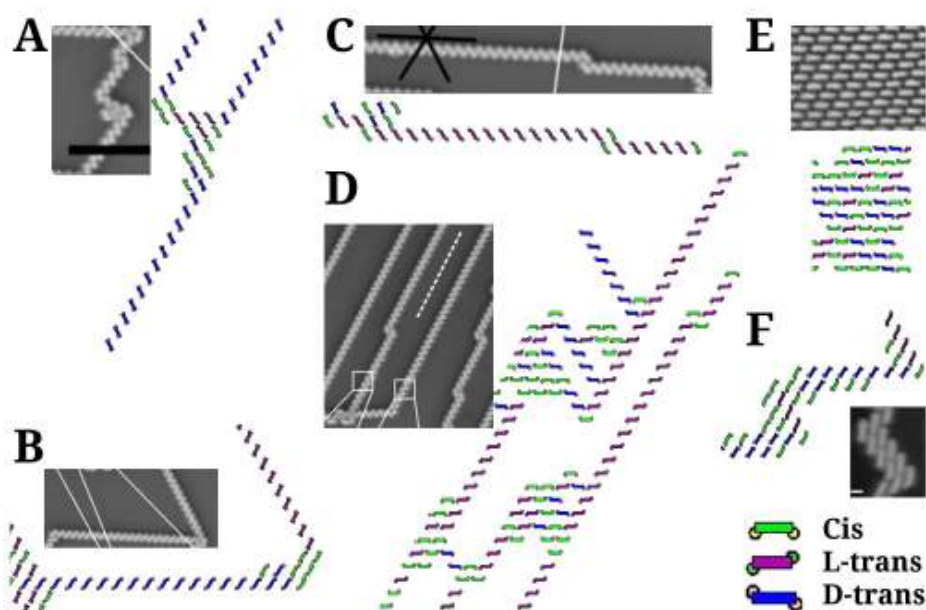


Figure 11 Sections of the 85x85 KMC simulation cell corresponding to a 20% coverage and a 10^{-7} ps $^{-1}$ deposition rate are compared with experimental STM images (adapted with permission from Ref. 5). The experimental STM high-resolution image used for A, B, C, D and F was taken at 8 K on Ag(111) with a coverage of 0.1 ML, and STM image in E was taken at room temperature. A, B and C STM images have been horizontally mirrored to facilitate the comparison with the structures found in the simulations. (A) A long chiral chain formed by D-trans, with some molecules aggregated around a kink. It is also seen that a CCC-Lin linker binds a long L-trans with a short D-trans chain. (B) Two long chains of the two different isomers bound by a double CCC-Lin linker. (C) A long chiral chain formed by L-trans with a TCC-Lin linker in the middle forming a kink. (D) Long parallel chains with all kinds of linkers; note that it is seen in the example provided that clusters may condense between chains in our KMC simulations. (E) A small piece of an island formed by a mixture of both C and T isomers. (F) Side-by-side chains growing from linkers. Green rectangles represent cis, blue D-trans, and magenta L-trans isomers. The snapshots A, B and C correspond to the step 198000000 of simulation number 01 that was run at 200 K, snapshots D and E were taken from the step 755000000 of the simulation number 02 run at 175 K, and F was taken from the step 760000000 of the simulation 03 run at 300 K. The movies of these KMC simulations are given in the Supplementary Information.

Conclusions

In this paper we considered the kinetics of growth at small and intermediate coverages of assemblies of pTmDC molecules on the Ag(111) surface. We have used a toolkit of methods, from DFT modeling of adsorption geometries and NEB calculations of diffusion and isomerization energy barriers and mechanisms, to KMC modeling of the actual growth of assemblies. It was found that the dispersion interaction is the main contributor that binds the molecular assemblies to the surface with particularly favored adsorption sites through NAS interactions in which N atoms are placed above surface Ag atoms. This naturally leads to a slightly corrugated surface landscape for the molecules. Also, the preferred sites are those where phenyl rings avoid Ag atoms underneath. The molecule can be viewed as standing on two legs. The fact that the dispersion contribution dominates molecule-surface interactions leads to the molecules being quite mobile on the surface at RT and diffuse exploiting the pivoting mechanism when one “leg” serves as a pivot while another moves to the new available site. We also investigated possibilities of interconversion of C and T isomers into each other on the surface. We find that monomers may easily undergo transformations into each other following the under-side mechanism which ensures the lowest energy barrier; moreover, the transformation occurs with equal rates implying equal amounts of both C and T monomers on the surface.

However, as molecules come closer to each other, they bind via a hydrogen bonding interaction forming dimers, chains, clusters and linkers. These structures were found to be almost identical to those found in our previous gas phase DFT calculations.⁶ We find that H bonds are up to 1.5 times stronger on the surface than in the gas phase and this proves the dominant role the H bonding plays in binding the molecules together in the observed assemblies.⁵ At the same time, we find that the growth is greatly facilitated by the assisted isomerization mechanism. Of course, lowering of the system free energy due to formation of H bonds between molecules is the main driving force behind the assembly formation. However, the assisted isomerization mechanism is the key mechanism of growth of linkers, islands and long ribbons. This is because it leads to maximizing the number of double H bonds between molecules. Hence, this specific mechanism is capable of explaining the structures observed in the experiment.⁵

In our KMC simulations, we find that during the growth process chiral ribbons are created and destroyed at room temperature and can interconnect between themselves, creating more complex patterns by means of the linkers, where small clusters start to condensate. At the ends of the ribbons is a monomer with a free end that can isomerize easily facilitating further growth. At submonolayer coverages supramolecular islands coexist with a disordered fluid phase of highly mobile monomers as was also observed in the experiment.⁵

Importantly, no evidence was found in our theoretical investigation on the alleged chiral selectivity related to abundance of the T isomers upon the assembly as was suggested in,⁵ the claim which was made entirely on analyzing the STM images. Instead, we find that both isomers are present almost in equal amounts. Moreover, islands are suggested to be not static: they are in a dynamic equilibrium whereby the three isomers (C and both T isomers) interconvert one into the other continuously at RT. However, the edges of islands are formed mainly by cis isomers.

Our study shows the importance of theoretical modeling in making conclusions concerning observed assemblies and the mechanisms responsible for their growth. We hope that this investigation sheds light on the mechanism of self-assembly of pTmDC molecules on the Ag(111) surface, demonstrating clearly, on the one hand, the role of their interaction with the surface which provides their high mobility via the pivoting mechanism, and, on the other, establishes the relevance of the assisted isomerization reaction which are the key for understanding the observed supramolecular assemblies. This detailed atomistic self-assembly mechanism may be behind the growth of many other hydrogen bonding structures of chiral molecules.

Acknowledgment

D.A.-P. and J.M.R. acknowledge support by the Spanish MINECO and the ERDF of the European Union (project no. CTQ2012-38599-C02). We belong to the MALTA Team (CSD2007-0045 project, MEC Consolider Ingenio 2010 program). D.A.-P. thanks the now extinct Spanish MICINN for an FPI grant. Via our membership of the UK's HPC Materials Chemistry Consortium, which is funded by EPSRC (EP/F067496), this work made use of the facilities of HECToR, the UK's national high-performance computing service, which is funded by the Office of Science and Technology through EPSRC's High End Computing Programme. MALTA computational facilities are also acknowledged.

References

- [1] Barth, J. V.; Costantini, G.; Kern, K. Engineering Atomic and Molecular Nanostructures at Surfaces. *Nature* **2005**, *437*, 671–679.
- [2] Bandyopadhyay, A.; Pati, R.; Sahu, S.; Peper, F.; Fujita, D. Massively Parallel Computing on an Organic Molecular Layer. *Nat. Phys.* **2010**, *6*, 369–375.
- [3] Mura, M.; Silly, F.; Burlakov, V.; Castell, M. R.; Briggs, G. A. D.; Kantorovich, L. N. Formation Mechanism for a Hybrid Supramolecular Network Involving Cooperative Interactions. *Phys. Rev. Lett.* **2012**, *108*, 176103.
- [4] Barlow, S. M.; Raval, R. Complex Organic Molecules at Metal Surfaces: Bonding, Organisation and Chirality. *Surf. Sci. Rep.* **2003**, *50*, 201–341.
- [5] Marschall, M.; Reichert, J.; Seufert, K.; Auwärter, W.; Klappenberger, F.; Weber-Bargioni, A.; Klyatskaya, S.; Zoppellaro, G.; Nefedov, A.; Strunskus, T. et al. Supramolecular Organization and Chiral Resolution of p-Terphenyl-m-Dicarbonitrile on the Ag(111) Surface. *ChemPhysChem* **2010**, *11*, 1446–1451.
- [6] Abbasi-Pérez, D.; Recio, J. M.; Kantorovich, L. Building Motifs During Self-Assembly of para-Terphenyl-meta-Dicarbonitrile on a Metal Surface: a Gas Phase Study. *J. Phys. Chem. C* **2014**, *118*, 10358–10365.
- [7] Jónsson, H.; Mills, G.; Jacobsen, K. W. In *Classical and Quantum Dynamics in Condensed Phase Simulations*; Berne, B. J., Ciccotti, G., Coker, D. F., Eds.; World Scientific, 1998; Chapter Nudged Elastic Band Method for Finding Minimum Energy Paths of Transitions.
- [8] Mills, G.; Jónsson, H.; Schenter, G. K. Reversible Work Transition State Theory: Application to Dissociative Adsorption of Hydrogen. *Surf. Sci.* **1995**, *324*, 305–337.
- [9] VandeVondele, J.; Krack, M.; Mohamed, F.; Parrinello, M.; Chassaing, T.; Hutter, J. Quickstep: Fast and Accurate Density Functional Calculations Using a Mixed Gaussian and Plane Waves Approach. *Comput. Phys. Commun.* **2005**, *167*, 103 – 128.
- [10] Lippert, G.; Jurg, H.; Parrinello, M. A Hybrid Gaussian and Plane Wave Density Functional Scheme. *Mol. Phys.* **1997**, *92*, 477–488.
- [11] Goedecker, S.; Teter, M.; Hutter, J. Separable Dual-Space Gaussian Pseudopotentials. *Phys. Rev. B* **1996**, *54*, 1703–1710.
- [12] Perdew, J. P.; Burke, K.; Ernzerhof, M. Generalized Gradient Approximation Made Simple. *Phys. Rev. Lett.* **1996**, *77*, 3865–3868.
- [13] Grimme, S.; Antony, J.; Ehrlich, S.; Krieg, H. A Consistent and Accurate ab initio Parametrization of Density Functional Dispersion Correction (DFT-D) for the 94 Elements H-Pu. *J. Chem. Phys.* **2010**, *132*, 154104.
- [14] VandeVondele, J.; Hutter, J. Gaussian Basis Sets for Accurate Calculations on Molecular Systems in Gas and Condensed Phases. *J. Chem. Phys.* **2007**, *127*, 114105.
- [15] Boys, S.; Bernardi, F. The Calculation of Small Molecular Interactions by the Differences of Separate Total Energies. Some Procedures with Reduced Errors. *Mol. Phys.* **1970**, *19*, 553.
- [16] Henkelman, G.; Jónsson, H. Improved Tangent Estimate in the Nudged Elastic Band Method for Finding Minimum Energy Paths and Saddle Points. *J. Chem. Phys.* **2000**, *113*, 9978–9985.
- [17] Henkelman, G.; Uberuaga, B. P.; Jónsson, H. A Climbing Image Nudged Elastic Band Method for Finding Saddle Points and Minimum Energy Paths. *J. Chem. Phys.* **2000**, *113*, 9901–9904.
- [18] Otero, R.; Schock, M.; Molina, L. M.; Legsgaard, E.; Stensgaard, I.; Hammer, B.; Besenbacher, F. Guanine Quartet Networks Stabilized by Cooperative Hydrogen Bonds. *Angew. Chem. Int. Ed.* **2005**, *44*, 2270.
- [19] Kelly, R. E. A.; Kantorovich, L. Planar Nucleic Acid Base Super-Structures. *J. Mater. Chem.* **2006**, *16*, 1894–1905.

- [20] Mura, M.; Gulans, A.; Thonhauser, T.; Kantorovich, L. Role of Van der Waals Interaction in Forming Molecule-Metal Junctions: Flat Organic Molecules on the Au(111) Surface. *Phys. Chem. Chem. Phys.* **2010**, *12*, 4759–4767.
- [21] Johnson, E. R.; Keinan, S.; Mori-Sánchez, P.; Contreras-García, J.; Cohen, A. J.; Yang, W. Revealing Noncovalent Interactions. *J. Am. Chem. Soc.* **2010**, *132*, 6498–6506.
- [22] Contreras-García, J.; Yang, W.; Johnson, E. R. Analysis of Hydrogen-Bond Interaction Potentials from the Electron Density: Integration of Noncovalent Interaction Regions. *J. Phys. Chem. A* **2011**, *115*, 12983–12990.
- [23] Contreras-García, J.; Calatayud, M.; Piquemal, J.-P.; Recio, J. Ionic Interactions: Comparative Topological Approach. *Comput. Theor. Chem.* **2012**, *998*, 193 – 201.
- [24] Voter, A. F. In *Radiation effects in solids*; Sickafus, K. E., Kotomin, E. A., Uberuaga, B. P., Eds.; NATO Publishing unit Handbook of Material Modeling, Part A. Methods; Springer, NATO Publishing Unit, Dordrecht, The Netherlands, 2005.
- [25] Reuter, K.; Stampfl, C.; Scheffler, M. In *Ab initio Atomistic Thermodynamic and Stastical Mechanics of Surface Properties and Functions*; Yip, S., Ed.; Handbook of Material Modeling, Part A. Methods; Springer, 2005; Vol. Part A; p 149.

Supplementary Information

Role of Isomerization in Kinetics of Self-Assembly: p-Terphenyl-m-Dicarbonitrile on Ag(111) Surface

David Abbasi-Pérez and J. Manuel Recio

MALTA-Consolider Team and Departamento de Química Física y Analítica, Facultad de Química,
Universidad de Oviedo, 33006 Oviedo, Spain

Lev Kantorovich*

Physics Department, King's College London, Strand, London, WC2R 2LS, United Kingdom
lev.kantorovitch@kcl.ac.uk

Monomers on the surface

To explore the potential energy surface of a monomer on the silver surface, we started by selecting six sites on the surface, Fig. S1, where one N atom of the molecule was placed, and then, using the chosen N atom as a pivoting point, considered various orientations of the molecule by rotating its molecular backbone prior to full geometry optimization.

An extended selection of DFT relaxed adsorption geometries of the C and T monomers on the surface is shown in Figs. S2 and S3, respectively. The mean distances to the surface of the carbon skeleton of the monomers is around 3.25 Å and of the N atoms is around 2.61 and 2.68 Å for the cis and trans isomers respectively. The dihedral angle between rings for trans monomers lay in the range of 9-15°, and between 18-20° for the cis.

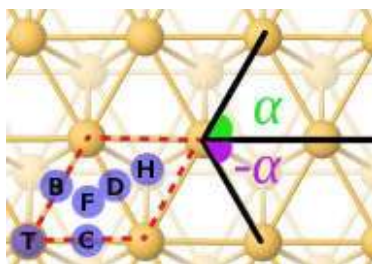


Figure S1 Docking sites on the Ag (111) surface. T label is used for top sites, B, C and D are used for the different bridge sites, and F and H are used for the fcc and hcp hollow sites, respectively. Red dotted line indicates the primitive surface unit cell. The angle the backbone of the molecule makes with respect to one of the Ag-Ag surface symmetry directions (chosen as the horizontal axis in the picture) are considered positive if measured in the counterclockwise (green alpha) and negative if measured in the clockwise directions (purple alpha), respectively. Orange balls represent silver atoms

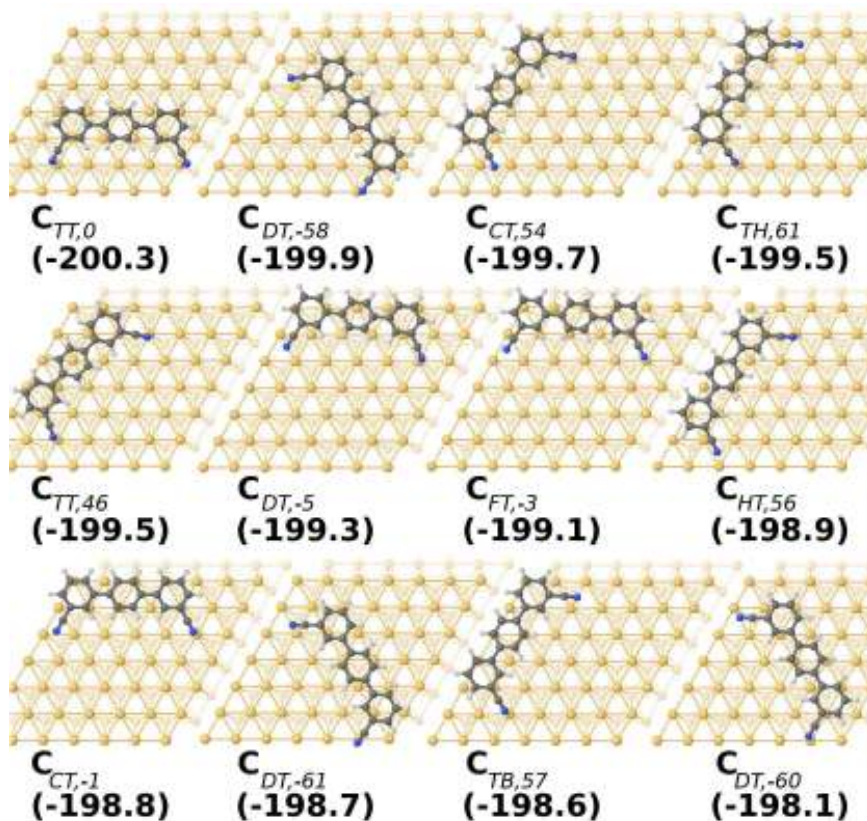


Figure S2 Twelve most stable cis conformers (C) on the surface found after the DFT geometry relaxation. The suggested nomenclature is meant to indicate the adsorption site and orientation of the molecule. The first subscript indicates the docking site of the left N atom, the second subscript indicates the docking site of the right N atom, and the number after the comma indicates the alpha angle (see Fig. S1). The corresponding binding energies (in kJ/mol) are also given underneath the symbol of the structure in round brackets. Orange, gray, white and blue balls correspond to Ag, C, H and N atoms, respectively.

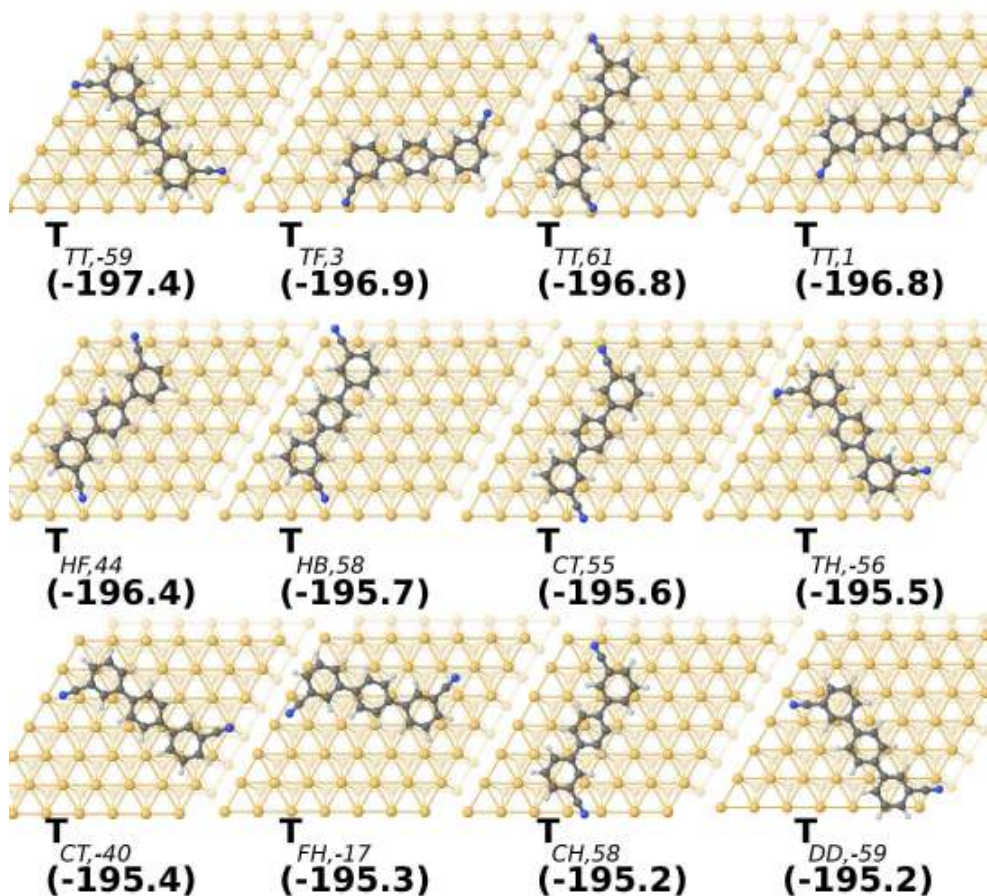


Figure S3 Twelve most stable trans conformers (T) on the surface found after the DFT geometry relaxation. The subscript of the nomenclature for each structure and the color code used are the same as in Fig. S2. When both N atoms align along a vertical line, then the first subscript refers to the bottom atom. The corresponding binding energies (in kJ/mol) are also given. Only L isomers are shown for clarity; the corresponding D isomers with identical binding energies are obtained by appropriate flipping of the molecules (not shown).

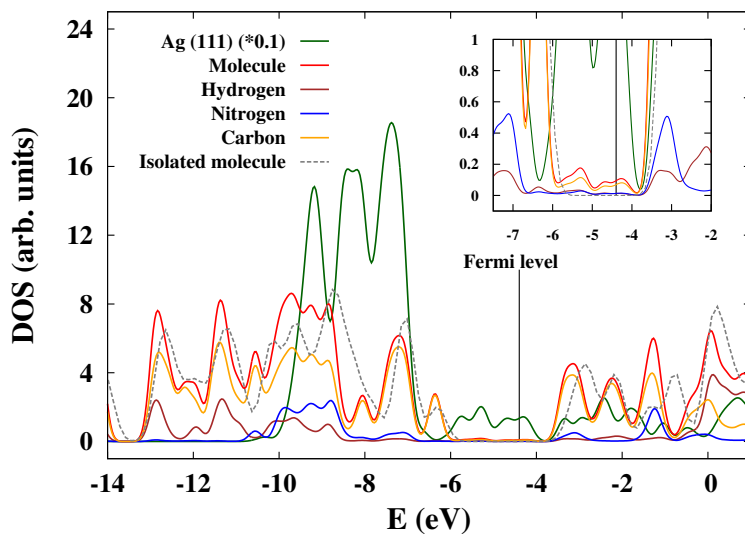


Figure S4 Comparison of PDOS for the cis structure $C_{TT,0}$ (solid lines) and the molecule in the gas phase (dashed line). The inset shows the region around the metal Fermi energy in more detail. Notice the negligible contribution of the monomer to the DOS in this region

A projected density of states (PDOS) of a cis molecule $C_{TT,0}$ (see Fig. 2 of the main text) placed on the surface is compared with the PDOS calculated for an isolated molecule. We see that the HOMO and LUMO levels of the molecule are clearly positioned on the left and right of the Fermi energy of the surface, with small variations with respect to the isolated molecule.

In Fig.S5 the DFT+NEB calculated diffusion path for a T monomer on the surface is shown exploiting two mechanisms: pivoting and sliding. The latter mechanism results in higher energy barrier similarly to the case of diffusion of a C monomer, Fig. 5 of the main text.

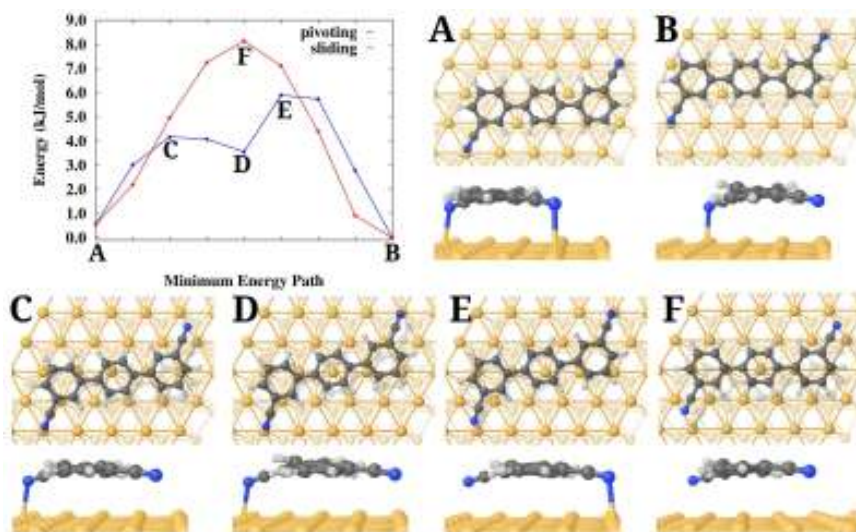


Figure S5 Diffusion paths for a T monomer on the Ag(111) surface. For the explanations, see the caption to Fig. 5 of the main text.

Dimers on the surface

A number of stable dimer structures, fully relaxed with our DFT method, together with their total binding energies per molecule and H bond binding energies (in round and square brackets, respectively) are shown in Fig. S6. The H bonding binding energies of dimers on the surface can be directly compared with those for the dimers in the gas phase reported previously.¹ The tendency in both cases is the same, but the H bond is up to 1.5 times stronger on the surface than in the gas phase. In fact, dimers with a single H bond and a totally planar geometry that are unstable in the gas phase, become stable on the surface with the central ring slightly rotated by the dihedral angle of around 12.5.

We also defined a (positive) *deformation energy* $\Delta E_{def}^A = E_A - E_A^0$ for any component (surface and/or molecule) of the whole system, where E_A is the energy of the component A in the complex. This energy shows the cost for the component A to be in the complex. Cis and trans monomers have a mean deformation energy of 6.4 and 12.9 kJ/mol, respectively, when they are bound to the surface, and this deformation energy increases to 13.0 and 14.0 kJ/mol when they form a dimer. On the other hand, the surface has a deformation energy of around 1.8 kJ/mol when a monomer is bound to it and increases to a mean value of 4.8 kJ/mol in the case of dimers. This suggests that it is easier for a trans conformer to form a dimer once it is deposited on the surface.

An example of the EDD is shown for the dimer CC-P_{2a} in Fig. S7. It is seen by comparing panels E and F of the same Figure that the contribution of the dispersion interaction between molecules increases when the dimer is placed on the surface. Similar analysis has been conducted for other dimers as well, and in all cases qualitatively similar EDD were observed for the dimers in the gas phase and on the surface. This observation confirms that binding between monomers in dimers on the surface can still be characterized in terms of the H-bonding with significant contribution coming from the dispersion interaction, as discussed above and in our previous study.¹ The H bond distances also follow the same tendency as in the gas phase; however, on the surface these distances become around 0.04 shorter for P geometries (with a distance around 2.44 for the bond where the carbonitrile groups and the H atoms lie along a line) and more than 0.10 shorter for Tri geometries, where the H bond is around 2.25 for the shortest non-linear H bond as in the CC-Tri₂ geometry. The mean distance of the molecule to the surface is 3.29 and 3.18 for the N atoms.

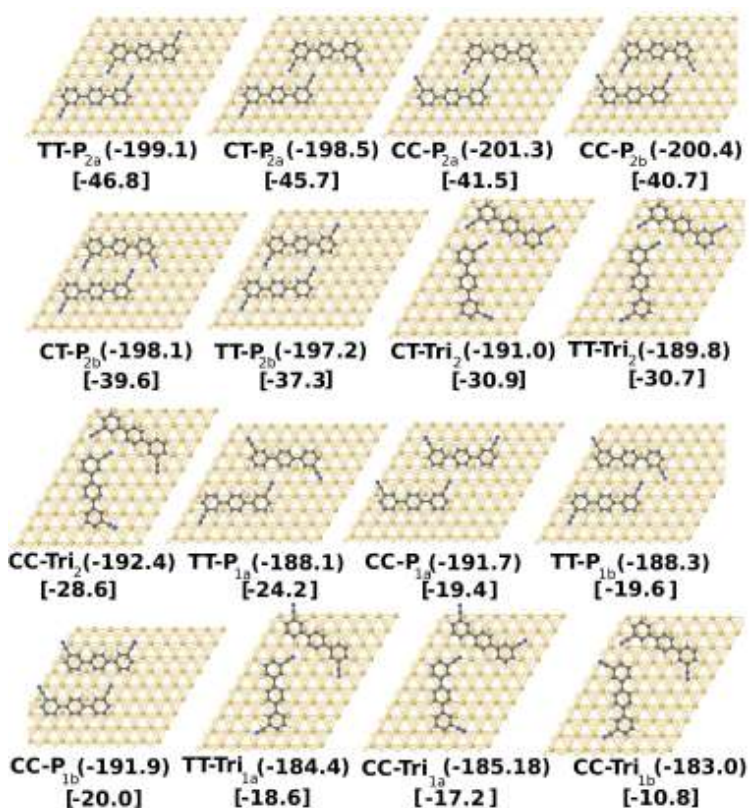


Figure S6 A more extensive selection of dimers. The legend used to denote the dimers means: the first two characters are composed of either C or T corresponding to the cis or trans conformations of the constituent monomers; the next letters are either P or Tri referring to either parallel or triangular forms, respectively; the index 1 or 2 that follows corresponds to the number of hydrogen bonds in the dimer; finally, a subscript *a* or *b* is used to differentiate between similar parallel and triangular structures.

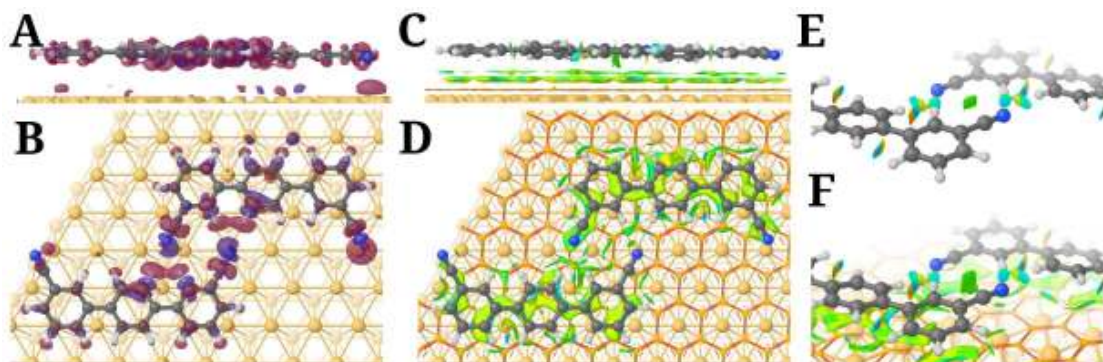


Figure S7 Electron density plots of the dimer $CC-P_{2a}$ on the surface shown either via EDD (side (A) and top (B) views) or NCI (side (C) and top (D) views). NCI shows the H bonds and attractive dispersion interaction between the carbonitrile groups in a dimer without (E) and with (F) the surface. Note the bigger green area in (F) related with the dispersion interactions between carbonitrile groups. The same color scheme as in Fig. 3 of the main text is used.

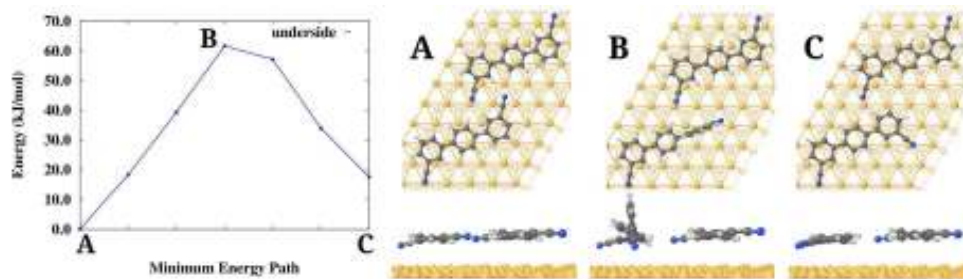


Figure S8 The MEP (the left panel) and the initial (A), final (C) and transition state (B) geometries for the NEB+DFT relaxed under-side isomerization transition between T-T and a T-C dimers.

The isomerization reaction between T-T and T-C dimers is shown in Fig. S8. Only the under-side mechanism was studied as it is bound to be more favourable as follows from other calculations discussed in the main text.

Ribbons and linkers on the surface

More views of the two studied ribbon structures are given in Fig. S9. The mean distance of the N atoms to the surface in the ribbons is between 3.2 and 3.3 due that the carbonitrile group being not bent towards the surface when engaged in the H bond. The dihedral angle is about 10° which is very close to the value in the gas phase.

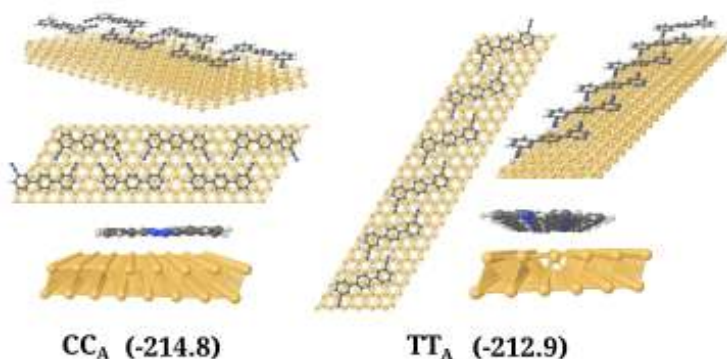


Figure S9 Relaxed geometries and corresponding binding energies (per molecule, in brackets and in kJ/mol) of the CC_A and TT_A ribbons on the silver surface (perspective, top and side views).

More studied linker structures are shown in Fig. S10. The molecules in the linker structures are at 3.29 Å above the surface and the carbonitrile groups, involved or not in the H bonds, become parallel to the surface.

We showed previously that in the gas phase the linear H bond is stronger than the non linear one.¹ The same happens on the surface as we can see comparing the H bond binding energies of the P and Tri dimers, Fig. S6. This explains why the CCC-Tri linker, which has 3 linear and 3 non linear H bonds, is more stable than the other linkers with 4 linear H bonds.

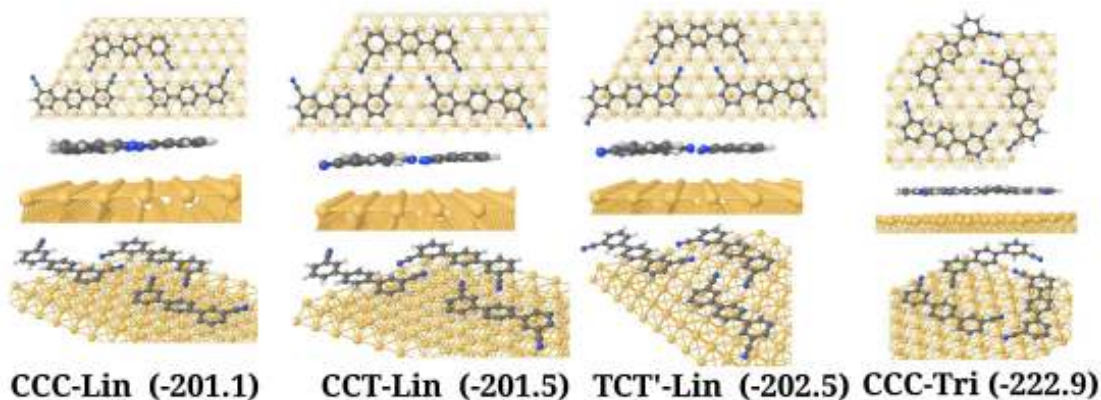


Figure S10 Relaxed geometries and corresponding binding energies (per molecule, in brackets, in kJ/mol) of several linker clusters on the silver surface (top, side and perspective views).

Molecules in brickwall islands

The MEP and the relaxed geometries of the initial, final and transition states (both top and side views) of the isomerization reaction of a monomer in the T island is shown in Fig. S11.

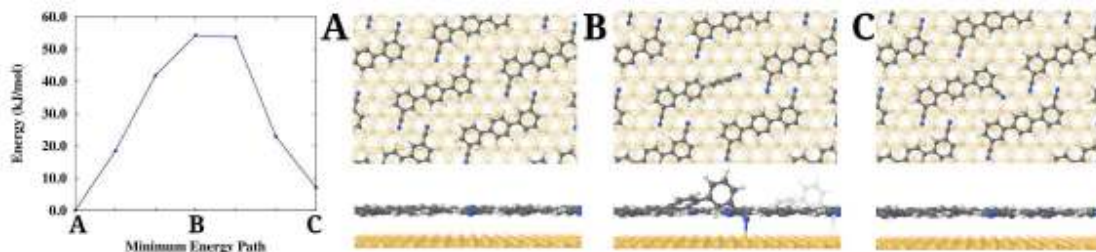


Figure S11 MEP (left panel) of the cis-trans isomerization of a monomer inside a monolayer with the corresponding initial (A), transition (B), and final state (C) relaxed geometries (top and side views) obtained with the NEB+DFT method.

A typical STM image of a brickwall T monolayer from² is shown in Fig. S12. The superimposed molecular images correspond to the structure proposed in² and consisting only of the T isomers. However, bright white areas on the other sides of the corresponding benzonitrile groups (some of these areas are circled) indicate that a portion of the time during the scan of these regions the group was directed the other way round. An animation of this effect can be seen in the movie *Isomerization_In_Island.mp4* provided.

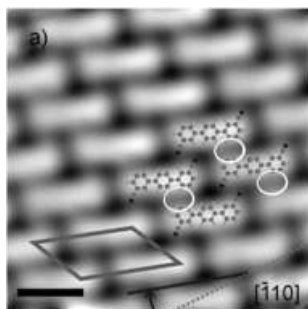


Figure S12 High resolution STM image (adapted with permission from Ref. 2) of a pTmDC island on the silver surface at room temperature. White circles indicate additional bright areas between chains.

KMC simulations

In Figs. S13-S15 snapshots of KMC simulations for several coverages are displayed. We also provide several movies of the KMC runs in which every 500000-th move has been displayed.

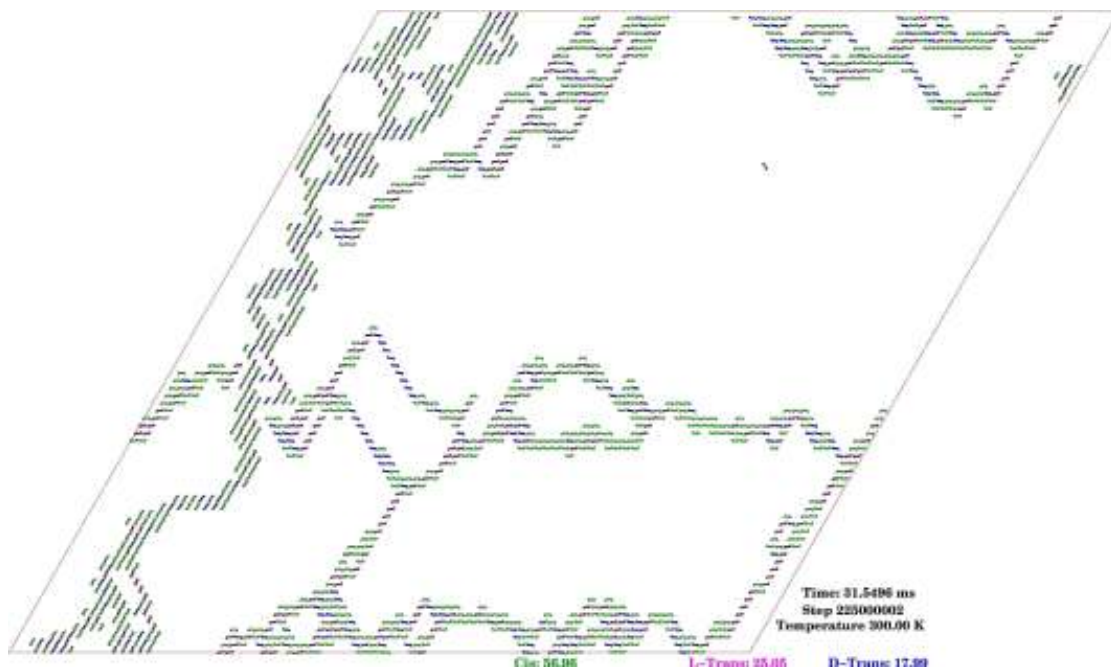


Figure S13 Snapshot of a KMC simulation at 300 K with the coverage of 20% in a 85x85 cell, and a deposition rate of 10^{-7} ps $^{-1}$. Green, purple and blue rectangles are cis, L-trans and D-trans monomers, respectively. Their proportions are given with the same color code at the bottom in the image. The KMC step number and the simulation time corresponding to the snapshot are also indicated.

Besides the snapshots, a number of movies of the KMC simulations at different temperatures and coverages are also provided (see Table S1 for details).

Movie number	Cell size	T (K)	Deposition rate (ps $^{-1}$)	Coverage (%)
01	85	200	10^{-7}	20
02	85	175	10^{-7}	20
03	85	300	10^{-7}	20
04	85	300	10^{-7}	20
05	50	300	10^{-7}	50
06	50	300	10^{-7}	80

Table S1 Parameters of the different movies.

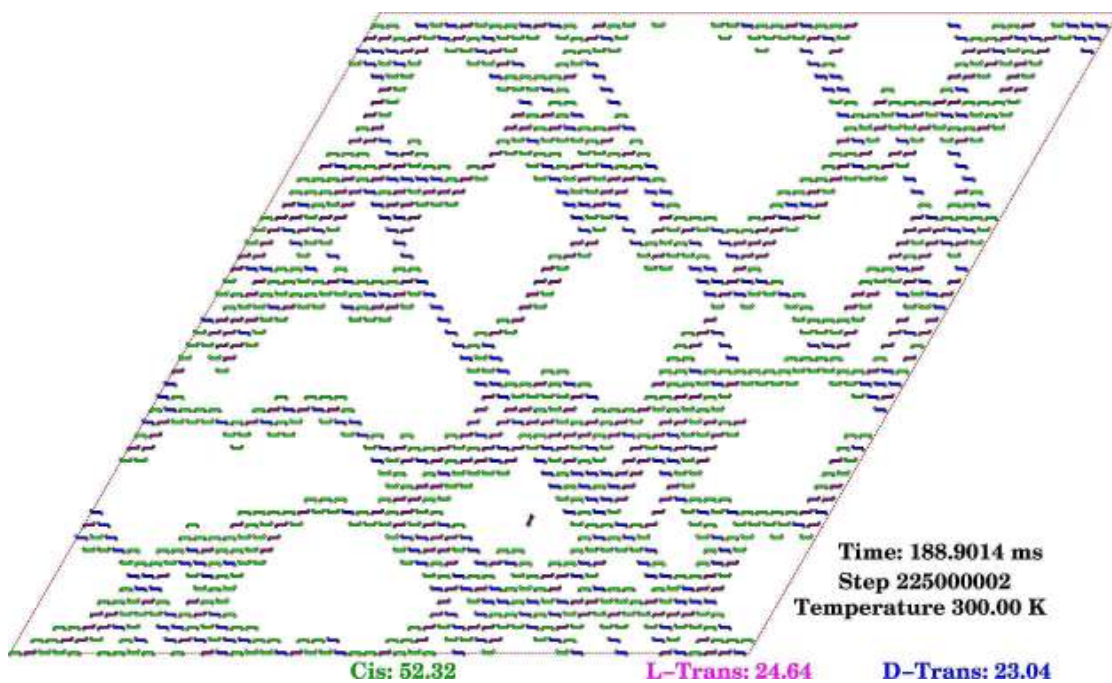


Figure S14 A snapshot of a KMC run corresponding to the 50x50 simulation cell for 300K, the coverage of 50% and deposition rate of 10^{-7}ps^{-1} . The same color code as in Fig. S13 is used.

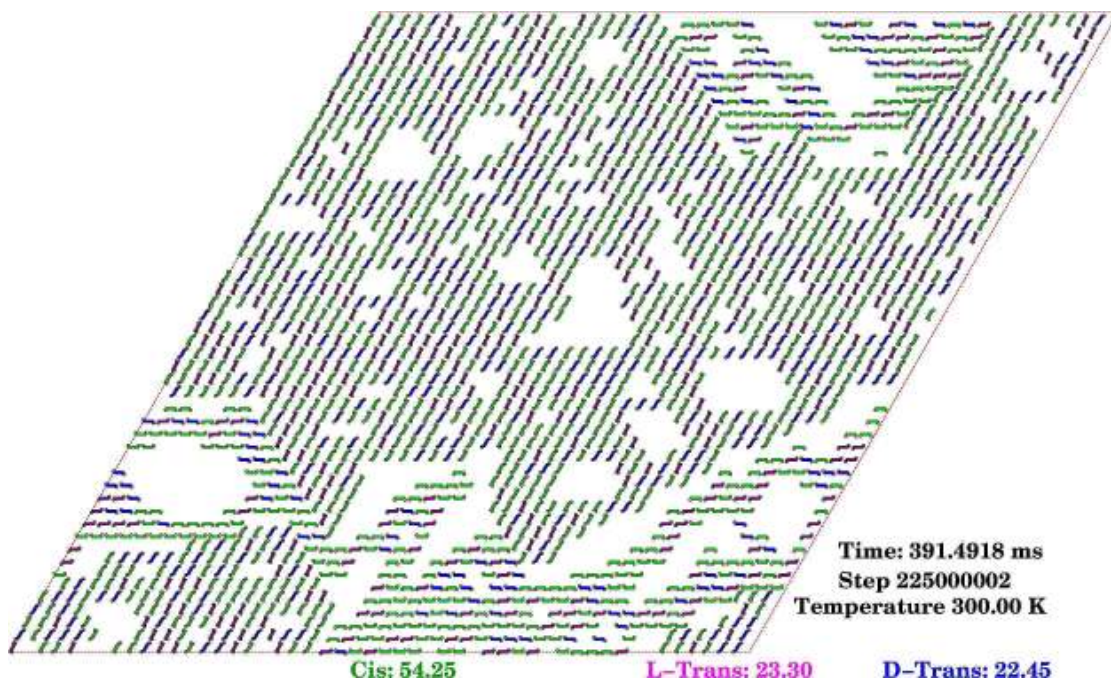


Figure S15 A snapshot of a KMC run corresponding to the 50x50 simulation cell for 300K, the coverage of 80% and deposition rate of 10^{-7}ps^{-1} . The same color code as in Fig. S13 is used.

References

- [1] D. Abbasi-Pérez, J. M. Recio and L. Kantorovich, *J. Phys. Chem. C*, 2014, **118**, 10358–10365.
- [2] M. Marschall, J. Reichert, K. Seufert, W. Auwärter, F. Klappenberger, A. Weber-Bargioni, S. Klyatskaya, G. Zoppellaro, A. Nefedov, T. Strunskus, C. Wöll, M. Ruben and J. V. Barth, *ChemPhysChem*, 2010, **11**, 1446–1451.

B | INFORME DEL ÍNDICE DE IMPACTO DE LAS PUBLICACIONES

COMO dicta la normativa actual, la tesis presentada por compendio de publicaciones ha de ir acompañada de un informe con el factor de impacto de cada uno de los artículos. Estos artículos se corresponden con las referencias [102,3,1,2](#) y se listan a continuación:

1. GIBBS2: A new version of the quasiharmonic model code. II. Models for solid-state thermodynamics, features and implementation, Otero-de-la Roza, A., Abbasi-Pérez, D. and Luaña, V. (2011), *Computer Physics Communications*, vol. 182 (10), pp. 2232–2248.
2. Modeling graphite under stress: Equations of state, vibrational modes, and interlayer friction, Abbasi-Pérez, D., Menéndez, J., Recio, J., Otero-de-la Roza, A., del Corro, E., Taravillo, M., Baonza, V. and Marqués, M. (2014), *Phys. Rev. B*, vol. 90 (5), p. 054 105.
3. Building Motifs during Self-Assembly of para-Terphenyl-meta-dicarbonitrile on a Metal Surface: A Gas-Phase Study, Abbasi-Pérez, D., Recio, J. M. and Kantorovich, L. (2014), *J. Phys. Chem. C*, vol. 118, pp. 10 358-10 365.
4. Role of Isomerization in Kinetics of Self-Assembly: p-Terphenyl-m-Dicarbonitrile on Ag(111) Surface, Abbasi-Pérez, D., Recio, J. M. and Kantorovich, L. (2015), *PCCP* (accepted, minor corrections).

. Las cuatro revistas presentan un alto índice de impacto estando en el primer cuartil en sus correspondientes categorías. La revista *Journal of Physical Chemistry C*, pertenece a tres categorías, y en una de ellas (*NANOSCIENCE & NANOTECHNOLOGY*) se encuentra en el segundo cuartil, estando en las demás en el primero. En la siguiente tabla se muestran los índices de impacto y posición de cada una de las revistas donde los trabajos de investigación han sido publicados.

Cabe destacar que el artículo donde se presenta GIBBS2¹⁰² tiene 50 citas hasta la fecha, lo que da muestras de la utilidad del programa. Además ha sido publicado como código libre bajo la licencia pública general GNU v3, lo que le aporta un valor añadido al trabajo y una mayor accesibilidad a la comunidad científica en general. El artículo del grafito bajo condiciones no hidrostáticas³ ha sido citado una vez, de momento en [arXive](#), en un trabajo del grupo del profesor David Dunstan. Los autores destacan que nuestro trabajo es el primero publicado con resultados teóricos sobre la respuesta del

Table 4: Índices de impacto y posición de cada revista dentro de sus respectivas categorías. El campo “Ranking” representa la posición dentro de la categoría con respecto al total de revistas en la categoría. La información ha sido recogida del Journal Citation Reports correspondiente al año 2013 a través de la ISI Web of Knowledge.

Revista	Factor de Impacto	Categoría	Ranking
Comput. Phys. Commun.	2.407	COMPUTER SCIENCE, INTERDISCIPLINARY APPLICATIONS PHYSICS, MATHEMATICAL	12/102 5/55
Phys. Rev. B	3.664	PHYSICS, CONDENSED MATTER	14/67
J. Phys. Chem. C	4.835	CHEMISTRY, PHYSICAL MATERIALS SCIENCE, MULTIDISCIPLINARY NANOSCIENCE & NANOTECHNOLOGY	29/136 29/251 19/73
PCCP	4.198	CHEMISTRY, PHYSICAL PHYSICS, ATOMIC, MOLECULAR & CHEMICAL	33/136 5/33

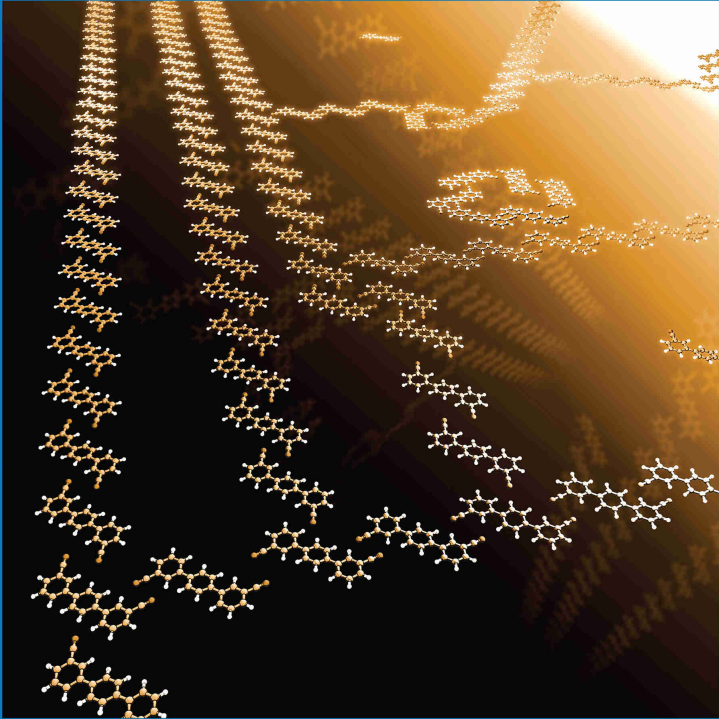
grafito en condiciones no hidrostáticas. Además, el artículo publicado en el JPCC¹ fue portada de la revista como se muestra en la imagen.

JPCC

MAY 15, 2014
VOLUME 118
NUMBER 19
pubs.acs.org/JPC

THE JOURNAL OF PHYSICAL CHEMISTRY

C



Shedding Light on Self-Assembly Processes: From Building Blocks to More Complex Organized Motifs (see page 10358)

ENERGY CONVERSION AND STORAGE, OPTICAL AND ELECTRONIC DEVICES,
INTERFACES, NANOMATERIALS, AND HARD MATTER

 ACS Publications
Most Trusted. Most Cited. Most Read.

www.acs.org

Figure 54: Cover Art related to the paper: Building Motifs during Self-Assembly of para-Terphenyl-meta-dicarbonitrile on a Metal Surface: A Gas-Phase Study.

ÍNDICE DE FIGURAS

1. Cis and trans isomers of pTmDC . 8
2. Static $E - V$ fitting Vinet EOS curves. Energy units are given in Hartree and volumes are given in bohr³ per formula unit. 14
3. Experimental and calculated Γ -frequencies for the scheelite (top) and BaWO₄-II (bottom) phase. The frequencies in the latter were computed at $p = 1.8$ GPa by J. López-Solano (private communication), and scaled down to $p = 0$ GPa using the Fleche's approach. Scheelite and BaWO₄-II experimental frequencies taken from Manjón *et al.*⁸⁰ and Lacomba-Perales *et al.*⁷¹ 16
4. V vs p curves obtained for the scheelite phase with the static, Debye and Debye-Einstein models at 0 K and 300 K. Experimental results are obtained from the results of Errandonea *et al.*⁴⁰ and Panchal *et al.*¹⁰³. 17
5. Temperature effects on C_p and α for scheelite at $p = 0$ GPa (top) and BaWO₄-II at $p = 6$ GPa (bottom). Curves stand for Debye (solid line) and Debye-Einstein (dashed line) models. 18
6. Temperature effects on S and G for scheelite at $p = 0$ GPa (top) and BaWO₄-II at $p = 6$ GPa (bottom). Curves stand for Debye (solid line) and Debye-Einstein (dashed line) models. 19
7. Enthalpy of scheelite (solid line) and BaWO₄-II (dashed line) phases. Static transition pressure is obtained at 4.78 GPa. 20
8. Left: Phase diagram of the barium tungstate obtained with the Debye-Einstein model. Right: Variation of ΔG with the temperature. ΔG is defined as $G_{\text{monoclinic}} - G_{\text{tetragonal}}$, which means that in positive ΔG regions scheelite is the most favourable phase. 21
9. Schematic energy profiles at increasing pressures (from left to right) for the tetragonal to the monoclinic transformation. 21
10. Tri-layer system with the central layer B (in red) sliding two different displacements s (indicated for each direction) at 0, 60 and 90 degrees. 27

11. Isoline of the $a=b$ (left) and c (right) lattice parameters of graphite under uniaxial (σ_z) and biaxial ($\sigma_x=\sigma_y$) conditions. Results for triaxialities (including hydrostatic) can also be inferred from this plot (see text). 28
12. Enthalpy *versus* c for different uniaxial (σ_z) stresses (left). Isolines of the enthalpy potential of graphite (right) corresponding to uniaxial (σ_z) and biaxial ($\sigma_x=\sigma_y$) conditions. Results for triaxialities (including hydrostatic) can also be inferred from this plot (see text). 31
13. Frequency isoline maps (top) and atomic displacements (bottom) of the vibrational modes $E_{2g}(2)$ (left) and $E_{2g}(1)$ of graphite under uniaxial (σ_z) and biaxial ($\sigma_x=\sigma_y$) conditions. Results for triaxialities (including hydrostatic) can also be inferred from this plot (see text). 34
14. Potential energy surface of the 3-slab model of graphite under zero stress (left) and $\sigma_z=16$ GPa (right) conditions. Displacements (s) and directions (Θ) ranged by the middle layer start in the ABA configuration. 35
15. Energy differences relative to the equilibrium energy of 3LG as a function of the sliding displacement of the B central layer, s , at a interlayer distance of 3.25 \AA ($\sigma_z = 0$ GPa, left) and at a interlayer distance of 2.91 \AA ($\sigma_z = 10$ GPa, right). Different lines mean selected directions at the labeled angles. The solid (colored) wide line represents the minimum energy sliding path for the B layer following different angles. 37
16. Friction forces between graphite layers *versus* σ_z for displacement directions from 0 to 60 degrees. 38
17. From top to bottom, frequency isoline maps and atomic displacements for the modes $B_{2g}(1)$, $B_{2g}(2)$, A_{2u} , and E_{1u} of graphite under uniaxial (σ_z) and biaxial ($\sigma_x=\sigma_y$) conditions. Results for triaxialities (including hydrostatic) can also be inferred from this plot (see main text). 39
18. Scheme of our experimental and theoretical strategies. Graphite specimens are directly compressed between the culets of two moissanite anvils. The different stress components acting on the sample are indicated by arrows with size approximately proportional to their relative values. On a tri-layer slab model with an initial ABA structure we displaced the central layer (B) at different sliding directions and for selected inter-layer distances. 43

19. (a) Raman spectra containing superimposed contributions from the front anvil and the sample at selected loading stresses. Both contributions are plotted separately for moissanite (green) and graphite (blue-violet). The inset shows a photograph of the graphite sample (in black) between the moissanite anvils in the pressure cell. (b) Second derivative analysis of the collected spectra providing unambiguous separation of ω_G of graphite and ω_{2LO} of moissanite. (c) Dependence of ω_G with σ_{load} , as measured by the ω_{2LO} of moissanite (upper axis). Different symbols stand for different experimental runs. The black solid line represents the fitting function shown on top to account for the sub-linear dependence of ω_G with σ_{load} . [44](#)
20. (a) Calculated lattice parameters, a and c , of graphite as function of the stress applied along the normal direction to graphene layers (σ_{load}), ($c/2$) corresponds to the interlayer distance between two graphene sheets. (b) Calculated Raman shift of the G band of graphite (referred to ω_G at zero pressure) as function of different stress components. (c) Comparison of calculated $\Delta\omega_G$ values under biaxial stress (solid line) and hydrostatic pressure (P_H) experiments (symbols) from Ref. [53](#). [45](#)
21. Calculated energy differences relative to the equilibrium energy of tri-layer graphene as a function of the sliding distance of the B central layer, s , (a) for selected sliding angles at an interlayer distance of 0.325 nm and (b) for the 0° direction at selected interlayer distances. (c) Rendering of the load (red) and friction (blue) forces acting on the graphite samples squeezed between the opposed anvils. As the sample is loaded, graphene layers tend to displace in all directions (colored arrows), but the confinement of the sample induces friction stresses opposed to the relative motion of the graphene layers. (d) Friction parameter in the 2D-FKT model (calculated with Eq. (1) at different load stresses) as a function of the sliding angle. [47](#)

22. (a) Calculated static friction stress along selected sliding directions as a function of σ_{load} ; symbols stand for different sliding directions using the same color definitions of Fig. 21a; lines are fits to Eq. 4.2. These results correspond to the maximum stresses found along the selected sliding directions before reaching the first energy maximum in Fig. 21a. (b) Comparison of the calculated static friction stress from (a) with the experimental values derived from Fig. 19c. The dashed line represents Eq. 4.2. using averaged values of the characteristics parameters shown in Fig 23; continuous lines represent the limiting values (sliding directions of 0° and 60° plotted in (a)). 49
23. (a to c) Parameters in the Hertzian model with attractive forces, Eq. 4.2, in the static (black) and dynamic (red) regimes. The static results derive directly from the results plotted in Figure 22a, while dynamic results are obtained from the maximum stress found at large, formally infinite, sliding distances. (d) Friction coefficient at zero load as a function of the angle of the selected sliding directions for the static and dynamic regimes. (e) Static friction coefficient calculated along selected sliding directions as a function of σ_{load} , obtained from the derivative of σ_s , with respect to σ_{load} (Fig. 22a), using the parameters of Eq. 4.2. 51
24. DFT relaxed geometries found for different conformers of the pTmDC molecule. Legends: C- cis, T- trans; subscript pl - planar, p - parallel and np - non-parallel (see definitions in the text). Numbers next to the labels are relative energies in kJ/mol. Blue ends represent the N atoms, white ends H atoms and grey color corresponds to C atoms. 55
25. The DFT calculated MEP of the isomerization process considered by rotating one end ring of the molecule by 360° around its backbone using the NEB method. Colors as in Fig. 24. Reading the graph from left to right, the obtained geometries correspond to a clockwise rotation of the front ring. Correspondingly, each conformer has two possible paths for isomerization into another one following one of the two possible directions. 57

26. DFT calculated binding energies (in kJ/mol, the central panel) and relaxed geometries of dimers considered here. The legend used to denote the dimers means: the first two characters are composed of either C or T corresponding to the cis or trans conformations of the constituent monomers; the next letter is either L, T, P, Tri or Lin and refers to L-like, T-like, Parallel, Triangular or Linear forms, respectively; the index 1 or 2 that follows corresponds to the number of hydrogen bonds in the dimer; finally, a n subscript is used for non-planar triangular dimers, and a subscript a or b is used to differentiate between similar parallel structures involved in the H-bond, respectively, when they have one or two benzonitrile rings in each monomer. All dimers are numbered from 1 to 20, and their binding energies are shown in the plot in the centre of the Figure. Around the energy plot all 20 relaxed structures are shown. Yellow and green frames are used to indicate stable non-planar and planar geometries, respectively, while the red frame is used for unstable planar structures found. 58
27. Electronic density difference maps of the most representative dimers with the hydrogen bonds distances being between 2.37 and 2.61 Å. The purple isosurface indicates an excess and the maroon a depletion of the electron density in the dimers compared to two isolated monomers. Isosurfaces are drawn at $\pm 0,0007$ electron/Å³. 61
28. Comparison of the charge density difference (A) and NCI (B) plots for the dimer CC-P_{2b}. In (A) the same colours and the density value were used as in Fig. 27, while the value of $s = 0,5$ was used in (B) for the NCI plot (see Section Methods for the explanation of the colour scheme used), 61
29. DFT relaxed considered ribbon conformations. The building-block motif is boxed in green. C or T letters denote cis or trans monomers. Notice that subscript A and B refer to chains formed by parallel dimers of kind P_{2a} and P_{2b}, respectively, and Lin for the linear one (see Fig. 26). Yellow and green numbers correspond to the binding energies (in kJ/mol) of the non-planar and planar geometries, respectively. Charge density differences are shown for each structure with the color scheme as in Fig. 27. 63

30. Some structures observed experimentally in STM images (adapted with permission from Ref. 83) and its proposed atomistic models constructed from the dimers building-blocks. Different linkers involved in the structure are placed in a green box-like frame. 64
31. DFT relaxed geometries and binding energies (in kJ/mol) of several linkers investigated in this study. The actual systems computed were isolated clusters containing several molecules; they are indicated by a box-like green frame. In each case also a schematics is given of how ribbons may actually connect to the linkers; the molecules in the ribbons were not included in the calculations. Legend: the first three characters, either C or T, show which monomers are involved in the linker. Prime is used to note that trans isomers in the linker are stereoisomers. The index Lin is used when all monomers are parallel, while Tri is used if they form a triangle; finally, B designates the linker type when the features of both conformations (Lin and Tri) are present. Yellow numbers correspond to the binding energies of non-planar, while green for the relaxed planar conformations; red color is used for the unstable planar triangular structure. 65
32. Docking sites on the Ag (111) surface. T label is used for top sites, B, C and D are used for the different bridge sites, and F and H are used for the fcc and hcp hollow sites respectively. Red dotted line indicates the primitive surface unit cell. The angle the backbone of the molecule makes with respect to one of the Ag-Ag surface symmetry directions (chosen as the horizontal axis in the picture) are considered positive if measured in the counterclockwise (green alpha) and negative if measured in the clockwise directions (purple alpha), respectively. Orange balls represent silver atoms. 69
33. Twelve most stable cis conformers (C) on the surface found after the DFT geometry relaxation. The suggested nomenclature is meant to indicate the adsorption site and orientation of the molecule. The first subscript indicates the docking site of the left N atom, the second subscript indicates the docking site of the right N atom, and the number after the comma indicates the alpha angle (see Fig. 32). The corresponding binding energies (in kilojoules per mole) are also given underneath the symbol of the structure in round brackets. Orange, gray, white and blue balls correspond to Ag, C, H and N atoms, respectively. 70

34. Twelve most stable trans conformers (T) on the surface found after the DFT geometry relaxation. The subscript of the nomenclature for each structure and the color code used are the same as in Fig. 33. When both N atoms align along a vertical line, then the first subscript refers to the bottom atom. The corresponding binding energies (in kilojoules per mole) are also given. Only L isomers are shown for clarity; the corresponding D isomers with identical binding energies are obtained by appropriate flipping of the molecules (not shown). 71
35. Comparison of the charge density difference (A,B) and NCI (C,D) plots for the cis $C_{TT,0}$ (A,C) and trans $T_{TT,1}$ (B,D) monomers adsorbed on the Ag(111) surface. In (A,B) the purple isosurface indicates an excess and the maroon depletion of the electron density, with the isosurfaces drawn at $\pm 0,0007$ electron/ \AA^3 . The value of $s = 0,5$ was used in (C,D) for the NCI plots, see Methods for the explanation of the color scheme used. 72
36. Comparison of PDOS for the cis structure $C_{TT,0}$ (solid lines) and the molecule in the gas phase (dashed line). The inset shows the region around the metal Fermi energy in more detail. Notice the negligible contribution of the monomer to the DOS in this region 73
37. Cis-trans isomerization transition paths connecting the initial T (A) and final C (D) configurations via two possible mechanisms: (i) the upper-side with the transition state (B), and (ii) the under-side with the transitions state (C). 74
38. Diffusion paths for a C monomer on the Ag(111) surface. In the top-left panel the pivoting (blue) and sliding (red) MEP bands are shown labeled with the corresponding states shown in separate panels: initial and final (A and B), transition (C, F, E) and intermediate (D) states, as well as their geometries (top and perspective views). In the transition and intermediate states a ghost image of the molecule is superimposed showing its previous state. 75
39. Diffusion paths for a T monomer on the Ag(111) surface. For the explanations, see the caption to Fig. 38 76

40. A selection of DFT relaxed dimers on the silver surface together with the corresponding total binding energies per molecule (in round brackets), and H bonding energies (in square brackets), all given in kJ/mol. The legend used to denote the dimers means: the first two characters are composed of either C or T corresponding to the cis or trans conformations of the constituent monomers; the next letters are either P or Tri referring to either parallel or triangular forms; the index 1 or 2 that follows corresponds to the number of hydrogen bonds in the dimer; finally, a subscript *a* or *b* is used to differentiate between similar structures. 77
41. Electron density plots of the dimer CC-P_{2a} on the surface. EDD side (A) and top (B) views. NCI side (C) and top (D) views. NCI showing the H bonds and attractive dispersion interaction between the carbonitrile groups in a dimer without (E) and with (F) the surface. Note the bigger green area in (F) related with the dispersion interactions between carbonitrile groups. The same color scheme as in Fig. 35 is used. 79
42. Schematics of the *assisted isomerization* reaction between two molecules on the surface: (A) the right molecule weakens its bonding and detaches from the left molecule increasing the system energy; (B) the right incoming molecule establishes a double H bond with the left molecule reducing the energy of the system. 80
43. The MEP of cis-assisted isomerization and the NEB+DFT relaxed geometries of the initial (A), final (D), and transition states for the upper-side (B) and under-side (C) mechanisms. 80
44. The MEP (left panel) and the initial (A), final (C) and transition state (B) geometries for the NEB+DFT relaxed isomerization transition between a T-T and a T-C dimers. 81
45. Relaxed geometries and corresponding binding energies (per molecule, in brackets and in kilojoules per mole) of the CC_A and TT_A ribbons on the silver surface. 81
46. Relaxed geometries and corresponding binding energies (per molecule, in brackets, in kilojoules per mole) of several linker clusters on the silver surface. 82
47. MEP (left panel) of the cis-trans isomerization of a monomer inside an island. Initial (A), transition (B), and final state (C) relaxed geometries (top and side views) obtained with the NEB+DFT method. 83

48. High resolution STM images (adapted with permission from Ref. 83) of pTmDC islands on the silver surface at room temperature. White circles indicate additional bright areas between chains. 84
49. Schematic view of configurations, interactions and moves implemented in the KMC simulation. (A) All 12 possible non-equivalent states of a monomer on the surface. The central point of the hexagon is the net point occupied by the molecule. (B) Various arrangements for a monomer (placed in the center) with its four neighbors (only some may be present in a real simulation). Strength of the pair interactions is indicated with green labels (from A to F), which values were tuned according to our DFT results and are detailed in the light gray box (in kJ/mol). Only shown interactions for monomers 1 to 4. Two more sets of interactions exist by rotating the monomers by 60° (monomers 5 to 8) and 120° (monomers 9 to 12), that yields a total of 192 interactions. (C) The four diffusion mechanisms for a representative monomer. (D) Possible isomerization transformations for an isolated molecule and (E) the assisted isomerization transformations, where the barrier for the reaction “a” is the same as for an isolated monomer and “b” involves the breaking of one H bond. The energy barriers (in brackets) are given in kJ/mol. Blue rectangle represents the aromatic chain of the monomer, orange circles the carbonitrile groups, and the vertices of the hexagonal grid are the Ag atoms of the surface. 85
50. Sections of 85x85 KMC cells simulation with a 20% coverage and a 10^{-7} deposition rates compared with experimental results, adapted with permission from Ref. 83. Experimental STM high-resolution image was taken at 8 K on Ag(111) with a coverage of 0.1 ML. A, B and C STM images has been horizontally mirrored to facilitate the comparison with the simulation that was run at 200 K. Simulation of D and E was run at 175 K. A) Long quiral chain formed by L-trans with a TCC-Lin linker in the middle forming a kink. B) Long quiral chains formed by D-trans, with some molecules aggregated around a kink. CCC-Lin liker binds a long L-trans with a short D-trans chain. C) Two long chains of the two different stereoisomers bound by a double CCC-Lin linker. D) Long parallel chains with all kinds of linkers. E) A small piece of an island formed by a mixture of C and both T isomers. Green rectangles represent cis, blue D-trans, and magenta L-trans isomers. 89

51. Snapshot of a KMC simulation at 300 K with the coverage of 20 % in a 85x85 cell, and a deposition rate of 10^{-7}ps^{-1} . Green, purple and blue rectangles are cis, L-trans and D-trans monomers, respectively. Their proportions are given with the same color code at the bottom in the image. The KMC step number and the simulation time corresponding to the snapshot are also indicated. 90
52. A snapshot of a KMC run corresponding to the 50x50 simulation cell for 300K, the coverage of 50 % and deposition rate of 10^{-7}ps^{-1} . The same color code as in Fig. 51 is used. 91
53. A snapshot of a KMC run corresponding to the 50x50 simulation cell for 300K, the coverage of 80 % and deposition rate of $10 \cdot 10^{-7} \text{ps}^{-1}$. The same color code as in Fig. 51 is used. 91
54. Cover Art related to the paper: Building Motifs during Self-Assembly of para-Terphenyl-meta-dicarbonitrile on a Metal Surface: A Gas-Phase Study. 195

BIBLIOGRAFÍA

- [1] ABBASI-PÉREZ, D., RECIO, J. M. and KANTOROVICH, L. (2014), «Building Motifs During Self-Assembly of para-Terphenyl-meta-Dicarbonitrile on a Metal Surface: a Gas Phase Study», *J. Phys. Chem. C*, vol. 118, pp. 10 358–10 365. (Cited on pages 76, 78, 81, 82, 96, 100, 193, and 194.)
- [2] ABBASI-PÉREZ, D., RECIO, J. M. and KANTOROVICH, L. (2015), «Role of Isomerization in Kinetics of Self-Assembly: p-Terphenyl-m-Dicarbonitrile on Ag(111) Surface», *PCCP*, vol. Accepted, minor corrections. (Cited on page 193.)
- [3] ABBASI-PÉREZ, D., MENÉNDEZ, J., RECIO, J., OTERO-DE-LA ROZA, A., DEL CORRO, E., TARAVILLO, M., BAONZA, V. and MARQUÉS, M. (2014), «Modeling graphite under stress: Equations of state, vibrational modes, and interlayer friction», *Phys. Rev. B*, vol. 90 (5), p. 054 105. (Cited on pages 6, 42, 46, 48, and 193.)
- [4] AKAHAMA, Y. and KAWAMURA, H. (2005), «Raman study on the stress state of [111] diamond anvils at multimegabar pressure», *J. Appl. Phys.*, vol. 98 (8), p. 083 523. (Cited on page 46.)
- [5] ARRAS, E., SEITSONEN, A. P., KLAPPENBERGER, F. and BARTH, J. V. (2012), «Nature of the Attractive Interaction Between Proton Acceptors and Organic Ring Systems», *Phys. Chem. Chem. Phys.*, vol. 14, p. 15 995. (Cited on pages 7 and 60.)
- [6] ASHCROFT, N. W. and MERMIN, N. D. (1976), *Solid State Physics*. (Cited on page 12.)
- [7] BANDYOPADHYAY, A., PATI, R., SAHU, S., PEPPER, F. and FUJITA, D. (2010), «Massively Parallel computing on an Organic Molecular Layer», *Nat. Phys.*, vol. 6 (5), pp. 369–375. (Cited on pages 6 and 7.)
- [8] BAONZA, V. G., TARAVILLO, M., ARENCIBIA, A., CACERES, M. and NÚÑEZ, J. (2003), «Diamond as pressure sensor in high-pressure Raman spectroscopy using sapphire and other gem anvil cells», *J. Raman Spectrosc.*, vol. 34 (4), pp. 264–270. (Cited on page 41.)
- [9] BARLOW, S. M. and RAVAL, R. (2003), «Complex Organic Molecules at Metal Surfaces: Bonding, Organisation and Chirality», *Surf. Sci. Rep.*, vol. 50 (6), pp. 201–341. (Cited on page 7.)
- [10] BARTH, J. V., COSTANTINI, G. and KERN, K. (2005), «Engineering Atomic and Molecular Nanostructures at Surfaces», *Nature*, vol. 437, pp. 671–679. (Cited on pages 6 and 7.)

- [11] BAUGHMAN, R. H. (2003), «Auxetic materials: Avoiding the shrink», *Nature*, vol. 425 (6959), pp. 667–667. (Cited on page 45.)
- [12] BHUSHAN, B. (2013), *Introduction to tribology*, John Wiley & Sons. (Cited on page 5.)
- [13] BHUSHAN, B., ISRAELACHVILI, J. N. and LANDMAN, U. (1995), «Nanotribology: friction, wear and lubrication at the atomic scale», *Nature*, vol. 374 (6523), pp. 607–616. (Cited on page 5.)
- [14] BLANCO, M. A., FRANCISCO, E. and LUNA, V. (2004), «GIBBS: isothermal-isobaric thermodynamics of solids from energy curves using a quasi-harmonic Debye model», *Comput. Phys. Comm.*, vol. 158 (1), pp. 57–72, URL <http://www.sciencedirect.com/science/article/pii/S0010465503005472>. (Cited on pages 3, 11, 12, and 13.)
- [15] BORN, M. (1940), «On the stability of crystal lattices. I», in «Mathematical Proceedings of the Cambridge Philosophical Society», vol. 36, pp. 160–172, Cambridge Univ Press. (Cited on page 50.)
- [16] BOSAK, A., KRISCH, M., MOHR, M., MAULTZSCH, J. and THOMSEN, C. (2007), «Elasticity of single-crystalline graphite: inelastic X-ray scattering study», *Phys. Rev. B*, vol. 75 (15), p. 153 408. (Cited on page 45.)
- [17] BOUDEN, F. and TABOR, D. (1954), *The Friction and Lubrication of Solids*, Oxford. (Cited on page 6.)
- [18] BOULFELFEL, S. E., OGANOV, A. R. and LEONI, S. (2012), «Understanding the nature of “superhard graphite”», *Sci. Rep.*, vol. 2. (Cited on page 48.)
- [19] BOWDEN, F. and LEBEN, L. (1938), «Nature of sliding and the analysis of friction», *Nature*, vol. 141, p. 691. (Cited on page 5.)
- [20] BOYS, S. and BERNARDI, F. (1970), «The Calculation of Small Molecular Interactions by the Differences of Separate Total Energies. Some Procedures with Reduced Errors», *Mol. Phys.*, vol. 19, p. 553. (Cited on pages 54 and 68.)
- [21] BUCKO, T., HAFNER, J., LEBEGUE, S. and ANGYÁN, J. G. (2010), «Improved description of the structure of molecular and layered crystals: ab initio DFT calculations with van der Waals corrections», *J. Phys. Chem. A*, vol. 114 (43), pp. 11 814–11 824. (Cited on page 6.)
- [22] CHARLIER, J.-C., GONZE, X. and MICHENAUD, J.-P. (1991), «First-principles study of the electronic properties of graphite», *Phys. Rev. B*, vol. 43 (6), p. 4579. (Cited on page 33.)

- [23] CHARLIER, J.-C., MICHENAUD, J.-P. and GONZE, X. (1992), «First-principles study of the electronic properties of simple hexagonal graphite», *Phys. Rev. B*, vol. 46 (8), p. 4531. (Cited on page 33.)
- [24] COLONNA, F., FASOLINO, A. and MEIJER, E. (2011), «High-pressure high-temperature equation of state of graphite from Monte Carlo simulations», *Carbon*, vol. 49 (2), pp. 364–368. (Cited on pages 4, 27, and 29.)
- [25] CONTRERAS-GARCÍA, J., YANG, W. and JOHNSON, E. R. (2011), «Analysis of Hydrogen-Bond Interaction Potentials from the Electron Density: Integration of Noncovalent Interaction Regions», *J. Phys. Chem. A*, vol. 115 (45), pp. 12 983–12 990. (Cited on pages 54, 60, 68, and 72.)
- [26] CONTRERAS-GARCÍA, J., CALATAYUD, M., PIQUEMAL, J.-P. and RECIO, J. (2012), «Ionic Interactions: Comparative Topological Approach», *Comput. Theor. Chem.*, vol. 998 (0), pp. 193 – 201. (Cited on pages 54, 68, and 72.)
- [27] DE ANDRES, P., GUINEA, F. and KATSNELSON, M. (2012), «Density functional theory analysis of flexural modes, elastic constants, and corrugations in strained graphene», *Phys. Rev. B*, vol. 86 (24), p. 245 409. (Cited on pages 29 and 33.)
- [28] DE ANDRES, P., RAMÍREZ, R. and VERGÉS, J. A. (2008), «Strong covalent bonding between two graphene layers», *Phys. Rev. B*, vol. 77 (4), p. 045 403. (Cited on page 33.)
- [29] DEL CORRO, E., TARAVILLO, M. and BAONZA, V. G. (2012), «Nonlinear strain effects in double-resonance Raman bands of graphite, graphene, and related materials», *Phys. Rev. B*, vol. 85 (3), p. 033 407. (Cited on pages 41 and 44.)
- [30] DEL CORRO, E., GONZÁLEZ, J., TARAVILLO, M., FLAHAUT, E. and BAONZA, V. G. (2008), «Raman spectra of double-wall carbon nanotubes under extreme uniaxial stress», *Nano Lett.*, vol. 8 (8), pp. 2215–2218. (Cited on page 41.)
- [31] DEL CORRO, E., TARAVILLO, M., GONZÁLEZ, J. and BAONZA, V. (2011), «Raman characterization of carbon materials under non-hydrostatic conditions», *Carbon*, vol. 49 (3), pp. 973–979. (Cited on pages 4 and 44.)
- [32] DEL CORRO, E., OTERO-DE-LA ROZA, A., TARAVILLO, M. and BAONZA, V. G. (2012), «Raman modes and Grüneisen parameters of graphite under compressive biaxial stress», *Carbon*, vol. 50 (12), pp. 4600–4606. (Cited on pages 4, 41, 44, and 45.)
- [33] DEL CORRO, E., IZQUIERDO, J., GONZÁLEZ, J., TARAVILLO, M. and BAONZA, V. (2013), «3D Raman mapping of uniaxially loaded 6H-SiC crystals», *J. Raman Spectrosc.*, vol. 44 (5), pp. 758–762. (Cited on pages 6, 43, and 46.)

- [34] DEL CORRO, E., ABBASI-PÉREZ, D., MENÉNDEZ, J., RECIO, J., OTERO-DE-LA ROZA, A., TARAVILLO, M., BAONZA, V. and MARQUÉS, M. (2014), «Frictional forces in graphite under compression», *Phys. Rev. B (Submitted)*, vol. xxx (xxx), p. xxx. (Cited on page 32.)
- [35] DENG, Z., SMOLYANITSKY, A., LI, Q., FENG, X.-Q. and CANNARA, R. J. (2012), «Adhesion-dependent negative friction coefficient on chemically modified graphite at the nanoscale», *Nat. Mater.*, vol. 11 (12), pp. 1032–1037. (Cited on pages 5, 94, and 98.)
- [36] DIENWIEBEL, M., VERHOEVEN, G. S., PRADEEP, N., FRENKEN, J. W., HEIMBERG, J. A. and ZANDBERGEN, H. W. (2004), «Superlubricity of graphite», *Phys. Rev. Lett.*, vol. 92 (12), p. 126 101. (Cited on pages 5, 38, and 51.)
- [37] DIRAC, P. A. (1929), «Quantum mechanics of many-electron systems», in «Proceedings of the Royal Society of London A: Mathematical, Physical and Engineering Sciences», vol. 123, pp. 714–733, The Royal Society. (Cited on page 1.)
- [38] DIVINCENZO, D., MELE, E. and HOLZWARTH, N. (1983), «Density-functional study of interplanar binding in graphite», *Phys. Rev. B*, vol. 27 (4), p. 2458. (Cited on page 33.)
- [39] DONG, Y., VADAKKEPATT, A. and MARTINI, A. (2011), «Analytical models for atomic friction», *Tribol. Lett.*, vol. 44 (3), pp. 367–386. (Cited on pages 5, 46, and 48.)
- [40] ERRANDONEA, D., PELLICER-PORRES, J., MANJÓN, F. J., SEGURA, A., FERRER-ROCA, C., KUMAR, R. S., TSCHAUNER, O., LÓPEZ-SOLANO, J., RODRÍGUEZ-HERNÁNDEZ, P., RADESCU, S., MUJICA, A., MUÑOZ, A. and AQUILANTI, G. (2006), «Determination of the high-pressure crystal structure of BaWO₄ and PbWO₄», *Phys. Rev. B*, vol. 73, p. 224 103. (Cited on pages 15, 17, 20, and 197.)
- [41] FERRARO, J. R. (2006), *Vibrational Spectroscopy at High External Pressures*, John Wiley & Sons, Ltd. (Cited on page 6.)
- [42] FILLETER, T., MCCHESENEY, J., BOSTWICK, A., ROTENBERG, E., EMTSEV, K., SEYLLER, T., HORN, K. and BENNEWITZ, R. (2009), «Friction and dissipation in epitaxial graphene films», *Phys. Rev. Lett.*, vol. 102 (8), p. 086 102. (Cited on page 5.)
- [43] FLECHE, J. L. (2002), «Thermodynamical functions for crystals with large unit cells such as zircon, coffinite, fluorapatite, and iodoapatite from *ab initio* calculations», *Phys. Rev. B*, vol. 65, p. 245 116. (Cited on pages 3, 12, and 13.)
- [44] FLÓREZ, M., CONTRERAS-GARCÍA, J., RECIO, J. M. and MARQUÉS, M. (2009), «Quantum-mechanical calculations of zircon to scheelite transition pathways in ZrSiO₄», *Phys. Rev. B*, vol. 79, p. 104 101. (Cited on page 22.)

- [45] FRANCISCO, E., BERMEJO, M., BAONZA, V. G., GERWARD, L. and RECIO, J. (2003), «Spinodal equation of state for rutile TiO₂», *Phys. Rev. B*, vol. 67 (6), p. 064 110. (Cited on page 50.)
- [46] FRANK, I., TANENBAUM, D. M., VAN DER ZANDE, A. and MCEUEN, P. L. (2007), «Mechanical properties of suspended graphene sheets», *J. Vac. Sci. Technol., B*, vol. 25 (6), pp. 2558–2561. (Cited on page 29.)
- [47] GIANNOZZI, P., BARONI, S., BONINI, N., CALANDRA, M., CAR, R., CAVAZZONI, C., CERESOLI, D., CHIAROTTI, G. L., COCCIONI, M., DABO, I. and OTHERS (2009), «QUANTUM ESPRESSO: a modular and Open-Source software project for quantum simulations of materials», *J. Phys. Condens. Matter*, vol. 21 (39), p. 395 502. (Cited on pages 14, 25, and 42.)
- [48] GOEDECKER, S., TETER, M. and HUTTER, J. (1996), «Separable Dual-Space Gaussian Pseudopotentials», *Phys. Rev. B*, vol. 54, pp. 1703–1710. (Cited on pages 53 and 67.)
- [49] GONCHAROV, A. F. (1992), «Graphite at high pressures: Amorphization at 44 GPa», *High Pressure Res.*, vol. 8 (4), pp. 607–616. (Cited on pages 4 and 44.)
- [50] GRIMME, S. (2006), «Semiempirical GGA-type density functional constructed with a long-range dispersion correction», *J. Comput. Chem.*, vol. 27 (15), pp. 1787–1799. (Cited on pages 6, 25, and 42.)
- [51] GRIMME, S., ANTONY, J., EHRlich, S. and KRIEG, H. (2010), «A consistent and accurate ab initio parametrization of density functional dispersion correction (DFT-D) for the 94 elements H-Pu», *J. Chem. Phys.*, vol. 132 (15), 154104. (Cited on pages 53 and 67.)
- [52] GUO, Y., GUO, W. and CHEN, C. (2007), «Modifying atomic-scale friction between two graphene sheets: A molecular-force-field study», *Phys. Rev. B*, vol. 76 (15), p. 155 429. (Cited on page 33.)
- [53] HANFLAND, M., BEISTER, H. and SYASSEN, K. (1989), «Graphite under pressure: Equation of state and first-order Raman modes», *Phys. Rev. B*, vol. 39 (17), p. 12 598. (Cited on pages 4, 29, 32, 33, 36, 44, 45, 46, 50, and 199.)
- [54] HENKELMAN, G. and JÓNSSON, H. (2000), «Improved Tangent Estimate in the Nudged Elastic Band Method for Finding Minimum Energy Paths and Saddle Points», *J. Chem. Phys.*, vol. 113 (22), pp. 9978–9985. (Cited on pages 54, 56, and 68.)
- [55] HENKELMAN, G., UBERUAGA, B. P. and JÓNSSON, H. (2000), «A Climbing Image Nudged Elastic Band Method for Finding Saddle Points and Minimum Energy Paths», *J. Chem. Phys.*, vol. 113 (22), pp. 9901–9904. (Cited on pages 54, 56, and 68.)

- [56] HIRANO, M. and SHINJO, K. (1990), «Atomistic locking and friction», *Phys. Rev. B*, vol. 41, pp. 11 837–11 851. (Cited on page 5.)
- [57] HOHENBERG, P. and KOHN, W. (1964), «Inhomogeneous Electron Gas», *Phys. Rev.*, vol. 136, pp. B864–B871. (Cited on pages 1, 53, and 67.)
- [58] HOLZAPFEL, W. (1996), «Physics of Solids Under Strong Compression», *Rep. Prog. Phys.*, vol. 59 (1), p. 29. (Cited on page 3.)
- [59] JOHNSON, E. R., KEINAN, S., MORI-SÁNCHEZ, P., CONTRERAS-GARCÍA, J., COHEN, A. J. and YANG, W. (2010), «Revealing Noncovalent Interactions», *J. Am. Chem. Soc.*, vol. 132 (18), pp. 6498–6506. (Cited on pages 54, 68, and 72.)
- [60] JOHNSON, K. L. and JOHNSON, K. L. (1987), *Contact mechanics*, Cambridge university press. (Cited on pages 48 and 49.)
- [61] JÓNSSON, H., MILLS, G. and JACOBSEN, K. W. (1998), *Classical and Quantum Dynamics in Condensed Phase Simulations*, chap. Nudged Elastic Band Method for Finding Minimum Energy Paths of Transitions, World Scientific. (Cited on pages 9, 54, and 68.)
- [62] JURECKA, P., SPONER, J., CERNY, J. and HOBZA, P. (2006), «Benchmark Database of Accurate (MP2 and CCSD(T) Complete Basis Set Limit) Interaction Energies of Small Model Complexes, DNA Base Pairs, and Amino Acid Pairs», *Phys. Chem. Chem. Phys.*, vol. 8, p. 1985. (Cited on pages 53 and 60.)
- [63] KAMITANI, K., GRIMSDITCH, M., NIPKO, J., LOONG, C.-K., OKADA, M. and KIMURA, I. (1997), «The elastic constants of silicon carbide: A Brillouin-scattering study of 4H and 6H SiC single crystals», *J. Appl. Phys.*, vol. 82 (6), pp. 3152–3154. (Cited on page 46.)
- [64] KANTOROVICH, L. (1996-2014), «User-friendly visualisation program for ab initio DFT codes», URL <http://www.mth.kcl.ac.uk/~lev/codes/lev00/index.html>. (Cited on page 26.)
- [65] KELLY, R. E. A. and KANTOROVICH, L. (2006), «Planar Nucleic Acid Base Super-Structures», *J. Mater. Chem.*, vol. 16, pp. 1894–1905. (Cited on pages 59, 68, and 72.)
- [66] KELLY, R. E. A., LUKAS, M., KANTOROVICH, L. N., OTERO, R., XU, W., MURA, M., LAESGAARD, E., STENSGAARD, I. and BESENBACHER, F. (2008), «Understanding disorder of the DNA base cytosine on the Au(111) surface», *J. Chem. Phys.*, vol. 129, p. 184 707. (Cited on page 7.)
- [67] KITT, A. L., QI, Z., RÉMI, S., PARK, H. S., SWAN, A. K. and GOLDBERG, B. B. (2013), «How graphene slides: measurement and theory of strain-dependent frictional

- forces between graphene and SiO₂», *Nano Lett.*, vol. 13 (6), pp. 2605–2610. (Cited on page 5.)
- [68] KLOTZ, S., CHERVIN, J., MUNSCH, P. and LE MARCHAND, G. (2009), «Hydrostatic limits of 11 pressure transmitting media», *J. Phys. D: Appl. Phys.*, vol. 42 (7), p. 075 413. (Cited on page 4.)
- [69] KOHN, W. and SHAM, L. J. (1965), «Self-Consistent Equations Including Exchange and Correlation Effects», *Phys. Rev.*, vol. 140, pp. A1133–A1138. (Cited on pages 1, 53, and 67.)
- [70] KRESSE, G. and FURTHMÜLLER, J. (1996), «Efficient iterative schemes for ab initio total-energy calculations using a plane-wave basis set», *Phys. Rev. B*, vol. 54, pp. 11 169–11 186. (Cited on pages 15, 25, and 42.)
- [71] LACOMBA-PERALES, R., MARTÍNEZ-GARCÍA, D., ERRANDONEA, D., LE GODEC, Y., PHILIPPE, J., LE MARCHAND, G., CHERVIN, J. C., POLIAN, A., MÚÑOZ, A. and LÓPEZ-SOLANO, J. (2010), «Experimental and theoretical investigation of the stability of the monoclinic BaWO₄-II phase at high pressure and high temperature», *Phys. Rev. B*, vol. 81, p. 144 117. (Cited on pages 15, 16, 18, 19, 20, 21, and 197.)
- [72] LATIL, S. and HENRARD, L. (2006), «Charge carriers in few-layer graphene films», *Phys. Rev. Lett.*, vol. 97 (3), p. 036 803. (Cited on page 33.)
- [73] LEE, C., WEI, X., KYSAR, J. W. and HONE, J. (2008), «Measurement of the elastic properties and intrinsic strength of monolayer graphene», *Science*, vol. 321 (5887), pp. 385–388. (Cited on page 29.)
- [74] LEE, C., LI, Q., KALB, W., LIU, X.-Z., BERGER, H., CARPICK, R. W. and HONE, J. (2010), «Frictional characteristics of atomically thin sheets», *Science*, vol. 328 (5974), pp. 76–80. (Cited on page 5.)
- [75] LIANG, Y., MIRANDA, C. R. and SCANDOLO, S. (2007), «Tuning oxygen packing in silica by nonhydrostatic pressure», *Phys. Rev. Lett.*, vol. 99 (21), p. 215 504. (Cited on page 4.)
- [76] LIPPERT, G., JURG, H. and PARRINELLO, M. (1997), «A Hybrid Gaussian and Plane Wave Density Functional Scheme», *Mol. Phys.*, vol. 92 (3), pp. 477–488. (Cited on pages 53 and 67.)
- [77] LIU, X., METCALF, T. H., ROBINSON, J. T., HOUSTON, B. H. and SCARPA, F. (2012), «Shear modulus of monolayer graphene prepared by chemical vapor deposition», *Nano Lett.*, vol. 12 (2), pp. 1013–1017. (Cited on page 50.)

- [78] LIU, Z., YANG, J., GREY, F., LIU, J. Z., LIU, Y., WANG, Y., YANG, Y., CHENG, Y. and ZHENG, Q. (2012), «Observation of microscale superlubricity in graphite», *Phys. Rev. Lett.*, vol. 108 (20), p. 205 503. (Cited on page 5.)
- [79] MALARD, L., PIMENTA, M., DRESSSELHAUS, G. and DRESSSELHAUS, M. (2009), «Raman spectroscopy in graphene», *Phys. Rep.*, vol. 473 (5), pp. 51–87. (Cited on pages 6 and 50.)
- [80] MANJÓN, F. J., ERRANDONEA, D., GARRO, N., PELLICER-PORRES, J., RODRIGUEZ-HERNÁNDEZ, P., RADESCU, S., LÓPEZ-SOLANO, J., MUJICA, A. and MUÑOZ, A. (2006), «Lattice dynamics study of scheelite tungstates under high pressure I. BaWO₄», *Phys. Rev. B*, vol. 74, p. 144 111. (Cited on pages 16 and 197.)
- [81] MARQUÉS, M., MCMAHON, M. I., GREGORYANZ, E., HANFLAND, M., GUILLAUME, C. L., PICKARD, C. J., ACKLAND, G. J. and NELMES, R. J. (2011), «Crystal Structures of Dense Lithium: A Metal-Semiconductor-Metal Transition», *Phys. Rev. Lett.*, vol. 106, p. 095 502. (Cited on page 1.)
- [82] MARQUÉS, M., SANTORO, M., GUILLAUME, C. L., GORELLI, F. A., CONTRERAS-GARCÍA, J., HOWIE, R. T., GONCHAROV, A. F. and GREGORYANZ, E. (2011), «Optical and electronic properties of dense sodium», *Phys. Rev. B*, vol. 83, p. 184 106. (Cited on page 1.)
- [83] MARSCHALL, M., REICHERT, J., SEUFERT, K., AUWRÄRTER, W., KLAPPENBERGER, F., WEBER-BARGIONI, A., KLYATSKAYA, S., ZOPPELLARO, G., NEFEDOV, A., STRUNSKUS, T., WÖLL, C., RUBEN, M. and BARTH, J. V. (2010), «Supramolecular Organization and Chiral Resolution of p-Terphenyl-m-Dicarbonitrile on the Ag(111) Surface», *ChemPhysChem*, vol. 11 (7), pp. 1446–1451. (Cited on pages 7, 8, 56, 57, 60, 62, 63, 64, 73, 78, 82, 83, 84, 86, 87, 89, 95, 96, 99, 100, 101, 202, and 205.)
- [84] MATE, C., MCCLELLAND, G., ERLANDSSON, R., CHIANG, S. and OTHERS (1987), «Atomic-scale friction of a tungsten tip on a graphite surface.», *Phys. Rev. Lett.*, vol. 59 (17), p. 1942. (Cited on pages 5 and 44.)
- [85] MAUGIS, D. (1992), «Adhesion of spheres: the JKR-DMT transition using a Dugdale model», *J. Colloid Interface Sci.*, vol. 150 (1), pp. 243–269. (Cited on page 50.)
- [86] MAUGIS, D. (2000), *Contact, adhesion and rupture of elastic solids*, vol. 130, Springer. (Cited on pages 6, 36, 38, and 51.)
- [87] MILLOT, M., DUBROVINSKAIA, N., ČERNOK, A., BLAHA, S., DUBROVINSKY, L., BRAUN, D., CELLIERS, P., COLLINS, G., EGGERT, J. and JEANLOZ, R. (2015), «Shock compression of stishovite and melting of silica at planetary interior conditions», *Science*, vol. 347 (6220), pp. 418–420. (Cited on page 2.)

- [88] MILLS, G., JÓNSSON, H. and SCHENTER, G. K. (1995), «Reversible Work Transition State Theory: Application to Dissociative Adsorption of Hydrogen», *Surf. Sci.*, vol. 324 (2-3), pp. 305–337. (Cited on pages 9, 54, and 68.)
- [89] MIŁOWSKA, K., BIROWSKA, M. and MAJEWSKI, J. (2011), «Structural and Electronic Properties of Functionalized Graphene», *Acta Phys. Pol. A*, vol. 120, pp. 842–844. (Cited on page 33.)
- [90] MISHRA, M., EGBERTS, P., BENNEWITZ, R. and SZLUFARSKA, I. (2012), «Friction model for single-asperity elastic-plastic contacts», *Phys. Rev. B*, vol. 86 (4), p. 045 452. (Cited on page 6.)
- [91] MO, Y., TURNER, K. T. and SZLUFARSKA, I. (2009), «Friction laws at the nanoscale», *Nature*, vol. 457 (7233), pp. 1116–1119. (Cited on page 5.)
- [92] MONKHORST, H. J. and PACK, J. D. (1976), «Special points for Brillouin-zone integrations», *Phys. Rev. B*, vol. 13, pp. 5188–5192. (Cited on page 14.)
- [93] MONKHORST, H. J. and PACK, J. D. (1976), «Special points for Brillouin-zone integrations», *Phys. Rev. B*, vol. 13, pp. 5188–5192. (Cited on page 25.)
- [94] MURA, M., GULANS, A., THONHAUSER, T. and KANTOROVICH, L. (2010), «Role of Van der Waals Interaction in Forming Molecule-Metal Junctions: Flat Organic Molecules on the Au(111) Surface», *Phys. Chem. Chem. Phys.*, vol. 12, pp. 4759–4767. (Cited on pages 59, 68, and 72.)
- [95] MURA, M., SILLY, F., BURLAKOV, V., CASTELL, M. R., BRIGGS, G. A. D. and KANTOROVICH, L. N. (2012), «Formation Mechanism for a Hybrid Supramolecular Network Involving Cooperative Interactions», *Phys. Rev. Lett.*, vol. 108, p. 176 103. (Cited on pages 6, 7, and 86.)
- [96] MURNAGHAN, F. (1944), «The compressibility of media under extreme pressures», *Proc. Natl. Acad. Sci. U.S.A.*, vol. 30 (9), p. 244. (Cited on page 50.)
- [97] MUSER, M. H., URBAKH, M. and ROBBINS, M. O. (2003), «Statistical mechanics of static and low-velocity kinetic friction», *Adv. Chem. Phys.*, vol. 126, pp. 187–272. (Cited on page 5.)
- [98] NEMANICH, R., LUCOVSKY, G. and SOLIN, S. (1977), «Infrared active optical vibrations of graphite», *Solid State Commun.*, vol. 23 (2), pp. 117–120. (Cited on page 32.)
- [99] NEMANICH, R. J. and SOLIN, S. A. (1979), «First- and second-order Raman scattering from finite-size crystals of graphite», *Phys. Rev. B*, vol. 20, pp. 392–401. (Cited on page 44.)

- [100] OTERO, R., SCHOCK, M., MOLINA, L. M., LEGSGAARD, E., STENSGAARD, I., HAMMER, B. and BESENBACHER, F. (2005), «Guanine Quartet Networks Stabilized by Cooperative Hydrogen Bonds», *Angew. Chem. Int. Ed.*, vol. 44, p. 2270. (Cited on pages 59, 68, and 72.)
- [101] OTERO, R., LUKAS, M., KELLY, R. E. A., XU, W., LÆGSGAARD, E., STENSGAARD, I., KANTOROVICH, L. N. and BESENBACHER, F. (2008), «Elementary structural motifs in a random network of cytosine adsorbed on a Au(111) surface», *Science*, vol. 319, pp. 312–315. (Cited on page 7.)
- [102] OTERO-DE-LA ROZA, A., ABBASI-PÉREZ, D. and LUAÑA, V. (2011), «GIBBS2: A new version of the quasiharmonic model code. II. Models for solid-state thermodynamics, features and implementation», *Computer Physics Communications*, vol. 182 (10), pp. 2232–2248. (Cited on pages 3, 13, 20, and 193.)
- [103] PANCHAL, V., GARG, N., CHAUHAN, A., SANGEETA and SHARMA, S. M. (2004), «High pressure phase transitions in BaWO₄», *Solid State Commun.*, vol. 130 (3–4), pp. 203 – 208. (Cited on pages 17 and 197.)
- [104] PARLINSKI, K. (2008), «PHONON Software», URL <http://wolf.ifj.edu.pl/phonon/>. (Cited on page 15.)
- [105] PEÑA-ÁLVAREZ, M., DEL CORRO, E., BAONZA, V. G. and TARAVILLO, M. (2014), «Probing the Stress Effect on the Electronic Structure of Graphite by Resonant Raman Spectroscopy», *J. Phys. Chem. C*, vol. 118 (43), pp. 25 132–25 140. (Cited on page 44.)
- [106] PERDEW, J., BURKE, K. and ERNZERHOF, M. (1996), «Generalized Gradient Approximation Made Simple», *Phys. Rev. Lett.*, vol. 77, p. 3865. (Cited on pages 14, 25, 42, 53, and 67.)
- [107] PROKOPENKO, V., DUBROVINSKY, L., DMITRIEV, V. and WEBER, H.-P. (2001), «In situ characterization of phase transitions in cristobalite under high pressure by Raman spectroscopy and X-ray diffraction», *J. Alloys Compd.*, vol. 327 (1), pp. 87–95. (Cited on page 4.)
- [108] RAN, D., XIA, H., SUN, S., LING, Z., GE, W. and ZHANG, H. (2006), «Thermal conductivity of BaWO₄ single crystal», *Mater. Sci. Eng., B*, vol. 130 (1–3), pp. 206 – 209. (Cited on page 18.)
- [109] RAPPE, A. M., RABE, K. M., KAXIRAS, E. and JOANNOPOULOS, J. D. (1990), «Optimized pseudopotentials», *Phys. Rev. B*, vol. 41, pp. 1227–1230. (Cited on pages 25 and 42.)
- [110] REGUZZONI, M., FASOLINO, A., MOLINARI, E. and RIGHI, M. (2012), «Friction by shear deformations in multilayer graphene», *J. Phys. Chem. C*, vol. 116 (39), pp. 21 104–21 108. (Cited on page 33.)

- [111] REICH, S., THOMSEN, C. and ORDEJON, P. (2002), «Elastic properties of carbon nanotubes under hydrostatic pressure», *Phys. Rev. B*, vol. 65 (15), p. 153 407. (Cited on page 29.)
- [112] REUTER, K., STAMPFL, C. and SCHEFFLER, M. (2005), *Ab initio atomistic thermodynamic and stastical mechanics of surface properties and functions*, vol. Part A of *Handbook of Material Modeling, Part A. Methods*, p. 149, Springer. (Cited on page 86.)
- [113] SARASAMAK, K., KULKARNI, A., ZHOU, M. and LIMPIJUMNONG, S. (2008), «Stability of wurtzite, unbuckled wurtzite, and rocksalt phases of SiC, GaN, InN, ZnO, and CdSe under loading of different triaxialities», *Phys. Rev. B*, vol. 77 (2), p. 024 104. (Cited on page 25.)
- [114] SAVAGE, R. H. (1948), «Graphite lubrication», *J. Appl. Phys.*, vol. 19 (1), pp. 1–10. (Cited on page 5.)
- [115] SAVINI, G., DAPPE, Y., ÖBERG, S., CHARLIER, J.-C., KATSNELSON, M. and FASOLINO, A. (2011), «Bending modes, elastic constants and mechanical stability of graphitic systems», *Carbon*, vol. 49 (1), pp. 62–69. (Cited on pages 4, 27, 29, and 33.)
- [116] SCHRÖDINGER, E. (1926), «An undulatory theory of the mechanics of atoms and molecules», *Physical Review*, vol. 28 (6), p. 1049. (Cited on page 1.)
- [117] SCHWARZ, U. D., ZWÖRNER, O., KÖSTER, P. and WIESENDANGER, R. (1997), «Quantitative analysis of the frictional properties of solid materials at low loads. I. Carbon compounds», *Phys. Rev. B*, vol. 56 (11), p. 6987. (Cited on pages 44 and 49.)
- [118] SMOLYANITSKY, A. and KILLGORE, J. (2012), «Anomalous friction in suspended graphene», *Phys. Rev. B*, vol. 86 (12), p. 125 432. (Cited on page 5.)
- [119] SOCOLIUC, A., BENNEWITZ, R., GNECCO, E. and MEYER, E. (2004), «Transition from stick-slip to continuous sliding in atomic friction: entering a new regime of ultralow friction», *Phys. Rev. Lett.*, vol. 92 (13), p. 134 301. (Cited on pages 5 and 48.)
- [120] TAN, P., HAN, W., ZHAO, W., WU, Z., CHANG, K., WANG, H., WANG, Y., BONINI, N., MARZARI, N., PUGNO, N. and OTHERS (2012), «The shear mode of multilayer graphene», *Nat. Mater.*, vol. 11 (4), pp. 294–300. (Cited on page 36.)
- [121] TINDER, R. F. (2008), *Tensor properties of solids: phenomenological development of the tensor properties of crystals*, vol. 4, Morgan & Claypool Publishers. (Cited on pages 4 and 23.)

- [122] VANDEVONDELE, J. and HUTTER, J. (2007), «Gaussian Basis Sets for Accurate Calculations on Molecular Systems in Gas and Condensed Phases», *J. Chem. Phys.*, vol. 127 (11), 114105. (Cited on pages 53 and 67.)
- [123] VANDEVONDELE, J., KRACK, M., MOHAMED, F., PARRINELLO, M., CHASSAING, T. and HUTTER, J. (2005), «Quickstep: Fast and Accurate Density Functional Calculations Using a Mixed Gaussian and Plane Waves Approach», *Comput. Phys. Commun.*, vol. 167 (2), pp. 103 – 128. (Cited on pages 53 and 67.)
- [124] VANOSSI, A., MANINI, N., URBAKH, M., ZAPPERI, S. and TOSATTI, E. (2013), «Colloquium: Modeling friction: From nanoscale to mesoscale», *Rev. Mod. Phys.*, vol. 85 (2), p. 529. (Cited on page 33.)
- [125] VINET, P., FERRANTE, J., SMITH, J. and ROSE, J. (1986), «A universal equation of state for solids», *J. Phys. C: Solid State Phys.*, vol. 19 (20), p. L467. (Cited on page 15.)
- [126] VOTER, A. F. (2005), *Radiation effects in solids*, NATO Publishing unit Handbook of Material Modeling, Part A. Methods, Springer, NATO Publishing Unit, Dordrecht, The Netherlands. (Cited on page 86.)
- [127] WALLACE, D. C. (1972), «Thermodynamics of Crystals», . (Cited on pages 4 and 23.)
- [128] WANG, Y., ALSMEYER, D. C. and MCCREERY, R. L. (1990), «Raman spectroscopy of carbon materials: structural basis of observed spectra», *Chem. Mater.*, vol. 2 (5), pp. 557–563. (Cited on page 6.)
- [129] WEISS, M. and ELMER, F.-J. (1996), «Dry friction in the Frenkel-Kontorova-Tomlinson model: Static properties», *Phys. Rev. B*, vol. 53 (11), p. 7539. (Cited on page 5.)
- [130] ZAKHARCHENKO, K., KATSNELSON, M. and FASOLINO, A. (2009), «Finite temperature lattice properties of graphene beyond the quasiharmonic approximation», *Phys. Rev. Lett.*, vol. 102 (4), p. 046 808. (Cited on page 30.)
- [131] ZHAO, J., ANGEL, R. and ROSS, N. (2010), «Effects of Deviatoric Stresses in the Diamond-Anvil Pressure Cell on Single-Crystal Samples», *J. Appl. Cryst.*, vol. 43 (4), pp. 743–751. (Cited on page 3.)
- [132] ZHAO, Y. X. and SPAIN, I. L. (1989), «X-ray diffraction data for graphite to 20 GPa», *Phys. Rev. B*, vol. 40 (2), p. 993. (Cited on page 29.)
- [133] ZUREK, E. and GROCHALA, W. (2015), «Predicting crystal structures and properties of matter under extreme conditions via quantum mechanics: the pressure is on», *Phys. Chem. Chem. Phys.*, vol. 17, pp. 2917–2934. (Cited on page 1.)